UNIVERSITÀ DEGLI STUDI DI MILANO

Scuola di Dottorato in Fisica, Astrofisica e Fisica Applicata
Dipartimento di Fisica

Corso di Dottorato in Fisica, Astrofisica e Fisica Applicata
Ciclo XXXV

Characterization and engineering of quantum systems for quantum technologies

Settore Scientifico Disciplinare FIS/03

Supervisore: Professor Matteo G.A. PARIS

Coordinatore: Professor Matteo G.A. PARIS

Tesi di Dottorato di:
Alessandro CANDELORO

Anno Accademico 2022/2023

Commission of the final examination:

External Referee:

Dott.ssa Ilaria SILOI (Università degli Studi di Padova, Italy)
Prof. Vahid KARIMIPOUR (Sharif University of Technology, Iran)
Prof. Alessio SERAFINI (University College London, United Kingdom)

External Member:

Prof.ssa Anna NAPOLI (Università degli Studi di Palermo, Italy)
Prof. Paolo BORDONE (Università degli Studi di Modena e Reggio Emilia, Italy)

Internal Member:

Prof. Matteo G.A. PARIS (Università degli Studi di Milano, Italy)

Final examination:

Date: December 22nd, 2022

Dipartimento di Fisica "Aldo Pontremoli"
Università degli Studi di Milano Milano
Via Celoria 16, 20133 Milano, Italy

C'è una vita che corre attraverso di noi ma senza di noi... Non è solo quella scatola nera sprofondata dentro di noi che si sono inventati, e che non è niente, non conta niente, ce la siamo inventata solo per stare tranquilli, per rassicurarci fingendo di spaventarci. C'è ben altro! Siamo dentro ben altro!

– Antonio Moresco, *Canti del Caos*

To Melissa

Cover illustration:

NightCafe's AI Art Generator

Internal illustrations:

Alessandro CANDELORO
Luca RAZZOLI

MIUR subjects:

FIS/03

PACS:

03.67.-a
03.65.Yz

Contents

List of Publications

As of December 19, 2022

Material discussed in this thesis

Refereed publications

1. CANDELORO, A., AND PARIS, M. G. A. Discrimination of Ohmic thermal baths by quantum dephasing probes, *Physical Review A 103 (1), 012217* (2021)

2. CANDELORO, A., RAZZOLI, L., BORDONE, P., AND PARIS M. G. A. Role of topology in determining the precision of a finite thermometer, *Physical Review E 104 (1), 014136* (2021)

3. CANDELORO, A., RAZAVIAN, S., PICCOLINI, M., TEKLU, B., OLIVARES, S., AND PARIS M. G. A. Quantum probes for the characterization of nonlinear media, *Entropy 23 (10), 1353* (2021)

4. CANDELORO, A., PARIS, M. G. A., AND GENONI, G. M. On the properties of the asymptotic incompatibility measure in multiparameter quantum estimation, *Journal of Physics A: Mathematical and Theoretical 54 (48), 485301* (2021)

5. CANDELORO, A., BENEDETTI, C., GENONI, M. G., AND PARIS, M. G. A. Feedback-assisted quantum search by continuous-time quantum walks, *Advanced Quantum Technologies* (In press) (2022)

Other material

Refereed publications

1. CANDELORO, A., RAZZOLI, L., CAVAZZONI, S., BORDONE, P., AND PARIS, M. G. A. Continuous-time quantum walks in the presence of a quadratic perturbation, *Physical Review A 102 (4), 042214* (2020)

2. CANDELORO, A., MEREGHETTI, C., PALANO, B., CIALDI, S., PARIS, M. G. A., AND OLIVARES, S. An enhanced photonic quantum finite automaton, *Applied Sciences 11 (18), 8768* (2021)

Publications in preparation

1. PAZHOTAN, Z., CANDELORO, A., AND PARIS, M. G. A. Dimensionality of Hilbert spaces as a resource in multiparameter quantum metrology
2. CAMATI, P., CANDELORO, A., BRESQUE, L., PICCIONE, N., MAFFEI, M., AND AUFFÈVES, A. Energetics of Interacting Quantum Systems
3. BRESSANINI, G., CANDELORO, A., GENONI, M. G., AND PARIS, M. G. A. Multiparameter quantum estimation in Gaussian systems

Acknowledgments

In questi 3 anni e 3 mesi una infinità di cose sono successe: credo sia giusto ricordare le persone con cui le ho condivise.

In primo luogo sono estremamente grato al mio supervisore Matteo. Ricordo bene il primo giorno in cui ci siamo incontrati in un freddo pomeriggio di Febbraio 2019: credo di aver imparato molto lungo questo cammino, e sarò sempre riconoscente per avermi introdotto al mondo della ricerca. Grazie soprattutto per la libertà concessami in questi tre anni, in cui ho avuto l'enorme fortuna di poter esplorare tanti e diversi aspetti dell'informatica e della metrologia quantistica. In secondo luogo vorrei ringraziare tutti coloro con cui ho avuto il piacere di collaborare nel gruppo: vorrei quindi dire grazie a Marco Genoni, Claudia Benedetti e Stefano Olivares per la loro disponibilità e per avermi trasmesso la loro passione e le loro conoscenze, ma soprattuto per la pazienza e per il tempo dedicatomi. Vorrei anche ringraziare Paolo Bordone e Luca Razzoli, i primi con cui mi sono incamminato in questo percorso: è stato un piacere poter discutere di fisica e di random walk con voi.

Non posso non ringraziare gli amici con cui ho condiviso questo percorso in via Celoria. È impossibile quantificare la gratitudine che ho per la magnifica coppia formata da Andrea Smirne e Matteo Bina: senza di voi non so come avrei fatto. Vorrei anche dire grazie Francesco Albarelli e Dario Tamascelli, con cui ho passato piacevoli momenti. Vorrei ringraziare i vari amici che sono passati per il nostro ufficio, ovvero Michele, Davide, Daniele, Massimo ed Heng Ji: che lo scrambling quantistico possa proliferare nel nostro corridoio. Vorrei anche dire grazie a Matteo Magi e Roberto Rubboli, ex compagni di studi con cui ho la fortuna di poter parlare ancora di fisica, scienza e tanto altro.

Ci tengo a ringraziare anche tutti i ragazzi che ho conosciuto a Grenoble. In primo luogo, Alexia Auffeves per avermi accettato nel suo gruppo. Un grazie speciale, non solo scientifico ma anche personale, va Patrice Camati, per i vari momenti e discussioni condivise insieme: nonostante il poco tempo passato insieme, mi sono sentito particolarmente legato. Ci tengo a ringraziare anche Lea Bresque, Nicolo Piccione, Samyak Prasad, Maria Maffei e Bruno Goes, Raphaël Mothe, Marco Fellous Asiani, Hippolyte Dourdent e Konstantina Koteva coi quali ho condiviso discussioni scientifiche, camminate, sciate e tanto altro.

Il mondo non è fatto solo di scienza e di scienziati (fortunatamente...): per questo vorrei anche ringraziare gli amici che mi hanno sostenuto, in maniera diretta ed indiretta, in questi anni. In primis, Stefano Biagi, che sento vicino come dieci anni fa, nonostante la lontananza. Non posso non essere grato ai miei amici della braga bianca di Saruman: anche se non sono sempre fisicamente con voi, ogni volta che vi rivedo è come tornare a casa. Ci tengo a ringraziare anche Roberto, un amico speciale.

Infine, sono estremamente grato alla mia famiglia tutta. Il vostro supporto silenzioso e da dietro le quinte è più prezioso di quanto si possa mai quantificare.

Vorrei dedicare questa tesi a Melissa, che conosce le parti più buie e nascoste di me.

Introduction

Motivation

Characterization and engineering are the basis for any technological development that aspires to exploit scientific breakthroughs and novel physical phenomena. Nowadays, it is impossible to ignore the exceptional results and developments that quantum mechanics, in combination with information theory, has developed in recent decades.

The first quantum revolution was fundamentally based on the wave-particle duality [124]. Thinking of matter as a wave allowed us to explain chemical reactions or electronic behaviour in atoms and semiconductor physics. Conversely, thinking of waves as particles resulted in the development of laser fields. Other technological advancements are indebted to this new paradigm: it is sufficient to remember nuclear technologies or semiconductor physics to understand the relevant role that quantum mechanics has acquired in the last half of the XXth century. In particular, chip technology based on semiconductor physics has completely transformed our age, which is by someone now referred to as *the information age* [202, 345].

The impact of information theory in the development of quantum mechanics and its applications has become increasingly evident since the end of the XXth century. In the second quantum revolution we are witnessing today, we are actively employing quantum mechanics to produce novel physical states of light and matter, which promise to have enhanced properties of sensitivity and non-classical correlations, that aims to provide significant improvements for a specific range of applications [111]. These peculiar quantum properties, such as superposition, entanglement and contextuality, are not usually experienced in classical physics and must be properly engineered to be successfully exploited.

We can circumscribe four areas that have been most affected by this second quantum revolution:

- *Quantum sensing and metrology*. The high sensitivity of quantum systems is crucial for the efficient acquisition of information and for performing more precise measurements. The first generation of quantum sensors relied on classical physics and electronic devices, whereas the new generation promises to improve the accuracy using phenomena such as entanglement and non-local correlations [114]. It is also worth mentioning that the engineering of devices at the nanoscale, and thus inevitably quantum, could enable high-precision and extremely low-invasive measurements, a paradigm often referred to as *quantum probing*.

- *Quantum control of complex systems*. One of the key lessons of cybernetics and the information age is that no complex technology can efficiently work in a broad range of situations without incorporating control and feedback mechanism. The presence of noise and stochastic behaviour (whether classical or quantum in nature) makes it necessary to continuously correct systems to achieve efficient and reliable performance. The development of quantum control techniques is thus crucial for building peculiar non-classical states, which may then be used to perform specific tasks.

- *Quantum communications and cryptography*. Quantum systems can be used to store and exchange information. Understanding how to do this with more secure and efficient protocols is of paramount importance in our digital age. The use of nonlocal correlations and quantum superpositions aims to provide new protocols for secure communication and faster and more reliable transmission of information.

- *Quantum computing and simulation*. The possibility of using quantum properties to process information and perform computational tasks is related to the formulation of new algorithms capable of outperforming classical computing paradigms. Quantum interference, coherence and entanglement are the fundamental concepts behind this new computational approach. Furthermore, a systematic development of measurement, control and communication on the quantum scale will facilitate the building of quantum computers.

The emergent field of quantum technologies not only promises to outperform standard protocols already present in the market, but they also offer new and unexplored paradigms, as well as a new wave of industrial applications [98]. This is also why it has attracted great attention, even outside the narrow circle of experts. Recent studies show interest in topics that are not strictly scientific-related, such as the impact on society [130] and the legislative apparatus [180]. Moreover, governments and political entities have found it essential to propose coordinated strategic development plans for this field of research [294]. Not least, the recent Nobel Prizes assigned to Haroce and Wineland in 2012, and Aspect, Clauser and Zeilinger [293, 309] in 2022, only confirm this interest in quantum technologies and the non-classical aspects that they promise to exploit for the development of new and increasingly powerful tools.

Achieving such results and the so-called quantum advantages can only pass through the development of new theoretical and experimental methodologies, and the claim of super-classical performance must rely on precise assessments of the *resources* under play. As already stated, all these new technologies rely on high-precision measurements and engineering: these will be the topics that this thesis covers.

The scope of this work is to provide new results regarding quantum sensing and quantum control. The need for quantum systems to work in well-established temperature regimes has brought much attention to quantum thermometry. Moreover, understanding the relevant property in building quantum thermometry is quite relevant to achieve and surpass classical limits. This engineering problem can be studied using the mathematical tools that have been developed and that enable us to characterize this kind of system. Indeed, establishing new methods to probe temperatures of fragile systems and in very unstable regimes, such as in the low-temperature one, is critical for the development of trustworthy quantum devices that can retain quantum features over long periods of time. Decoherence and noise are detrimental for many tasks in all the four key areas mentioned above. On the other side, the paradigm of quantum probing offers a new perspective on decoherence. Instead of considering it as detrimental, it exploits the

inherent fragility to probe features of the environment and to better characterize it, for instance in temperature measurements. We will report the results of quantum thermometry in Part II, where we will show the fundamental resources that enable advantages in temperature sensing.

The ability to jointly estimate parameters is of pivotal importance in several fields, from imaging to gravitational wave detectors. The measurement of quantum systems has limitations that can be very different in nature: this might come from external sources, such as the interaction with external environments, or it might be quantum in nature, such as the impossibility of simultaneously measuring non-commutative observables. Both these scenarios limit our ability to probe quantum systems, and their fundamental understanding can have an impact both at the foundational and applicative levels. We will see in Part III how to characterize this *quantum noise* coming from measurement incompatibility. We will do this in a general setting, but also for a more concrete example, i.e. for the characterization of quantum optical devices.

Finally, the last contribution of this PhD thesis consists of a new proposal for quantum search with continuous-time quantum walks. Using the principles of quantum mechanics to do computation was first proposed by Feynman. In particular, quantum search algorithms make use of quantum superposition and phase interference to find items in a structured graph, and they aim to provide speedup compared to equivalent classical algorithms. The proposed protocol combines three different fields of research, i.e. continuous measurement, feedback and quantum walks, to provide a novel method to perform quantum search protocols on graphs. We will dedicate Part IV to show the results and compare the advantages with known protocols.

Thesis overview

The PhD thesis consists of a preliminary part, three main parts, conclusions and a final appendix, for a total of 10 chapters. Part I introduce the notation and basic tools to understand the rest of the thesis. Part II is focused on the thermometric properties of quantum systems. Part III is dedicated to results on the characterization of quantum systems in multi-parameter metrology. Part IV deals with feedback and control with continuous-time quantum walks.

- In Chapter 1, we present the postulates of quantum mechanics from a modern perspective. We introduce the basic mathematical tools to deal with quantum states, quantum evolution and quantum measurements.
- In Chapter 2, we discuss the most important results in quantum metrology, namely Helstrom bound in quantum discrimination, and the quantum Cramer-Rao and Holevo bound in multi-parameter estimation. We also present the notion of measurement incompatibility and how to quantify it.
- In Chapter 3, we present the basic formalism to describe continuous-time quantum walks in terms of the adjacent and Laplacian matrix.
- In Chapter 4, we study the role of topology in the estimation precision of temperature. We analyze different topological aspects of the structure of a quantum walker and characterize the optimal systems in low and high-temperature regimes. Results have been published in [74].
- In Chapter 5, we study how to exploit pure dephasing probes in a thermometry discrimination task. We evaluate the minimum probability of error and we provide

the optimal strategy to achieve it. More in general, we identify the main resources to achieve better performance with respect to equilibrium probes. Results have been published in [71].

- In Chapter 6, we analyze the simultaneous estimation of non-linearities with Gaussian probes. We prove that squeezing is an important resource to reach the ultimate limit in the individual and joint estimation of the parameters, and we establish with analytical and numerical tools the ultimate bounds, also with respect to the initial preparation. Results have been published in [73].
- In Chapter 7, we investigate the asymptotic incompatibility measure, a quantifier of measurement incompatibility in multi-parameter quantum metrology. We prove new properties of this quantity related to the maximal number of incompatible parameters. We also study it in the problem of full tomography, conjecturing that its value is related to the fictitious temperature of the state. Results have been published in [72].
- In Chapter 8, we analyze the use of continuous measurement and feedback operations on continuous-time quantum walks that perform quantum search. The numerical results for a cycle graph show advantages compared to the already established protocols. Results have been published in [70].

Part I

Preliminaries

CHAPTER 1

Mathematical tools for quantum mechanics

This thesis is mainly concerned with quantum mechanics and its applications in three main topics: quantum thermometry, quantum metrology, and quantum random walks. As a result, this preliminary section is devoted to a basic introduction to the mathematical tools used in modern quantum mechanics. In particular, we present the formalism from an information perspective [263], which is more suitable for the application we are interested in. In this chapter, we aim to introduce the notation and concepts that will return in the thesis. Our main references are [263, 127], but there are other approaches, see for instance [99, 257].

This chapter is organized as follows. In Sec. 1.1, we first familiarize with the main ingredients used to describe a statistical theory: states, transformation and measurement. Then, we present in order how these are formalized in quantum mechanics: in Sec. 1.1.1 we review the state postulate, introducing the wave function and the density matrix formalism. In Sec. 1.1.2 we review the evolution of quantum system, i.e. the Schrödinger equation. We also briefly introduce quantum operations, a generalization of unitary transformations. Finally in Sec. 1.1.3 we present the measurement postulate and the mathematical framework of positive-operator valued measurements (POVMs).

1.1 The postulates of quantum mechanics

The postulates of quantum mechanics have long been debated [186], and still today there is no complete agreement on the minimal assumptions leading to the theory of quantum mechanics [75, 235]. In this thesis, we embrace an agnostic approach, and we just present the necessary mathematical structures required for describing quantum systems.

Quantum mechanics is a statistical framework for the description of a certain class of phenomena. From an information perspective, the formalism does not specify the physical system, neither the physical laws that that system must satisfy. Rather, it provides the building blocs that connects the mathematical formalism to the observed phenomena. In this setting, the fundamental blocks are three:

1. **state space** $\mathcal{H}$: every elements in $\mathcal{H}$ represents a physical state of the system, encoding all the relevant physical degrees of freedom.

2. **transformation rules** $\mathcal{E}$: every $\mathcal{E}$ prescribes how the states in $\mathcal{H}$ change, eventually under the interaction with external systems.

3. **measurements** $\mathbf{\Pi}$: a rule that predicts the results of a measurement process, the only way we can obtain information on the systems degrees of freedom.

We would like to mention that also classical mechanics can be rephrased in this language: the states are a collection of independent coordinates and momenta $\{q_i, p_i\}$, while the evolution are given in terms of differential equation. Finally, the rule that predicts the result of measurements are probability measures [127].

In the quantum realm, these prescriptions are also referred as the *postulates* of quantum mechanics. For each of the three postulates, we first present their standard formulation usually seen in undergraduate courses with pure states, unitary maps and quantum observables. For each of them we will see that suitable generalization are necessary to give a complete description of the systems under study, in terms of density matrix, quantum operations and POVMs.

1.1.1 Postulate 1: Quantum states

The first postulate specify the state space $\mathcal{H}$, or the physical degrees of freedom are encoded. We present it using the Dirac formalism.

Postulate 1: State of quantum systems

The degrees of freedom of a quantum system are described by normalized vectors $|\psi\rangle$ in a separable complex Hilbert space $\mathcal{H}$. Composite systems are associated to the tensor product $\mathcal{H}_1 \otimes \mathcal{H}_2 \otimes \dots$ of the Hilbert spaces corresponding to each component of the system.

We recall that a complex Hilbert space is a complete vector space on a complex field endowed with a scalar product $\langle\psi|\phi\rangle \in \mathbb{C}$, which is necessary to define the notion of probability, as we are going to see in the last section. Instead, the properties of linearity and complex field are needed in order to accommodate all interference phenomena that radiation and matter display in the quantum realm. This also implies that if $|\psi_1\rangle$ and $|\psi_2\rangle$ are states, than any normalized linear combination of the two $\alpha|\psi_1\rangle + \beta|\psi_2\rangle$ with $|\alpha|^2 + |\beta|^2 = 1$ is a proper state of the system, where α and β are complex number known as amplitudes. In the quantum mathematical jargon, this linear combination is known as the *superposition principle*. The main consequence of this fact will become clear with the introduction of observables. Finally, apart for mathematical convenience, the request of $\mathcal{H}$ to be separable ensures us that a numerable basis exists. From a physical point of view, this means that the state is uniquely determined by a countable number of measurements.

As a final remark, we notice that the requirement to have normalized states is not sufficient to identify a single vector in the Hilbert space: in fact, there is an arbitrary global phase $e^{i\alpha}$ such that the two states $|\psi\rangle$ and $e^{i\alpha}|\psi\rangle$ are completely equivalent. For this reason and to be more precise, quantum states should be identified with ray in $\mathcal{H}$, that is the equivalence classes of vectors of length 1 in $\mathcal{H}$. These are univocally determined by a rank-one projection operator in $\mathcal{H}$

$$\varrho = |\psi\rangle\langle\psi|, \tag{1.1}$$

satisfying $\varrho^2 = \varrho$. The ϱ is the *density matrix* of the system, and is a bounded, positive semi-definite, trace-one operator. Since this represent a physical state of the system, we assume that there is at least one physical procedure that prepares the physical system in such state with certainty. For this reason, such states are known as *pure states*.

However, the preparation of the physical system may not be completely under control. Then, a probabilistic description must be considered. This is given with respect to a certain statistical ensemble $\{p_i, |\psi_i\rangle\}$, where the ith state $|\psi_i\rangle$ is prepared with probability p_i. Since this is a classical ensemble, the state of the system can be written as a probabilistic mixture of the pure states in the ensemble as

$$\varrho = \sum_i p_i |\psi_i\rangle\langle\psi_i|. \tag{1.2}$$

Even in this case, the density matrix is a bounded, positive semi-definite, trace-one operator, and hence will have all the fundamental properties needed to derive a probabilistic rule from it. The only difference is that the state is not pure anymore, and its purity is always smaller than one $\mu[\varrho] = \mathrm{Tr}\left\{\varrho^2\right\} \leq 1$. The equality is obtained iff and only if the state is in the form of Eq. (1.1).

1.1.2 Postulate 2: Quantum evolution

The second postulate prescribe how the states defined in Postulate 1 change. The first formulation is given in terms of the Schrödinger equation as

Postulate 2: Evolution of quantum systems

The states of a system evolves in times according to the differential equation

$$i\hbar \frac{d}{dt}|\psi(t)\rangle = \widehat{H}(t)|\psi(t)\rangle, \tag{1.3}$$

known as the *Schrödinger equation*. The operator $\hat{H}(t)$ is the Hamiltonian of the system and $\hbar$ is the Planck's constant.

A formal solution of such equation can be derived in terms of unitary operator $U(t, t_0)$. Indeed, given an arbitrary initial condition $|\psi(0)\rangle$ at time $t = 0$, the state of the system at time t is given as

$$|\psi(t)\rangle = \widehat{U}(t, t_0)|\psi(0)\rangle, \tag{1.4}$$

where $U(t, t_0)$ can be formally written as

$$\widehat{U}(t, t_0) = \mathcal{T} \exp\left\{-\frac{i}{\hbar}\int_{t_0}^{t} dt' \widehat{H}(t')\right\}. \tag{1.5}$$

Here, $\mathcal{T}$ is the time-ordering operator, whose effect is to put non-commuting operators in the correct chronological order

$$\mathcal{T}\widehat{H}(t_1)\widehat{H}(t_2) = \begin{cases} \widehat{H}(t_1)\widehat{H}(t_2) & \text{if} \quad t_1 < t_2 \\ \widehat{H}(t_2)\widehat{H}(t_1) & \text{if} \quad t_1 > t_2 \end{cases} \tag{1.6}$$

Differently from the differential equation (1.3), that describe the evolution continuously in time, the formulation in terms of unitary operator describes how to map a quantum state from time t_0 to time t.

It is a straightforward exercise to prove that we can also write Eqs. (1.3)–(1.4) in terms of the density matrix ϱ respectively as

$$\frac{d}{dt}\varrho(t) = -\frac{i}{\hbar}[\widehat{H}(t), \varrho(t)] \tag{1.7}$$

$$\varrho(t) = \widehat{U}(t, t_0)\varrho(0)\widehat{U}(t, t_0)^\dagger \tag{1.8}$$

A time-dependent Hamiltonian $\widehat{H}(t)$ in general means that the system is not closed, but it varies according to some experimentalist's control. Instead, in the case where $\widehat{H}(t) \to \widehat{H}$ is time-independent, the system is closed and isolated. In this case, an exact closed solution for the evolution can be obtained. If we denote with E_λ and $\{|e_\lambda\rangle\}$ respectively the eigenvalues and the eigenstates of $\widehat{H}$, then we can write explicitly the unitary operator as

$$\widehat{U}(t, t_0) = \exp\left\{-\frac{i}{\hbar}\widehat{H}(t - t_0)\right\} = \sum_\lambda e^{-i\frac{i}{\hbar}E_\lambda(t-t_0)}|e_\lambda\rangle\langle e_\lambda| \tag{1.9}$$

and then the evolved state is simply

$$|\psi(t)\rangle = \sum_\lambda c_\lambda(0)e^{-\frac{i}{\hbar}E_\lambda(t-t_0)}|e_\lambda\rangle \tag{1.10}$$

where the $c_\lambda(0)$ are the amplitudes of the initial state in the energy eigenbasis $|\psi(0)\rangle = \sum_\lambda c_\lambda(0)|e_\lambda\rangle$.

From a more general perspective, a transformation of a system is a map that transform quantum states ϱ in quantum states $\mathcal{E}[\varrho]$. These are known as *quantum operation* or quantum channel and in principle are the most general way to describe the evolution of quantum systems. Here we briefly characterize their mathematical structure and we see how they reconcile with the formulation in terms of unitary operations.

We can list three fundamental properties of quantum operations $\mathcal{E}[\varrho]$, necessary for a complete and consistent description of quantum systems:

1. The map must be positive $\mathcal{E}[\varrho]$ and trace preserving $\mathrm{Tr}\{\mathcal{E}[\varrho]\} = 1$. In this way, the output of the map is a density matrix and preserve the normalization of states.

2. The map $\mathcal{E}[\varrho]$ is linear
$$\mathcal{E}\left[\sum_i p_i\varrho_i\right] = \sum_i p_i\mathcal{E}[\varrho_i] \tag{1.11}$$
This means that the state obtained from a certain statistical ensemble mixture $\{p_i, \varrho_i\}$ is the ensemble of evolved states $\mathcal{E}[\varrho_i]$.

3. The map is completely positive $\mathcal{E}[\varrho]$. This means that any extended map $\mathcal{E} \otimes \mathbb{I}$ on the auxiliary system $\mathcal{H} \otimes \mathcal{H}_a$ is positive as well, independently on the dimension of $\mathcal{H}_a$. Physically, it means that the map is a faithful quantum operation even if we look at it from a larger systems.

Given all these request, each capturing different well defined physical property, the following theorem fully characterize quantum operations [207]

Theorem 1: Kraus operator-sum representation

A map $\mathcal{E}[\varrho]$ is a quantum operation, i.e. satisfy the three properties presented above, if and only if is the partial trace of a unitary evolution on a larger Hilbert space $\mathcal{H}\otimes\mathcal{H}_a$ with factorized initial condition

$$\mathcal{E}[\varrho(t_0)] = \mathrm{Tr}_a\left\{U(t,t_0)\varrho(t_0)\otimes\varrho_a(t_0)U(t,t_0)^\dagger\right\} \tag{1.12}$$

This is equivalent to the Kraus decomposition

$$\mathcal{E}[\varrho] = \sum_k M_k \varrho M_k^\dagger \tag{1.13}$$

where $\{M_k\}$ are the Kraus operator satisfying $\sum_k M_k^\dagger M_k = \mathbb{I}$.

The theorem is also known as the Stinespring dilation theorem [328]. The Kraus representation is the generalization of unitary operations to arbitrary quantum evolution, satisfying the minimal properties that give rise to a proper quantum evolution. Unitary maps are included, and are identified as the one with a single Kraus operator M_k. These are also the only invertible quantum operations. We have presented the theorem from an axiomatic perspective, but since the theorem is an *if and only if*, it assures us a constructing method to build such map by tracing a unitary operation on a larger system. Finally, we also mention that the third condition on completely positivity may not be necessary to describe physical transformations [320].

1.1.3 Postulate 3: Quantum measurements

The third postulate specifies the observable quantities of the theory and what we can predict about the outcomes of measurements. The system is no longer isolated during these processes, hence a unitary dynamics does not provide a suitable dynamical description. Hence, we have to introduce another postulate that makes predictions on the outcomes of the theory and prescribes how the system change accordingly.

To do so, we first need to identify the observable quantities. In the quantum scenario, these are self-adjoint operator $\widehat{A}$, and they admit a spectral decomposition

$$\widehat{A} = \sum_m a_m P_m, \tag{1.14}$$

where the a_m are the eigenvalues of $\widehat{A}$ and represent the values of the possible outcomes, while the $P_m = |a_m\rangle\langle a_m|$ are projectors $P_m P_{m'} = \delta_{mm'} P_m$ on the eigenvectors $\{|a_m\rangle\}$ of $\widehat{A}$. These are a complete set of orthonormal states, i.e. $\langle a_m|a_{m'}\rangle = \delta_{mm'}$, from which it follows that $\sum_m P_m = \mathbb{I}_{\mathcal{H}}$. We can now state the rule that associate a probability to each possible outcome:

Postulate 3: Measurement of a quantum system

The probability of obtaining the mth outcome from the measurement of an observable $\widehat{A}$ given the state ϱ is given by the *Born rule*

$$p_m = \mathrm{Tr}\left\{\varrho P_m\right\} = \sum_i p_i |\langle\psi_i|a_m\rangle|^2 \tag{1.15}$$

In the case we measure the system and we observe the mth outcome, the post-measurement state is given by

$$\varrho_m = \frac{P_m \varrho P_m}{p_m} = |a_m\rangle\langle a_m|. \tag{1.16}$$

This is the fundamental recipe to assign probabilities to outcomes of an observable. Indeed, given a certain state, we can also evaluate average values of the observable $\widehat{A}$ as

$$\left\langle \widehat{A} \right\rangle = \mathrm{Tr}\left\{\varrho \widehat{A}\right\} = \sum_m a_m p_m = \sum_{m,i} a_m p_i |\langle\psi_i|a_m\rangle|^2. \tag{1.17}$$

An important feature of quantum mechanics is the presence of incompatible observables, i.e. pair of observables $\{\widehat{A}, \widehat{B}\}$ that do not commute $[\widehat{A}, \widehat{B}] \neq 0$. In this case, there is no common eigenbasis for the two operators. This has important physical consequences: if we measure the first observable and obtain the outcome a_m, there is no certainty about the outcome of the measure of the observable $\widehat{B}$, see Eq. (1.15). Conversely, if the two observable commutes $[\widehat{A}, \widehat{B}] = 0$, it means that they share a common set of projectos P_m and a joint measure is possible. Indeed, after we have measured $\widehat{A}$ and observed a_m, then the measure of $\widehat{B}$ will yield for sure the outcome b_m, and we can simultaneously assign the values $\{a_m, b_m\}$ to the state ϱ. As already mentioned, the presence of non-commuting observables is essentially equivalent to the possibility of having superpositions: superposed states coming from of a certain set of projectors can form non-commuting basis.

The density matrix formalism is particularly powerful in the description of subsystem of composite system. Let us assume that we have a bipartite system whose state is given by the density matrix ϱ^{AB}. Suppose the observable $\widehat{A}$ is on the partition A only, with overall observable $\widehat{\boldsymbol{A}} = \widehat{A} \otimes \mathbb{I}_B$. The probability distribution of the outcomes is given by (1.15), but since the observable is only on the partition A, we expect the Born rule to be valid even at the level of the single system. Hence, we need a function that properly maps a density matrix ϱ_{AB} to ϱ_A in such a way that the probability distribution given in (1.15) correspond to

$$p_m = \mathrm{Tr}_{AB}\left\{\varrho^{AB} P_m \otimes \mathbb{I}_B\right\} = \mathrm{Tr}_A\left\{\varrho^A P_m\right\}. \tag{1.18}$$

One can show that the only mapping from ϱ^{AB} to ϱ^A is given by the partial trace

$$\varrho^A = \mathrm{Tr}_B\left\{\varrho^{AB}\right\} \tag{1.19}$$

where the partial trace is formally defined as

$$\mathrm{Tr}_B\left\{|a_i\rangle\langle a_j| \otimes |b_k\rangle\langle b_l|\right\} = |a_i\rangle\langle a_j| \mathrm{Tr}\left\{|b_k\rangle\langle b_l|\right\}. \tag{1.20}$$

One can prove that the partial trace yields to a positive unit trace operator ϱ^A and hence is the unique operation that allows to maintain the Born rule, i.e. consistency in the prediction both at the bipartite and at the single level description. Here, we recover another interpretation of the density matrix, i.e. the state of a system whose knowledge is only partial with respect to a larger global picture.

In an analogous way as with unitary operation and quantum operation, it is not necessary to restrict ourself to observables in order to prescribe outcomes probabilities. Indeed, by analyzing the fundamental properties that define a probability distribution, we can look for some generalizations. This yields to definition of *generalized measurements*, or POVMs.

A closer look at the Born rule in Eq. (1.15) allows us to rewrite it as

$$p_m = \mathrm{Tr}\left\{\varrho P_m\right\} = \mathrm{Tr}\left\{\varrho P_m^2\right\}. \tag{1.21}$$

Since the only request to have a probability are the fact that the p_m are positive and their sum is 1, it is quite natural to observe that a sufficient condition to obtain positive p_m consists in asking that the ϱP_m^2 are positive semi-definite. Since ϱ is a state and is positive semi-definite by definition, we may relax the request of P_m^2 as projectors, and just asking them to be semi-definite positive operator Π_m. Of course, to preserve the fact that the p_m are a probability, we need that $\sum_m \Pi_m = \mathbb{I}_{\mathcal{H}}$. These define a POVM $\mathbf{\Pi} = \{\Pi_m\}$ and the Π_m are the POVM elements. Differently from the observable case, where the number of projector is equal to the dimension of the Hilbert space, here the number of the POVM elements is not constrained, and might be larger then $\dim\mathcal{H}$.

With this generalization, we have lost some information in the description of the measurement. Indeed, generalized measurements given by POVMs have sufficient mathematical structure to define probability distribution on the Hilbert space, but it is not possible to determine the post-measurement state as in Eq. (1.16). A further structure is needed, which is formalized in terms of *quantum instruments*.

To obtain such structure, it is sufficient to introduce a set of operators called *detection operators* D_m which yields the post measurement according to (1.16), i.e.

$$\varrho \to \varrho_m = \frac{D_m \varrho D_m^\dagger}{p_m}, \tag{1.22}$$

with

$$p_m = \mathrm{Tr}\left\{D_m \Pi_m D_m^\dagger\right\} = \mathrm{Tr}\left\{\Pi_m D_m^\dagger D_m\right\}. \tag{1.23}$$

Since $D_m^\dagger D_m$ is positive semi-definite, we see that a specific set of detection operators give rise to a unique POVM as

$$D_m^\dagger D_m = \Pi_m. \tag{1.24}$$

However, the converse is not true: given a POVM $\mathbf{\Pi} = \{\Pi_m\}$, any detection scheme $\{U_m D_m\}$ with $D_m = \sqrt{\Pi_m}$ correctly describes the same POVM. Actually, any POVM defines a class of detection schemes $\{U_m D_m\}$, where $D_m = \sqrt{\Pi_m}$ are fixed by $\{\Pi_m\}$. In other words, the POVM fixes the probability, but not completely the post-measurement states: from a physical point of view this means that there is an infinite number of experiment/detection schemes yielding the same probability distribution of the outcomes. We can also see the detection operator D_m and the POVM elements Π_m respectively as a generalization of the P_m and P_m^2. We will refer to POVMs made of projectors as projection-valued measures (PVMs).

Analogous to Kraus's theorem , we can prove that any generalized measurement $\mathbf{\Pi}$ can be described by the measure of an observable in a larger Hilbert space. Such process

can be viewed as a consequence of Stinespring's dilation Theorem 1 and bares the name of Naimark theorem [263]

Theorem 2: Naimark theorem

For a given POVM $\mathbf{\Pi} = \{\Pi_m\}$ on $\mathcal{H}$ there exists an ancillary system $\mathcal{H}_a$, a pure state $|\psi_a\rangle\langle\psi_a|$, a unitary operation on $\mathcal{H} \otimes \mathcal{H}_a$ and a projective measurement P_m on $\mathcal{H}_a$ such that the POVM elements Π_m are given as

$$\Pi_m = \mathrm{Tr}_a \left\{ U\mathbb{I} \otimes |\psi_a\rangle\langle\psi_a| U^\dagger \mathbb{I} \otimes P_m \right\} \tag{1.25}$$

The setup is referred to as a Naimark extension of the POVM.

This theorem simply states that there is a one-to-one correspondence between POVMs and indirect measurements of the type describe above. In other words, an indirect measurement in which a projective measurement is performed on the ancillary system, sometimes also named as *pointer* or *meter*, may be seen as the physical implementation of a POVM. At the same time, any POVMs have a suitable representation with respect to an indirect measurement with projective measurement, establishing the possibility of a physical implementation of POVMs.

The possible Naimark extensions are infinite, corresponding to the intuitive idea that there are infinite ways, with an arbitrary number of ancillary systems, of measuring a given quantity. This is nothing but the fact that there are infinite possible detection operators $\{D_m\}$ with the same POVM $\mathbf{\Pi}$.

CHAPTER 2

Introduction to quantum metrology

Metrology is the science of measurement, and it consists of devising schemes that can extract as much information as possible from the system of interest using methods from statistical inference. The usual topics range from the estimation of parameters to the acceptance or rejection of a certain hypothesis. Each of these problems is based on experimental data, and as a result, the mathematical tools of quantum sensing are essentially based on statistical science. As one may imagine, this is a vast field of research that intersects with several other disciplines: starting with the purest sciences such as physics, and chemistry, moving on to the medical sciences, biology, and even economics and sociology, and many others. The countless applications are far too many to list here, and they had an immense impact on the world today [284]. In the quantum realm, we usually refer to all these protocols of estimation and discrimination as quantum metrology or quantum sensing.

In this thesis, we are interested in quantum physical science and in developing the mathematical tools regarding *quantum discrimination* and *local quantum parameter estimation*. Here, problems are usually formulated in three steps: probe preparation, interaction with a certain system and a final readout. Although errors inevitably affect any measurements, the appropriate choice of these stages may enhance sensitivity and precision. In particular, quantum metrology seeks scenarios where possibly non-classical resources provide enhancement over classical strategies and tries to identify and quantify them.

Indeed, in the classical setting, there is an equivalence between the information encoded in the state and the information potentially accessible. For instance, the state variables (position q and momentum p) are also observables and there is no fundamental limitation on the precision with which we can measure them. On the other side, in the previous chapter we presented the postulates of quantum mechanics and their mathematical foundation. Different classes of objects were introduced, and we saw that states and observables quantities are *two distinct and separate* mathematical objects. The first can be considered as the carrier of all the information we have on the physical degree of freedom of our system, whereas the second are the quantities that we can practically observe and measure. We have already seen some limitations on what we can say about the physical degrees of freedom when we discussed incompatible observables. In this chapter, we will see how this affects quantum sensing as well.

A question naturally arises: to what extent can we determine the state ϱ of a quantum system? There are different approaches to this problem, which depend on the physical setting and the prior knowledge we have of the physical system itself. The first we introduce is the discrimination problem in Sec. 2.1. In this case, we have a set of possible states $\{\varrho_k\}$ that forms a hypothesis set, and we wish to determine in which state the system is with the maximum confidence.

The second approach is given in terms of parameter estimation, and it is presented in Sec. 2.2. Even in the classical scenario, several quantities of interest are not directly observable. Usually, they are described by parameters that we use to model the theory behind the experiment. To find their values, one has to deal with random data and needs statistical tools to obtain the most precise estimate of the parameter under study. The randomness may come from noisy disturbance, like in electrical communication, or because the nature of the phenomenon is intrinsically stochastic. A set of parameters can be used to describe the underlying probabilities, and estimation theory is the branch of statistics that aims to find the best procedures and the most fundamental limits in the parameters' estimation. In the quantum setting, this means that we have some prior knowledge of the structure of the state, and usually, it is a family of states that depends on a set of parameters $\boldsymbol{\theta}$, and we wish to determine with the highest precision such parameters. In both cases, since experimentalists can have access to quantum states only through observable quantities, we wish to determine the optimal physical procedure, i.e. the POVM, that yields the maximum confidence.

2.1 Quantum Discrimination

The problem of discriminating different hypotheses is ubiquitous in many scientific fields. In the quantum realm, quantum discrimination has had an impact on the development of several quantum technologies, especially in optical communication [21]. One of the most important achievements has been the B92 quantum key distribution protocol, in which it was proposed to use the unambiguous discrimination of two nonorthogonal states as the basis to form a quantum cryptographic protocol [38], and see also [217, 30, 29] for recent experimental implementation with continuous variable systems. Quantum discrimination is also involved in foundational questions of the theory, see the Pusey–Barrett–Rudolph (PBR) theorem [283, 310]. They also have been investigated in ψ-epistemic theory [216] or in generalized probabilistic theories [20]. More recently, contextual advantage has also been proved for quantum discrimination in different settings [311, 136].

The problem is usually formulated as follows [88, 246, 26, 21, 40, 41, 39]: let us assume that one party, Alice, can prepare a set of quantum states $\{\varrho_i\}_{i=1}^N$ each with a certain probability q_i. These ϱ_i are the a priori quantum states and the q_i correspond to the a priori probabilities. We will refer to the pair $\{\varrho_i, q_i\}$ as the *hypothesis set*. This hypothesis set is shared with Bob, whose goal is to determine which element in the hypothesis set was generated by the probabilistic preparation procedure of Alice. Since Bob can not directly measure the state of the system, all the information he gains comes from the outcomes of a certain measurement scheme he performs. The main difficulty in such a problem is that, due to the superposition principle, there must exist non-orthogonal states that have nonzero overlap. As we are going to see, a straightforward consequence is that, for these states, there is no way to determine with certainty which state was prepared [88]. This is in strict connection with the no-cloning theorem [355], according to which no procedure can generate an identical copy of an unknown quantum state.

To address this problem, different approaches have been developed in the last 50 years, which depend on the kind of hypothesis set we have and which kind of prediction Bob wants to obtain from his measurement outcomes. We can identify three main strategies to address a quantum discrimination task [39]:

1. **Minimum error discrimination strategy**: in this case, we ask to have only conclusive results. This means that we want to be able to draw a conclusion concern-

ing the elements in the hypothesis set, whatever the outcome of the measurement is. As a result, errors are unavoidable when the states in the hypothesis are non-orthogonal since we can not perfectly distinguish them. To have conclusive results only, each outcome must be associated with one and only one of the hypotheses. The probability of guessing the correct state given certain outcomes yields an overall probability of error, which is the main figure of merit that must be minimized. Historically, this was the first strategy introduced in seminal works of Helstrom [172] and Holevo [178].

2. **Unambiguous discrimination strategy**: in this scenario, the observer is not allowed to draw wrong conclusions: if the apparatus yields the outcomes corresponding to a certain element in the hypothesis set, then we must conclude with certainty that the state was this one. However, the presence of non-orthogonal states in the hypothesis set does not always allow us to have definite answers. Consequently, there is also a non-zero probability to obtain inconclusive answers from which we can not draw any conclusion about the hypothesis. Hence, the goal of this procedure is to minimize the probability of obtaining this inconclusive outcome. This strategy was first introduced in [187] and then solved for $N = 2$ hypothesis with pure states in [122, 268].

3. **Maximum confidence discrimination strategy**: this is a generalization of the unambiguous strategy, where the hypothesises are not linearly independent and was introduced more recently in [106]. It optimizes the posterior probability $P(\varrho_i|i)$ (called confidence) that the state was prepared in ϱ_i and the corresponding outcome i was detected.

In this thesis, we are going to deal specifically with the first strategy, which is going to be reviewed in the following section.

2.1.1 Minimum error Discrimination

Many applications in quantum communication and quantum cryptography need only to have conclusive answers. This means that, based on the outcome of the measurement, Bob has to draw a conclusion, which is unavoidably affected by some error to be wrong. In this section, we are going to derive this probability of error and the optimal measurement that minimizes it, following the approach in [40, 41].

Let us assume that our hypothesis set is given by $\mathrm{H} = \{p_k, \varrho_k\}$ with $k = 1, ..., N$, where p_k is the probability that the system is prepared in ϱ_k. This means that the state prepared by Alice and sent to Bob is a classical statistical mixture

$$\varrho = \sum_{k=1}^{N} p_k \varrho_k. \tag{2.1}$$

The system is measured according to a certain POVM $\{\Pi_k\}_{k=1}^{N}$ such that each detection operator Π_k is associated with one hypothesis in the set H. Then, the probability of correctly inferring the kth state given that the state was precisely prepared in the state ϱ_k is

$$p_k^{\mathrm{INF}} = \mathrm{Tr}\left\{\varrho_k \Pi_k\right\}. \tag{2.2}$$

Furthermore, since each of the hypotheses ϱ_k was prepared with an *a priori* probability p_k, the total successful probability of inferring the state in the correct hypothesis is given

by

$$p^{\text{SUC}} = \sum_{k=1}^{N} p_k p_k^{\text{INF}}, \tag{2.3}$$

while the probability that one fails is simply

$$p^{\text{ERR}} = 1 - p^{\text{SUC}} = 1 - \sum_{k=1}^{N} p_k p_k^{\text{INF}}. \tag{2.4}$$

The goal of minimum-error discrimination theory is to find the POVM that minimize this average probability of error among all the hypothesis available. The general solution for the optimal measurement is non-trivial and might not be unique. However, in the discrimination problem with just two hypotheses, it is possible to determine the optimal discrimination strategy.

In this case, the hypothesis set is $\{p_i, \varrho_i\}_{i=1}^2$, and the POVM elements are $\{\Pi_1, \Pi_2\}$. Actually, these are not linearly independent, since a POVM must satisfy

$$\Pi_1 + \Pi_2 = \mathbb{I}. \tag{2.5}$$

As a result, the average probability of error can be expanded as

$$\begin{aligned} p^{\text{ERR}} &= 1 - p_1 \text{Tr}\left\{\varrho_1 \Pi_1\right\} - p_2 \text{Tr}\left\{\varrho_2 \Pi_2\right\} = \\ &= 1 - p_1 \text{Tr}\left\{\varrho_1 (\mathbb{I} - \Pi_2)\right\} - p_2 \text{Tr}\left\{\varrho_2 (\mathbb{I} - \Pi_1)\right\} = \\ &= p_1 \text{Tr}\left\{\varrho_1 \Pi_2\right\} + p_2 \text{Tr}\left\{\varrho_2 \Pi_1\right\}, \end{aligned} \tag{2.6}$$

The two elements in the sum represent exactly the probabilities of incorrectly inferring the wrong hypothesis, weighted by their a priori probabilities. We can alternatively write this as

$$p^{\text{ERR}} = p_1 + \text{Tr}\left\{\Lambda \Pi_1\right\} = p_2 - \text{Tr}\left\{\Lambda \Pi_2\right\}, \tag{2.7}$$

where we have defined the hermitian operators

$$\Lambda = p_2 \varrho_2 - p_1 \varrho_1 = \sum_{k=1}^{d} \lambda_k |\psi_k\rangle\langle\psi_k|. \tag{2.8}$$

Here, d is the dimension of the Hilbert space, and λ_k and $|\psi_k\rangle$ are respectively the eigenvalues and eigenvectors of the operator Λ. Using this spectral decomposition, we obtain that

$$p^{\text{ERR}} = p_1 + \sum_{k=1}^{d} \lambda_k \langle\psi_k|\Pi_1|\psi_k\rangle = p_2 - \sum_{k=1}^{d} \lambda_k \langle\psi_k|\Pi_2|\psi_k\rangle. \tag{2.9}$$

To find the optimal measurement strategy we must minimize p^{ERR}, a request that corresponds to two conditions

$$\min_{\Pi_1 > 0} \left\{ \sum_{k=1}^{d} \lambda_k \langle\psi_k|\Pi_1|\psi_k\rangle \right\}, \tag{2.10}$$

$$\max_{\Pi_2 > 0} \left\{ \sum_{k=1}^{d} \lambda_k \langle\psi_k|\Pi_1|\psi_k\rangle \right\}. \tag{2.11}$$

The first is minimized when $\langle\psi_k|\Pi_1|\psi_k\rangle = 1$ for negative eigenvalues λ_k, and $\langle\psi_k|\Pi_1|\psi_k\rangle = 0$ for positive eigenvalues λ_k, while the opposite constraints applies to Π_2. If we regroup the eigenvalues so that $\{\lambda_k\}_{k=1}^{d_0}$ are the negative ones, while the $\{\lambda_k\}_{k=d_0+1}^{d}$ correspond to the positive ones, we obtain that the optimal POVM must be

$$\Pi_1 = \sum_{k=1}^{d_0} |\psi_k\rangle\langle\psi_k|, \quad \Pi_2 = \sum_{k=d_0+1}^{d} |\psi_k\rangle\langle\psi_k|. \tag{2.12}$$

The presence of zero eigenvalues does not affect the splitting since they do not contribute to the probability of error p^{ERR}. However, they must be included, otherwise, the condition given by Eq. (2.5) is not satisfied. In other words, the eigenvectors corresponding to zero eigenvalues can be included in both POVM elements' decomposition without changing the final result.

Once we have obtained the optimal measurement, we can evaluate the minimum-error i.e.

$$p^{\text{ERR}} = p_1 - \sum_{k=1}^{d_0} |\lambda_k| = p_2 - \sum_{k=d_0+1}^{d} |\lambda_k|. \tag{2.13}$$

With the use of some algebraic manipulation, we eventually obtain a symmetric quantity

$$p^{\text{ERR}} = \frac{1}{2}\left(1 - \sum_{k=1}^{d} |\lambda_k|\right). \tag{2.14}$$

This expression can be translated to the celebrated Helstrom bound [172]

$$p^{\text{ERR}} = \frac{1}{2}\Big(1 - \|p_2\varrho_2 - p_1\varrho_1\|\Big), \tag{2.15}$$

where we have introduced the trace norm

$$\|A\| = \text{TrAbs}\,\{A\} = \text{Tr}\left\{\sqrt{A^\dagger A}\right\}. \tag{2.16}$$

This further simplifies if the two states are pure as

$$p^{\text{ERR}} = \frac{1}{2}\left(1 - \sqrt{1 - 4p_1p_2|\langle\psi_1|\psi_2\rangle|^2}\right). \tag{2.17}$$

We summarize the result in the following box

Result 1: Error probability for binary quantum discrimination

Given a binary hypothesis set $\{p_i, \varrho_i\}_{i=1}^2$ and a binary POVM $\{\Pi_1, \Pi_2\}$, the minimum error discrimination is given by

$$p^{\text{ERR}} = \frac{1}{2}\Big(1 - \|p_2\varrho_2 - p_1\varrho_1\|\Big), \tag{2.18}$$

and the optimal POVM is given by Eq. (2.12).

Some considerations about the optimal measurement and minimum probability are in order. An interesting case occurs when there are no positive eigenvalues of Λ (the same conclusions can be drawn in the case without negative eigenvalues). In this case, $\Pi_2 = 0$ and $\Pi_1 = \mathbb{I}_{d_0}$, which means that the optimal strategy is to always guess the first hypothesis ϱ_1 without measuring the system. In other words, there are cases where measuring the system increases the probability of wrongly guessing the state, as already observed in [184].

The bound so derived is valid for single-shot experiments, in which the measurement is applied only once. A more general strategy occurs when it is possible to use a collection of identically and independently distributed (i.i.d.) prepared states [272, 21]. In this way, the state from Bob's perspective is

$$\varrho = \sum_i p_i \varrho_i^{\otimes n} \tag{2.19}$$

For a binary discrimination problem and equal a priori probability, the error is given as derived above. In the asymptotic limit, this has been proved to scale exponentially as

$$p^{\text{ERR}} \sim \exp\{-n\xi_{\text{QCB}}\} \tag{2.20}$$

where ξ_{QCB} is the quantum Chernoff bound, reminiscent of the classical Chernoff bound. Its explicit form has been derived in [19] and reads as

$$\xi_{\text{QCB}} = -\log\left(\min_{0\leq s\leq 1} \text{Tr}\left\{\varrho_1^s \varrho_2^{1-s}\right\}\right). \tag{2.21}$$

which is the counterpart of the classical Chernoff bound.

2.2 Quantum parameter estimation

The birth of modern statistical and estimation theory is mainly due to the contributions of Fisher, Cramer and Rao in the first half of the previous century [271]. The most fundamental result was the inequality for the variance of any estimator on finite samples derived by Cramer and Rao [286]. Their result is mainly based on geometrical arguments in the language of Riemannian manifolds and the Fisher metric tensor [135]. After 30 years, Rao's ideas were extended to formulate an asymptotic theory of statistical inference [125]. In the following decades, thanks to the work of Amari et al. [11, 14], the geometrization of statistical models enabled the proof that the maximal likelihood estimator is optimal in the asymptotic theory [12]. The field of information geometry found several applications, and it has been proven to provide powerful tools for classical estimation theory [13]. All these results regard local theories, where we have good knowledge of the interval where the true value of the parameters lie, and this will be our setting in all the following discussions. To completeness, we also mention the cases where we do not know the range of the parameters. In this setting, estimation procedures are known as global strategies. For instance, Bayesian estimation protocols rely on the fact that the parameter is itself a random variable [148, 214]. Examples of Bayesian bounds are the Ziv-Zakai [368] and Weiss-Weinstein bounds [343].

Moving to the quantum realm, the rapid growth of quantum technologies required an equally rapid characterization of quantum systems [266, 338]. One of the first theoretical proposals to exploit quantum resources such as squeezing was already analyzed in

the early 80s [81, 80], and then this idea was employed to enhance sensitivity in currently used gravitational wave detectors [1, 116]

Generally speaking, the extension of concepts from classical estimation theory to the quantum realm has caused a great interest in the community. Several results have been obtained, such as the development of tools to establish the optimal procedure and the ultimate bounds in parameters estimation [272, 117, 218, 181, 7]. The first results date back to the 1960s when Helstrom generalized the notion of differential equations to quantum states, called symmetric logarithmic derivative (SLD) and, derived the multi-parameter quantum Cramer-Rao bound [173]. This was followed by the study by Yuen and Lax [360], where they studied the estimation of coherent states in thermal noise, while one year later the notion of most informative bound was introduced [171]. All these results were generalized by Holevo in [178], where the Holevo bound was introduced and which now is regarded as the most informative bound in multi-parameter quantum metrology. The proof of its achievability was only provided recently, using techniques from the newly developed theory of quantum local asymptotic normality (QLAN) [162, 197, 164, 358]. For the single parameter estimation, a relevant conceptual contribution came from the works of Braunstein and Caves, where they were able to separate a classical and quantum optimization, clearly showing the necessary conditions for the saturation of the quantum Cramer-Rao bound [56, 57]. They showed that the classical estimation procedure regards the search for an optimal estimator, whereas the quantum part concerns the search for the optimal POVM, and the two can be pursued separately. It is also possible to address the problem of the optimal probe achieving the ultimate limit in channel estimation and with multiple parameters, [144, 6].

It is in the determination of the optimal measurement and the optimal probe that the quantum feature reveals themselves [332, 117], and the role of incompatibility plays a fundamental role. We also briefly mention that the geometry of quantum states also has fundamental consequences in all of the results and bound mentioned, and it has attracted interest recently, especially in its abstract formulation within differential geometry [324, 255, 256, 96, 95]. Finally, we would also like to highlight that estimation and discrimination theory are strongly connected. The underlying mathematical structure of estimation theory, i.e. Fisher information metric, is strongly connected with quantities related to discrimination theory and the distinguishability measures. Technical insights of this connection are discussed in [198].

The use of quantum resources to beat the shot-noise limit (SNL), where the achievable precision $\Delta\theta^2$ scales as $1/N$ with N is the number of probes, has been extensively studied, especially with quantum resources such as squeezing and entanglement [155, 156]. Indeed, entangled probes, such as GHZ or N00N states, can surpass the SNL scaling [215, 241, 215, 251], and the so-called Heisenberg scaling $\Delta\theta^2 \sim 1/N^2$ can be attained [179]. These results have been experimentally tested within many platforms. The advancements have been particularly rapid for atoms that exploit entanglement [274], or for squeezed spin states that surpass the SNL [347, 223]. Heisenberg limit has been proved also for particle and optical interferometry [50, 213]. More in general, spin qubits, trapped ions, and flux qubits have proved to be excellent platforms in which quantum enhancements are possible [114], as well as in photonic quantum sensing [277], and in quantum illumination tasks [219, 367, 27].

Nonetheless, in more recent years, it has been shown that uncorrelated noises strongly affect such scalings behaviour, which is downscaled back to the SNL scaling [128]. Indeed, a small amount of noise is sufficient to bring the scaling from $1/N^2$ to $1/N$ [204, 119]. In general, the effect of decoherence is always detrimental and reduces the scaling, even when the use of quantum resources is allowed [118, 205, 326]. The effect of

inefficient detectors also has been studied in [32] to figure out how it affects the scaling behaviour.

Attempt to restore the Heisenberg scaling have been proposed, based again on the use of entangled ancillary systems [120], or the continuous monitoring of the environment [8]. At a more fundamental level, techniques to achieve better precision without using entangled probes, which are difficult to produce and stabilize and not particularly robust to noise, have been addressed, and an extensive review can be found in [55]. They include the use of more general quantum correlations such as quantum discord [243], identical particles [33, 34], nontrivial Hamiltonians that exploit non-linearities [303, 108, 48, 49, 222], or the use of quantum phase transitions [146, 138, 225, 361]. Other recent attempts try to use also non-causal order to achieve better scaling [366, 87]. The use of feedback to achieve optimal phase estimation was also studied by [44, 43, 42, 174].

In this section, we are going to provide a review of the mathematical tools developed to deal with problems in quantum estimation theory. In Sec. 2.2.1 we briefly review the language of estimation theory, namely probability and statistics. Then, in Sec. 2.2.2 we move to classical parameter estimation, proving the main results and bounds. Finally, we present its quantum version, both in the single and multi-parameter case, respectively in Sec. 2.2.3 and Sec. 2.2.4.

2.2.1 Probability and statistics

The abstract theory of probability was formalized by Kolmogorov in the last century [203], and here we review its mathematical structure. First, we need to select a collection of event $\{E_i\}$ that belongs to the *sample space* Ω, i.e. the set of possible outcomes of a random event. A probability is a way of assigning every event a value between zero and one. But before this, we need to properly define the set of $\{E_i\}$, since not every subset of Ω constitutes an event. If we denote with $\mathcal{E}$ a collection of subsets of Ω, then we ask the following

1. the empty set should be an event, i.e. $\emptyset \in \mathcal{E}$. This represents an experiment without an outcome.

2. if $E \in \mathcal{E}$, then its complement E^c is also in $\mathcal{E}$. This corresponds to having the logical negation of the event E as a possible event.

3. The union of a countable collection of E_i in $\mathcal{E}$ is also an element of $\mathcal{E}$

These properties define a σ-algebra, while the pair $(\Omega, \mathcal{E})$ is called a *measurable space*.

The assignment of a numerical counterpart to a single event can be specified by a new function called *probability measure* μ, which satisfies the following properties

Definition 1: Probability space $(\Omega, \mathcal{E}, \mu)$

A probability space is a triple $(\Omega, \mathcal{E}, \mu)$ where μ where Ω is a sample space, $\mathcal{E}$ is a σ-algebra and μ is a function from $\mathcal{E}$ having the following properties

1. The function μ assigns to each event a non-negative number
$$\mu : \mathcal{E} \to \mathbb{R}^+; \tag{P.1}$$
2. The unit measure assumption
$$\mu(\Omega) = 1 \tag{P.2}$$
3. The σ-additivity assumption
$$\mu\left(\bigcup_{i=1}^{+\infty} E_i\right) = \sum_{i=1}^{+\infty} \mu(E_i). \tag{P.3}$$
with $\{E_i\}_{i=1}^{+\infty}$ a countable collection of mutually disjoint elements of $\mathcal{E}$.

From the three axioms, it immediately follows that $0 \leq \mu(E) \leq 1$, where the lower and upper bounds are respectively achieved only with the empty set $\emptyset$ and the full space Ω. We also mention that quasiprobability distributions, that arise naturally in quantum mechanics formulated in phase space, relax the first axiom.

A quick comment on these axioms is in order here. The last property is fundamental to be consistent with the frequentist interpretation of probability, which is the one that is naturally used when dealing with events in the laboratory. Indeed, Eq. (P.3) represent the following: if two disjoint events E_1 and E_2 have respectively the relative frequency f_1 and f_2, then the event $E_1 \cup E_2$ must have the relative frequency $f_1 + f_2$. The axiom extends this property even in the case of countable mutually disjoint events.

The probability measure μ assigns values to elements of the σ-algebra $\mathcal{E}$ rather than to the set possible outcomes Ω. One would also like to define a function whose domain is Ω, which represents more concretely what is observed in experiments. This is described by a *random variable* X_r, which so defined [141]

Definition 2: Random variable X_r

Given a probability space $(\Omega, \mathcal{E}, \mu)$ and a measurable space $(\Upsilon, \mathcal{Y})$, a random variable is a function $X_r : \Omega \to \Upsilon$ that assign to each event a certain quantity y in Υ. This function must satisfy the following: if Y is a set of quantities y_i that belongs to the σ-algebra $\mathcal{Y}$, then $X_r^{-1}(Y)$ is an element of the σ-algebra $\mathcal{E}$. The measurable space $(\Upsilon, \mathcal{Y})$ can be naturally extended to a probability space $(\Upsilon, \mathcal{Y}, \nu)$ with the probability measure $\nu : \mathcal{Y} \to [0, 1]$ defined as

$$\nu(Y) = \mu(X_r^{-1}(Y)) \tag{2.22}$$

with Y measurable set in $\mathcal{Y}$. This probability measure is said to be induced by X_r from μ.

In other words, Υ is the set of values that the random variable can assume, and $\mathcal{Y}$ is a measurable subset of Υ. The random variable is then a function from any possible outcomes in Ω to a quantity in the set of Υ such that the outcomes leading to any useful subset of quantities, i.e. $X_r^{-1}(Y)$ have a well-defined probability, i.e. belongs to the σ-algebra $\mathcal{E}$. We can see that random variable transforms probability space to probability space. Usually, the distinction between the two probability spaces $(\Omega, \mathcal{E}, \mu)$ and $(\Upsilon, \mathcal{Y}, \nu)$ is not made clear, and one usually says that the outcomes of a random experiment are elements of Υ rather than event in $\mathcal{E}$ [318].

In statistics, random variables are usually limited to real value, i.e. $\Upsilon = \mathbb{R}$. In this case, all the probability measures on this space ν have a clear classification and can be expressed in terms of distribution functions. Indeed, one can show that the function $P : \mathbb{R} \to [0, 1]$ defined as

$$P(x) = \nu((-\infty, x]) \tag{2.23}$$

is the distribution function of ν. If X_r is the random variable that induces ν, then we will also say that P is the distribution function of X_r. It can be also proven that for each distribution function there exists a unique probability ν on $(\mathbb{R}, \mathcal{Y})$ [141]. The relationship between the random variable and the distribution is easily understood when P are strictly increasing and continuous: in this case, X_r and P are simply inverse functions of each other. In the other cases, X_r is left continuous and jumps may occur, that correspond to intervals of constancy of P, and vice-versa.

If the distribution function admits an integral representation

$$P(x) = \int_{-\infty}^{x} p(t)dt \tag{2.24}$$

we say that $p(x)$ is the *probability density function* of P and also of the corresponding probability measure ν and random variable X_r. This $p(x)$ is unique if we ask for $p(x)$ to be continuous on the support of P. The concept of probability density can be also extended where Υ is a countable set or finite set. For the technical details, we refer the reader to Chap. 8 in [141].

The knowledge of $p(x)$ fully characterizes any random experiments whose outcomes are described by the random variable X_r. Indeed, any probability of any event $Y \in \mathcal{Y}$ is obtained just by integrating p on the corresponding Y. Henceforth, we will speak of random outcomes and experiment directly in terms of probability density function p.

Once we have formalized the abstract probability theory, we can move on to the study of more practical problems. As said before, estimation theory is a branch of statistics, whose main concern is the collection of data $\vec{x} = \{x_1, ..., x_M\}$ and their analysis and interpretations. In classical inference and decision theory, the outcomes are postulated to come from the observation of a random variable, which now we know is described in terms of a certain probability distribution $p(x)$. These can be modelled in terms of a set of parameters $\boldsymbol{\theta}$, and the goal of statistical analysis is to find proper values of $\boldsymbol{\theta}$ such that the observed data is more optimally explained by the probability evaluated at this value. The specification of a single value of the parameters is known as *point estimation*, which is one of the main strategies in statistical inference. Moreover, the precision of the estimated value will not depend only on the strategy, but also on the definition of the figure of merit (also known as loss function or risk function) that quantifies the optimality above mentioned[214]. This will be the topic of the next section.

2.2.2 Classical estimation theory

After the introduction of the building blocks of probability statistics, we can now present the usual setting in which a parameter estimation problem is formulated. We consider an experiment whose outcomes are described by a random variable X_r. Associated with the random variable there is a probability space $(\mathcal{X}, \mathcal{B}, \nu)$ and a *true* probability density $p(x)$, which is not known. The goal is to find a procedure that reconstructs the probability distribution $p(x)$ from a sample of M outcomes $\vec{x} = \{x_1, ..., x_M\}$. In principle, there might be theoretical or experimental arguments that allow us to guess a functional form of p that depends on a finite number of parameters n (the case where the number of parameters is infinite are known as semi-parametric or non-parametric models [206]). Within this approach, we say that the probability density $p(x)$ belongs to *parametric family* of probability densities $\{p(x|\boldsymbol{\theta})\}_{\boldsymbol{\theta}\in\Theta}$ where $\Theta \subset \mathbb{R}^n$ is the *parameter space*. The true value of the parameters $\boldsymbol{\theta}^\star \in \Theta$ is the one such that $p(x|\boldsymbol{\theta}^\star) = p(x)$.

In general, to estimate the true value of the parameter $\boldsymbol{\theta}^\star$ from a sample of M data $\vec{x} = \{x_1, ..., x_M\}$ we need an *estimator* $\tilde{\boldsymbol{\theta}}^{(M)}$, i.e. a function from the space of M independent, identically distributed (i.i.d.) random variables to the parameter space Θ. An *estimate* of $\boldsymbol{\theta}$ is a particular realization of this function $\tilde{\boldsymbol{\theta}}^{(M)}(\vec{x})$. Given that this function is a function of random variables, it is itself a random variable, while the estimate $\boldsymbol{\theta}$, given the data $\vec{x} = \{x_1, ..., x_M\}$, is a fixed real value, or a fixed real vector in the multi-parameter case.

We define *unbiased estimators* the one satisfying $\mathbb{E}_{\boldsymbol{\theta}}(\tilde{\boldsymbol{\theta}}^{(M)} - \boldsymbol{\theta}) = 0$ for all $\boldsymbol{\theta}$, where the expectation value is given as

$$\mathbb{E}_{\boldsymbol{\theta}}\left(\tilde{\boldsymbol{\theta}}^{(M)}\right) = \sum_{\vec{x}\in\mathcal{X}^M} \tilde{\boldsymbol{\theta}}^{(M)}(\vec{x}) p(\vec{x}|\boldsymbol{\theta}). \tag{2.25}$$

where $p(\vec{x}|\boldsymbol{\theta}) = \prod_{i=1}^{M} p(x_i|\boldsymbol{\theta})$ since $\vec{x}$ are i.i.d. . This means that, for every possible value of $\boldsymbol{\theta}$, and not only for the true value $\boldsymbol{\theta}^\star$, the estimator can correctly guess it, without bias on the values of the parameters. If this is not the case, the deviation of $\tilde{\boldsymbol{\theta}}^{(M)}$ from the value of $\boldsymbol{\theta}$ is quantified by the bias

$$B_{\boldsymbol{\theta}}(\tilde{\boldsymbol{\theta}}^{(M)}) = \mathbb{E}_{\boldsymbol{\theta}}(\tilde{\boldsymbol{\theta}}^{(M)}) - \boldsymbol{\theta}. \tag{2.26}$$

Systematic errors are the one quantified by a non-null bias $B_{\boldsymbol{\theta}}(\tilde{\boldsymbol{\theta}}^{(M)})$, hence they are a property of the estimator $\tilde{\boldsymbol{\theta}}^{(M)}$, not of the estimate $\boldsymbol{\theta}$. In other words, it does not depend on a particular set of data $\vec{x}$, but rather on the functional definition of $\tilde{\boldsymbol{\theta}}^{(M)}$. We notice that the unbiasedness condition might be too restrictive: one would like to have a good estimator for the true values of the parameters $\boldsymbol{\theta}^\star$ only. Hence, to enlarge the set of available functions, we can define *locally unbiased estimators* as

Definition 3: Locally unbiased estimators

We define locally unbiased estimators as the ones satisfying

$$\mathbb{E}_{\boldsymbol{\theta}^\star}(\tilde{\boldsymbol{\theta}}^{(M)} - \boldsymbol{\theta}^\star) = 0 \tag{2.27}$$

for the true value of the parameter $\boldsymbol{\theta} = \boldsymbol{\theta}^\star$. We also ask that the derivative of this equation is zero, i.e.

$$\partial_{\boldsymbol{\theta}} \mathbb{E}_{\boldsymbol{\theta}^\star}(\tilde{\boldsymbol{\theta}}^{(M)} - \boldsymbol{\theta}^\star) = 0. \tag{2.28}$$

This request means that the estimator $\tilde{\boldsymbol{\theta}}^{(M)}$ can track the true value of the parameter up to the first order around the $\boldsymbol{\theta}^\star$, and excludes pathological estimators.

We also introduce *asymptotically unbiased estimator* as

$$\lim_{M\to\infty} \mathbb{E}_{\boldsymbol{\theta}}(\tilde{\boldsymbol{\theta}}^{(M)}) = \boldsymbol{\theta}, \tag{2.29}$$

that are unbiased as the size of the sample goes to infinity.

To quantify how much a sampled data $\vec{x} = \{x_1, ..., x_M\}$ deviates from the corresponding expected value, we define the *sampling deviation* as

$$\Delta(\vec{x}) = \tilde{\boldsymbol{\theta}}^{(M)}(\vec{x}) - \mathbb{E}_{\boldsymbol{\theta}}(\tilde{\boldsymbol{\theta}}^{(M)}) \tag{2.30}$$

This quantity depends on the sample, and as a result, it is not a property of the estimator. Moreover, it is a random quantity that exhibits fluctuations around zero. Hence, averaging the product of the squared sampling deviation we obtain a numerical figure of merit that quantify the average deviation of the possible samples from the expected value. In this way, we obtain the *covariance matrix*

$$V(\tilde{\boldsymbol{\theta}}^{(M)})_{ij} = \mathbb{E}_{\boldsymbol{\theta}}\left[\left(\tilde{\theta}_i^{(M)} - \mathbb{E}_{\boldsymbol{\theta}}(\tilde{\theta}_i^{(M)})\right)\left(\tilde{\theta}_j^{(M)} - \mathbb{E}_{\boldsymbol{\theta}}(\tilde{\theta}_j^{(M)})\right)\right], \tag{2.31}$$

which is the quantity that captures the performance of an estimator. The diagonal elements $V(\tilde{\boldsymbol{\theta}}^{(M)})_{ii}$ are the variance of the single parameters θ_j and indicate, on average, how far the collection of estimates are from the expected value. Instead, non-zero off-diagonal elements denote the presence of correlations between the estimators $\tilde{\theta}_i^{(M)}$.

A similar concept is given by the *mean square error*

$$\mathrm{MSE}(\tilde{\boldsymbol{\theta}}^{(M)})_{ij} = \mathbb{E}_{\boldsymbol{\theta}}\left[\left(\tilde{\theta}_i^{(M)} - \theta_i\right)\left(\tilde{\theta}_j^{(M)} - \theta_j\right)\right] \tag{2.32}$$

whose diagonal element instead indicate how far, on average, the collection of estimates is from the value of $\boldsymbol{\theta}$, rather than from the expected value.

Remarkably, the two quantities are connected by the bias function $B_{\boldsymbol{\theta}}(\tilde{\boldsymbol{\theta}}^{(M)})$ as

$$\mathrm{MSE}(\tilde{\boldsymbol{\theta}}^{(M)})_{ij} = V(\tilde{\boldsymbol{\theta}}^{(M)})_{ij} + B_{\boldsymbol{\theta}}(\tilde{\theta}_i^{(M)})B_{\boldsymbol{\theta}}(\tilde{\theta}_j^{(M)}) \tag{2.33}$$

This can be interpreted by the fact that the MSE is the second moment (about the origin) of the error $\theta_i^{(M)} - \theta_i$. Hence, it includes how much the estimate from data samples is spread (quantified by the variance), but also how far off the average estimated value is

from the true value (quantified by the bias). The connection between bias and variance here is quite evident: the bias is related to systematic errors, while the variance is to statistical error. This relationship is analogous to the distinction between accuracy and precision respectively. We notice that for unbiased estimators the covariance matrix and MSE matrix coincide. Since our interest is to study the limits of precision using quantum probes, we consider only unbiased estimators. This assumption is not too much restrictive, since we can always be unbiased in the asymptotic limit, as in Eq. (2.29).

The main result in statistical estimation regards a lower bound on the variance that is independent of the estimator used. In this way, the lower bound represent a property of the probability distribution only $p(x|\boldsymbol{\theta})$. To see this, we first rewrite the variance in matrix form as follows

$$\boldsymbol{V}(\tilde{\boldsymbol{\theta}}^{(M)}) = \sum_{\vec{x}} p(\kappa|\boldsymbol{\theta})(\tilde{\boldsymbol{\theta}}^{(M)}(\vec{x}) - \boldsymbol{\theta})(\tilde{\boldsymbol{\theta}}^{(M)}(\vec{x}) - \boldsymbol{\theta})^T, \tag{2.34}$$

Then, the fundamental result in classical estimation theory is the following theorem

Theorem 3: The Cramer-Rao inequality

Given a parametric family of probability densities $\{p(x|\boldsymbol{\theta})\}_{\boldsymbol{\theta}\in\Theta}$, the variance of any estimator is lower bounded as [286, 105]

$$\boldsymbol{V}(\tilde{\boldsymbol{\theta}}^{(M)}) \succeq \min_{\{\tilde{\boldsymbol{\theta}}^{(M)}\}} \boldsymbol{V}(\tilde{\boldsymbol{\theta}}^{(M)}) = \frac{1}{M}\boldsymbol{\mathcal{F}}^{-1}(\boldsymbol{\theta}) \tag{2.35}$$

where M is the number of measurements, and

$$\begin{aligned}\mathcal{F}(\boldsymbol{\theta})_{ij} &= \sum_{x\in\mathcal{X}} p(x|\boldsymbol{\theta})\left(\partial_i \ln p(x|\boldsymbol{\theta})\right)\left(\partial_j \ln p(x|\boldsymbol{\theta})\right) = \\ &= \sum_{x\in\mathcal{X}} \frac{1}{p(x|\boldsymbol{\theta})}\left(\partial_i p(x|\boldsymbol{\theta})\right)\left(\partial_j p(x|\boldsymbol{\theta})\right)\end{aligned} \tag{2.36}$$

are the elements of the Fisher information matrix (FIM) [135]. This is a positive semidefinite matrix. If the estimator is only locally unbiased the inequality holds only at $\boldsymbol{\theta} = \boldsymbol{\theta}^\star$. The symbol $\boldsymbol{A} \succeq \boldsymbol{B}$ means that $\boldsymbol{A} - \boldsymbol{B}$ is semidefinite positive [14, 105, 168].

As we see from its definition, the FIM is independent of the set of outcomes $\vec{x} = \{x_1, ..., x_M\}$ and on the estimator $\tilde{\boldsymbol{\theta}}$. In this sense, it is a general bound for any estimator and data sample. For these reasons, we can interpret the FIM as a measure of the amount of information that the random variable described by the probability distribution $p(x|\boldsymbol{\theta})$ carries about the parameter $\boldsymbol{\theta}$. The larger the FIM, the larger the information and the smaller the lower bound. From a heuristic point of view, the probability distribution is more sensitive to parameter changes. We also notice that in the Cramer-Rao bound in Eq. (2.35) the inverse of the FIM is involved. In the case where the FIM is not invertible, i.e. when one of its eigenvalues is zero, we have a *singular statistical model*. This implies that two or more parameters are not independent, and we can estimate only a function of them.

We can also interpret the FIM as a distinguishability metric which provides a statistical distance on the space of probability distributions [14]. It quantifies how easily we can distinguish neighbouring probability distributions when separated by an infinitesimally change in the values of the parameters. Seen from this perspective, non-null off-diagonal elements in the FIM indicate that the coordinate system, i.e. the parametrization, is not orthogonal.

The saturability of the CRb in Eq. (2.35) is crucial in establishing the relevance of the FIM. In general, not all estimators saturate the bound, and those that do are called *efficient*. In the finite-sample scenario, the existence of an efficient estimator is, in general, not guaranteed for an arbitrary statistical model. However, in the asymptotic limit and under some regularity conditions, it can be proved [214] that the lower bound given by the variance is achieved by maximum likelihood estimator $\tilde{\boldsymbol{\theta}}^{(M)}_{\text{max}}$

$$\lim_{M\to\infty} M\boldsymbol{V}(\tilde{\boldsymbol{\theta}}^{(M)}_{\text{max}}) = \boldsymbol{\mathcal{F}}^{-1}(\boldsymbol{\theta}). \tag{2.37}$$

To summarize, the FIM represent the attainable bound realizing the ultimate precision in classical estimation theory, and in the worst case is achieved asymptotically.

In general, dealing with matrix inequalities can be problematic, as the order in the space of matrices is only partial. For this reason, one can introduce scalar bounds using a suitable cost matrix $\boldsymbol{W}$ and a cost function defined as

$$\mathcal{C}[\boldsymbol{V}(\tilde{\boldsymbol{\theta}}^{(M)}), \boldsymbol{W}] = \text{tr}\left\{\boldsymbol{W}\boldsymbol{V}(\tilde{\boldsymbol{\theta}}^{(M)})\right\}. \tag{2.38}$$

where we have introduced the tr $\{\bullet\}$ as the trace over the parameter space, to distinguish it from Tr $\{\bullet\}$, the trace over the Hilbert space of the quantum states. This inequality is easily translated into a scalar CRb

$$\mathcal{C}[\boldsymbol{V}(\tilde{\boldsymbol{\theta}}^{(M)}), \boldsymbol{W}] \geq \text{tr}\left\{\boldsymbol{W}\boldsymbol{\mathcal{F}}^{-1}(\boldsymbol{\theta})\right\} \tag{2.39}$$

Cost matrices, also referred to as weight matrices, are positive, real $n \times n$ matrices, and they represent the relative importance between the parameters. Scalar bounds will play a fundamental role in multi-parameter quantum metrology, as we are going to see soon.

2.2.3 Single parameter quantum metrology

In this section, we discuss what happens when a parametric statistical model emerges from quantum theory [166, 167]. We first discuss single-parameter estimation, which significantly differs from the multi-parameter setting, where quantum incompatibility in the form of non-commutativity makes things more complicated. These results have been first obtained by Helstrom [172] and Holevo [178] in the 70s. However, a major breakthrough occurred only 20 years later, when Braunstein and Caves [56] showed the quantity previously derived can be obtained by maximizing the classical Fisher information on the set of all measurements, establishing a clear and operational connection with classic estimation theory. Our presentation is based on a more recent review of these results [266].

When we move to the quantum realm, probability distributions naturally emerge from quantum mechanics postulates. Indeed, the Born rule is

$$p(\kappa|\theta) = \text{Tr}\left\{\varrho_\theta \Pi_\kappa\right\}. \tag{2.40}$$

Here we have assumed that the parameter is fully encoded in the state of the system, rather than in the POVM as well[1].

An important quantity in quantum metrology is the symmetric logarithmic derivative $\widehat{L}_\theta$, which is a generalization of the classical notion of logarithmic derivative that enters the definition of the FI in Eq. (2.36) $\partial_\theta p(x|\theta) = p(x|\theta)L_{cl}$. The straightforward generalization of this is obtained by substituting to the probability the density matrix and by a proper symmetrization to avoid order ambiguities [324]. We obtain that the definition of the $\widehat{L}_\theta$ is given as a Lyapunov equation

$$\partial_\theta \varrho_\theta = \frac{1}{2}\left(\widehat{L}_\theta \varrho_\theta + \varrho_\theta \widehat{L}_\theta\right). \tag{2.41}$$

There are other ways to obtain a generalization of the derivative $\partial_\theta p(x|\theta)$, essentially based on other notions of distance in the Hilbert space and symmetrization [166, 324]. In the single-parameter scenario, they are not particularly relevant, since the bound they provide is less informative than the one obtained with the SLD.

The score of the probability distribution can be written in terms of $\widehat{L}_\theta$ as

$$\partial_\theta p(x|\theta) = \mathrm{Tr}\left\{\partial_\theta \varrho_\theta \Pi_x\right\} = \Re\left\{\mathrm{Tr}\left\{\varrho_\theta \Pi_x \widehat{L}_\theta\right\}\right\} \tag{2.42}$$

which allows us to rewrite the FI as

$$\mathcal{F}(\theta) = \sum_{x\in\mathcal{X}} \frac{\Re\left\{\mathrm{Tr}\left\{\varrho_\theta \Pi_x \widehat{L}_\theta\right\}\right\}^2}{\mathrm{Tr}\left\{\varrho_\theta \Pi_x\right\}} \tag{2.43}$$

So far, this is just a rewriting of the classical Cramer-Rao bound in terms of a certain $\{\Pi_x\}_{x\in\mathcal{X}}$ and state ϱ_θ. However, we can try to optimize among the set of POVMs [266]. Using the fact that $\Re\{\lambda\}^2 \leq |\lambda|^2$, we can write

$$\mathcal{F}(\theta) \leq \sum_{x\in\mathcal{X}} \left| \frac{\left\{\mathrm{Tr}\left\{\varrho_\theta \Pi_x \widehat{L}_\theta\right\}\right.}{\sqrt{\mathrm{Tr}\left\{\varrho_\theta \Pi_x\right\}}} \right|^2 = \sum_{x\in\mathcal{X}} \left| \mathrm{Tr}\left\{ \frac{\sqrt{\varrho_\theta}\sqrt{\Pi_x}}{\sqrt{\mathrm{Tr}\left\{\varrho_\theta \Pi_x\right\}}} \sqrt{\Pi_x}\widehat{L}_\theta\sqrt{\varrho_\theta} \right\} \right|^2, \tag{2.44}$$

and this inequality is saturated when $\mathrm{Tr}\left\{\varrho_\theta \Pi_x \widehat{L}_\theta\right\}$ is a real number. We can further lower bound this last expression using the Schwartz inequality

$$\left|\mathrm{Tr}\left\{A^\dagger B\right\}\right|^2 \leq \mathrm{Tr}\left\{A^\dagger A\right\} \mathrm{Tr}\left\{B^\dagger B\right\} \tag{2.45}$$

with $A^\dagger = \mathrm{Tr}\left\{\sqrt{\varrho_\theta}\sqrt{\Pi_x}\right\} / \sqrt{\mathrm{Tr}\left\{\varrho_\theta \Pi_x\right\}}$ and $B = \sqrt{\Pi_x}\widehat{L}_\theta\sqrt{\varrho_\theta}$. Indeed, we obtain

$$\begin{aligned}\mathcal{F}(\theta) &\leq \sum_{x\in\mathcal{X}} \mathrm{Tr}\left\{ \frac{\sqrt{\varrho_\theta}\sqrt{\Pi_x}}{\sqrt{\mathrm{Tr}\left\{\varrho_\theta \Pi_x\right\}}} \frac{\sqrt{\Pi_x}\sqrt{\varrho_\theta}}{\sqrt{\mathrm{Tr}\left\{\varrho_\theta \Pi_x\right\}}} \right\} \mathrm{Tr}\left\{ \sqrt{\varrho_\theta}\widehat{L}_\theta \sqrt{\Pi_x}\sqrt{\Pi_x}\widehat{L}_\theta\sqrt{\varrho_\theta} \right\} = \\ &= \sum_{x\in\mathcal{X}} \mathrm{Tr}\left\{\varrho_\theta \widehat{L}_\theta \Pi_x\right\} = \mathrm{Tr}\left\{\varrho_\theta \widehat{L}_\theta^2\right\}\end{aligned} \tag{2.46}$$

[1] In the case where also the POVM depends on the parameter, things are more complicated and generalization have been studied, see [319].

which is now independent on the POVM $\{\Pi_x\}_{x\in\mathcal{X}}$. This last inequality is saturated when the two A and B are orthogonal, i.e. when

$$\frac{\sqrt{\Pi_x}\sqrt{\varrho_\theta}}{\mathrm{Tr}\left\{\varrho_\theta\Pi_x\right\}} = \frac{\sqrt{\Pi_x}\widehat{L}_\theta\sqrt{\varrho_\theta}}{\mathrm{Tr}\left\{\varrho_\theta\Pi_x\widehat{L}_\theta\right\}} \tag{2.47}$$

for all θ and x. This equality is satisfied if and only if the $\{\Pi_x\}$ are eigenprojectors of the $\widehat{L}_\theta$, meaning that the eigenstates of the SLD operator realize the optimal POVM, given the additional condition $\mathrm{Tr}\left\{\varrho_\theta\Pi_\kappa\widehat{L}_\theta\right\}$ is real. This is a projective measurement and depends on the true parameter θ. Paradoxically, one should know the value of the parameter in advance to implement the optimal measurement. Nonetheless, this challenge is often solved by using adaptive strategies, in which one accumulates preliminary statistics to obtain an intermediate estimate, that is then used to perform a more refined adapted measurement until the optimal measurement is asymptotically reached [25, 142]. The result is summarized as follows

Theorem 4: The quantum Cramer-Rao bound

Given a statistical model encoded in a density matrix ϱ_θ and the set of all possible POVM $\mathbf{\Pi}$, we can maximize the FI such as that

$$\mathcal{F}(\theta) \leq \max_{\mathbf{\Pi}} \mathcal{F}(\theta) = \mathcal{Q}(\theta) = \mathrm{Tr}\left\{\varrho_\theta\widehat{L}_\theta^2\right\} = \mathrm{Tr}\left\{\partial_\theta\varrho_\theta\widehat{L}_\theta\right\} \tag{2.48}$$

where $\mathcal{Q}(\theta)$ is the quantum Fisher information (QFI). This inequality yields the quantum Cramer-Rao (QCRB) bound

$$V(\tilde{\theta}^{(M)}) \geq \frac{1}{M\mathcal{F}(\theta)} \geq \frac{1}{M\mathcal{Q}(\theta)} \tag{2.49}$$

The first inequality is saturated by the PVM given by the eigenprojector of the SLD operator $\{|\lambda_k\rangle\langle\lambda_k|\}_k$, with the additional condition that $\mathrm{Tr}\left\{\varrho_\theta\Pi_\kappa\widehat{L}_\theta\right\}$ is real. The optimal estimator $\widehat{O}_\theta = \sum_k \tilde{\theta}_k|\lambda_k\rangle\langle\lambda_k|$ that saturates also the classical inequality is a function of the eigenvalues of $\widehat{O}_\theta$, and is given by

$$\widehat{O}_\theta = \theta\mathbb{I} + \frac{\widehat{L}_\theta}{\mathcal{Q}(\theta)}, \tag{2.50}$$

The optimality of the estimator can be proved directly by evaluating the variance of $\widehat{O}_\theta$.

This bound has been derived for measurements on single-copy preparation of the state ϱ_θ. However, if we have M identically prepared state, the most general scenario consists of a POVM on the whole Hilbert space, which might be also collective. In this case, the overall variance is written as

$$V(\tilde{\theta}^{(M)}) = \sum_k \left(\tilde{\theta}^{(M)}(k) - \theta\right)^2 \mathrm{Tr}\left\{\varrho_\theta^{\otimes M}\Pi^{(M)}(k)\right\}. \tag{2.51}$$

Nonetheless, one can show that this quantity is lower bounded by the QFI given in Eq. (2.48), which means that non-collective strategies are optimal [167]. This differs significantly from the multi-parameter case, as we are going to see in the next section.

An explicit expression of the QFI can be derived using a formal solution of the Lyapunov equation (2.41)

$$\widehat{L}_\theta = 2\int_0^{+\infty} e^{-t\varrho_\theta}(\partial_\theta \varrho_\theta)e^{-t\varrho_\theta}dt = \tag{2.52}$$

$$= \sum_{n,m} \frac{\langle\psi_m|\partial_\theta\varrho_\theta|\psi_n\rangle}{p_m+p_n}|\psi_m\rangle\langle\psi_n| \tag{2.53}$$

with $p_m + p_n > 0$ and where we have used the spectral decomposition $\varrho_\theta = \sum_n p_n|\psi_n\rangle\psi_n|$. Using the last expression, the QFI can be written as

$$\mathcal{Q}(\theta) = \sum_{n,m} \frac{|\langle\psi_m|\varrho_\theta|\psi_n\rangle|^2}{p_m+p_n} \tag{2.54}$$

or equivalently as

$$\mathcal{Q}(\theta) = \sum_n \frac{(\partial_\theta p_n)^2}{p_n} + 2\sum_{n,m}\frac{(p_n-p_m)^2}{p_n+p_m}|\langle\psi_m|\partial_\theta\psi_n\rangle|^2 \tag{2.55}$$

The first term is nothing but the classical FI for the probability distribution $\{p_n\}$ for θ, while the second term accounts for the change of the eigenstates with respect to changes in θ. Unfortunately, these equations are only useful when it is possible to diagonalise ϱ_θ, otherwise, it is not particularly feasible. Despite that, alternative expressions of the QFI that do not require diagonalisation of ϱ_θ have been derived [307].

The QFI satisfies a few relevant properties:

(i) Similarly to the classical case, the QFI of uncorrelated states is additive [143]

$$\mathcal{Q}[\varrho_\theta \otimes \varsigma_\theta] = \mathcal{Q}[\varrho_\theta] + \mathcal{Q}[\varsigma_\theta] \tag{2.56}$$

where we have slightly changed the notation for the QFI, i.e. $\mathcal{Q}[\varrho_\theta] = \mathcal{Q}(\theta)$. The additivity shows that the QFI for M i.i.d. probes $\varrho^{\otimes M}$ scales as M, realizing an SNL scaling. We conclude that to improve this scaling, correlations are necessary among the probes.

(ii) It is not a convex function of the input state but satisfies an *extended convexity* inequality [10]

$$\mathcal{Q}\left[\sum_n p_n\varrho_n\right] \leq \sum_n p_n\mathcal{Q}\left[\varrho_n\right] + \mathcal{F}\left[\{p_n\}\right] \tag{2.57}$$

where $\mathcal{F}\left[\{p_n\}\right]$ is the classical FI of the probability distribution $\{p_n\}$, similarly to (2.55). The only way we recover full convexity is if this term vanishes, and this happens when the parameter is not encoded in the $\{p_n\}$. In the latter case, we see that the achievable estimation sensitivity cannot be increased by classically mixing states with mixing probabilities independent of the parameter [54].

(iii) The QFI is monotone for quantum operations [273]

$$\mathcal{Q}[\varrho_\theta] \geq \mathcal{Q}[\mathcal{E}[\varrho_\theta]], \tag{2.58}$$

where $\mathcal{E}[\bullet]$ does not depend on the parameter. Equality occurs when the quantum operation is unitary.

(iv) In the case of a pure state $|\psi_\theta\rangle$ the QFI simplifies as

$$\mathcal{Q}[|\psi_\theta\rangle] = 4\left(\langle\partial_\theta\psi_\theta|\partial_\theta\psi_\theta\rangle + (\langle\partial_\theta\psi_\theta|\psi_\theta\rangle)^2\right) \tag{2.59}$$

Furthermore, if the parameter is encoded via a unitary operator $|\psi_\theta\rangle = \exp\{i\theta\widehat{G}\}|\psi_0\rangle$, where $\widehat{G}$ is the generator, then the QFI is proportional to the variance of the generator on the initial state $|\psi_0\rangle$

$$\mathcal{Q}[|\psi_\theta\rangle; \widehat{G}] = 4V(\widehat{G}) = 4\left(\langle\psi_0|\widehat{G}^2|\psi_0\rangle - \langle\psi_0|\widehat{G}|\psi_0\rangle^2\right) \tag{2.60}$$

The latter is upper-bounded as

$$\mathcal{Q}[|\psi_\theta\rangle; \widehat{G}] \leq (g_{max} - g_{min})^2 \tag{2.61}$$

where g_{max} (g_{min}) are the largest (smallest) eigenvalue of $\widehat{G}$. The inequality is tight if $|\psi_0\rangle = 2^{-1/2}(|g_{max}\rangle + |g_{min}\rangle)$.

(v) The QFI has a geometrical interpretation in terms of the Bures distance

$$D_B(\varrho_1, \varrho_2) = \sqrt{2(1 - F[\varrho_1, \varrho_2])} \tag{2.62}$$

where the fidelity is $F[\varrho_1, \varrho_2] = \mathrm{Tr}\left\{\sqrt{\sqrt{\varrho_1}\varrho_2\sqrt{\varrho_1}}\right\}$. The corresponding metric is the Bures metric

$$ds_B^2 = D_B^2[\varrho_\theta, \varrho_{\theta+d\theta}] = 4\mathcal{Q}[\varrho_\theta]d\theta^2 \tag{2.63}$$

This can be also written as the limit

$$\mathcal{Q}[\varrho_\theta] = \lim_{\varepsilon\to 0} \frac{8(1 - F[\varrho_\theta, \varrho_{\theta+\varepsilon}])}{\varepsilon^2} \tag{2.64}$$

For pure states, the fidelity is the overlap of the two states $F[|\psi_\theta\rangle, |\psi_{\theta+\varepsilon}\rangle] = |\langle\psi_\theta|\psi_{\theta+\varepsilon}\rangle|$, and the QFI can be also written as

$$\mathcal{Q}[|\psi_\theta\rangle] = 4\partial_{\theta'}\partial_{\theta''}(\log|\langle\psi_{\theta'}|\psi_{\theta''}\rangle|)|_{\theta'=\theta''=\theta} \tag{2.65}$$

With suitable generalizations, all these properties are also valid in the multi-parameter case, but the tightness of many bounds might be lost.

We conclude this section by noticing the following: the derivation of the quantum Cramer-Rao bound has made clear that there are two optimization steps. The first is at the level of measurement, where we found that the optimal PVM is given by the eigen-projectors of the SLD operator. The second is at the level of estimator functions, whose optimization can be considered a classical problem. If we have sufficient control over the system under study, another degree of freedom is still available: the initial preparation of the probe. We can formalize this in terms of parameter-dependent channels $\varrho_\theta = \mathcal{E}_\theta[\varrho]$, and the problem of maximizing the QFI and finding the optimal probe has been studied and solved by Fujiwara in [144].

2.2.4 Multiparameter quantum metrology

Things become more complicated when we move to multi-parameter quantum metrology. We can see this from a heuristic example. Let us consider two parameters $\boldsymbol{\theta} = \{\theta_1, \theta_2\}$ encoded in a certain density matrix $\varrho_{\boldsymbol{\theta}}$. From the previous section, we know that the two optimal strategies for individual estimation of the parameters are given in terms of the eigen-projectors of the $\widehat{L}_{\theta_i}$. However, the two optimal observables may not commute, meaning that an optimal measurement for the simultaneous estimation can not be performed. One may ask whether there exists another POVM that allows an optimal and joint estimate of the two parameters and what is the corresponding bound. These are the questions multi-parameter metrology deals with and are closely linked to the peculiar characteristics of quantum mechanics, namely the incompatibility of observables.

As we have seen, in the multi-parameter setting the usual figure of merit is the covariance matrix, that now we can write as

$$\boldsymbol{V}(\tilde{\boldsymbol{\theta}}^{(M)}) = \sum_{\kappa} \left\{ \left(\tilde{\boldsymbol{\theta}}^{(M)} - \boldsymbol{\theta}\right) \left(\tilde{\boldsymbol{\theta}}^{(M)} - \boldsymbol{\theta}\right)^T \mathrm{Tr}\left\{ \varrho_{\boldsymbol{\theta}}^{\otimes M} \Pi_{\kappa}^{(M)} \right\} \right\} \tag{2.66}$$

where $\{\Pi_{\kappa}^{(M)}\}_{\kappa}$ is a POVM on the whole Hilbert space of the M i.i.d. probes $\varrho_{\boldsymbol{\theta}}^{\otimes M}$. Similarly to the single-parameter case, our goal is to minimize such quantity over all the possible POVMs and the corresponding estimator $\tilde{\boldsymbol{\theta}}^{(M)}$.

To do so, we first introduce the generalization of the QFI in the multi-parameter setting

Definition 4: Quantum Fisher information matrix (QFIM)

Given a density matrix $\varrho_{\boldsymbol{\theta}}$, then the Quantum Fisher information matrix elements are defined as

$$\mathcal{Q}(\boldsymbol{\theta})_{ij} = \frac{1}{2}\mathrm{Tr}\left\{ \varrho_{\boldsymbol{\theta}} \{\widehat{L}_{\theta_i}, \widehat{L}_{\theta_j}\} \right\} \tag{2.67}$$

where $\{\bullet, \blacktriangle\}$ is the anticommutator of $\bullet$ and $\blacktriangle$. The diagonal elements of the matrix correspond to the single-parameter QFI of the ith parameter, as defined in (2.48).

A reparametrization affects the QFIM so defined. Indeed, consider a new set of parameter $\boldsymbol{\vartheta}$ that is a function $\boldsymbol{f}(\boldsymbol{\theta})$ of all the old parameters $\boldsymbol{\theta}$, i.e. $\boldsymbol{\vartheta} = \boldsymbol{f}(\boldsymbol{\theta})$. The derivatives with the new variable denoted with a prime are given by

$$\frac{\partial}{\partial \vartheta_i} = \sum_j B_{ij} \frac{\partial}{\partial \theta_j}, \tag{2.68}$$

where the matrix elements are $B_{ij} = \partial\theta_j/\partial\vartheta_i$. In this way, the SLDs in the new parametrization are given as

$$\widehat{\boldsymbol{L}}_{\boldsymbol{\vartheta}} = \boldsymbol{B}\widehat{\boldsymbol{L}}_{\boldsymbol{\theta}} \tag{2.69}$$

and as a result, the QFIM is

$$\boldsymbol{\mathcal{Q}}(\boldsymbol{\vartheta}) = \boldsymbol{B}\boldsymbol{\mathcal{Q}}(\boldsymbol{\theta})\boldsymbol{B}^T \tag{2.70}$$

A similar formula holds for the FIM in Eq. (2.36).

The QFIM and the variance satisfy a quantum version of the matrix inequality, which is named SLD-Cramer-Rao bound since it is based on the symmetric generalization of the logarithmic derivative (RLD). There exist other bounds that rely on different generalizations, such as the right logarithmic derivative [5]. The bound is given as follows

Theorem 5: Matrix and scalar SLD-Cramer-Rao bound

Given a density matrix $\varrho_{\boldsymbol{\theta}}$ and locally unbiased estimator $\tilde{\boldsymbol{\theta}}^{(M)}$, then the variance satisfy the following matrix inequality known as SLD-Cramer-Rao bound (SLD-CRb)

$$\boldsymbol{V}(\tilde{\boldsymbol{\theta}}^{(M)}) \succeq \frac{1}{M}\boldsymbol{\mathcal{Q}}^{-1}(\boldsymbol{\theta}) \tag{2.71}$$

A scalar bound can also be introduced with respect to a certain weight matrix $\boldsymbol{W}$ of the parameters using the cost function defined in Eq. (2.38). We obtain the scalar-SLD-CRb

$$\mathcal{C}[\boldsymbol{V}(\tilde{\boldsymbol{\theta}}^{(M)}), \boldsymbol{W}] \geq \frac{1}{M}\mathrm{Tr}\left\{\boldsymbol{W}\boldsymbol{\mathcal{Q}}^{-1}(\boldsymbol{\theta})\right\} = \frac{1}{M}\mathcal{C}^{\mathrm{SLD}}[\varrho_{\boldsymbol{\theta}}, \boldsymbol{W}] \tag{2.72}$$

These bounds are in general not attainable.

Despite being similar to the one obtained in the single-parameter case, and the QFIM share many properties with the QFI, this bound also features some differences, given that this bound is not in general attainable. The reason goes back to the incompatibility of optimal measurement that we have heuristically discussed at the beginning of the section. The condition to have a tight bound in Eq. (2.71) can not be directly derived from the definition of the QFIM. We are going to discuss the possible necessary and sufficient conditions for the saturability of the SLD-Cramer-Rao bound in the following section.

Before moving to this discussion, we need to present other relevant bounds in the multi-parameter scenario, which are more informative compared to the SLD-CRb. The latter bound can be derived mostly with geometrical arguments, not with constructive arguments or a true minimization like the classical one. An appropriate minimization would yield to the *most informative bound* on a single copy as

$$\mathcal{C}^{\mathrm{MI}}[\varrho_{\boldsymbol{\theta}}, \boldsymbol{W}] = \min_{\boldsymbol{\Pi}, \tilde{\boldsymbol{\theta}}^{(1)}} \left\{\mathrm{tr}\left\{\boldsymbol{W}\boldsymbol{\mathcal{F}}^{-1}(\boldsymbol{\theta})\right\}\right\} \tag{2.73}$$

This bound is achievable by construction, but it must be emphasized that, in general, a priori knowledge of the value of the parameter is necessary to carry out the optimal measurement. This issue is already present at the single-parameter level.

A tighter bound was derived by Holevo [178] and is defined as follows

Definition 5: The Holevo-Cramer-Rao-bound (HCRb)

The Holevo-Cramer-Rao bound is obtained by the following minimization

$$\mathcal{C}^{\mathrm{H}}[\varrho_{\boldsymbol{\theta}}, \boldsymbol{W}] = \min_{\boldsymbol{V}\in\mathbb{S}^n, \widehat{\boldsymbol{X}}\in\mathcal{X}_{\boldsymbol{\theta}}} \left\{ \mathrm{tr}\left\{\boldsymbol{W}\boldsymbol{V}\right\} | \boldsymbol{V} \succeq \boldsymbol{Z}\left[\widehat{\boldsymbol{X}}\right] \right\} \tag{2.74}$$

where $\mathbb{S}^n$ is the set of real symmetric n-dimensional matrices. The $n\times n$ matrix $\boldsymbol{Z}\left[\widehat{\boldsymbol{X}}\right]$ is defined as

$$\boldsymbol{Z}\left[\widehat{\boldsymbol{X}}\right]_{ij} = \mathrm{Tr}\left\{X_i X_j \varrho_{\boldsymbol{\theta}}\right\} \quad i,j = 1,...,n, \tag{2.75}$$

while the collection of n operators $\widehat{\boldsymbol{X}}$ belongs to the set

$$\mathcal{X}_{\boldsymbol{\theta}} = \left\{ \widehat{\boldsymbol{X}} = (X_1,...,X_n) | X_i \in \mathcal{L}_h(\mathcal{H}) \ \ \& \ \ \mathrm{Tr}\left\{X_i \partial_j \varrho_{\boldsymbol{\theta}}\right\} = \delta_{ij} \right\} \tag{2.76}$$

A pedagogical derivation of the bound can be found in [117]. This bound is regarded as the most fundamental scalar bound for multi-parameter quantum estimation since it was proved to be equivalent to the most informative bound of the asymptotic model, where collective measurements on a large number of copies $\varrho_{\boldsymbol{\theta}}^{\otimes M}$ with $M \to \infty$ are performed [358]. There are few cases where it is known that the HCRb is achievable with single copies: for pure states [236], and for displacement estimation with Gaussian states [178]. Closed formulas for non-trivial cases are known only in a few scenarios: for instance, for qubits [330], and two-parameter estimation with pure states [236]. In many other cases, the analytical solution for the minimization is non-trivial, and one has to resort to numerical methods. Indeed, the minimization in Eq. (2.74) has been proven to be a semi-definite program for finite-dimensional system [7], and hence its evaluation is numerically feasible.

There are other equivalent formulations of the HCRb [117, 166, 169, 236], that we report here for completeness and will be useful in the following. The first one explicitly performs the minimization over $\boldsymbol{V} \in \mathbb{S}^n$, obtaining

$$\mathcal{C}^{\mathrm{H}}[\varrho_{\boldsymbol{\theta}}, \boldsymbol{W}] = \min_{\widehat{\boldsymbol{X}}\in\mathcal{X}_{\boldsymbol{\theta}}} \{ \mathrm{tr}\left\{ \boldsymbol{W}\Re\{\boldsymbol{Z}[\widehat{\boldsymbol{X}}]\}\right\} + \|\sqrt{\boldsymbol{W}}\Im\{\boldsymbol{Z}[\widehat{\boldsymbol{X}}]\}\sqrt{\boldsymbol{W}}\|_1\}. \tag{2.77}$$

The second expression is

$$\mathcal{C}^{\mathrm{H}}[\varrho_{\boldsymbol{\theta}}, \boldsymbol{W}] = \min_{Y_i} \left\{ \mathrm{tr}\left\{\boldsymbol{W}\boldsymbol{Z}[\widehat{\boldsymbol{Y}}]\right\} \middle| \Im\{\boldsymbol{Z}[\widehat{\boldsymbol{Y}}]\} = 0 \right\}, \tag{2.78}$$

with $Y_i \in \mathcal{L}_h(\mathcal{H}\oplus\mathbb{C}^n)$. This has proven to be particularly useful in the proof of saturability for parametric families of pure states. All the bounds discuss so far satisfy the following hierarchy

$$\mathcal{C}[\varrho_{\boldsymbol{\theta}}, \boldsymbol{W}] \geq \mathcal{C}^{\mathrm{MI}}[\varrho_{\boldsymbol{\theta}}, \boldsymbol{W}] \geq \mathcal{C}^{\mathrm{H}}[\varrho_{\boldsymbol{\theta}}, \boldsymbol{W}] \geq \mathcal{C}^{\mathrm{SLD}}[\varrho_{\boldsymbol{\theta}}, \boldsymbol{W}] \tag{2.79}$$

In the next section, we discuss the different conditions that have been put forward for the saturability of these inequalities, with particular concern for the inequality between the HCRb and the SLD-CRb.

2.2.4.1 Compatibility conditions

To study the saturability condition of the HCRb with respect to the SLD-CRb, it is useful to introduce a scalar product in the Hilbert space $\mathcal{H}$

$$\langle \widehat{\boldsymbol{X}}, \widehat{\boldsymbol{Y}} \rangle_{\varrho_{\boldsymbol{\theta}}} = \frac{1}{2}\mathrm{Tr}\left\{\varrho_{\boldsymbol{\theta}}\{\widehat{\boldsymbol{X}}, \widehat{\boldsymbol{Y}}\}\right\} \tag{2.80}$$

where $\widehat{\boldsymbol{X}} = \{\widehat{X}_1, ..., \widehat{X}_d\}^T$ is a vector of operator, and $\{\widehat{\boldsymbol{X}}, \widehat{\boldsymbol{Y}}\} = (\widehat{\boldsymbol{X}}\widehat{\boldsymbol{Y}}^T + \widehat{\boldsymbol{X}}\widehat{\boldsymbol{Y}}^T)/2$.

We introduce now a vector of n operators $\widehat{\boldsymbol{X}}$ (we recall that n is the number of parameters) and such that

$$\widehat{\boldsymbol{X}} = \sum_{\kappa} \left(\tilde{\boldsymbol{\theta}}(\kappa) - \boldsymbol{\theta}\right) \Pi_{\kappa}, \tag{2.81}$$

where $\{\Pi_\kappa\}_{\kappa=1}^{\tilde{d}}$, and $\tilde{\boldsymbol{\theta}}$ are respectively an arbitrary POVM and a vector of locally unbiased estimators as defined in Def. 3. The conditions for unbiasedness, i.e. Eq.s (2.27)–(2.28) can be rewritten in terms of $\widehat{\boldsymbol{X}}$ as

$$\mathrm{Tr}\left\{\varrho_{\boldsymbol{\theta}}\widehat{\boldsymbol{X}}\right\} = 0 \tag{2.82}$$

$$\mathrm{Tr}\left\{\partial_{\boldsymbol{\theta}}\varrho_{\boldsymbol{\theta}}\widehat{\boldsymbol{X}}^T\right\} = \mathbb{I}_n \tag{2.83}$$

The second equation in particular can be expressed in terms of the scalar product defined in Eq. (2.80), and the vector of SLD operators $\widehat{\boldsymbol{L}} = \{\widehat{L}_{\theta_1}, ...\widehat{L}_{\theta_n}\}$[2] for the parameter $\boldsymbol{\theta}$ as

$$\langle \widehat{\boldsymbol{L}}, \widehat{\boldsymbol{X}} \rangle_{\varrho_{\boldsymbol{\theta}}} = \frac{1}{2}\mathrm{Tr}\left\{\varrho_{\boldsymbol{\theta}}\{\widehat{\boldsymbol{L}}, \widehat{\boldsymbol{X}}\}\right\} = \frac{1}{2}\mathrm{Tr}\left\{\{\varrho_{\boldsymbol{\theta}}, \widehat{\boldsymbol{L}}\}\widehat{\boldsymbol{X}}^T\right\} = \tag{2.84}$$

$$= \mathrm{Tr}\left\{\partial_{\boldsymbol{\theta}}\varrho_{\boldsymbol{\theta}}\widehat{\boldsymbol{X}}^T\right\} = \mathbb{I}_n. \tag{2.85}$$

Actually, the vector of operators $\widehat{\boldsymbol{X}}$ can be decomposed in the parallel $X_i^{\parallel}$ and orthogonal component $X_i^{\perp}$ for the space spanned by the SLDs. This can be always done if we restrict the scalar product to the subspace $\mathcal{L}(\mathcal{H})/\mathcal{L}(\ker(\varrho_{\boldsymbol{\theta}}))$, see [117] for more details. By definition, the parallel component is written in terms of the SLDs operators as $\widehat{\boldsymbol{X}}^{\parallel} = \boldsymbol{B}\widehat{\boldsymbol{L}}$, where $\boldsymbol{B}$ correspond to a certain $n \times n$ real matrix. Using the last equation we see that

$$\mathbb{I}_n = \langle \widehat{\boldsymbol{L}}, \widehat{\boldsymbol{X}}^T \rangle_{\varrho_{\boldsymbol{\theta}}} = \langle \widehat{\boldsymbol{L}}, (\widehat{\boldsymbol{X}}^{\parallel})^T \rangle_{\varrho_{\boldsymbol{\theta}}} = \boldsymbol{B}\langle \widehat{\boldsymbol{L}}, \widehat{\boldsymbol{L}}^T \rangle_{\varrho_{\boldsymbol{\theta}}} = \boldsymbol{B}\boldsymbol{\mathcal{Q}}(\boldsymbol{\theta}). \tag{2.86}$$

Hence, $\boldsymbol{B}$ is nothing but the inverse of the QFIM $\boldsymbol{\mathcal{Q}}^{-1}(\boldsymbol{\theta})$, while there is no restriction on the perpendicular part $\widehat{\boldsymbol{X}}^{\perp}$. We can also evaluate the real part of $\boldsymbol{Z}[\widehat{\boldsymbol{X}}]$, that enters the definition of the HCRb, as

$$\Re\boldsymbol{Z}[\widehat{\boldsymbol{X}}] = \langle \widehat{\boldsymbol{X}}, \widehat{\boldsymbol{X}}^T \rangle_{\varrho_{\boldsymbol{\theta}}} = \Re\boldsymbol{Z}[\widehat{\boldsymbol{X}}^{\parallel}] + \Re\boldsymbol{Z}[\widehat{\boldsymbol{X}}^{\perp}], \tag{2.87}$$

since $\langle \widehat{\boldsymbol{X}}^{\parallel}, (\widehat{\boldsymbol{X}}^{\perp})^T \rangle_{\varrho_{\boldsymbol{\theta}}} = 0$ by definition of scalar product. In particular

$$\Re\boldsymbol{Z}[\widehat{\boldsymbol{X}}^{\parallel}] = \Re\mathrm{Tr}\left\{\varrho_{\boldsymbol{\theta}}\boldsymbol{\mathcal{Q}}^{-1}(\boldsymbol{\theta})\widehat{\boldsymbol{L}}\widehat{\boldsymbol{L}}^T\boldsymbol{\mathcal{Q}}^{-1}(\boldsymbol{\theta})\right\} = \tag{2.88}$$

$$= \boldsymbol{\mathcal{Q}}^{-1}(\boldsymbol{\theta})\Re\mathrm{Tr}\left\{\varrho_{\boldsymbol{\theta}}\widehat{\boldsymbol{L}}\widehat{\boldsymbol{L}}^T\right\}\boldsymbol{\mathcal{Q}}^{-1}(\boldsymbol{\theta}) = \boldsymbol{\mathcal{Q}}^{-1}(\boldsymbol{\theta}). \tag{2.89}$$

[2]Henceforth, we drop the subscript $\boldsymbol{\theta}$ for the SLDs

Then, we have that the first term in Eq. (2.77) can be expanded as

$$\mathrm{tr}\left\{\boldsymbol{W}\Re\{\boldsymbol{Z}[\widehat{\boldsymbol{X}}]\}\right\} = \mathrm{tr}\left\{\boldsymbol{W}\Re\{\boldsymbol{Z}[\widehat{\boldsymbol{X}}^{\parallel}]\}\right\} + \mathrm{tr}\left\{\boldsymbol{W}\Re\{\boldsymbol{Z}[\widehat{\boldsymbol{X}}^{\perp}]\}\right\} = \tag{2.90}$$

$$= \mathrm{tr}\left\{\boldsymbol{W}\boldsymbol{\mathcal{Q}}^{-1}(\boldsymbol{\theta})\right\} + \mathrm{tr}\left\{\boldsymbol{W}\Re\{\boldsymbol{Z}[\widehat{\boldsymbol{X}}^{\perp}]\}\right\} = \tag{2.91}$$

$$= \mathcal{C}^{\mathrm{SLD}}[\varrho_{\boldsymbol{\theta}}, \boldsymbol{W}] + \mathrm{tr}\left\{\boldsymbol{W}\Re\{\boldsymbol{Z}[\widehat{\boldsymbol{X}}^{\perp}]\}\right\}. \tag{2.92}$$

In this way, we obtain that the HCRb can be written as

$$\mathcal{C}^{\mathrm{H}}[\varrho_{\boldsymbol{\theta}}, \boldsymbol{W}] = \mathcal{C}^{\mathrm{SLD}}[\varrho_{\boldsymbol{\theta}}, \boldsymbol{W}] + \tag{2.93}$$

$$+ \min_{\widehat{\boldsymbol{X}}^{\perp}}\left\{\mathrm{tr}\left\{\boldsymbol{W}\Re\{\boldsymbol{Z}[\widehat{\boldsymbol{X}}^{\perp}]\}\right\} + \|\sqrt{\boldsymbol{W}}\Im\{\boldsymbol{Z}[\widehat{\boldsymbol{X}}^{\parallel} + \widehat{\boldsymbol{X}}^{\perp}]\}\sqrt{\boldsymbol{W}}\|_1\right\} \tag{2.94}$$

where we have to remember that the parallel component is fixed to be $\widehat{\boldsymbol{X}}^{\parallel} = \boldsymbol{\mathcal{Q}}^{-1}(\boldsymbol{\theta})\widehat{\boldsymbol{L}}$. Moreover, the imaginary component can be expanded as

$$\Im\{\boldsymbol{Z}[\widehat{\boldsymbol{X}}^{\parallel} + \widehat{\boldsymbol{X}}^{\perp}]\} = \Im\{\boldsymbol{Z}[\widehat{\boldsymbol{X}}^{\parallel}]\} + \Im\{\boldsymbol{Z}[\widehat{\boldsymbol{X}}^{\perp}]\} \tag{2.95}$$

since

$$\Im\{\boldsymbol{Z}[\widehat{\boldsymbol{X}}]\} = \frac{1}{2i}\mathrm{Tr}\left\{\varrho_{\boldsymbol{\theta}}[\widehat{\boldsymbol{X}}, \widehat{\boldsymbol{X}}^T]\right\} \tag{2.96}$$

and where we used $[\widehat{\boldsymbol{X}}, \widehat{\boldsymbol{Y}}^T] = \widehat{\boldsymbol{X}}\widehat{\boldsymbol{Y}}^T - \widehat{\boldsymbol{Y}}\widehat{\boldsymbol{X}}^T$. Then, the first term in Eq. (2.95) can be written as

$$\Im\{\boldsymbol{Z}[\widehat{\boldsymbol{X}}^{\parallel}]\} = \frac{1}{2i}\mathrm{Tr}\left\{\varrho_{\boldsymbol{\theta}}[\widehat{\boldsymbol{X}}^{\parallel}, (\widehat{\boldsymbol{X}}^{\parallel})^T]\right\} = \tag{2.97}$$

$$= \frac{1}{2i}\mathrm{Tr}\left\{\varrho_{\boldsymbol{\theta}}[\boldsymbol{\mathcal{Q}}^{-1}(\boldsymbol{\theta})\widehat{\boldsymbol{L}}, \widehat{\boldsymbol{L}}^T\boldsymbol{\mathcal{Q}}^{-1}(\boldsymbol{\theta})]\right\} = \tag{2.98}$$

$$= \boldsymbol{\mathcal{Q}}^{-1}(\boldsymbol{\theta})\frac{1}{2i}\mathrm{Tr}\left\{\varrho_{\boldsymbol{\theta}}[\widehat{\boldsymbol{L}}, \widehat{\boldsymbol{L}}^T]\right\}\boldsymbol{\mathcal{Q}}^{-1}(\boldsymbol{\theta}) = \tag{2.99}$$

$$= \boldsymbol{\mathcal{Q}}^{-1}(\boldsymbol{\theta})\boldsymbol{\mathcal{U}}(\boldsymbol{\theta})\boldsymbol{\mathcal{Q}}^{-1}(\boldsymbol{\theta}), \tag{2.100}$$

where we have defined the *asymptotic incompatibility matrix*

$$\boldsymbol{\mathcal{U}}(\boldsymbol{\theta}) = \frac{1}{2i}\mathrm{Tr}\left\{\varrho_{\boldsymbol{\theta}}[\widehat{\boldsymbol{L}}, \widehat{\boldsymbol{L}}^T]\right\}, \tag{2.101}$$

which is by definition traceless and hermitian. In the literature, this is known also as Uhlman curvature [78]. We notice that if

$$\sqrt{\boldsymbol{W}}\boldsymbol{\mathcal{Q}}^{-1}(\boldsymbol{\theta})\boldsymbol{\mathcal{U}}(\boldsymbol{\theta})\boldsymbol{\mathcal{Q}}^{-1}(\boldsymbol{\theta})\sqrt{\boldsymbol{W}} = 0, \tag{2.102}$$

then the minimization in Eq. (2.94) is obtained for $\widehat{\boldsymbol{X}}^{\perp} = 0$ and the HCRb and the SLD-CRb coincide. Things simplify if the weight matrix $\boldsymbol{W}$ is full rank, i.e. we are not estimating functions of parameters. Then, condition in Eq. (2.102) can be simplified as

$$\Im\{\boldsymbol{Z}[\widehat{\boldsymbol{X}}^{\parallel}]\} = \boldsymbol{\mathcal{Q}}^{-1}(\boldsymbol{\theta})\boldsymbol{\mathcal{U}}(\boldsymbol{\theta})\boldsymbol{\mathcal{Q}}^{-1}(\boldsymbol{\theta}) = 0 \tag{2.103}$$

Further, if the model is not singular, i.e. $\boldsymbol{\mathcal{Q}}(\boldsymbol{\theta})$ is invertible, this is completely equivalent to

$$\boldsymbol{\mathcal{U}}(\boldsymbol{\theta}) = 0 \tag{2.104}$$

which is also known as *weak compatibility condition* [5]. We see that this is satisfied if all the SLDs commute *on average*. Viceversa, if we ask for $\mathcal{C}^{\mathrm{H}}[\varrho_{\boldsymbol{\theta}}, \boldsymbol{W}] = \mathcal{C}^{\mathrm{SLD}}[\varrho_{\boldsymbol{\theta}}, \boldsymbol{W}]$, then we obtain again that this condition is sufficient [285]. Thus, we conclude that the condition in Eq. (2.104) is necessary and sufficient for the HCRb and scalar-SLD bound to coincide.

We also want to remark on an important thing here. Assuming the weak compatibility condition, we notice that the operator that realizes the minimum in Eq. (2.77) coincides with the parallel component $\widehat{\boldsymbol{X}} = \widehat{\boldsymbol{X}}^{\parallel} = \boldsymbol{\mathcal{Q}}^{-1}(\boldsymbol{\theta})\widehat{\boldsymbol{L}}$. Hence, one could imagine that this also realizes the optimal single-copy measurement. If we write the SLDs as $\widehat{L}_k = \sum_l \lambda_l^{(k)} |\lambda_l^{(k)}\rangle\langle\lambda_l^{(k)}|$, with $\langle\lambda_l^{(k)}|\lambda_{l'}^{(k)}\rangle = \delta_{ll'}$, then we can write

$$\widehat{\boldsymbol{X}}_i = \sum_{k=1}^{n} \boldsymbol{\mathcal{Q}}^{-1}(\boldsymbol{\theta})_{ik} \widehat{L}_k = \sum_{\kappa} f_i(\kappa)\Pi_\kappa = \sum_{\kappa} \left(\tilde{\theta}_i(\kappa) - \theta_i\right)\Pi_\kappa, \tag{2.105}$$

where we have identified κ as the multi-index (k, l), the function

$$f_i(\kappa) = f_i(k, l) = n\boldsymbol{\mathcal{Q}}^{-1}(\boldsymbol{\theta})_{ik}\lambda_l^{(k)}, \tag{2.106}$$

and the POVM as

$$\Pi_\kappa = \Pi_{k,l} = \frac{1}{n}|\lambda_l^{(k)}\rangle\langle\lambda_l^{(k)}|. \tag{2.107}$$

Each Π_κ is a projector, but they are not all linear independent. Nonetheless we have

$$\sum_{\kappa}\Pi_\kappa = \sum_{k=1}^{n}\sum_{l=1}^{\tilde{d}} \frac{1}{n}|\lambda_l^{(k)}\rangle\langle\lambda_l^{(k)}| = \sum_{k=1}^{n}\frac{1}{n}\mathbb{I}_{\tilde{d}} = \mathbb{I}_{\tilde{d}}. \tag{2.108}$$

However, this is *not* the case, i.e. the optimal measurement that achieves the scalar-SLD bound in the scenario where (2.104) holds is not given by this one. The issue relies on the fact that the covariance matrix given by the set of estimator $\widehat{\boldsymbol{X}}$ does not attain the matrix nor the scalar-SLD bound as we can see

$$\boldsymbol{V}(\tilde{\boldsymbol{\theta}}) = \sum_{\kappa}\mathrm{Tr}\left\{\varrho_{\boldsymbol{\theta}}\Pi_\kappa\right\}(\tilde{\boldsymbol{\theta}}(\kappa) - \boldsymbol{\theta})(\tilde{\boldsymbol{\theta}}(\kappa) - \boldsymbol{\theta})^T \succeq \tag{2.109}$$

$$\succeq \mathrm{Tr}\left\{\varrho_{\boldsymbol{\theta}}\widehat{\boldsymbol{X}}\widehat{\boldsymbol{X}}^T\right\}^{3} = \frac{1}{2}\mathrm{Tr}\left\{\varrho_{\boldsymbol{\theta}}\left\{\widehat{\boldsymbol{X}}, \widehat{\boldsymbol{X}}^T\right\}\right\} = \boldsymbol{\mathcal{Q}}^{-1}(\boldsymbol{\theta}) \tag{2.110}$$

The equality is only reached if the POVM elements form a set of projective operators $\Pi_\kappa\Pi_{\kappa'} = \delta_{\kappa\kappa'}$. This in general happens if and only if all the SLDs commute in the operator sense, i.e. not on average, or in the pure case scenario. A very recent development on the attainability of scalar-SLD bound in the single-copy scenario was addressed in [101]. We summarize the results in the following

Result 2: Asymptotically classical model and weak commutativity

A quantum statistical model $\varrho_{\boldsymbol{\theta}}$ is *asymptotically classical* if all the SLD operators commute on average, i.e. if they satisfy the *weak commutativity* condition

$$\boldsymbol{\mathcal{U}}(\boldsymbol{\theta}) = \frac{1}{2i}\mathrm{Tr}\left\{\varrho_{\boldsymbol{\theta}}[\widehat{\boldsymbol{L}}, \widehat{\boldsymbol{L}}^T]\right\} = 0. \tag{2.111}$$

This is a necessary and sufficient condition for the HCRb and the scalar SLD-CRb to coincide

$$\mathcal{C}^{\mathrm{H}}[\varrho_{\boldsymbol{\theta}}, \boldsymbol{W}] = \mathcal{C}^{\mathrm{SLD}}[\varrho_{\boldsymbol{\theta}}, \boldsymbol{W}]. \tag{2.112}$$

The optimal measurement is in general a collective measurement.

So far, we have analyzed the relationship between the SLD-CRb and the HCRb, and the conditions under which the two coincide. In the following section, we study the opposite case in which the SLD-CRb and the HCRb *are not* equal, and we try to quantify their difference.

2.2.4.2 Asymptotic incompatibility measure

This section aims to study the difference between the HCRb and SLD-CRb and try to quantify their difference in a simple way. By looking at Eq. (2.77), we notice that if we evaluate the argument of the minimum with the set of operators given by $\widehat{\boldsymbol{X}} = \boldsymbol{\mathcal{Q}}^{-1}(\boldsymbol{\theta})\widehat{\boldsymbol{L}}$, this is always larger than the HCRb. Thus, using Eqs. (2.89)–(2.100) and the decomposition $\boldsymbol{Z}[\widehat{\boldsymbol{X}}] = \Re\boldsymbol{Z}[\widehat{\boldsymbol{X}}] + i\Im\boldsymbol{Z}[\widehat{\boldsymbol{X}}]$, we obtain

$$\begin{aligned}\mathcal{C}^{\mathrm{H}}[\varrho_{\boldsymbol{\theta}}, \boldsymbol{W}] &\leq \mathrm{tr}\left\{\boldsymbol{W}\boldsymbol{\mathcal{Q}}^{-1}(\boldsymbol{\theta})\right\} + \|\sqrt{\boldsymbol{W}}\boldsymbol{\mathcal{Q}}^{-1}(\boldsymbol{\theta})\boldsymbol{\mathcal{U}}(\boldsymbol{\theta})\boldsymbol{\mathcal{Q}}^{-1}(\boldsymbol{\theta})\sqrt{\boldsymbol{W}}\|_1 = \\ &= \mathcal{C}^{\mathrm{SLD}}[\varrho_{\boldsymbol{\theta}}, \boldsymbol{W}] + \|\sqrt{\boldsymbol{W}}\boldsymbol{\mathcal{Q}}^{-1}(\boldsymbol{\theta})\boldsymbol{\mathcal{U}}(\boldsymbol{\theta})\boldsymbol{\mathcal{Q}}^{-1}(\boldsymbol{\theta})\sqrt{\boldsymbol{W}}\|_1\end{aligned} \tag{2.113}$$

Then, we have the following chain of inequalities

$$\begin{aligned}\mathcal{C}^{\mathrm{H}}[\varrho_{\boldsymbol{\theta}}, \boldsymbol{W}] - \mathcal{C}^{\mathrm{SLD}}[\varrho_{\boldsymbol{\theta}}, \boldsymbol{W}] &\leq \|\sqrt{\boldsymbol{W}}\boldsymbol{\mathcal{Q}}^{-1}(\boldsymbol{\theta})\boldsymbol{\mathcal{U}}(\boldsymbol{\theta})\boldsymbol{\mathcal{Q}}^{-1}(\boldsymbol{\theta})\sqrt{\boldsymbol{W}}\|_1 \leq \\ &\leq \|\boldsymbol{\mathcal{Q}}^{-1/2}(\boldsymbol{\theta})\boldsymbol{W}\boldsymbol{\mathcal{Q}}^{-1}(\boldsymbol{\theta})\boldsymbol{\mathcal{U}}(\boldsymbol{\theta})\boldsymbol{\mathcal{Q}}^{-1/2}(\boldsymbol{\theta})\|_1 \leq \\ &\leq \|\boldsymbol{\mathcal{Q}}^{-1/2}(\boldsymbol{\theta})\boldsymbol{W}\boldsymbol{\mathcal{Q}}^{-1/2}(\boldsymbol{\theta})\|_1\|\boldsymbol{\mathcal{Q}}^{-1/2}(\boldsymbol{\theta})\boldsymbol{\mathcal{U}}(\boldsymbol{\theta})\boldsymbol{\mathcal{Q}}^{-1/2}(\boldsymbol{\theta})\|_\infty,\end{aligned} \tag{2.114}$$

where, in order, we have used

1. $\|AB\|_1 \leq \|BA\|_1$ for AB normal, with $A = \boldsymbol{W}\boldsymbol{\mathcal{Q}}^{-1}(\boldsymbol{\theta})\boldsymbol{\mathcal{U}}(\boldsymbol{\theta})\boldsymbol{\mathcal{Q}}^{-1/2}(\boldsymbol{\theta})$ and $B = \boldsymbol{\mathcal{Q}}^{-1}(\boldsymbol{\theta})\sqrt{\boldsymbol{W}}$ (since the product of the two is a skew-symmetric matrix, it is also normal) [45]
2. $\|AB\|_1 \leq \|A\|_p\|B\|_q$ with $1/p + 1/q = 1$ (Hölder's inequality) for the specific case of $p = 1$, $q = \infty$ and $A = \boldsymbol{\mathcal{Q}}^{-1/2}(\boldsymbol{\theta})\boldsymbol{W}\boldsymbol{\mathcal{Q}}^{-1/2}(\boldsymbol{\theta})$ and $B = \boldsymbol{\mathcal{Q}}^{-1/2}(\boldsymbol{\theta})\boldsymbol{\mathcal{U}}(\boldsymbol{\theta})\boldsymbol{\mathcal{Q}}^{-1/2}(\boldsymbol{\theta})$. In this case, $\|B\|_\infty$ is the operator norm, that for matrices is the largest eigenvalue of the symmetric matrix $B^\dagger B$.

Furthermore, since the matrix $\boldsymbol{\mathcal{Q}}^{-1/2}(\boldsymbol{\theta})\boldsymbol{W}\boldsymbol{\mathcal{Q}}^{-1/2}(\boldsymbol{\theta})$ is positive semi-definite, it can be written as $(\boldsymbol{W}^{-1/2}\boldsymbol{\mathcal{Q}}^{-1/2}(\boldsymbol{\theta}))^\dagger(\boldsymbol{W}^{-1/2}\boldsymbol{\mathcal{Q}}^{-1/2}(\boldsymbol{\theta}))$. It follows that the first element in the

product in Eq. (2.114) is

$$\|\mathcal{Q}^{-1/2}(\boldsymbol{\theta})\boldsymbol{W}\mathcal{Q}^{-1/2}(\boldsymbol{\theta})\|_1 = \mathrm{tr}\left\{\mathcal{Q}^{-1/2}(\boldsymbol{\theta})\boldsymbol{W}\mathcal{Q}^{-1/2}(\boldsymbol{\theta})\right\} = \tag{2.115}$$

$$= \mathrm{tr}\left\{\boldsymbol{W}\mathcal{Q}^{-1}(\boldsymbol{\theta})\right\} = \mathcal{C}^{\mathrm{SLD}}[\varrho_{\boldsymbol{\theta}}, \boldsymbol{W}] \tag{2.116}$$

Regarding the second element in Eq. (2.114), we notice that $\mathcal{Q}^{-1}(\boldsymbol{\theta})\mathcal{U}(\boldsymbol{\theta})$ and $\mathcal{Q}^{-1/2}(\boldsymbol{\theta})\mathcal{U}(\boldsymbol{\theta})\mathcal{Q}^{-1/2}(\boldsymbol{\theta})$ have the same eigenvalues. Indeed, suppose that $\boldsymbol{U}$ is the matrix that diagonalize the latter, that is $\mathcal{Q}^{-1/2}(\boldsymbol{\theta})\mathcal{U}(\boldsymbol{\theta})\mathcal{Q}^{-1/2}(\boldsymbol{\theta}) = \boldsymbol{U}^\dagger\boldsymbol{H}\boldsymbol{U}$, with $\boldsymbol{H}$ diagonal matrix. Then, we have

$$\mathcal{Q}^{-1}(\boldsymbol{\theta})\mathcal{U}(\boldsymbol{\theta}) = \mathcal{Q}^{-1/2}(\boldsymbol{\theta})\boldsymbol{U}^\dagger\boldsymbol{H}\boldsymbol{U}\mathcal{Q}^{1/2}(\boldsymbol{\theta}) = \boldsymbol{S}^{-1}\mathcal{U}(\boldsymbol{\theta})\boldsymbol{S} \tag{2.117}$$

with $\boldsymbol{S} = \boldsymbol{U}\mathcal{Q}^{1/2}(\boldsymbol{\theta})$. Hence the two matrices have the same eigenvalues. To conclude, Eq. (2.114) becomes

$$\frac{\mathcal{C}^{\mathrm{H}}[\varrho_{\boldsymbol{\theta}}, \boldsymbol{W}] - \mathcal{C}^{\mathrm{SLD}}[\varrho_{\boldsymbol{\theta}}, \boldsymbol{W}]}{\mathcal{C}^{\mathrm{SLD}}[\varrho_{\boldsymbol{\theta}}, \boldsymbol{W}]} \leq \|\mathcal{Q}^{-1}(\boldsymbol{\theta})\mathcal{U}(\boldsymbol{\theta})\|_\infty = \mathcal{R}_{\boldsymbol{\theta}} \tag{2.118}$$

where we have defined the *asymptotic incompatibility measure* or *quantumness* $\mathcal{R}_{\boldsymbol{\theta}}$. This represents an upper bound on the relative difference between the HCRb and the SLD-CRb [77].

Furthermore, we can prove that the value of $\mathcal{R}_{\boldsymbol{\theta}}$ is upper bounded. Indeed, since $\boldsymbol{Z}[\widehat{\boldsymbol{X}}] \succeq 0$, and that

$$\boldsymbol{Z}[\mathcal{Q}^{-1}(\boldsymbol{\theta})\widehat{\boldsymbol{L}}] = \mathcal{Q}^{-1}(\boldsymbol{\theta})\widehat{\boldsymbol{L}} + i\mathcal{Q}^{-1}(\boldsymbol{\theta})\mathcal{U}(\boldsymbol{\theta})\mathcal{Q}^{-1}(\boldsymbol{\theta}) \tag{2.119}$$

it follows that

$$\mathcal{Q}^{1/2}(\boldsymbol{\theta})\boldsymbol{Z}[\widehat{\boldsymbol{X}}]\mathcal{Q}^{1/2}(\boldsymbol{\theta}) = \mathbb{I}_n + i\mathcal{Q}^{-1/2}(\boldsymbol{\theta})\mathcal{U}(\boldsymbol{\theta})\mathcal{Q}^{-1/2}(\boldsymbol{\theta}) \succeq 0 \tag{2.120}$$

The main consequence is that the eigenvalues of $i\mathcal{Q}^{-1/2}(\boldsymbol{\theta})\mathcal{U}(\boldsymbol{\theta})\mathcal{Q}^{-1/2}(\boldsymbol{\theta})$ lie in the interval $[-1, +1]$, and since these are the same of $\mathcal{Q}^{-1}(\boldsymbol{\theta})\mathcal{U}(\boldsymbol{\theta})$, we obtain that

$$\mathcal{R}_{\boldsymbol{\theta}} = \|\mathcal{Q}^{-1}(\boldsymbol{\theta})\mathcal{U}(\boldsymbol{\theta})\|_\infty = \|i\mathcal{Q}^{-1}(\boldsymbol{\theta})\mathcal{U}(\boldsymbol{\theta})\|_\infty \leq 1, \tag{2.121}$$

where we have used the fact that the imaginary unit does not change the ∞-norm. This means that we have the following chain of inequality

$$\mathcal{C}^{\mathrm{SLD}}[\varrho_{\boldsymbol{\theta}}, \boldsymbol{W}] \leq \mathcal{C}^{\mathrm{H}}[\varrho_{\boldsymbol{\theta}}, \boldsymbol{W}] \leq (1 + \mathcal{R}_{\boldsymbol{\theta}})\mathcal{C}^{\mathrm{SLD}}[\varrho_{\boldsymbol{\theta}}, \boldsymbol{W}] \leq 2\mathcal{C}^{\mathrm{SLD}}[\varrho_{\boldsymbol{\theta}}, \boldsymbol{W}] \tag{2.122}$$

It results that the HCRb is at most twice the SLD-CRb, i.e. the measurement incompatibility add just a factor of two on the overall precision. It also means that any improvement in the scaling present in the HCRb can be already read from the scalar SLC-CRb. The results can be summarized as follows

Result 3: Asymptotic incompatibility measure $\mathcal{R}_\theta = 1$

The relative difference between the HCRb and the scalar SLD-CRb is given as

$$0 \leq \frac{\mathcal{C}^{\mathrm{H}}[\varrho_{\boldsymbol{\theta}}, \boldsymbol{W}] - \mathcal{C}^{\mathrm{SLD}}[\varrho_{\boldsymbol{\theta}}, \boldsymbol{W}]}{\mathcal{C}^{\mathrm{SLD}}[\varrho_{\boldsymbol{\theta}}, \boldsymbol{W}]} \leq \mathcal{R}_{\boldsymbol{\theta}} \leq 1 \tag{2.123}$$

Statistical models with $\mathcal{R}_{\boldsymbol{\theta}} = 1$ are maximally incompatible, whereas models $\mathcal{R}_{\boldsymbol{\theta}} = 0$ are asymptotically classical, as defined in Result 2.

This quantity $\mathcal{R}_{\boldsymbol{\theta}} = 1$ just depends on the two matrices $\boldsymbol{\mathcal{Q}}(\boldsymbol{\theta})$ and $\boldsymbol{\mathcal{U}}(\boldsymbol{\theta})$, and it is a way to quantify the incompatibility of the optimal measurements in attaining the scalar SLD-QCRb. To conclude, we also mention that a notion of probe incompatibility has been studied in [6], which quantifies the incompatibility between the optimal probes of the single parameters.

CHAPTER 3

Quantum walks

The classical notion of a walker on a discrete space, usually described by a graph, can be generalized to the quantum realm [200, 340, 279]. The process can be discrete in time and governed by an ancillary system named quantum coin, yielding to discrete-time quantum walks (DTQWs) and firstly introduced in [4, 3]. On the other side, we can consider continuous time processes, in which the walker, usually a particle, evolves according to a first-order differential equation, the Schrödinger equation. These systems are known as continuous-time quantum walks (CTQWs) and were first developed in [131, 92]. In this thesis, we are going to focus only on the second case, and in particular how to exploit such systems both in sensing and search protocol.

The study of CTQWs stands at the interface of several disciplines, such as quantum physics [279], computer science [15], biology [244], and even at the foundational level [161], and for these reasons, its applications are inherently interdisciplinary. Interest in these systems is mainly driven by the potential that quantum theory offers in the enhance of several protocols, such as transport, search and communications. Indeed, quantum walks have found several applications in these fields. Relevant examples belongs to quantum computation [175, 90, 352], quantum transport [199, 249, 334], and environment-assisted transport in photosynthetic complexes [278, 291]. Further, a relevant field that has been strongly influenced by CTQWs is the field of quantum algorithms. Here, quantum speedup has been proven [91], and they have been also exploited to find efficiently ground state solutions to spin glass systems [68] or high-quality solutions to certain classes of NP-hard combinatorial problems [229].

Since a CTQW evolves over a graph, it is strongly related to applications over networks, including quantum spatial search. Indeed, CTQWs were specifically used to generalize quantum algorithms for the search problem [94, 322, 82]. Several results have been proved for the spatial search algorithm [93, 275, 298, 115], finding optimal conditions for spatial search [84], and also for fast quantum search [189]. Great efforts have focused on the use of oracles to find a target node [83, 265, 351], and on its implementations [201, 36]. The topic of the spatial search will be addressed in detail in Chapter 8, where we will introduce a novel method for quantum search that relies on another emergent field, quantum control with continuous measurement.

The use of CTQWs in quantum metrology and quantum sensing was also only recently addressed [317, 289, 362]. In Chapter 4, we follow this path, and we analyze quantum thermometry within a CTQW perspective. In particular, we try to characterize systems' sensitivity in terms of the topological features of the underlying graph.

Different platforms have been proposed to implement CTQWs, or QWs more in general, going from ultra-cold Rydberg atoms in optical lattices [104, 269, 281, 239], to optical waveguides [269, 270]. The combination of such platforms with optical tweezers

has proved to achieve rapid reconfigurability of the network parameters [359]. Moreover, the continuous monitoring of observables in such systems has been considered in [210]. These two last examples put the basis for possible implementations of control and feedback operations for CTQWs, which may be related to our theoretical proposal in Chapter 8. For a comprehensive review, we suggest the reader to [341]. Recently, efforts have been focused also on photonic chips [335], in superconducting systems [357, 158] and again in optical waveguides to perform search algorithms [36].

In this chapter, we quickly review CTQWs. First, in Sec. 3.1 we introduce classical Markov chains, on which the classical and quantum continuous-time walks are based. We show how the Laplacian matrix emerges and how stochastic evolution is related to the underlying graph structure. In Sec. 3.2 we generalize the classical scenario to the quantum one.

3.1 Classical Markov chains

Classical random walks are built upon continuous time classical Markov chains. These describe the motion over a discrete set of positions of a particle, or more in general, a *walker*. The underlying structure is naturally described by a pair $G = (V, E)$, where V is the set of vertices, while E is the set of edges, i.e. the set of unordered pair of elements of V which identify the connections between the nodes. We say that two vertices are *adjacent* if their corresponding pair is in the set E. We also denote the order of the graph as the number of nodes $N = |V|$, and we also restrict our future discussions to graphs without loops or multiple edges. All these information determines the topology of the graph and is fully encoded in the adjacency matrix A

$$A_{jk} = \begin{cases} 1 & \text{if } (j,k) \in E \\ 0 & \text{otherwise} \end{cases} \tag{3.1}$$

Associated with A there is a Laplacian matrix, defined as

$$L = D - A, \tag{3.2}$$

where D is a diagonal matrix, with $D_{kk} = d_k = \sum_{j=0}^{N-1} A_{kj}$ the degree of the kth vertex.

A step in a classical random walk can be described by a matrix M that transforms the probability distribution over V. The entry M_{ij} is related to the probability to go from the ith vertex to the jth vertex and is constrained by the structure of G, and more specifically on the set of edges E. If the state of the walker is described by a probability distribution $\boldsymbol{p}^t$ at a certain time step t, then the probability distribution at the following time step $t+1$ is given by

$$\boldsymbol{p}^{t+1} = M\boldsymbol{p}^t. \tag{3.3}$$

This formalism allows us to transform probabilities at integer times. To derive a continuous in-time evolution, we have to assume that the transitions occur at all times with a constant-in-time jumping rate γ. In other words, γ represents the probability of transition per unit of time. If the jth vertex has degree d_j (the number of vertices with which is connected), then after a time τ, there is a probability of $d_j\gamma\tau$ that the walker jump from j to one of the connected vertices. Here we tacitly assume that the jumps are all equiprobable, i.e. the edges are not weighted. Instead, the probability of staying in j is $1 - d_j\gamma\tau$. We see that the more the vertex is connected, the more probably the walker

will jump away from it. Since M describes exactly these transitions rates, we have that for an infinitesimal τ

$$M_{jk}(\tau) = \begin{cases} \gamma\tau + O(\tau^2) & \text{if } j \neq k \text{ and } (j,k) \in E \\ 0 & \text{if } j \neq k \text{ and } (j,k) \notin E \\ 1 - d_j\gamma\tau + O(\tau^2) & \text{if } j = k \end{cases} \tag{3.4}$$

As the state of a Markov chain only depends on the current-in-time configuration, we can multiply the transition matrix at different times t and ε to obtain the final transition at time $t + \varepsilon$

$$M_{ij}(t+\varepsilon) = \sum_k M_{ik}(t) M_{kj}(\varepsilon) \tag{3.5}$$

where the sum k runs over all vertices. By explicitly writing down the term $k = j$, we obtain

$$M_{ij}(t+\epsilon) = M_{ij}(t) M_{jj}(\varepsilon) + \sum_{k \neq j} M_{ik}(t) M_{kj}(\varepsilon) = \tag{3.6}$$

$$= M_{ij}(t)(1 - \varepsilon H_{jj}) - \varepsilon \sum_{k \neq j} M_{ik}(t) H_{kj} \tag{3.7}$$

where we have isolated the infinitesimal term ε and introduced the time-independent generating matrix

$$H_{ij} = \begin{cases} d_j\gamma & \text{if } i = j \\ -\gamma & \text{if } i \neq j \text{ and } (i,j) \in E \\ 0 & \text{if } i \neq j \text{ and } (i,j) \notin E \end{cases}. \tag{3.8}$$

By rearranging the terms in Eq. (3.7) and in the limit of $\varepsilon \to 0$ we obtain a differential equation

$$\frac{dM_{ij}(t)}{dt} = -\sum_k M_{ik}(t) H_{kj}. \tag{3.9}$$

The solution of this equation given the natural initial condition $M_{ij}(0) = \delta_{ij}$ is

$$M(t) = e^{-Ht}. \tag{3.10}$$

Then if the initial distribution of the walker among the nodes is given by $\boldsymbol{p}(0)$, we obtain that the evolved probability distribution is now

$$\boldsymbol{p}(t) = M(t)\boldsymbol{p}(0). \tag{3.11}$$

It is also easy to show that the probability distribution itself satisfies a differential equation

$$\frac{dp_i(t)}{dt} = -\sum_k H_{ki} p_k(t) \quad \to \quad \frac{d}{dt}\boldsymbol{p}(t) = -H\boldsymbol{p}(t), \tag{3.12}$$

that will be the starting point to generalize continuous-time random walk to the quantum realm. We also notice that the generating matrix is proportional to the Laplacian matrix

$$H = \gamma L. \tag{3.13}$$

3.2 Continuous-time quantum walks

The extension of continuous-time random walks to the quantum case was addressed by [131] and can be summarized as follows.

In the standard process of quantization, the vector of probability $\boldsymbol{p}(t)$ is replaced with a state vector $|\psi(t)\rangle$ that belongs to a N-dimensional Hilbert space $\mathcal{H}$, where N is the size of the graph. A preferred basis is the position basis $|j\rangle$, where $j \in V$, and the system in the state $|j\rangle$ represents a localized walker. In such a way, we can write the probability of finding the walker in the node j as

$$p_j(t) = |\langle j|\psi(t)\rangle|^2. \tag{3.14}$$

In the quantization procedure, the differential equation in Eq. (3.12) is replaced with a Schrödinger equation

$$\frac{d}{dt}|\psi(t)\rangle = -i\widehat{H}_{\text{QW}}|\psi(t)\rangle \tag{3.15}$$

where H_{QW} is the Hamiltonian of the quantum walker. As we know, the solution can be expressed in terms of the unitary operator $\mathcal{U}(t)$ as

$$|\psi(t)\rangle = \widehat{U}(t)|\psi(0)\rangle = e^{-i\widehat{H}_{\text{QW}}t}|\psi(0)\rangle, \tag{3.16}$$

There is a natural correspondence we can draw: the transition matrix $M(t)$ in the classical random walk corresponds to the unitary evolution, while H in the classical correspond to $\widehat{H}_{\text{QW}}$. Hence, we simply define $\widehat{H}_{\text{QW}} = H = \gamma L$. Thus, the Laplacian matrix is promoted to be the generator of the quantum dynamics as well, where the parameter $\gamma > 0$ is the hopping rate between the nodes and it accounts for the energy scale of the system. A more physical argument passes through correspondence between L and the discretized kinetic operator for regular lattices [353].

We want to remark that the choice of L as the dynamics generator is only one of the possible (infinitely many) choices for the quantum-walker Hamiltonian $\widehat{H}_{\text{QW}}$. Indeed, any Hermitian operator that preserve the topology of the graph can be used as a legit CTQW Hamiltonian [353, 221, 339, 139, 140]. We also mention that, within this formulation, the CTQWs is a closed system. As we know, this is an ideal case, since any physical system inherently interacts with an external environment, yielding decoherence processes. For systems like quantum walks, these processes have been studied and reviewed in [201].

Part II

Thermometry in the quantum regime

From classical to quantum thermometry

The concept of temperature was originally a qualitative notion connected to the natural flow of heat, and associated with the intuitive notion of "hot" and "cold". The first attempt to formalize this concept dates back as far as Galileo. Together Sanctorius, they invented the thermoscope, an instrument that measured the change of temperature based on the changes in liquid's height in a tube [323, 134]. This instrument can be considered the ancestor of modern thermometers: in fact, the latter does not only display qualitative differences but also possess a measuring scale, facilitating quantitative analysis. By the end of the XVII century, the precision of these instruments was improving, but there were no universal standard thermometers and temperature scales. Conversely, each thermometer was unique and possessed its scale. The basic reason for this proliferation was that there were no phenomena that were known to take place always at the same temperature, and for such reason could be used as a universal thermometric benchmark.

In the early XVIII century, several attempts were made in finding reliable universal phenomena [1]. Here came the main contribution of Fahrenheit [86], who exploited the property of mercury to build more precise devices. Moreover, his thermometer was much smaller compared to the previous ones, and as a result, measuring the temperature was much easier. In addition, it was scalable, i.e. feasible for industrial production. Not only Fahrenheit introduced such a mercury thermometer, but he also proposed a universal thermometric scale: the age of precision thermometry was born.

Furthermore, by the middle of the XVIII century, a consensus emerged about using the boiling and freezing point of water as the preferred fixed point of thermometry, thanks to the work of Anders Celsius, among others. This caused several debates among the main scientists of the time, led by the Royal Society of London. For more information about that, we suggest the reader to the Book of Chan [86], where the chronology of the concepts, scale definitions and historical problems regarding a universally accepted thermometric scale is reported in great historical detail.

The XIX was the century of thermodynamics. Many concepts, like work and heat, were formalized. Among them, also the concept of temperature was operationally standardized. Indeed, the measurability of T is now based on the zeroth principle of thermodynamics formulated at the time: if A and B are at thermal equilibrium, i.e. no heat flow is observed between the two, and B and C are at thermal equilibrium too, then A and C are at equilibrium with each other. All these objects at equilibrium with each other are

[1] A nice attempt that I believe is worth mentioning is the one by Joachim Dalencé, which used the melting point of butter as its upper fixed point.

said to have the same temperature T. Most classical thermometers work at equilibrium by having some macroscopic property that depends on the thermometer's temperature T in a well-defined way. The operational ways to measure T are based on the zeroth principle illustrated above: once the thermometer and the system have reached equilibrium, one can read the temperature of S by looking at the temperature scale on the thermometer.

Clearly, a possible drawback of this strategy is that one has to ensure that during the equilibration process the temperature of the system S does not change due to the process itself, i.e. they do not reach equilibrium at a temperature T_{EQ} different from the one to be probed. Unfortunately, this happens only in the idealized case: the thermometer needs to exchange some energy to reach the equilibrium, and this comes from the system S. If the thermometer and S have respectively heat capacity C_t and C_S, and their initial temperature is T_t and T_S (with $T_S > T_t$), we have that the energy exchanged to reach the equilibrium at temperature T_{EQ} is given by

$$C_t(T_{\text{EQ}} - T_t) = C_S(T_S - T_{\text{EQ}}). \tag{3.17}$$

With some algebra, we get

$$T_{\text{EQ}} = T_S \frac{1 + \frac{C_t}{C_S} T_t}{1 + \frac{C_t}{C_S}} \tag{3.18}$$

which approximates the temperature to be probed T_S if $C_t \lll C_S$. Thus, a precise thermometer should not exchange too much energy during the process, i.e. its heat capacity should be much smaller than the heat capacity of the system. Mercury, for instance, satisfies the request properties.

In the last century, the search for optimal thermometers was addressed with the use of several physical properties having reliable responses to changes in temperature. Even more recently, the demand for even smaller and less invasive thermometers has emerged due to the advent of nanotechnologies, given the natural weakness of these systems [61, 76, 190]. Quantum thermometry has also been found of fundamental relevance in pushing the limits of technology in measuring temperature within cells or tiny electronic circuits [224, 208].

However, in moving away from the standard thermodynamic regime, several difficulties arise, even for the definition of temperature [282]. This also happens for other thermodynamic variables, such as heat and work, and it is even more evident in the quantum regime. Although these issues affect the concept of the temperature outside the thermodynamic limit, in the chapters that follow we are interested in the regime where the temperature, at least from the statistical perspective, is well defined. For this reason, in the following chapters, the temperature will be nothing but a statistical parameter T labelling the system at equilibrium.

As we have already observed, the key property for a thermometer based on the zeroth principle is to have a small heat capacity. This line of reasoning leads to considering small thermometers, possibly subject to the laws of quantum mechanics [154]. An extensive review of the last theoretical and experimental achievement of quantum thermometry can be found in [238, 267]. Here we review some of the most relevant results that most closely relate to the work presented in this thesis.

As we mentioned, one of the quantities that define the efficiency of a thermometer is the heat capacity. Since this quantity depends on temperature, one is led to investigate whether the heat capacity of a thermometer may be tailored for a specific range of temperatures [248]. Moreover, a general expression for the local heat capacity for a locally

probed quantum system has been proposed in [112], quantified by the local thermal response of arbitrary quantum systems at equilibrium in terms of metrological quantities.

The study of the metrological power in the estimation of temperature has been extensively studied in the quantum realm with the tools of quantum metrology presented in Chapter 2. A connection between classical thermometric precision and quantum one was presented in [264]. Here, the Landau bound on the precision of a temperature estimate for a classical and not too small system is $\Delta T^2 \geq T^2/C$, with C the heat capacity, and it was proved to be valid also for finite quantum systems with vanishing gap in the low-temperature regime. The tools of quantum estimation theory also provided proof that energy measurement is the optimal one. However, in the case of a minimum gap δ, the temperature can be estimated efficiently only down to a threshold, below which the variance of any estimators diverges exponentially as $\Delta T^2 \geq T^4 e^{\delta/T}$. This bound seemed to imply that measuring cold temperatures using a thermalized probe can be exponentially difficult. However, this is not always the case. Indeed, the limitation of the latter inequality lies in the fact that it does not hold in the case of continuous spectra or in the case where we have limited access to the probe. This happens when we do not have the possibility of performing a projective measurement of the system energy and the ability to completely distinguish all the energy levels, being both experimental demanding requests. These problems have been discussed in [280] where the framework for finite-resolution quantum thermometry has been introduced, and tighter bound have been derived in [196] in the limit of $T \to 0$. Finite resolution thermometry is also studied in [182].

The manipulation and engineering of single finite quantum systems have raised the question about the optimal system that can be used as a quantum thermometer. This question was addressed in [102], where the optimal probe is found to be a two-level system with a maximally degenerate excited state and an optimal fine-tuned gap. This is not in contradiction with the previous result by [264], since we assume there are no restrictions on the value of the gap. Similar results were derived in [69] regardless of the dimensionality of the probe.

The approach of thermometry discussed so far relies on local estimation theory, i.e. when the range of the true value of the parameter is well known. In the case of poor data, a bayesian approach is more appropriate. Hence, it is relevant to mention the recent interest in global quantum thermometry [304, 47], where a method for global thermometry was presented. The problem of the optimal probe was also addressed in [245], while attainability via adaptive strategies was studied in[237]. Finally, a connection with the thermodynamic length was established in [195].

We see how the quest for optimal equilibrium thermometry has spanned different fields and established several results and fundamental bounds. In this thesis, the first contribution is given by studying the role of the topology in the estimation of T and showing the optimal topological configurations in the underlying graph structure of our probe. Results are presented in Chapter 4

The equilibrium paradigm dominated thermometry since the very first definition of temperature. Nonetheless, a completely different approach has been explored in the last years that goes beyond the equilibration and thermalization process and exploits other features of a quantum system that can carry information on T. This is crucial in the development of novel quantum technologies, where one wants to probe systems at the nanoscale without destroying the samples. It is clear that at this scale, traditional strategies are not feasible. These experimental difficulties sparked interest in the search for new methods to determine the temperature T by using strategies that did not require reaching equilibrium, departing from the classical scheme established by the zero law of

thermodynamics. These new methods allow temperature estimation even in the out-of-equilibrium regime, where the temperature can be read from the statistic of the out-of-equilibrium probe that has interacted with the sample.

Different methods have been devised that use quantum probes $\mathcal{P}$ to measure the temperature. A possible strategy assumes that $\mathcal{P}$ interacts with the system $\mathcal{S}$ and eventually thermalizes: if the interaction is sufficiently weak, then, as in the standard paradigm described by the zeroth principle of thermodynamics, we can measure the temperature T measuring the probe $\mathcal{P}$ only. However, in the quantum regime, we can go beyond this standard strategy inherited from classical thermodynamics and exploit the transient evolution [238] to obtain more information compared to equilibrium probes. One of the first proposals for a quantum out-of-equilibrium probe used an atomic interferometer[327]. In this setting, the temperature is encoded in the relative phase which can be estimated using interferometer techniques. Exploiting a special class of non-classical states such as N00N, that yield a Heisenberg scaling in the phase estimation, one can induce the same scaling in temperature estimation. Similarly, a quantum interferometric thermometer using single-mode Gaussian state was studied in [191], and it was proved reliable in the nanokelvin regime and compared to a classical non-invasive thermometer, the pyrometer, which use the thermal radiation to estimate the temperature.

Using out-of-equilibrium probes proved to be particularly successful with a micromechanical oscillator platform. Here, the temperature can be probed by measuring the population of an external two-level system interacting via a Jaynes-Cummings interaction [65]. Similarly, the same strategy can be used in qubit-boson couplings in the mesoscopic regime, again measuring only the qubit [66]. In another study, authors also went beyond the Jaynes cummings approximation, studying a situation with large coupling strength and large detuning between qubit and oscillator and showed that, exploiting the ac Stark shift, precise thermometry can be performed.

Furthermore, out-of-equilibrium quantum thermometry greatly improved low-temperature sensing in the field of cold atoms and Fermi gas. Using a technique called in-situ thermometry, and exploiting non-equilibrium impurities dynamics, it was possible to probe the system's temperature with interferometric protocols [242], and also probing individual atomic wires [110]. The non-invasiveness of such strategies is very important in the context of cold atom gases, due to the inherent fragility of such systems.

The use of finite quantum systems proved to be useful in temperature estimation. However, many relevant physical systems that can be engineered belongs to infinite dimensional probe. Studying the out-of-equilibrium dynamics of a Gaussian thermometer [227], entanglement showed to be a useful resource. Nonetheless, differently from the qubit case, out-of-equilibrium is not always proven to be better than equilibrium probes. The use also of non-Gaussian interaction was addressed in optomechanical systems used to measure the temperature [247]. Another thermometer exploits a system undergoing quantum Brownian motion in the strong coupling regime [103]. A relevant property that proved to be useful in the temperature estimation is non-markovianity, both in continuous variable [363], where quantum criticality proved to enhance the temperature sensitivity, and single qubit systems [365].

Other approaches in quantum thermometry used different properties of quantum systems, bared from other thermodynamics setups. For instance, the use of thermal machines is worth to be mentioned [176, 211]. Another interesting approach is the sequential probing without reinitialization proposed in [113], which is more robust when the initial kownledge of T is poor and does not depend too much on the initial state of the probe. In the same spirit, the use of collisional models in quantum thermometry was addressed in [260, 313].

As mentioned, at the beginning of this introduction, distinguishing "hot" from "cold" was the most primitive form of thermometry. This primordial statement can be rephrased in the language of discrimination theory as a binary discrimination problem. Also for this task, out-of-equilibrium quantum probes proved to be useful compared to the thermalized ones [192]. In this work, a probe undergoing a markovian Lindblad master equation in the weak coupling limit was used to probe the temperature of the reservoir. However, many systems are not properly described in the weak coupling limit. In Chapter 5, we study another interesting case for temperature discrimination, i.e. a pure dephasing quantum probe. We assess the role of quantum resources and compare these probes with thermalized ones to see whether pure dephasing can be used as a resource. Pure dephasing was already found to be useful in temperature estimation [356, 287], and we found similarities and differences with our results.

A remark is in order here: in the following chapters, we are going to use indistinctly the temperature T_i or the inverse temperature $\beta_i = 1/k_B T_i$ and we label them as temperature.

CHAPTER 4

On the role of topology in determining the precision of a finite thermometer

In this chapter we study the connection between the role of topology and the precision of a finite thermometer. In particular, upon modeling a finite thermometer as a set of connected subunits , we employ graph theory, together with QFI, to assess the role of topology on the thermometric performance of the system. We show that measuring the energy of the system is the best way to estimate temperature and we explore which topological features play a role in the temperature estimation. We study whether connectivity is a useful resource to build precise thermometers and in which regime, i.e low or high temperature. We also compare the optimal precision with the one achievable by measuring the position of thermal excitations. Our results indicate that quantum probes are especially useful at low temperatures and that systems with low connectivity provide more precise thermometers.

Reference models are physical systems in which the connectivity plays a relevant role, e.g. quantum dots arranged in lattices [22] and qubits in quantum annealers [212, 258]. Evidences suggest that a system of qubits in D-Wave quantum annealers quickly thermalizes with the cold environment [67] and that a pause mid-way through the annealing process increases the probability of successfully finding the ground state of the problem Hamiltonian, and this has been related to the thermalization of the system [230].

The chapter is structured as follows. In Sec. 4.1 and 4.2 we consider the sensitivity of equilibrium states of the Laplacian matrix of simple graphs, both with the optimal strategy and measuring the position of the walker. In Sec. 4.3 and 4.4 we address the efficiency of our probes in both the high-temperature and low-temperature regime. In Sec. 4.5 we derive analytical and numerical results for some remarkable simple graphs and two-dimensional lattices. Finally, in Sec. 4.6 we analyze the relation between the QFI and the coherences and in Sec. 4.7 we summarize and discuss our results and findings. In this chapter we have set the Boltzmann constant k_B equal to 1.

4.1 QFI for equilibrium thermometry

In this chapter of the thesis, our focus is mainly on finite-size quantum system described by an N-dimensional Hilbert space and by a Hamiltonian operator

$$\widehat{H} = \sum_{k=0}^{N-1} E_k |e_k\rangle\langle e_k| \tag{4.1}$$

The idea is to use such a finite system as a probe to estimate the temperature T of an external environment. For that reason, we consider the usual thermodynamic situation

that occurs for thermalized systems, i.e. when a system is in contact with a thermal bath at temperature T. After undergoing some transient dynamics, we assume that the former reaches equilibrium at the same temperature of the bath. The final state of the probe is thus in a Gibbs state form

$$\varrho_{\mathcal{P}}(T) = \frac{e^{-\widehat{H}/T}}{Z(T)} = \sum_{k=0}^{N_g-1} \sum_{j=1}^{g_k} \frac{e^{-E_k/T}}{Z(T)} |e_{k,j}\rangle\langle e_{k,j}| \tag{4.2}$$

where we have make explicit the possible degeneracy of the energy levels. Here, N_g labels the total number of distinct energy levels, while g_k is the degeneracy of the corresponding kth energy level. We have also introduced the partition function

$$Z(T) = \sum_{k=0}^{N-1} e^{-E_k/T} = \sum_{k=0}^{N_g-1} g_k e^{-E_k/T}. \tag{4.3}$$

The precision with which we can estimate the temperature can be determined by the tools of quantum estimation theory introduced in Sec. 2.2. We can immediately notice that the state in Eq. (4.2) is diagonal in the energy eigenbasis, and the dependence on the parameter is only in the eigenvalues. This means that estimating the temperature from such an equilibrium state reduces to classical-like estimation problem, where the optimal POVM is realized by an energy measurement $\{|e_{k,j}\rangle\langle e_{k,j}|\}_{k,j}$. We obtain the following result

Result 4: QFI for equilibrium temperature estimation

The QFI for temperature estimation is given by

$$\mathcal{Q}(T) = \frac{1}{T^4}\left(\langle \widehat{H}^2\rangle - \langle \widehat{H}\rangle^2\right) \tag{4.4}$$

and corresponds to the FI of an energy measurement.

4.2 Fisher information for the position measurement

The focus of this chapter is to study the role of topology in the temperature estimation using graph theory and CTQW. In this scenario, where a system is confined to a discrete set of positions, a position measurement is the most natural measurement we can perform. For this reason, it may be interesting to compare the corresponding FI for the T with the QFI obtained in Eq. (4.4).

The POVM is given by $\{|j\rangle\langle j|\}_{j=0}^{N-1}$, and the probability of observing the system in the jth position given that the state has thermalized at temperature T is

$$p(j|T) = \mathrm{Tr}\{\varrho_{\mathcal{P}}(T)|j\rangle\langle j|\} = \sum_{k=0}^{N-1} \frac{e^{-E_k/T}}{Z(T)} |\langle j|e_k\rangle|^2. \tag{4.5}$$

The FI is given by Eq. (2.36) and reads as

$$\mathcal{F}^{\mathrm{POS}}(T) = \sum_{j=0}^{N-1} \frac{\left(\partial_T p(j|T)\right)^2}{p(j|T)} \tag{4.6}$$

To evaluate this, we recall the identity for the partition function

$$\partial_T Z(T) = \frac{Z\langle \widehat{H} \rangle}{T^2}. \tag{4.7}$$

Then, the first derivative of the probability is given by

$$\partial_T p(j|T) = \sum_{k=0}^{N-1} \partial_T \left(\frac{e^{-E_k/T}}{Z(T)} \right) |\langle j|e_k\rangle|^2 = \tag{4.8}$$

$$= \frac{1}{T^2} \sum_{k=0}^{N-1} e^{-E_k/T} \left(\frac{E_k - \langle \widehat{H} \rangle}{Z(T)} \right) |\langle j|e_k\rangle|^2 = \tag{4.9}$$

$$= \frac{1}{T^2} \left(\langle \widehat{H} \varrho_{\mathcal{P}} \rangle_j - \langle \widehat{H} \rangle p(j|T) \right), \tag{4.10}$$

where we have defined

$$\langle \widehat{H} \varrho_{\mathcal{P}} \rangle_j = \sum_{k=0}^{N-1} \frac{e^{-E_k/T} E_k}{Z(T)} |\langle j|e_k\rangle|^2. \tag{4.11}$$

From the former expression, we obtain

$$\mathcal{F}^{\text{POS}}(T) = \frac{1}{T^4} \sum_{j=0}^{N-1} \frac{\langle \widehat{H} \varrho_{\mathcal{P}} \rangle_j^2}{p(j|T)} + \frac{1}{T^4} \langle \widehat{H} \rangle^2 \sum_{j=0}^{N-1} p(j|T) - \frac{2}{T^4} \langle \widehat{H} \rangle \sum_{j=0}^{N-1} \langle \widehat{H} \varrho_{\mathcal{P}} \rangle_j \tag{4.12}$$

After some algebra and using the completeness relation $\sum_{j=0}^{N-1} |\langle j|e_k\rangle|^2 = 1$, we have that

$$\sum_{j=0}^{N-1} \langle \widehat{H} \varrho_{\mathcal{P}} \rangle_j = \langle \widehat{H} \rangle, \tag{4.13}$$

from which we eventually obtain the following result

Result 5: FI for T estimation with position measurement

The FI for the temperature estimation and with a position measurement of the walker is

$$\mathcal{F}^{\text{POS}}(T) = \frac{1}{T^4} \left(\sum_{j=0}^{N-1} \frac{\langle \widehat{H} \varrho_{\mathcal{P}} \rangle_j^2}{p(j|T)} - \langle \widehat{H} \rangle^2 \right) \tag{4.14}$$

Actually, this formula holds true for any projective PVM, since we did not use any particular properties of the position measurement.

4.3 Thermometry in the low-temperature regime

The first regime we analyze is the low temperature regime. We assume that the system is mostly in the ground state and can access only the first excitation energy, i.e. that

$E_n \ggg T$ for $k > 1$. Using the fact that $E_0 = 0$ and $g_0 = 1$, we have that the partition function becomes

$$Z_{\text{LOW}}(T) = 1 + g_1 e^{-E_1/T}. \tag{4.15}$$

For the same reasons, the mean value of the energy is $\langle \widehat{H} \rangle = g_1 E_1 e^{-E_1/T} Z^{-1}(T)$, and it follows that the QFI in the low-temperature regime can be approximated as

$$\mathcal{Q}_{\text{LOW}}(T) \simeq \frac{f_{g_1}(E_1/T)}{E_1^2} \tag{4.16}$$

where we have defined

$$f_{g_1}(x) = \frac{g_1 x^4 e^{-x}}{(1 + g_1 e^{-x})^2} \tag{4.17}$$

If we define $x = E_1/T$, the QFI now reads as

$$\mathcal{Q}_{\text{LOW}}(T) \simeq \frac{1}{T^2} \frac{f_{g_1}(x)}{x^2} \tag{4.18}$$

We see that the latter is maximum for small values of T. Moreover, we can also study how to maximize the second element in the product, i.e. $f_{g_1}(x)/x^2$. As a function of g_1, we obtain that

$$\frac{d}{dg_1} \frac{f_{g_1}(x)}{x^2} = \frac{e^x (e^x - g_1) x^4}{(e^x + g_1)^3} = 0 \tag{4.19}$$

Since $x > 0$ and $g_1 \geq 1$, $e^x - g_1$ has no solution. This means that it is a monotone function of g_1. In particular, if $x > \log(g_1)$, then it is a monotone increasing function of g_1, otherwise it is monotone decreasing.

Instead, as a function of x, we obtain that

$$\frac{d}{dx} \frac{f_{g_1}(x)}{x^2} = \frac{e^x g_1 x (g_1(2 + x) - e^x (x - 2))}{(e^x + g_1)^3} = 0 \tag{4.20}$$

The solution to this is in the transcendental equation

$$e^{x_{\text{MAX}}} = g_1 \frac{x_{\text{MAX}} + 2}{x_{\text{MAX}} - 2}. \tag{4.21}$$

The solutions are reported graphically in Fig. 4.1. The value of x_{MAX} depends only on the degeneracy g_1 and numerical results show that $x_{\text{MAX}}(g_1)$ is a sub-linear function, i.e. it increases less than linearly with g_1.

To evaluate the FI for a position measurement, we first find the approximated probability distribution in such regime

$$p(j|T) \simeq Z(T)^{-1} (N^{-1} + \exp(-E_1/T\eta_j)), \tag{4.22}$$

where $\eta_j = \sum_{k=1}^{g_1} |\langle j | e_{1,k} \rangle|^2$. In this case, since

$$\langle \widehat{H} \varrho_{\mathcal{P}} \rangle_j \simeq \frac{e^{-E_1/T} E_1 \eta_j}{Z(T)} \tag{4.23}$$

we obtain that

$$\mathcal{F}^{\text{POS}}_{\text{LOW}}(T) \simeq \frac{E_1^2 e^{-2E_1/T}}{Z(T) T^4} \left(\sum_{j=0}^{N-1} \frac{\eta_j^2}{N^{-1} + e^{-E_1/T} \eta_j} - \frac{g_1^2}{Z(T)} \right) \tag{4.24}$$

We conclude observing that the main topological quantity is the degeneracy of the first eigenvalue. We will study g_1 quantity and the metrological quantity for a few relevant example in a following section.

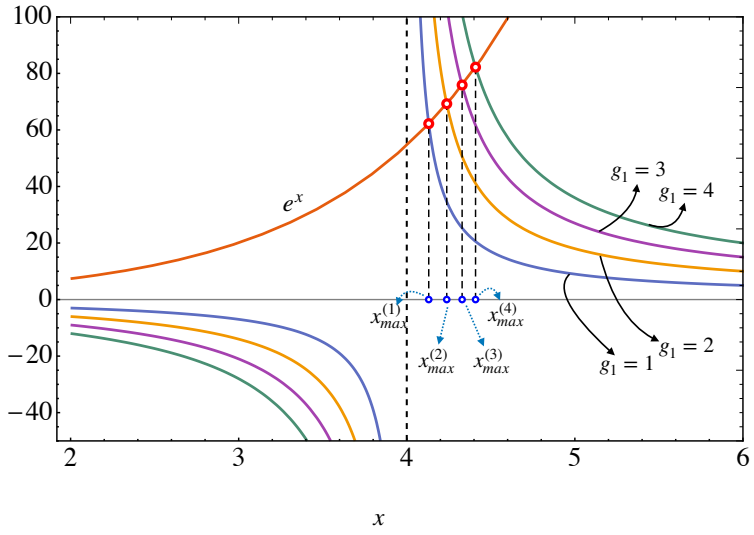

Figure 4.1: Graphical solution $x_{\text{MAX}}(g_1)$ of the transcendental equation (4.21) for different values of g_1.

4.4 Thermometry in the high-temperature regime

In the opposite regime of high temperature, we assume that $T \ggg E_k$ for all k. In this scenario, we have to stress that the single-walker probe is no longer valid in the high-temperature regime, where many excitations come into play. Nonetheless, the single walker approximation can be used for small thermometers with bounded spectrum and large energy gap $E_1 - E_0$, so that we may expect few excitations. In this case, the density matrix in the energy eignebasis can be approximated by the maximally mixed state $\varrho^{\mathcal{P}}(t) \simeq \mathbb{I}_N/N$, where $\mathbb{I}_N$ is the identity matrix. Accordingly, the QFI becomes

$$\mathcal{Q}_{\text{HIG}}(T) \simeq \frac{1}{T^4}\left(\frac{1}{N}\sum_{k=0}^{N-1} E_k^2 - \frac{1}{N^2}\left(\sum_{k=0}^{N-1} E_k\right)^2\right) \tag{4.25}$$

A more compact formula can be derived by rewriting the sum using the spectral properties of the laplacian matrix. First, the sum of the laplacian eigenvalues can be written as

$$\sum_{k=0}^{N-1} E_k = \text{Tr}\{L\} = \text{Tr}\{D\} = \sum_{k=0}^{N-1} d_k = 2M \tag{4.26}$$

where the last equality was first proved by Euler, and it is known as the degree sum formula or the handshaking lemma [129, 9]. In this formula we have denoted the degree of the kth vertex as d_k, while M is the total number of edges. Next, we consider the sum of the squared energy eigenvalues

$$\sum_{k=0}^{N-1} E_k^2 = \text{Tr}\left\{L^2\right\} = \text{Tr}\left\{D^2\right\} + \text{Tr}\left\{A^2\right\} - \text{Tr}\{DA\} - \text{Tr}\{AD\} \tag{4.27}$$

Using the definition of degree and adjacency matrix in Eq. (3.1), we see that

$$(DA)_{kj} = \begin{cases} 0 & \text{if } k = j \\ d_k A_{kj} & \text{otherwise} \end{cases} \tag{4.28}$$

$$(AD)_{kj} = \begin{cases} 0 & \text{if } k = j \\ A_{kj} d_j & \text{otherwise} \end{cases} . \tag{4.29}$$

Clearly we have that $\mathrm{Tr}\{DA\} = \mathrm{Tr}\{AD\} = 0$, whereas

$$\mathrm{Tr}\left\{A^2\right\} = \sum_{k=0}^{N-1} (A^2)_{kk} = \sum_{k=0}^{N-1}\sum_{m=0}^{N-1} A_{km}A_{mk} = \sum_{k=0}^{N-1}\sum_{m=0}^{N-1} A_{km} = \sum_{k=0}^{N-1} d_k = 2M \tag{4.30}$$

where we have used the symmetry of the adjacency matrix, and the fact that for simple graphs $A_{km} \in \{0,1\}$, hence $A_{km}^2 = A_{km}$. This is connected with the well-known fact that $(A^2)_{kj}$ represents the number of walks of length 2 connecting the vertexes k and j. Eventually, we obtain

$$\sum_{k=0}^{N-1} E_k^2 = \sum_{k=0}^{N-1} d_k^2 + 2M \tag{4.31}$$

In this way, the QFI at high temperatures can be written in terms of d_k and M, that is quantities that describes the topology of the graph, as

$$\mathcal{Q}_{\mathrm{HIG}}(T) \simeq \frac{1}{NT^4}\left(\sum_{k=0}^{N-1} d_k^2 + 2M\left(1 - \frac{2M}{N}\right)\right). \tag{4.32}$$

Actually, the sum of the squared degree can be bounded from above and below as

$$\frac{4M^2}{N} \leq \sum_{k=0}^{N-1} d_k^2 \leq M\left(\frac{2M}{N-1} + N - 2\right). \tag{4.33}$$

The upper bound is proved in [109] and is saturated by the complete graph. Instead, the lower bound follows from the Cauchy-Schwartz inequality for the inner product of two N-dimensional vectors $(1,...,1)$ and $(d_0,...,d_{N-1})$ and using Eq. (4.26). In this case, two possible graphs saturating the lower bound are the cycle graph and the complete bipartite graph whose partite sets have both cardinality $N/2$.

Using these two inequality we can also bound the QFI as

$$\frac{2M}{NT^4} \leq \mathcal{Q}_{\mathrm{HIG}}(T) \leq \frac{M}{T^4}\left(1 - \frac{2M(N-2)}{N^2(N-1)}\right) \tag{4.34}$$

The two bounds are saturated for the same graphs mentioned above. For a more detailed discussion of this quantity, we refer the reader to the next section, where a series of examples will be studied in detail. However, some general considerations can be drawn from these formulae. For instance, that for high temperatures the optimal thermometer is the complete graph, which, among the simple graphs, has the maximum number of edges M. Notice also that the complete graph has the maximum energy gap, since $E_1 - E_0 = N$. Thus, unlike the low-temperature regime, the graphs which perform better are those with high connectivity, quantified by the number of edges M.

Recalling that in the high-temperature regime $\varrho_{\mathcal{P}} \simeq \mathbb{I}_N/N$, we can also derive an approximate formula for the FI for the position measurement as

$$\mathcal{F}^{\text{POS}}_{\text{HIG}}(T) \simeq \frac{1}{N^2T^4}\left(N\sum_{j=0}^{N-1}\left(E_k|\langle j|e_k\rangle|^2\right)^2 - 4M^2\right) \tag{4.35}$$

Using the fact that

$$\sum_{k=0}^{N-1} E_k|\langle j|e_k\rangle|^2 = \sum_{k=0}^{N-1}\langle j|L|e_k\rangle\langle e_k|j\rangle = \langle j|L|j\rangle = d_j \tag{4.36}$$

we eventually obtain

$$\mathcal{F}^{\text{POS}}_{\text{HIG}}(T) \simeq \frac{1}{N^2T^4}\left(N\sum_{j=0}^{N-1} d_j^2 - 4M^2\right) \tag{4.37}$$

To understand the discrepancy between the optimal measurement and the position measurement in the high temperature regime, we evaluate the ratio

$$\frac{\mathcal{F}^{\text{POS}}_{\text{HIG}}(T)}{\mathcal{Q}_{\text{HIG}}(T)} = \frac{N\sum_{j=0}^{N-1} d_k^2 - 4M^2}{N\left(\sum_{k=0}^{N-1} d_k^2 + 2M\left(1-\frac{2M}{N}\right)\right)} = \frac{1}{1+\lambda_{N,M}} \tag{4.38}$$

which is temperature independent, and where we have introduced

$$\lambda_{N,M} = \frac{2M}{\sum_{k=0}^{N-1} d_k^2 - 4M^2N^{-1}}, \tag{4.39}$$

a quantity that depends only on topological quantities and that fully capture the different scaling of FI and QFI: small values of $\lambda_{N,M}$ means a ratio close to 1, i.e. $\mathcal{F}^{\text{POS}}_{\text{HIG}}(T) \simeq \mathcal{Q}_{\text{HIG}}(T)$, whereas large values of $\lambda_{N,M}$ means a ratio close to 0, and a position measurement is not optimal.

4.5 Results on network thermometry

This section is fully devoted to the study of the metrological performances of some remarkable connected simple graphs and some lattice graphs, using the previously found general results.

To avoid repetitions, we recall that the ground state energy in every graph we will consider is E_0 and is not degenerate, i.e. $g_0 = 1$. The corresponding eigenstate is

$$|e_0\rangle = \frac{1}{\sqrt{N}}\sum_{j=0}^{N-1}|j\rangle. \tag{4.40}$$

Results of QFI and FI for position measurement for graphs (see Fig. 4.2) are shown in Fig. 4.3 and 4.4, for lattices (see Fig. 4.5) in Fig. 4.6, and results of the ratio of FI and QFI for both graphs and lattices are summarized in Fig. 4.7. The analytical results suitable for a comparison are reported in Table 4.1.

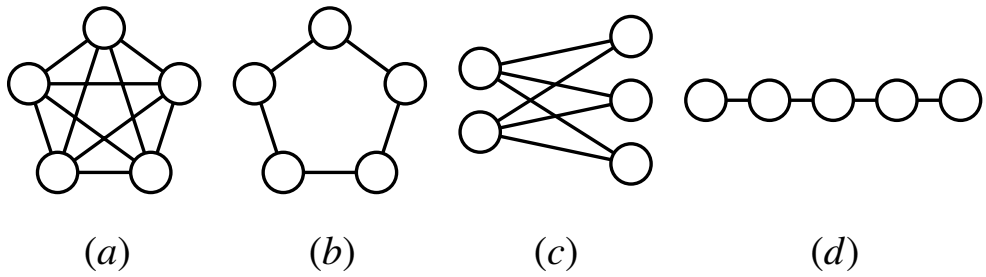

Figure 4.2: Graphs considered in the present chapter (example for $N = 5$ vertices): (a) Complete graph K_5, (b) cycle graph C_5, (c) complete bipartite graph $K_{2,3}$, and (d) path graph P_5.

4.5.1 Position measurement for circulant graph

In this section we prove that, for the special case of circulant graph, the FI for a position measurement is always zero, i.e. we do not gain any information on the temperature. Circulant graphs are defined as the regular graph whose adjacency matrix is circulant [126, 157]. The latter is a special Toeplitz matrix where every row of the matrix is a rich cyclic shift of the row above it, and remarkably, for this class of matrices the eigenproblem is analytically solved [160]. Indeed, the Laplacian eigenstates of circulant graphs are

$$|e_k\rangle = \frac{1}{\sqrt{N}} \sum_{j=0}^{N-1} \omega^{kj} |j\rangle, \tag{4.41}$$

where $\omega = \exp(2\pi i/N)$. This means that $|\langle j|e_k\rangle|^2 = 1/N$ for all k and the probability distribution becomes

$$p(j|T) = \frac{1}{N} \tag{4.42}$$

which is temperature independent, and hence the corresponding FI is null. We conclude that for circulant graphs, the position measurement does not carry any information on the temperature T. This result can be generalized to an arbitrary parameter encoded in the eigenvalues of a diagonal state in the energy eigenbasis of a circulant graph.

4.5.2 Complete graph

A complete graph is a simple graph whose vertices are pairwise adjacent, i.e. each pair of distinct vertices is connected by a unique edge (see Fig. 4.2 (a)). The complete graph with N vertices is denoted K_N, is $(N-1)$-regular, and has $M = N(N-1)/2$ edges. Its energy spectrum consists of two energy levels: the ground state and the second level $E_1 = N$ with degeneracy $g_1 = N - 1$. The graph is circulant, thus the eigenvectors are given by (4.41) and the FI for a position measurement is identically null.

In this case, the approximation for the low-temperature regime is actually exact and holds at all the temperatures, because the system has precisely two distinct energy levels. Hence, the QFI reads as

$$\mathcal{Q}(T) = \frac{N^2(N-1)e^{-N/T}}{T^4[1+(N-1)e^{-N/T}]^2}\,. \tag{4.43}$$

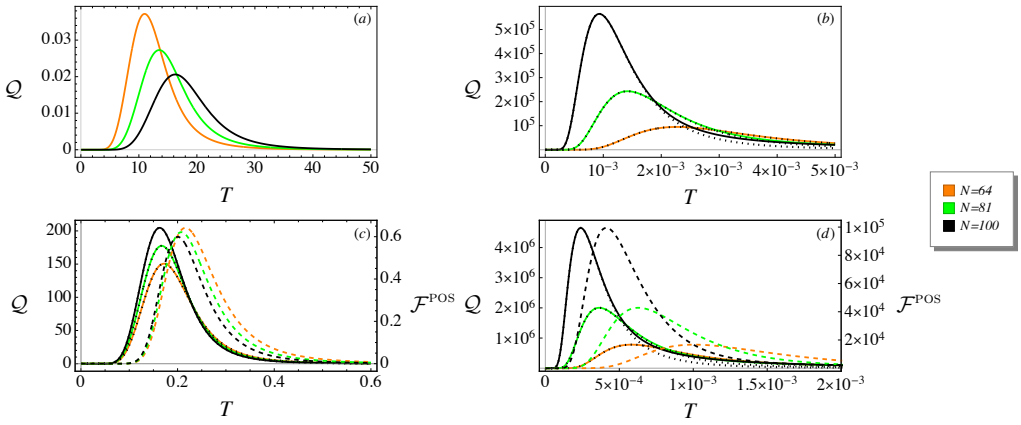

Figure 4.3: QFI and FI for position measurement for different graphs of order N: (a) complete graph, (b) cycle graph, (c) star graph, and (d) path graph. Solid colored line: QFI $Q(T)$. Dotted black line: QFI at low temperature $Q_{\rm LOW}$ (4.16) (not reported for the complete graph since it coincides with Eq. (4.43)). Dashed colored line: FI for position measurement $F^{\rm POS}(T)$. The FI for complete graph and cycle graph (circulant graphs) is null, and therefore is not shown. Because of the different ranges, values of QFI are referred to the left y-axis, and values of FI are referred to the right y-axis.

The algebraic connectivity $E_1 = N$ and the degeneracy $g_1 = N-1$ grow with the order N of the graph. In Fig. 4.3 (a) we observe that maxima of QFI occur at higher temperatures as N increases. According to Eq. (4.21) and Fig. 4.1, we expect the maximum of QFI to occur at increasing values of $x_{\rm MAX} = E_1/T_{\rm MAX}$ as g_1 (N) increases. Hence, this means that $T_{\rm MAX}$ increases less than linearly with N. For this reason the complete graph is not a good thermometer for low T. On the other hand, the complete graph saturates the upper bound in (4.34), since $M = N(N-1)/2$. It follows that in the high-temperature regime the complete graph is the optimal thermometer and, accordingly, the QFI is

$$\mathcal{Q}_{\rm HIGH}(T) = (N-1)/T^4. \tag{4.44}$$

4.5.3 Cycle graph

A cycle graph with $N \geq 3$ vertices (or N-cycle) is a simple graph whose vertices $\{v_j\}_{j=1,\dots,N}$ can be (re)labeled such that its edges are $v_1v_2, v_2v_3, \dots, v_{N-1}v_N$, and v_Nv_1 (see Fig. 4.2 (b)). In other words, we may think of it as a one-dimensional lattice with N sites and periodic boundary conditions. The cycle graph with N vertices is denoted C_N, is 2-regular, and has $M = N$ edges. Its energy spectrum is

$$E_k = 2[1 - \cos(2\pi k/N)], \tag{4.45}$$

with $k = 0, \dots, N-1$. The lowest energy level is not degenerate, while the degeneracy of the highest energy level depends on the parity of N: no degeneracy for even N, $g_{N/2} = 1$, but double degeneracy for odd N, $g_{(N+1)/2} = 2$. The remaining energy levels have degeneracy 2. The cycle graph is circulant, thus the eigenvectors are (4.41), the same of those of the complete graph, and the FI for a position measurement is identically null.

The algebraic connectivity $E_1 = 2[1 - \cos(2\pi/N)]$ decreases as N increases, while $g_1 = 2$ is constant. According to Eq. (4.21) and Fig. 4.1, we expect the maximum of

QFI to occur at the constant value of $x_{\text{MAX}} = E_1/T_{\text{MAX}}$ independently of N, because g_1 is constant. Since E_1 decreases as N increases, then T_{MAX} must also decrease to ensure x_{MAX} constant. Indeed, the maxima of QFI occur at lower temperatures as N increases, as shown in Fig. 4.3 (b). It follows that the larger N the better the cycle graph behaves as a low-temperature probe. Instead, the cycle graph saturates the lower bound in (4.34), since $M = N$, and so the QFI at high temperatures is the smallest possible

$$\mathcal{Q}_{\text{HIG}}(T) = 2/T^4. \tag{4.46}$$

4.5.4 Complete bipartite graph

A graph G is bipartite if the set of vertices $V(G)$ is the union of two disjoint independent sets V_1 and V_2, called partite sets of G, such that every edge of G joins a vertex of V_1 and a vertex of V_2. A complete bipartite graph is a simple bipartite graph such that two vertices are adjacent if and only if they are in different partite sets, i.e. if every vertex of V_1 is adjacent to every vertex of V_2 (see Fig. 4.2 (c)). The complete bipartite graph having partite sets with $|V_1| = N_1$ and $|V_2| = N_2$ vertices is denoted K_{N_1,N_2}, has $M = N_1N_2$ edges, and the total number of vertices is $N = N_1 + N_2$.

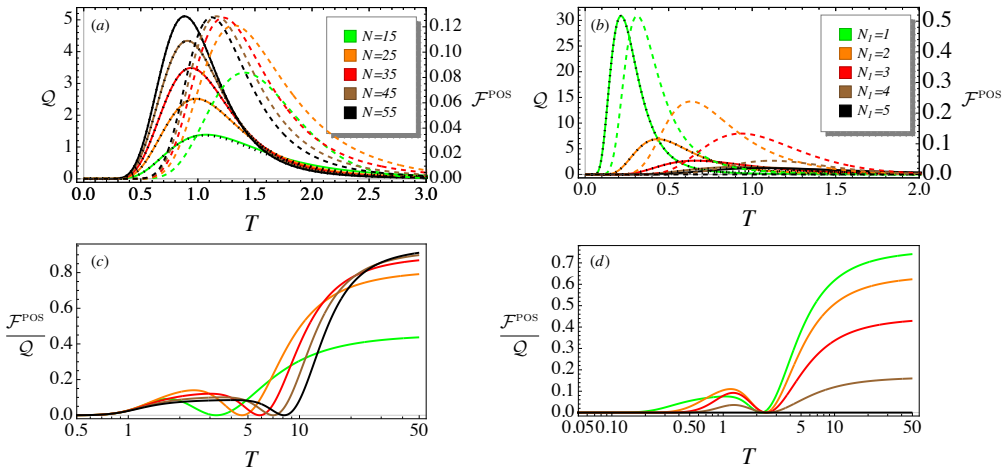

Figure 4.4: Results of the estimation problem of the temperature for the complete bipartite graph K_{N_1,N_2} of order $N = N_1 + N_2$. Left-column plots: results for different N at fixed $N_1 = 5$. Right-column plots: results for different N_1 at fixed $N = 10$. Values of $N_1 > N/2$ are not considered because of the symmetry of the graph when exchanging the two partite sets and so N_1 and N_2. For $N_1 = N_2 = N/2$ the FI is identically null because the corresponding complete bipartite graph is circulant. Top-row plots: QFI $Q(T)$ (solid colored line), QFI at low temperature $Q_{\text{LOW}}(T)$ (4.16) (dotted black line), and FI for position measurement $F^{\text{POS}}(T)$ (dashed colored line). Because of the different ranges, values of QFI are referred to the left y-axis, and values of FI are referred to the right y-axis. Bottom-row plots: ratio $F^{\text{POS}}(T)/Q(T)$.

Without loss of generality we assume $N_1 \leq N_2$. The energy spectrum is given by $E_1 = N_1$, $E_2 = N_2$, and $E_3 = N_1 + N_2$, with degeneracy $g_0 = 1$, $g_1 = N_2 - 1$, $g_2 = N_1 - 1$,

and $g_3 = 1$, respectively. The corresponding eigenvectors are

$$|e_1^n\rangle = \frac{1}{\sqrt{n(n+1)}} \left(\sum_{k=N_1}^{N_1-1+n} |k\rangle - n|N_1+n\rangle \right) \tag{4.47}$$

$$|e_2^m\rangle = \frac{1}{\sqrt{m(m+1)}} \left(\sum_{k=0}^{m-1} |k\rangle - m|m\rangle \right) \tag{4.48}$$

$$|e_3\rangle = \frac{1}{\sqrt{N}} \left(\sqrt{\frac{N_2}{N_1}} \sum_{k=0}^{N_1-1} |k\rangle - \sqrt{\frac{N_1}{N_2}} \sum_{k=N_1}^{N-1} |k\rangle \right) \tag{4.49}$$

where $n = 1, \ldots, N_2 - 1$ and $m = 1, \ldots, N_1 - 1$.

Note that for $N_1 = N_2 = N/2$ the complete bipartite graph is circulant and the spectrum reduces to E_0, $E_1 = N/2$, and $E_2 = N$, with degeneracy, respectively, $g_0 = 1$, $g_1 = N - 2$, and $g_2 = 1$. Instead, for $N_1 = 1$ and $N_2 = N - 1$ we obtain the star graph S_N, whose spectrum reduces to E_0, $E_1 = 1$, and $E_2 = N$, with degeneracy, respectively, $g_0 = 1$, $g_1 = N - 2$, and $g_2 = 1$.

Regarding the low-temperature regime, the algebraic connectivity is $E_1 = N_1$ while $g_1 = N_2 - 1$. The complete bipartite graph is completely defined only by the total number of vertices N, so we discuss where the maximum of the QFI occur according to Eq. (4.21) and Fig. 4.1 first for a given value N_1, and then for a given value of $N = N_1 + N_2$.

For N_1 fixed, we expect the maximum of QFI to occur at increasing values of $x_{\text{MAX}} = E_1/T_{\text{MAX}}$ as N increases, because N_2 and thus g_1 increase. Since E_1 is constant, then T_{MAX} must decrease to ensure that x_{MAX} increases. Indeed, for a given N_1, the maxima of QFI occur at lower temperatures as N increases, as shown in Fig. 4.4 (a). In particular, this is also the case of the star graph S_N, because it coincides with $K_{1,N-1}$, even if such behavior is less evident in Fig. 4.3 (c).

For N fixed, we expect the maximum of QFI to occur at decreasing values of $x_{\text{MAX}} = E_1/T_{\text{MAX}}$ as N_1 increases, because N_2 and thus g_1 decrease. Since E_1 increases as N_1 increases, then T_{MAX} must increase more than N_1 to ensure that x_{MAX} decreases. Indeed, for a given N, the maxima of QFI occur at higher temperatures as N_1 increases, as shown in Fig. 4.4 (b). This means that, at fixed N, we can tune the temperature at which the QFI is maximum just by varying the number of of vertices in the two partite sets. From Fig. 4.4 (b) we observe that the highest maximum of QFI is provided by the star graph S_N, whose algebraic connectivity $E_1 = 1$ is constant and minimum, while the lowest maximum of QFI is provided by $K_{N/2,N/2}$, i.e. for $N_1 = N_2$, whose algebraic connectivity $E_1 = N/2$ is the largest among all the complete bipartite graphs.

In the high-temperature regime, since

$$\sum_{k=0}^{N-1} d_k^2 = N_1 N_2 (N_1 + N_2) \tag{4.50}$$

and $M = N_1 N_2$, the QFI is

$$\mathcal{Q}_{\text{HIG}}(T) = \frac{N_1 N_2 \left[(N_1 - N_2)^2 + 2(N_1 + N_2) \right]}{T^4 (N_1 + N_2)^2} \tag{4.51}$$

Notice that for $N_1 = N_2 = N/2$, the complete bipartite graph is $N/2$-regular, and saturates the lower bound in (4.34), since $M = N^2/4$, and so the QFI at high temperatures simplifies to $\mathcal{Q}_{\text{HIG}}(T) = N/(2T^4)$.

The asymptotic behavior of the ratio $F^{\mathrm{POS}}_{\mathrm{HIG}}(T)/Q_{\mathrm{HIG}}(T)$ at high temperature (4.38) is characterized by $\lambda_{N_1+N_2,N_1N_2} = 2(N_1+N_2)/(N_2-N_1)^2$. Depending on the number of vertices in the two subsets, results differ. When $N_1 = N_2$, the difference $N_2 - N_1$ is null, the complete bipartite graph is circulant and so the FI is identically null, for any T. Instead, the difference $N_2 - N_1$ is maximum for the star graph S_N. This results in $\lambda_{N,N} = 2N/(N-2)^2$: hence, $\lambda_{N,N} \to 0$ for large N and, accordingly, the FI approaches the QFI in the limit of high temperatures. Actually, since for the star graph $\sum_k d_k^2 = N(N-1)$, the QFI in the high-temperature regime has the same asymptotic behavior of the complete graph, i.e. $\mathcal{Q}_{\mathrm{HIG}}(T) = (N-1)/T^4 + O(1/(NT^4))$.

In this section we have approximated the QFI for the complete bipartite graph under the assumptions of low or high temperature. For completeness, we also report the exact analytical expression of the QFI

$$\begin{aligned}\mathcal{Q}(T) =& \frac{e^{-2(N_1+N_2)/T}}{Z^2T^4}\Big\{N_1^2 e^{N_1/T}\left[(N_1-1)+e^{2N_2/T}(N_2-1)\right]\\ &+N_2^2 e^{N_2/T}\left[e^{2N_1/T}(N_1-1)+(N_2-1)\right]\\ &+e^{(N_1+N_2)/T}\left[N_1^3(N_2-1)-N_2^2(N_2-2)\right.\\ &\left.+N_1N_2^2(N_2+1)-N_1^2(2N_2^2-N_2-2)\right]\Big\}\,,\end{aligned} \tag{4.52}$$

4.5.5 Path graph

A path graph with N vertices is a simple graph whose vertices $\{v_j\}_{j=1,\dots,N}$ can be (re)labeled such that its edges are $v_1v_2, v_2v_3, \dots, v_{N-1}v_N$ (see Fig. 4.2 (d)). In other words, we may think of it as a one-dimensional lattice with N sites and open boundary conditions. The path graph with N vertices is denoted P_N, and has $M = N-1$ edges. Its nondegenerate energy spectrum is

$$E_k = 2[1-\cos(\pi k/N)], \tag{4.53}$$

with $k = 0, \dots, N-1$, and the corresponding eigenvectors are

$$|e_k\rangle = \sum_{j=0}^{N-1} \cos\left(\frac{\pi k}{2N}(2j-1)\right)|j\rangle \tag{4.54}$$

The energy spectrum is similar to that of the cycle, and this is reflected in its thermometric behavior. Indeed, the algebraic connectivity $E_1 = 2[1-\cos(\pi/N)]$ decreases as N increases, while $g_1 = 1$ is constant. Hence, as for the cycle graph, the maximum of the QFI occurs at lower temperature as N increases, as shown in Fig. 4.3 (d). Further, the similarity extends also in the high-temperature regime, where, we have that

$$\sum_k d_k^2 = 2(2N-3) \tag{4.55}$$

Since $M = N-1$, the QFI in this limit is

$$\mathcal{Q}_{\mathrm{HIG}}(T) = 2/T^4 + O(1/(N^2T^4)), \tag{4.56}$$

which is asymptotically equivalent to that of the cycle.

Nevertheless, there is a difference between the cycle and the path, and this is due to the different boundary conditions of the two graphs. In the first, the periodic boundary

conditions ensure that the cycle graph is a circulant graph, and consequently the FI for the position measurement is null. Instead, in the second, the open boundary conditions lead to a non-null FI for the position measurement. The asymptotic behavior of the ratio $\mathcal{F}^{\text{POS}}_{\text{HIG}}(T)/\mathcal{Q}_{\text{HIG}}(T)$ at high temperature (4.38) is characterized by $\lambda_{N,N-1} = N(N-1)/(N-2)$, which is monotonically increasing with the order of the graph. Thus, in the limit of high temperature the FI is very small compared to QFI, but still can provide some information on the temperature T, differently from the cycle graph.

4.5.6 Lattices

We now consider a different class of graphs, two dimensional lattices, and study their thermometric properties. In particular, we choose three regular tessellations composed of regular polygons symmetrically tiling the Euclidean plane: equilateral triangles, squares, and regular hexagons [Figs. 4.5(a)-(c)]. In addition to these we also consider the truncated square lattice in Fig. 4.5(d). Triangular and square lattices are Bravais lattices, while honeycomb and truncated square lattice are not. This difference is reflected in the spreading of CTQWs, which is ballistic on Bravais lattices and subballistic on non-Bravais lattices [290]. A generic vertex in the triangular lattice has degree 6, in the square lattice has degree 4, and both in the honeycomb and in the truncated square lattice has degree 3. We consider the lattices either with open boundary conditions (OBC) or with periodic boundary conditions (PBC). Notice that the lattices with PBC are regular, while the lattices with OBC are not, because the vertices at the boundaries have a lower degree than the vertices within the lattice.

Numerical results of QFI and FI for the lattices with OBC are shown in Fig. 4.6. We observe that the maximum of the QFI gets sharper and higher, and shifts to lower temperatures as the size of the lattice, i.e., the number of vertices, increases. A similar behavior occurs as the degree of the vertex of the lattice decreases: the maximum of the QFI for honeycomb and truncated square lattices is sharper and higher, and at lower temperature than the peak of the QFI for the triangular lattice. The predicted behavior of the QFI at low temperature (4.16) is a good approximation for honeycomb and truncated square lattices, because it fits the maximum of the QFI, its height and position. For the square it is fairly good approximation, but for the triangular lattices it fits only the QFI at the temperatures closer to zero. The FI of position measurement is a couple of orders of magnitude lower than the QFI [see the ratio $\mathcal{F}^{\text{POS}}(T)/\mathcal{Q}(T)$ in Fig. 4.7], and its maximum is at higher temperature than the maximum of the QFI.

For lattices with PBCs the behavior of the QFI is qualitatively the same as regards the goodness of the lower-temperature approximation (4.16) and the dependence of the QFI on the size of the lattice and the degree of the vertices. However, the maxima of QFI for lattices with PBCs are lower and occur at higher temperature than the maxima of QFI for lattices with OBCs. Remarkably, the FI for these lattices with PBCs is identically null.

Some analytical results can be obtained for the square lattice, both with OBCs and with PBCs. Indeed, the $m \times n$ square lattice with OBCs is actually a grid graph and is the Cartesian product of two path graphs, $G_{m,n} = P_m \square P_n$. Instead, the $m \times n$ square lattice with PBCs is actually the torus grid graph and is the Cartesian product of two cycle graphs, $T_{m,n} = C_m \square C_n$. For the Cartesian product $G_1 \square G_2$ of two graphs G_1 and G_2 we can analitically obtain the QFI and FI. To do so, we study the general properties of the cartesian product $G_1 \boxdot G_2$ of two graphs. If G_1 and G_2 are graphs on N_1 and N_2 vertices, respectively, then the Laplacian matrix of $G_1 \square G_2$ is

$$L(G_1 \boxdot G_2) = L(G_1) \otimes \mathbb{I}_{N_2} + \mathbb{I}_{N_1} \otimes L(G_2) \tag{4.57}$$

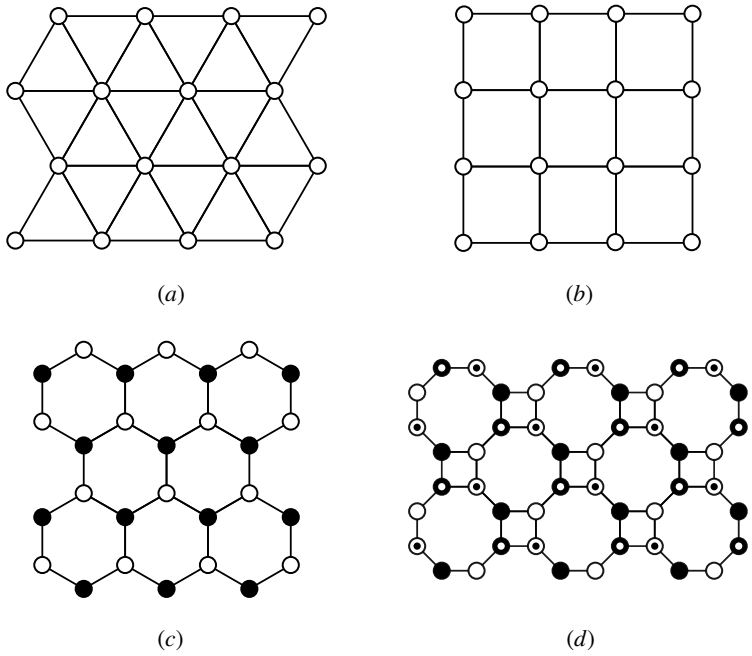

Figure 4.5: Two-dimensional lattices considered in the present work: (a) triangular, (b) square, (c) honeycomb, and (d) truncated square lattice. Equivalent vertices are equally represented.

where $\mathbb{I}_N$ denotes the $N \times N$ identity matrix. If $(E_1^{(1)}, \ldots, E_{N_1}^{(1)})$ and $(E_1^{(2)}, \ldots, E_{N_2}^{(2)})$ are the Laplacian spectra of G_1 and G_2, respectively, then the eigenvalues of $L(G_1 \square G_2)$ are

$$E_m^{(1)} + E_n^{(2)} \tag{4.58}$$

with $1 \leq m \leq N_1$ and $1 \leq n \leq N_2$. Moreover, if $|e_m^{(1)}\rangle$ is the eigenstate of $L(G_1)$ corresponding to $E_m^{(1)}$, and $|e_n^{(2)}\rangle$ the eigenstate of $L(G_2)$ corresponding to $E_n^{(2)}$, then

$$|e_m^{(1)}\rangle \otimes |e_n^{(2)}\rangle \tag{4.59}$$

is the eigenstate of $L(G_1 \square G_2)$ corresponding to $E_m^{(1)} + E_n^{(2)}$ [24].

Since the Laplacian matrix $L(G)$ is the Hamiltonian of a CTQW on the graph $G_1 \square G_2$, and according to the energy eigenvalues (4.58), the partition function is

$$Z(G_1 \boxdot G_2) = Z(G_1) Z(G_2) \tag{4.60}$$

where $Z(G_1)$ is the partition function for a CTQW on the graph G_1, and $Z(G_2)$ is the partition function for a CTQW on the graph G_2. It follows that the expectation value of the energy is

$$\langle \widehat{H}(G_1 \boxdot G_2) \rangle = \langle \widehat{H}(G_1) \rangle + \langle \widehat{H}(G_2) \rangle \tag{4.61}$$

Moreover

$$\langle \widehat{H}^2(G_1 \boxdot G_2) \rangle = \langle \widehat{H}^2(G_1) \rangle \langle \widehat{H}^2(G_2) \rangle + 2 \langle \widehat{H}(G_1) \rangle \langle \widehat{H}(G_2) \rangle \tag{4.62}$$

and the QFI follows directly from Eq. (4.4) as

$$Q(G_1 \boxdot G_2 | T) = Q(G_1 | T) + Q(G_2 | T). \tag{4.63}$$

is the sum of the two QFI evaluated on G_1 and G_2.

Regarding the FI for a position measurement, we have to consider that a position eigenstate in $G_1 \square G_2$ is $|j\rangle \otimes |k\rangle$. According to Eqs. (4.58)–(4.60), the Gibbs state is

$$\varrho_{\mathcal{P}}(T)(G_1 \boxdot G_2) = \varrho_{\mathcal{P}}(G_1) \otimes \varrho_{\mathcal{P}}(T)(G_2) \tag{4.64}$$

Then, the probability of finding the walker in (j,k) at a given temperature T is

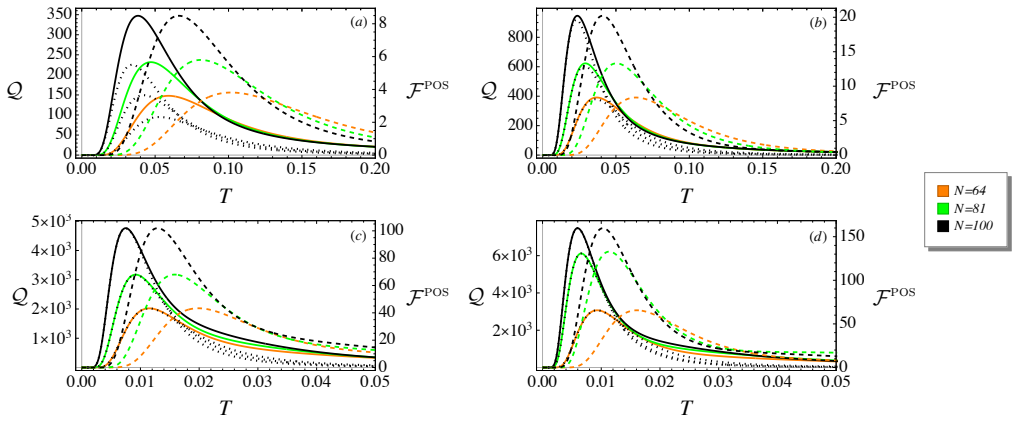

Figure 4.6: QFI and FI for position measurement for different $\sqrt{N} \times \sqrt{N}$ lattices with open boundary conditions (OBC): (a) Triangular lattice, (b) square lattice, (c) honeycomb lattice, and (d) truncated square lattice. Solid colored line: QFI $\mathcal{F}_q$. Dotted black line: QFI at low temperature $Q_{\rm LOW}$ (4.16). Dashed colored line: FI for position measurement $F^{\rm POS}$. Because of the different ranges, values of QFI are referred to the left y-axis, and values of FI are referred to the right y-axis.

$$p(j,k|T) = \mathrm{Tr}\left\{\varrho_{\mathcal{P}}(T)(G_1 \boxdot G_2)|j\rangle\langle j| \otimes |k\rangle\langle k|\right\} = \tag{4.65}$$

$$= \sum_{m=0}^{N_1-1} \frac{e^{-E_m^{(1)}/T}}{Z(G_1)} |\langle j|e_m^{(1)}\rangle|^2 \sum_{n=0}^{N_2-1} \frac{e^{-E_n^{(2)}/T}}{Z(G_2)} |\langle k|e_n^{(2)}\rangle|^2 = \tag{4.66}$$

$$= p_1(j|T)p_2(k|T) \tag{4.67}$$

where $p_1(j|T)$ is the probability of finding the walker in the vertex j of G_1, and, analogously, $p_2(k|T)$ is the probability of finding the walker in the vertex k of G_2. Notice that $\sum_j p_1(j|T) = \sum_k p_2(k|T) = 1$. Since

$$\partial_T p(j,k|T) = \partial_T p_1(j|T)p_2(k|T) + p_1(j|T)\partial_T p_2(k|T) \tag{4.68}$$

we find that the FI (4.14) is

$$\mathcal{F}^{\rm POS}(G_1 \boxdot G_2|T) = \sum_{j=0}^{N_1-1} \frac{(\partial_T p_1(j|T))^2}{p_1(j|T)} \sum_{k=0}^{N_2-1} p_2(k|T) + \tag{4.69}$$

$$+ \sum_{k=0}^{N_2-1} \frac{(\partial_T p_2(k|T))^2}{p_2(k|T)} \sum_{j=0}^{N_1-1} p_1(j|T) + \tag{4.70}$$

$$+ 2 \sum_{j=0}^{N_1-1} \partial_T p_1(j|T) \sum_{k=0}^{N_2-1} \partial_T p_2(k|T) \tag{4.71}$$

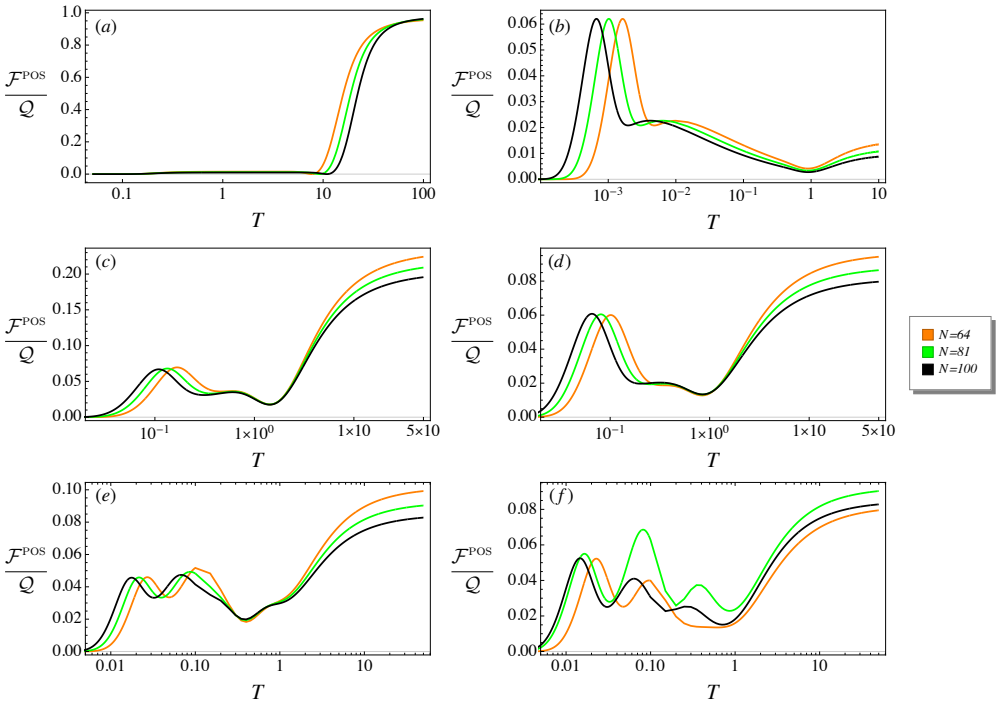

Figure 4.7: Ratio $\mathcal{F}_c/\mathcal{F}_q$ of FI and QFI for the graphs of order N and the $\sqrt{N} \times \sqrt{N}$ lattices providing non-null FI. (a) Star graph, (b) path graph, (c) triangular lattice (OBCs), (d) square lattice (OBCs), (e) honeycomb lattice (OBCs), and (f) truncated square (OBCs). Note the logarithmic scale of the temperature axis.

Given that $\sum_j \partial_T p_1(j|T) = \partial_T \sum_j p_1(j,T) = 0$ and analogously $\sum_k \partial_T p_2(k|T) = 0$, we obtain that

$$\mathcal{F}^{\text{POS}}(G_1 \boxdot G_2|T) = \mathcal{F}^{\text{POS}}(G_1|T) + \mathcal{F}^{\text{POS}}(G_2|T) \tag{4.72}$$

We conclude that also the FI of a position measurement is additive with respect to the cartesian product of graphs.

4.5.6.1 Grid graph and torus grid graph

In this section we offer some details to assess the QFI and the FI for the grid graph and torus grid graph in Table 4.1. In particular, we report the number of edges M and the sum of the degrees squared $\sum_k d_k^2$ required to compute the QFI (4.34) and the FI (4.37) in the high-temperature regime, as well as the energy level E_1 and its degeneracy g_1 required to compute the QFI (4.16) in the low-temperature regime.

The grid graph $G_{N,N} = P_N \square P_N$ is the Cartesian product of two path graphs P_N, and represents a $N \times N$ square lattice with OBCs. The total number of vertices is N^2, while the number of edges is $M = 2N(N-1)$. There are four vertices with degree 2 (the corners), $(N-2)$ vertices with degree 3 on each side of square lattice, and the remaining $N^2 - 4 - 4(N-2) = (N-2)^2$ vertices have degree 4. Hence $\sum_k d_k^2 = 4(4N^2 - 7N + 2)$. The path graph P_N has nondegenerate energies $E_0 = 0$ and $E_1 = 2[1 - \cos(\pi/N)]$. The

grid graph has exactly the same E_1 but with degeneracy $g_1 = 2$, since, according to Eq. (4.58), it results from the two possible combinations of E_0 and E_1 of the two P_N.

The torus grid graph $T_{N,N} = C_N \square C_N$ is the Cartesian product of two cycle graphs C_N, and represents a $N \times N$ square lattice with PBC. The total number of vertices is N^2, while the number of edges is $M = 2N^2$. It is 4-regular, hence $\sum_k d_k^2 = 16N^2$. The cycle graph C_N has nondegenerate energy $E_0 = 0$ and 2-degenerate energy $E_1 = 2[1 - \cos(2\pi/N)]$. The torus grid graph has exactly the same E_1 but with degeneracy $g_1 = 4$, since, according to Eq. (4.58), it results from the four possible combinations of E_0 and E_1 of the two C_N.

4.6 The role of coherences

Temperature is a classical parameter, i.e. any change in the temperature modifies the eigenvalues of the Gibbs state but not the eigenvectors, which coincide with the eigenvectors of the Hamiltonian at any temperature. As a consequence, one may wonder whether quantumness is playing any role in our analysis, which also does not rely upon quantum effects as entanglement. Despite the above arguments, the quantum nature of the systems under investigation indeed plays a role in determining topological effects in thermometry. In fact, thermal states (4.2) are diagonal in the Hamiltonian basis, but show quantum coherence in the position basis, which itself is the reference *classical basis* when looking at topological effects in graphs. In turn, as we will see in the following, the peak of the QFI occurs in the interval of temperatures over which the coherence starts to decrease.

In order to quantitatively assess the role of coherence, let us consider the l_1 norm of coherence [329]

$$\mathcal{C}[\varrho] = \sum_{j \neq k}^{N-1} |\rho_{jk}| \tag{4.73}$$

as a measure of quantum coherence of a state ρ. For convenience, we normalize this measure to its maximum value $\mathcal{C}(\rho_N) = N - 1$, thus defining $C(\rho) := \mathcal{C}(\rho)/(N-1)$. At $T = 0$, the system is at thermal equilibrium in its ground state and since the Hamiltonian of the system is the Laplacian of a simple graph, the ground state is the maximally coherent state $|\psi_N\rangle = \sum_{j=1}^{N} |j\rangle/\sqrt{N}$. The normalized coherence is thus equal to one.

As far as the temperature is very low, the ground state is robust, the coherence remains close to one, and the QFI is small, i.e. the robustness of the ground state prevents the system to effectively monitor any change in temperature. On the other hand, when temperature increases, thermal effects becomes more relevant, coherence decreases, and the QFI increases. In other words, it is the fragility of quantum coherence which makes the system a good sensor for temperature (a common feature in the field of *quantum probing*). For higher temperatures, the Gibbs state approaches a *flat* mixture, almost independent of temperature, and both the coherence and the QFI vanish. In order to illustrate the argument, let us consider the case of complete graphs, for which we have analytic expressions for the QFI, see Eq. (4.43), and for the normalized coherence

$$\mathcal{C}[\varrho_{\mathcal{P}}(T)] = \frac{|1 - e^{-N/T}|}{1 + (N-1)e^{-N/T}} \tag{4.74}$$

As it is clear from Fig. 4.8, where we show the two quantities, the peak of QFI indeed occurs in the interval of temperatures over which the coherence is reduced by a factor

Graph	Low-temperature	High-temperature		
	$T^4 Q_{\mathrm{LOW}}(T)$	$T^4 Q_{\mathrm{HIG}}(T)$	$T^4 F^{\mathrm{POS}}_{\mathrm{HIG}}(T)$	$F^{\mathrm{POS}}_{\mathrm{HIG}}(T)/Q_{\mathrm{HIG}}(T)$
K_N	$\frac{N^2(N-1)\exp(-N/T)}{[1+(N-1)\exp(-N/T)]^2}$	$N-1$	0	0
C_N	$\frac{32\exp[-4\sin^2(\pi/N)/T]\sin^4(\pi/N)}{\left(1+2\exp[-4\sin^2(\pi/N)/T]\right)^2}$	2	0	0
K_{N_1,N_2}	$\frac{\exp(-N_1/T)N_1^2(N_2-1)}{[1+(N_2-1)\exp(-N_1/T)]^2}$	$\frac{(N^2-\Delta^2)(\Delta^2+2N)}{4N^2}$	$\frac{(N^2-\Delta^2)\Delta^2}{4N^2}$	$\frac{1}{1+2N/\Delta^2}$
S_N	$\frac{(N-2)\exp(-1/T)}{[1+(N-2)\exp(-1/T)]^2}$	$\frac{(N-1)[N(N-2)+4]}{N^2}$	$\frac{(N-1)(N-2)^2}{N^2}$	$\frac{(N-2)^2}{N(N-2)+4}$
P_N	$\frac{16\exp[-4\sin^2(\pi/2N)/T]\sin^4(\pi/2N)}{\left(1+\exp[-4\sin^2(\pi/2N)/T]\right)^2}$	$\frac{2(N^2-2)}{N^2}$	$\frac{2(N-2)}{N^2}$	$\frac{N-2}{N^2-2}$
$G_{\sqrt{N},\sqrt{N}}$	$\frac{32\exp[-4\sin^2(\pi/2\sqrt{N})/T]\sin^4(\pi/2\sqrt{N})}{\left(1+2\exp[-4\sin^2(\pi/2\sqrt{N})/T]\right)^2}$	$\frac{4(N-2)}{N}$	$\frac{4(\sqrt{N}-2)}{N}$	$\frac{\sqrt{N}-2}{N-2}$
$T_{\sqrt{N},\sqrt{N}}$	$\frac{64\exp[-4\sin^2(\pi/\sqrt{N})/T]\sin^4(\pi/\sqrt{N})}{\left(1+4\exp[-4\sin^2(\pi/\sqrt{N})/T]\right)^2}$	4	0	0

Table 4.1: QFI $Q_{\text{LOW}}(T)$ (4.16) in the low-temperature regime and QFI $Q_{\text{HIG}}(T)$ (4.34), FI $F^{\text{POS}}_{\text{HIG}}(T)$ (4.37), and their ratio in the high-temperature regime for the graphs considered in the present work: complete graph K_N, cycle graph C_N, complete bipartite K_{N_1,N_2}, star graph S_N, and path graph P_N. Analytical results are also available for the $\sqrt{N} \times \sqrt{N}$ square lattice with OBC (grid graph $G_{\sqrt{N},\sqrt{N}}$) and with PBC (torus grid graph $T_{\sqrt{N},\sqrt{N}}$), since grid graph and torus grid graph are the Cartesian product of two path graphs and two cycle graphs respectively. To have a fair comparison in terms of the total number of vertices N, in the table we report the result for $\sqrt{N} \times \sqrt{N}$ square lattices, and for the complete bipartite graph K_{N_1,N_2} we write results as a function of $N = N_1 + N_2$ and $\Delta = N_2 - N_1$ ($N_2 \geq N_1$ as already assumed in the main text), except for the QFI in the low-temperature regime. The FI $F^{\text{POS}}_{\text{LOW}}(T)$ in the low-temperature regime is not reported, because an expression suitable for a comparison is not available, see Eq. (4.24). Both QFI and FI in the high-temperature regime depend on the temperature as T^{-4}, thus we report their values multiplied by T^4 to focus on the factor which depends on the topology of the graph. The same criterion is adopted for the QFI in the low-temperature regime for consistency. Numerical results show that graphs with low degree, e.g. C_N and P_N, exhibit the highest maxima of the QFI at low temperatures. Conversely, at high temperatures and at fixed N, the maximum QFI is obtained with the complete and the star graph, whose QFI scales linearly with the order N. Indeed, in the limit of $N \to \infty$, the QFI of P_N approaches that of C_N, as well as the QFI of $G_{\sqrt{N},\sqrt{N}}$ approaches that of $T_{\sqrt{N},\sqrt{N}}$.

$1/e$ (we have numerically observed analogous behavior also for the other graphs). Upon comparison of Eq. (4.43) with Eq. (4.74) we may also write

$$\frac{T^4 \mathcal{Q}(T)}{N-1} = (1 - \mathcal{C}[\varrho_{\mathcal{P}}(T)])\,(1 + (N-1)\mathcal{C}[\varrho_{\mathcal{P}}(T)])\,. \tag{4.75}$$

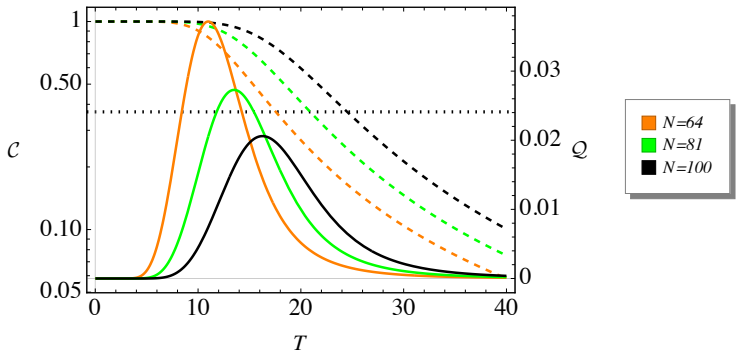

Figure 4.8: QFI $\mathcal{F}_q$ (solid line) and normalized coherence C (dashed line) of a Gibbs state ρ_T as a function of T for a complete graph of order N. The black horizontal dotted line represents the constant value $1/e$.

4.7 Conclusions

In this chapter we have studied the role of topology in determining the precision of thermometers. The key idea is to use a finite system as a probe for estimating the temperature T of an external environment. The probe is regarded as a connected set of subunits

and may be ultimately modeled as a quantum walker moving continuously in time on a graph.

In particular, we have considered equilibrium thermometry, and evaluated the quantum Fisher information for temperature parameter for a Gibbs state of the walker. Since the Hamiltonian of a quantum walker corresponds to the Laplacian matrix of the graph, the topology is inherently taken into account. We have considered some paradigmatic graphs and two-dimensional lattices, evaluated the Fisher information (FI) for a position measurement and compared it with the quantum Fisher information (QFI, energy measurement), providing analytical and numerical results on the performances in the different cases. In particular, we have focused on the low- and high-temperature regimes, which we have investigated by means of analytic approximations.

We have drawn several conclusions from the analytical and numerical results on the role of topology in the estimation of T. First, We have proved that the maximum of the QFI and the corresponding optimal temperature depend on three topological parameters of the graph: the algebraic connectivity E_1, and the degeneracy of the first energy level g_1, and the number of edges M. In our system, the algebraic connectivity also represents the energy gap between the first excited energy level and the ground state. In particular, we found that *the smaller is the algebraic connectivity, the higher is the maximum of the QFI*. These results are supported by a number of examples. In particular, graphs and lattices whose vertices have low degree, e.g. path and cycle graphs, as well as honeycomb and truncated square lattices, show the highest maxima of QFI. We also notice that the maximum of the QFI and the corresponding optimal T decrease as N increase in the complete graph, while in all the other cases we observe the opposite behavior.

At intermediate temperatures, the analytical approximation we have at low temperatures is no longer valid, as shown by the discrepancy between the dotted lines (analytical approximation) and the solid lines (exact results) in Figs. 4.3–4.4, and 4.6). However, the low-temperature approximation captures quite well the maximum of the QFI, after which the QFI decreases, tending to zero, as the temperature increases. This behavior is confirmed by the exact analytical expressions of the QFI we have for the complete graph, Eq. (4.43), the complete bipartite graph. We also have numerical evidence of it for the other graphs and lattices. Hence, no relevant structures of the QFI are expected at intermediate temperatures.

At high temperatures the QFI is of order $O(T^{-4})$, with a proportionality constant which depends on the topology of the graph. In this regime, the maximum QFI is attained by the complete graph, which is the simple graph that, at given number of vertices N, has the highest number of edges M. A remarkable thermometer is also obtained considering the complete bipartite graph. Despite its low QFI (if compared with the cycle and path graphs) it is possible to tune the position of the maximum of QFI just by varying the number of vertices in the two partite sets of the graph while keeping fixed their sum.

Finally, we have discussed the role of coherences in the position basis in determining the precision. Our results provides some general indications on the role of topology in using quantum probes for thermometry, and provide new insights in the thermometry of finite-size quantum systems at equilibrium, at least for the class of systems where the Hamiltonian is in the form of a Laplacian matrix. In particular, our results suggest that quantum probes are particularly efficient in the low-temperatures regime, where the QFI reaches its maximum. They also pave the way to investigate the role of topology in out-of-equilibrium thermometry.

CHAPTER 5

Discrimination of Ohmic thermal baths by quantum dephasing probes

Direct measure of the temperature is not possible, as already observed in the introduction of this part of the thesis. For this very reason, direct measurement of temperature is not available, and one should resort to indirect measurement procedures. During the last decade, quantum thermometric strategies have emerged, which are mostly based on using external quantum probes interacting with the system under investigation, with the assumption that the interaction between the probe and the system does not change the temperature of the latter. Those strategies are usually termed quantum probing schemes and are not based on the zeroth principle, but rather on the engineering of the interaction Hamiltonian, which is exploited to imprint the temperature of the system on the quantum state of the probe. As a matter of fact, *quantum probing exploits the inherent fragility of quantum systems* against decoherence, turning it into a *resource* to realize highly sensitive metrological schemes.

In this chapter of the thesis, we address the discrimination of structured baths at different temperatures by dephasing quantum probes. We derive the exact reduced dynamics and evaluate the minimum error probability achievable by three different kinds of quantum probes, namely, a qubit, a qutrit, and a quantum register made of two qubits. Our results indicate that dephasing quantum probes are useful in discriminating low values of temperature and that lower probabilities of error are achieved for intermediate values of the interaction time, where the minimum probability of error scales as $1/(2N)$, with N the number of energy levels of the probe.

The chapter is organized as follows. In Sec. 5.1, we first review temperature discrimination at equilibrium with a finite-dimensional probe, establishing our benchmark for the out-of-equilibrium scenario. In Sec. 5.2 we study in general the discrimination performances of out-of-equilibrium probes, whereas in Sec. 5.3 we introduce the main model of pure dephasing, and we provide the derivation of the exact dynamical solution in Appendix 10. In Sec. 5.4 we finally apply the tools of discrimination theory introduced in Chapter 2.1 to study the performances of our dephasing probe and compare it with the equilibrium one. We do this for different finite dimensional systems and using different resources: coherence and entanglement. The chapter concludes with Sec. 5.5, where we summarize the results and provide future perspectives.

5.1 Thermometry discrimination at thermal equilibrium

As a first step, we address the distinguishability problem of two finite dimensional probe of dimension N that have thermalized at the two possible temperature β_1 or β_2 [153]. Throughout the chapter, we consider an unbiased case where the two hypothesis are

equiprobable ($p_1 = p_2 = 1/2$ according to the notation in Chapter 2.1). The probe system $\mathcal{P}$ is governed by a certain hamiltonian $\widehat{H} = \sum_{n=0}^{N-1} E_n |e_n\rangle\langle e_n|$, and the equilibrium state of the probe is given by the Gibbs state

$$\varrho_{eq}(\beta) = \frac{1}{Z(\beta)} \sum_{n=0}^{N-1} e^{-\beta E_n} |e_n\rangle\langle e_n|, \tag{5.1}$$

where $Z(\beta) = \sum_{n=0}^{N-1} e^{-\beta E_n}$ is the partition function.

The Gibbs states we want to discriminate $\varrho_{eq}(\beta_1)$ and $\varrho_{eq}(\beta_2)$ are a full-rank density operators, and we know that they cannot be unambiguously discriminated. Hence, the minimum error probability is given by Eq. (2.18) and in our case is equal to

$$p^{\text{ERR}}_{eq;N}(\beta_1, \beta_2) = \frac{1}{2}\left(1 - \frac{1}{2}\sum_{n=0}^{N-1}\left|\frac{e^{-\beta_1 E_n}}{Z(\beta_1)} - \frac{e^{-\beta_2 E_n}}{Z(\beta_2)}\right|\right) \tag{5.2}$$

In the binary discrimination problem, the optimal measurement that attain the minimum-error in Eq. (5.2) is well known and it is obtained from the operator Λ in Eq. (2.8), that in our case becomes

$$\Lambda = \sum_{n=0}^{N-1} \lambda_n |e_n\rangle\langle e_n| = \frac{1}{2}\sum_{n=0}^{N-1}\left(\frac{e^{-\beta_2 E_n}}{Z(\beta_2)} - \frac{e^{-\beta_1 E_n}}{Z(\beta_1)}\right)|e_n\rangle\langle e_n| \tag{5.3}$$

The optimal discrimination strategy depends on the sign of the eigenvalues of Λ. Without loss of generality we can assume $\beta_1 > \beta_2$. In this case, $Z(\beta_2) > Z(\beta_1)$, which means that there exist a number $d \geq 2$ (that depends on β_1, β_2 and on the full shape of the energy spectrum $\{E_n\}_{n=0}^{N-1}$) such that $\lambda_n \leq 0$ for $n < d$. This means that the two detection operators are given by

$$\Pi_1 = \sum_{\lambda_n \leq 0} |e_n\rangle\langle e_n| = \sum_{n=0}^{d-1} |e_n\rangle\langle e_n| \tag{5.4}$$

$$\Pi_2 = \sum_{\lambda_n > 0} |e_n\rangle\langle e_n| = \sum_{n=d}^{N-1} |e_n\rangle\langle e_n| \tag{5.5}$$

From these operators, we see that the optimal discrimination is to accept the first hypothesis β_1 if we detect one of the first d energy level E_n, whereas we accept the second hypothesis β_2 if we detect one of the last $N - d$ energy level E_n.

Result 6: Optimal strategy for equilibrium discrimination

The optimal strategy in an equilibrium discrimination problem consists of an energy measurement of the probe $\mathcal{P}$: if the outcomes belongs to $\{E_n\}_{n=0}^{d-1}$ we accept the first hypothesis, otherwise the second.

The expressions simplifies for a bunch of special cases. For instance, if the probe $\mathcal{P}$ is a qubit with spacing ω_0, i.e. $E_0 = -\omega_0/2$ and $E_1 = \omega_0/2$, we have that

$$p^{\text{ERR}}_{eq;2}(\beta_1, \beta_2) = \frac{1}{2}\left(1 - \frac{1}{2}\left|\tanh\left(\frac{\omega_0\beta_2}{2}\right) - \tanh\left(\frac{\omega_0\beta_1}{2}\right)\right|\right) \tag{5.6}$$

Moreover, some limiting case are also interesting. If the smaller temperature vanishes $T_1 = 0$ ($\beta_1 \to +\infty$), then the first hypothesis corresponds to the ground state $|e_0\rangle\langle e_0|$, and the probability of error (5.2) becomes

$$p^{\mathrm{ERR}}_{eq;N}(+\infty, \beta_2) = \frac{1}{2}\left(1 - \frac{1}{2}\left(1 - \frac{e^{-\beta_2 E_0}}{Z(\beta_2)} + \sum_{n=1}^{N-1} \frac{e^{-\beta_2 E_n}}{Z(\beta_2)}\right)\right) \tag{5.7}$$

$$= \frac{1}{2}\left(1 - \left(1 - \frac{e^{-\beta_2 E_0}}{Z(\beta_2)}\right)\right) = \tag{5.8}$$

$$= \frac{1}{2}\frac{e^{-\beta_2 E_0}}{Z(\beta_2)} \tag{5.9}$$

In this case the corresponding strategy is quite natural: the first detection operator Π_1 is just the ground state, since the only negative eigenvalue is the first.

In the rest of the chapter and all the subsequent plots, we have set the value of ω_0 to 3.5 kHz, which corresponds to a realistic experimental situation of a quantum probe [51].

5.2 Out-of-equilibrium thermometry discrimination

So far we have reviewed the limits of equilibrium discrimination. As we have seen in the introduction, this is not the only available choice: out-of-equilibrium probes encodes some information on the temperature that can be suitable extracted. In this paradigm, the probe $\mathcal{P}$ is an open quantum system that interacts with the bath at equilibrium at one of the two temperatures T_1 or T_2. The whole dynamics is described by the total Hamiltonian $\widehat{H}_T = \widehat{H}_\mathcal{P} + \widehat{H}_\mathcal{B} + \widehat{H}_I$, where $\widehat{H}_\mathcal{P}$ is the Hamiltonian of the probe, $\widehat{H}_\mathcal{B}$ is the Hamiltonian of the thermal bath and $\widehat{H}_I$ describes how the two systems interact.

Before discussing the results for the specific model of the pure dephasing, we explore some general results regarding an out-of-equilibrium discrimination problem. The general setting is that we prepare the probe in some initial state $\varrho_\mathcal{P}(0) = \varrho_\mathcal{P}$, while the thermal bath is at equilibrium with respect to a certain temperature β_k, $k = 1, 2$. The evolution of the probe is determined by a completely positive and trace-preserving map (CPTP) Φ^k_t, also known as quantum channel in Chapter 1.1, that depends on the temperature β_k and can be written as

$$\varrho^k_\mathcal{P}(t) = \Phi^k_t[\varrho_\mathcal{P}] = \mathrm{Tr}_\mathcal{B}\left\{\widehat{U}(t)(\varrho_\mathcal{P} \otimes \varrho_{eq}(\beta_k))\widehat{U}(t)^\dagger\right\} \tag{5.10}$$

where $\widehat{U}(t)$ is the unitary evolution generated by the full Hamiltonian H_T. In other words, the two hypothesis define two distinct CPTP maps and the discrimination problems turns out to be a discrimination of CPTP maps. We know that the probability of error depends on the trace distance

$$D(\varrho_1, \varrho_2) = \frac{1}{2}\|\varrho_2 - \varrho_1\|, \tag{5.11}$$

and the trace distance is contractive under the action of trace preserving operation [257]. Since the partial trace is a trace preserving operation, we can write

$$D(\varrho^1_\mathcal{P}(t), \varrho^2_\mathcal{P}(t)) \leq D(\widehat{U}(t)(\varrho_\mathcal{P} \otimes \varrho_{eq}(\beta_1))\widehat{U}(t)^\dagger, \widehat{U}(t)(\varrho_\mathcal{P} \otimes \varrho_{eq}(\beta_2))\widehat{U}(t)^\dagger) \tag{5.12}$$

Now we can exploit another property of the trace distance, i.e. the invariance under unitary operation, that yields us to

$$D(\varrho^1_{\mathcal{P}}(t), \varrho^2_{\mathcal{P}}(t)) \leq D(\varrho_{\mathcal{P}} \otimes \varrho_{eq}(\beta_1), \varrho_{\mathcal{P}} \otimes \varrho_{eq}(\beta_2)) \tag{5.13}$$

Using the additivity with respect to the tensor product, we obtain that

$$D(\varrho^1_{\mathcal{P}}(t), \varrho^2_{\mathcal{P}}(t)) \leq D(\varrho_{eq}(\beta_1), \varrho_{eq}(\beta_2)) \tag{5.14}$$

Finally, we obtain a lower bound for the probability of error for an out-of-equilibrium probe, i.e.

$$p^{\text{ERR}}_{oeq}(\beta_1, \beta_2) \geq \frac{1}{2}\left(1 - D(\varrho_{eq}(\beta_1), \varrho_{eq}(\beta_2))\right) \tag{5.15}$$

We stress that this result is true for every discrimination problem where the quantum channel is determined by the initial state of the ancillary system that is traced out.

This bound depends only on the Hamiltonian of the bath $\mathcal{B}$ and on the two temperatures to be discriminated. This bound may be useful in dealing with a finite-size environment, whereas in the thermodynamical limit the $D(\varrho_{eq}(\beta_1), \varrho_{eq}(\beta_2))$ is likely to vanish.

Although it may seem that probing the full system is the optimal way, since the probability out of equilibrium is lower bounded by the probability of discriminating directly the two equilibrium states, this might not be the most feasible approach. For instance, when the temperatures are low, probing directly the temperature could be extremely invasive. At the same time, this lower bound is achieved with an energy measurement. However, for large or infinite dimensional systems, such a projective measurement is not easily implementable. For these reasons, the use of out-of-equilibrium probes can be helpful, providing an alternative way to indirectly discriminate the two temperatures.

5.3 An exactly solvable pure dephasing model

The probe-bath interaction we are going to study is the pure dephasing model, first introduced to account decoherence in a quantum computer [59, 261]. This model is quite relevant since the closed unitary dynamics is exactly solvable and allows a clear analysis of the mechanism of entanglement between qubit and environment. All the mathematical details regarding the derivation of the unitary evolution are provided in Appendix 10. Here, we briefly discuss the physical model and go directly to the final expression for the unitary $\widehat{U}(t)$.

We consider a general N dimensional quantum probes whose Hamiltonian is

$$\widehat{H}_{\mathcal{P}} = \sum_{n=0}^{N-1} E_n |e_n\rangle\langle e_n| \tag{5.16}$$

We can also isolate the energy scale with respect to the scaling defining $\delta_n = 2E_n/\omega_0$ and introducing an adimensional diagonal matrix $\widehat{H}^{(\eta)}_{\mathcal{P}} = \sum_{n=0}^{N-1} \delta_n |e_n\rangle\langle e_n|$, such that

$$\widehat{H}_{\mathcal{P}} = \frac{\omega_0}{2} \widehat{H}^{(\eta)}_{\mathcal{P}} \tag{5.17}$$

With this diagonal matrix $\widehat{H}^{(\eta)}_{\mathcal{P}}$ we can describe both single partite system with N energy levels, such as a qubit $\widehat{H}^{(2)} = \widehat{\sigma}_z$, as well as a quantum register of two qubits $\widehat{H}^{(2,2)} =$

$(\widehat{\sigma}_z \otimes \widehat{\mathbb{I}}_2 + \widehat{\mathbb{I}}_2 \otimes \widehat{\sigma}_z)$. For this reason, we understand the index η, where appropriate, as a multi-index $\eta = (N_1, N_2)$ with each index N_1 and N_2 associated respectively with dimension of the first and the second qubit, for instance.

The thermal reservoir is described by a continuous set of Bosonic modes $\widehat{H}_{\mathcal{B}} = \sum_{\boldsymbol{k}} \omega_{\boldsymbol{k}} \widehat{a}^\dagger_{\boldsymbol{k}} \widehat{a}_{\boldsymbol{k}}$, where $\omega_{\boldsymbol{k}}$, $\widehat{a}_{\boldsymbol{k}}$, and $\widehat{a}^\dagger_{\boldsymbol{k}}$ are respectively the frequency, the annihilation, and the creation operator of the of the $\boldsymbol{k}$th bosonic mode. The pure dephasing interaction is given by

$$\widehat{H}_I = \widehat{H}^{(\eta)}_{\mathcal{P}} \otimes \sum_{\boldsymbol{k}} \left(g_{\boldsymbol{k}} \widehat{a}^\dagger_{\boldsymbol{k}} + g^*_{\boldsymbol{k}} \widehat{a}_{\boldsymbol{k}} \right), \tag{5.18}$$

where $g_{\boldsymbol{k}}$ are the coupling constants. We see that each energy level interacts with the same coupling constant $g_{\boldsymbol{k}}$, namely they all feel the same local environment. This is justified by the assumption that the system is small compared to the size of the reservoir and a collective interaction is a good approximation. This also means that, in the case of a multipartite system, this Hamiltonian $\widehat{H}_I$ models an evolution in which each partition interacts locally with the same Bosonic modes.

This $\widehat{H}_I$ is an example of a spin-boson model, where we have used the adimensional matrix $\widehat{H}^{(\eta)}_{\mathcal{P}}$ in such a way that $[\widehat{H}_{\mathcal{P}}, \widehat{H}_I] = 0$. The latter condition exactly characterizes a model of pure dephasing. In fact, during the evolution the population of the $\mathcal{P}$ are constant, i.e. the probe does not change energy during the dynamics. Conversely, the interaction just affect the off-diagonal elements of $\varrho_{\mathcal{P}}(t)$, i.e. coherences in the energy basis are suppressed. As we already mentioned, this model is exactly solvable for the full closed system $\mathcal{P} + \mathcal{B}$, and the exact derivation is given in Appendix 10. The CPTP that describe the evolution of the probe only is given by

$$\Phi^\beta_t[\bullet] = \mathcal{V}^\beta(t) \circ \mathcal{R}(t) \circ \bullet \tag{5.19}$$

where the $\circ$ is the Hadamard product (entrywise product), while $\mathcal{V}^\beta(t)$ and $\mathcal{R}(t)$ are $N \times N$ matrices. We stress that this evolution is given in the interaction picture. The first depends on the temperature

$$\mathcal{V}^\beta(t) = \sum_{j,l=0}^{N-1} e^{\frac{(\delta_j - \delta_l)^2}{4} \Gamma(t|\beta)} |e_j\rangle\langle e_l|, \tag{5.20}$$

and depends on the function $\Gamma(t|\beta)$, also known as the decoherence function, defined as

$$\Gamma(t|\beta) = -4 \sum_{\boldsymbol{k}} \frac{|g_{\boldsymbol{k}}|^2}{\omega^2_{\boldsymbol{k}}} \left(1 - \cos(\omega_{\boldsymbol{k}})\right) \coth\left(\frac{\omega_{\boldsymbol{k}} \beta}{2}\right) \tag{5.21}$$

This encodes the rate of the damping due to the interaction and it is the one that depends on the temperature. Different temperatures yields different damping, and this is exactly the mechanism that allow us to distinguish between the two hypothesis.

The second contribution to the dynamics affects only the coherences between the energy levels and is a temperature independent contribution to the dynamics

$$\mathcal{R}(t) = \sum_{j,l=0}^{N-1} e^{i\xi(t) \frac{\delta_j^2 - \delta_l^2}{4}} |e_j\rangle\langle e_l|., \tag{5.22}$$

where the function $\xi(t)$ is given by

$$\xi(t) = -4 \sum_{\boldsymbol{k}} \frac{|g_{\boldsymbol{k}}|^2}{\omega_{\boldsymbol{k}}^2} \left(\omega_{\boldsymbol{k}} t - \sin(\omega_{\boldsymbol{k}} t)\right), \tag{5.23}$$

Being a temperature-independent phase function, it is the same for the two hypothesis and does not contribute to the probability of error. We notice also that for a qubit, this is the identity matrix $\mathbb{I}_2$.

In the continuous limit of the Bosonic modes, we replace $\sum_{\boldsymbol{k}}$ with $\int d\omega f(\omega)$, where $f(\omega)$ is the density of the modes at frequency ω (henceforth we neglect the index $\boldsymbol{k}$), while the absolute value of the coupling constants $|g_{\boldsymbol{k}}|^2$ is replaced with a function of the frequencies $|g(\omega)|^2$. In this limit, we also define the spectral density as $J(\omega) = 4f(\omega)|g(\omega)|^2$. In this way the decoherence and the phase function reads as

$$\Gamma(t|\beta) = -\int_0^{+\infty} d\omega J(\omega) \coth\left(\frac{\omega\beta}{2}\right) \frac{1-\cos(\omega t)}{\omega^2} \tag{5.24}$$

$$\xi(t) = -\int_0^{+\infty} d\omega J(\omega) \frac{\omega t - \sin(\omega t)}{\omega^2} \tag{5.25}$$

Furthermore, we can split the decoherence function in two contribution

$$\Gamma(t|\beta) = -\int_0^{+\infty} d\omega J(\omega) 2\langle n(\omega)\rangle_\beta \frac{1-\cos(\omega t)}{\omega^2} - \int_0^{+\infty} d\omega J(\omega) \frac{1-\cos(\omega t)}{\omega^2} \tag{5.26}$$

with the average number excitations at frequency ω and temperature β given by

$$\langle n(\omega)\rangle_\beta = \exp\left(-\frac{\omega\beta}{2}\right) \operatorname{cosech}\left(\frac{\omega\beta}{2}\right) \tag{5.27}$$

The first addendum in (5.26) is the contribution from the thermal noise and is temperature dependent, whereas the second is a vacuum quantum contribution to the dephasing, since it is present even in the case of a 0 temperature reservoir. The contribution due to this term is relevant only for $t < T^{-1}$, where the coherence loss are caused by quantum vacuum fluctuations. Instead for $t > T^{-1}$, the thermal contributions are larger.

In general, the spectral density $J(\omega)$ is characterized by a cut-off frequency which depends on the physical structure of the interaction between the probe and the thermal reservoir, and on the number of dimensions of the field. This can be modeled by an Ohmic-like spectral density

$$J_s(\omega|\omega_c) = \omega_c \left(\frac{\omega}{\omega_c}\right)^s e^{-\frac{\omega}{\omega_c}} \tag{5.28}$$

where s is the Ohmicity and ω_c is the cut-off frequency. The first in general depends on the dimensions of the field, i.e. on the density of state $f(\omega)$, while ω_c is related to the environmental correlation time. In general in the case of quantum-optical systems, $g(\omega) \propto \sqrt{\omega}$, while $G(\omega)$ can be constant for one-dimensional field or $G(\omega) \propto \omega^2$ for three-dimensional field [261]. In the first case $s = 1$ (Ohmic environment), while in the second $s = 3$ (superohmic environment). In the following analysis, we will consider generic values of ω_c and s, keeping in mind that these two particular values of s have a special physical relevance.

To conclude this section, we explicitly write the density matrix of the probe at time t in the interaction picture, highlighting its dependence on the hypothesis β_k

$$\varrho_{\mathcal{P}}^{k}(t) = \sum_{j,l=0}^{N-1} \langle e_j|\varrho_{\mathcal{P}}|e_l\rangle e^{i\xi(t)\frac{\delta_j^2-\delta_l^2}{4}} e^{\frac{(\delta_j-\delta_l)^2}{4}\Gamma(t|\beta_k)} |e_j\rangle\langle e_l|, \tag{5.29}$$

which will be the starting point of the following sections, where we present numerical results regarding our discrimination task.

5.4 Thermometry discrimination with pure dephasing probes

In this section, we study different systems with different dimensions that can be used as quantum probes for our task. We start with a qubit, then we consider a qutrit and a qudit. Eventually, we also consider a multipartite systems, also referred to as a quantum register.

5.4.1 Qubit probe

The qubit probe is given by $\widehat{H}_{\mathcal{P}}^{(2)} = \widehat{\sigma}_z$, or equivalently by $\delta_0 = -1$ and $\delta_1 = +1$ in our notation, with $|e_0\rangle \to |0\rangle$ and $|e_1\rangle \to |1\rangle$. As we have already noticed, for the special cose of the qubit $\mathcal{R}(t)$ is equal to I, and we eventually obtain that

$$\varrho_{\mathcal{P}}^{k}(t) = \begin{pmatrix} 1 & e^{\Gamma(t|\beta^k)} \\ e^{\Gamma(t|\beta_k)} & 1 \end{pmatrix} \circ \varrho_{\mathcal{P}} \tag{5.30}$$

We can easily evaluate the Λ operator in Eq. (2.8) as

$$\Lambda = \begin{pmatrix} 0 & \langle 1|\varrho_{\mathcal{P}}|0\rangle \\ \langle 0|\varrho_{\mathcal{P}}|1\rangle & 0 \end{pmatrix} \frac{e^{\Gamma(t|\beta_2)} - e^{\Gamma(t|\beta_1)}}{2} \tag{5.31}$$

The eigenvalues of Λ determines the probability of error, which is given by

$$p_{oeq}^{\text{ERR}}(\beta_1,\beta_2) = \frac{1}{2}\left(1 - \left|\langle 1|\varrho_{\mathcal{P}}|0\rangle \left(e^{\Gamma(t|\beta_2)} - e^{\Gamma(t|\beta_1)}\right)\right|\right) \tag{5.32}$$

This does not depend on the initial population of the energy levels and on the frequency ω_0 of the qubit, while just on the absolute value of the coherences $|\langle 1|\varrho_{\mathcal{P}}|0\rangle|$ between the two. This means that the optimal probe is the maximal coherent state $\varrho_{\mathcal{P}} = |\pm_2\rangle\langle\pm_2|$, where $|\pm_2\rangle = 1/\sqrt{2}(|0\rangle \pm |1\rangle)$.

We can also interpret this result in terms of the l_1 norm of coherence [329]

$$\mathcal{C}[\varrho] = \sum_{i\neq j} |\langle i|\varrho|j\rangle| \tag{5.33}$$

which in this case reads as

$$\mathcal{C}[\varrho_{\mathcal{P}}^{k}(t)] = 2|\langle 1|\varrho_{\mathcal{P}}|0\rangle| e^{\Gamma(t|\beta_k)} \tag{5.34}$$

In this way we can write the probability of error in Eq. (5.32) as

$$p_{oeq}^{\text{ERR}}(\beta_1,\beta_2) = \frac{1}{2}\left(1 - |\mathcal{C}[\varrho_{\mathcal{P}}^{2}(t)] - \mathcal{C}[\varrho_{\mathcal{P}}^{1}(t)]|\right) \tag{5.35}$$

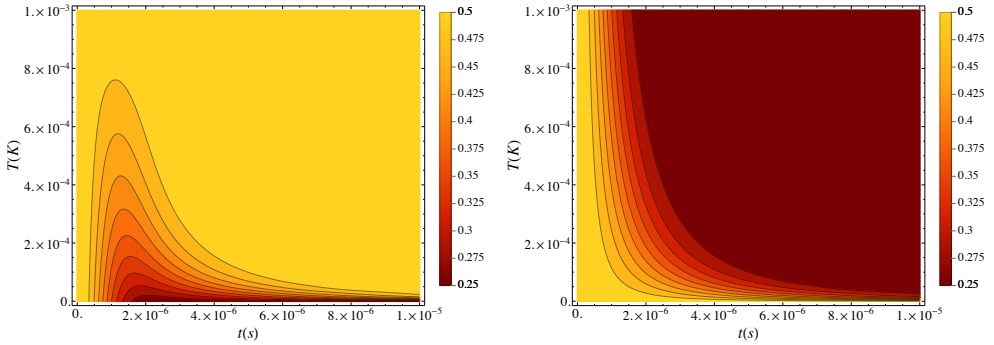

Figure 5.1: Probability of error $p_{oeq}^{\text{ERR}}(\beta_1, \beta_2)$ as a function of time and T_2 for a qubit (5.32) initially prepared in a maximally coherent state. Left panel: $T_1 = 1$ mK; right panel: $T_1 = 0$. We fixed $\omega_c = 7$ kHz and $s = 1$.

Better discrimination is obtained in the time-regime in which the difference between the coherences is larger. This is the main reason why maximally coherent states are optimal states, since they are more sensible to decoherence, which is the sole effect of the pure dephasing model.

Instead, the eigenvector of Λ determines the optimal measurement. Choosing the optimal initial state as $|+\rangle$ (the case with $|-\rangle$ is analogous but with a reversed role of the two detectors), we see that the optimal POVM saturating the Helstrom bound is given by

$$\Pi_1 = \frac{1}{2}\left(\mathbb{I}_2 + \sigma_x\right) \tag{5.36}$$

$$\Pi_2 = \frac{1}{2}\left(\mathbb{I}_2 - \sigma_x\right) \tag{5.37}$$

This is a measurement of the spin along the x axis, and remarkably does not depend niether on the two temperatures β_1 and β_2 nor in general on the structure of the thermal bath, i.e. the Ohmicity paramter s or the cut-off frequency ω_c. Not surprisingly, this is also the optimal measurement for the estimating temperature again in a pure dephasing probe [287].

Result 7: Optimal strategy for out-of-equilibrium qubit discrimination

The optimal qubit preparation is the maximally coherent state, to which correspond the optimal strategy of measuring the qubit observable σ_x. The key quantum resource is the coherence of the energy levels, quantified by the l_1 norm of coherence.

In order to understand the role of time, we numerically evaluate the probability of error in Eq. (5.32) for an Ohmic environment $s = 1$ with cut-off frequency $\omega_c = 7$ kHz and we report the results in Fig. 5.1. In the left panel of Fig. 5.1, we fix one of the two temperature to a finite value $T_1 = 1$ mK, and we plot p_{oeq}^{ERR} as a function of t and T_2. We see that there is an optimal time $t_{opt}(T_1, T_2)$, that depends on both temperatures, which minimize the overall value of p_{oeq}^{ERR}. Furthermore, the minimum values of p_{oeq}^{ERR} are obtained when T_2 is smaller than the fixed value of T_1, as one would expect.

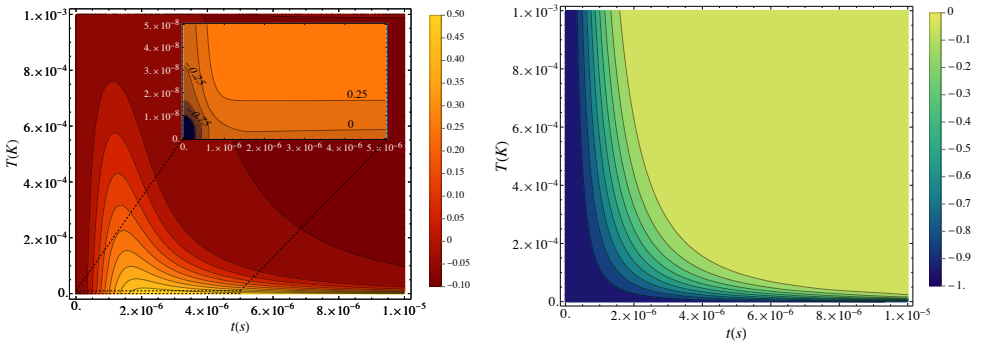

Figure 5.2: Gain factor η for the equilibrium vs out-of-equilibrium qubit prepared in a maximally coherent state given in Eq. (5.38). We report the result as a function of time t and the second temperature T_2, while we fix $T_1 = 1$ mK (left panel), and $T_1 = 0$K (right panel). We set $\omega_c = 7kHz$ and $s = 1$.

Instead, in the right panel of Fig. 5.1, we consider the case in which $T_1 = 0$ K. Here, for times of order 10^{-5} s, we see that there is a large optimal time interval, i.e. the darker red area where the p_{oeq}^{ERR} reaches the minimum. The main reason is that the decoherence function of the probe undergoing dephasing with the reservoir at zero-temperature does not feel the temperature-dependent term in Eq. (5.26), but only the loss due to the quantum vacuum fluctuations. As already discussed, quantum vacuum fluctuations are dominant in the early stage of the dephasing, but are temperature independent. Hence, the probe feel the same dephasing independently of the reservoir at temperature T_1 or T_2 for earlier times and the two hypothesis are indistinguishable. On the other side, when thermal fluctuations becomes dominant, the loss of coherences when the probe interacts with $T_2 \neq 0$ significantly deviate from the loss only due to quantum vacuum fluctuations, i.e. when $T_1 = 0$. As a result, the probe undergoes a significantly different dynamics during the thermal regime and hence the probability of error achieve its minimum.[1]

The results discussed above are qualitatively similar to the cases with $s \neq 1$, in which numerical results show just that the optimal time decreases. The same effect occurs for smaller cut-off frequency ω_c.

After having studied the performances of the out-of-equilibrium probe, it is particularly relevant to compare them with the discrimination performance of the equilibrium one. To have a faithful comparison, we define the gain factor

$$\eta(T_1, T_2) = 1 - \frac{p_{eq}^{\text{ERR}}(\beta_1, \beta_2)}{p_{oeq}^{\text{ERR}}(\beta_1, \beta_2)}. \tag{5.38}$$

Positive values of $\eta(T_1, T_2)$ indicate regions of parameters where the the out-of-equilibrium probe is better in the discrimination task and hence is preferable, whereas negative values indicate when the equilibrium outperforms the out-of-equilibrium. Usually, in the early time of the pure dephasing evolution the information about the temperature has not be transferred yet to the probe and hence its discrimination performances are poor. For this reasons we are more interested in the gain factor at the transient. This is reported in Fig. 5.2 for the same values of s, ω_c, T_1 and T_2 used before. In the left

[1] Forse si può dire meglio?

panel with $T_1 = 1$ mK, we notice that there is a threshold time: before this time, out-of-equilibrium probe outperform equilibrium one. After this time, equilibrium probe is better in discriminating. Again, this can be understood with the fact that, at larger times the pure dephasing probe looses information about the temperature. In the right panel, with $T_1 = 0$ K, we observe a completely different behavior. Here the reason lies in the fact that in the limit of $T_1 \to 0$, and for T_2 of the order of 10^{-3} K, the probability of error for the discrimination of equilibrium probes p_{eq}^{ERR} is approximately $1/4$, i.e. we are in the region where equilibrium probes are optimal. Hence, in principle, equilibrium are better if one is able to perform the corresponding POVM, i.e. the detection of the ground state $\Pi_1 = |e_0\rangle\langle e_0|$, as explained in Result 6.

5.4.2 Qutrit probe

Before moving to the general case of N dimensional systems, it may be interesting to explore the case of a three level probe to already grasp the peculiarities with respect to the paradigmatic and quite simple example of the qubit. To have a faithful comparison, we consider the same spacing of the energy levels as we have used for the qubit, which means that $\delta_0 = -2$, $\delta_1 = 0$ and $\delta_2 = +2$. We also identify $|e_0\rangle \to |0\rangle$, $|e_1\rangle \to |1\rangle$ and $|e_2\rangle \to |2\rangle$. The reduced dynamics is given by (5.19), with

$$\mathcal{V}^{\beta}(t) = \begin{pmatrix} 1 & e^{\Gamma(t|\beta)} & e^{4\Gamma(t|\beta)} \\ e^{\Gamma(t|\beta)} & 1 & e^{\Gamma(t|\beta)} \\ e^{4\Gamma(t|\beta)} & e^{\Gamma(t|\beta)} & 1 \end{pmatrix} \tag{5.39}$$

The other matrix now $\mathcal{R}(t)$ is not the identity. Despite being irrelevant for the evaluation of the probability of error, it is important to find the optimal POVM.

The formula of p_{oeq}^{ERR} for a general superposition of the energy levels is quite cumbersome and it does not yield to any physical insights. However, since in the qubit we have realized that coherences are the key resource, and to have a fai comparison, we consider two initial preparations: the maximally coherent state $|+_3\rangle = (|0\rangle + |1\rangle + |2\rangle)/\sqrt{3}$, and a qubit-like coherent state $|\varphi_q\rangle = (|0\rangle + |2\rangle)/\sqrt{2}$. To have compact formulas, we define the following function

$$\mathcal{D}_N(t;\beta_1,\beta_2) = e^{(N-1)^2\Gamma(t|\beta_2)} - e^{(N-1)^2\Gamma(t|\beta_1)} \tag{5.40}$$

which will be used extensively in the following and sometimes it will be shortened just to $\mathcal{D}_N$.

For the maximally coherent state we have that the probability of error is

$$p_{oeq}^{\text{ERR}}(\beta_1,\beta_2;|+_3\rangle) = \frac{1}{2}\left(1 - \frac{1}{6}\left|\mathcal{D}_3(t;\beta_1,\beta_2)\right|\left(1 + \sqrt{1 + 8\left(\frac{\mathcal{D}_2(t;\beta_1,\beta_2)}{\mathcal{D}_3(t;\beta_1,\beta_2)}\right)^2}\right)\right) \tag{5.41}$$

Here the optimal POVM is obtained as $\Pi_1 = \mathbb{I}_3 - \Pi_2$ and $\Pi_2 = |\lambda_0\rangle\langle\lambda_0|$, where

$$|\lambda_0\rangle = \frac{1}{\sqrt{2 + |c_+^{(3)}|^2}}\left(|\tilde{e}_0\rangle + c_+^{(3)}|\tilde{e}_1\rangle + |\tilde{e}_2\rangle\right) \tag{5.42}$$

where the coefficient $c_+^{(3)}$ is

$$c_+^{(3)} = -\frac{4\mathcal{D}_2^2 - \mathcal{D}_3^2 + \mathcal{D}_3\sqrt{8\mathcal{D}_2^2 + \mathcal{D}_3^2}}{\mathcal{D}_2(3\mathcal{D}_3 + \sqrt{8\mathcal{D}_2^2 + \mathcal{D}_3^2})} \tag{5.43}$$

and with the modified energy eigenbasis that now depends explicitly on time from $\xi(t)$, and is given by

$$|\tilde{e}_j\rangle = \exp(i\xi(t)\delta_j^2/4)|e_j\rangle \tag{5.44}$$

We conclude that in this case the optimal POVM depends on the structure of the thermal bath, i.e. Ohmicity s and cut-off frequency $omega_c$, as well as on the temperatures.

For the second state under studying $|\varphi_q\rangle$, the probability is much similar to that obtained for a qubit and reads as

$$p_{oeq}^{\text{ERR}}(\beta_1, \beta_2; |\varphi_q\rangle) = \frac{1}{2} - \frac{1}{4}\left|e^{4\Gamma(t|\beta_1)} - e^{4\Gamma(t|\beta_2)}\right| \tag{5.45}$$

The only difference the qubit's one is that the exponential have a more rapid decrease. As a result, the qualitative behavior is the same, but the minimum is achieved at smaller times.

We now want to compare the out-of-equilibrium qutrit with an equilibrium qutrit to study again under which conditions an enhancement is possible. Again, we define a gain function

$$\eta(\beta_1, \beta_2) = 1 - \frac{p_{oeq}^{\text{ERR}}(\beta_1, \beta_2; |+_3\rangle)}{p_{eq;3}^{\text{ERR}}(\beta_1, \beta_2)} \tag{5.46}$$

For positive values of the gain factor, the probability of error for the out-of-equilibrium probe has lower probability of error, i.e. the discrimination is better. We report the numerical results in Fig. 5.3, left panel, for the usual values of the parameters and with $T_1 = 1$ mK. We see that the gain factor is always positive for times smaller than a certain threshold, as already observed for the qubit.

To better understand the the enhancement coming from the dimension of the probe, we compare the performances for qubit and qutrit prepared in a maximally coherent state, i.e.

$$\eta_+(\beta_1, \beta_2) = 1 - \frac{p_{oeq}^{\text{ERR}}(\beta_1, \beta_2; |+_3\rangle)}{p_{oeq}^{\text{ERR}}(\beta_1, \beta_2; |+_2\rangle)} \tag{5.47}$$

where the subscript $+$ denotes that we are comparing the maximally coherent states and $p_{oeq}^{\text{ERR}}(\beta_1, \beta_2; |+_2\rangle)$ is Eq. (5.32) evaluated for $|+_2\rangle$. The numerical results are showed in Fig. 5.3, right panel, for $T_1 = 1$ mK. Positive values indicates a an improvement in the discrimination task when we use a qutrit instead of a qubit. As we may expect, the improvement occurs only for times smaller than a certain threshold and especially for a very small temperature T_2. The physical intuition behind this is that quantum coherence becomes more fragile for increasing dimension, and thus a qutrit probe is more sensitive than a qubit one, and this sensitivity is obtained at earlier times. In the next section we try to quantify the gain for a general N dimensional probe.

5.4.3 Qudit probe

We now address the question of whether and how much an N dimensional probe can improve the probability of error in the discrimination of the two temperatures. We focus again on the maximally coherent state, whose representation with a density matrix is given as $\varrho_{\mathcal{P}} = 1/N\mathbb{J}_N$, where $\mathbb{J}_N$ is the $N \times N$ matrix with all the entries equal to 1. In

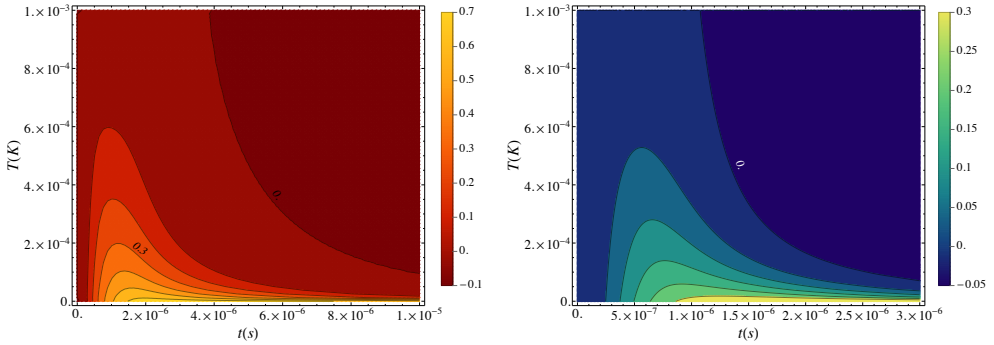

Figure 5.3: Left panel: gain factor η for the equilibrium vs out-of-equilibrium qutrit prepared in a maximally coherent state given in Eq. (5.46). Right panel: gain factor η_+ for the out-of-equilibrium qubit vs out-of-equilibrium qutriti given in Eq. (5.47). We report the result as a function of time t and the second temperature T_2, while we fix $T_1 = 1$ mK. We set $\omega_c = 7$ kHz, and $s = 1$.

this case the Λ operator reads as

$$\Lambda = \frac{1}{2N}\left(\mathcal{V}^{\beta_2}(t) - \mathcal{V}^{\beta_1}(t)\right) \circ \mathcal{R}(t) = \tag{5.48}$$

$$= \frac{1}{2N}\sum_{jl}\left(e^{\frac{(\delta_j-\delta_l)^2}{4}\Gamma(t|\beta_2)} - e^{\frac{(\delta_j-\delta_l)^2}{4}\Gamma(t|\beta_1)}\right)|\tilde{e}_j\rangle\langle\tilde{e}_l| \tag{5.49}$$

where the modified energy eigenbasis is defined in Eq. (5.44). To study how much we can gain with an N dimensional probe, we study the regime in which we already know there is an advantage, as we have concluded studying the qutrit probe. This is when $\Gamma(t|\beta_1) \lll 0$ and $\Gamma(t|\beta_2)$, i.e. when under the first temperature the probe has already decohered, while under the second temperature has not yet decohered. In this case, the operator Λ takes a much simpler expression, i.e.

$$\Lambda \simeq \frac{1}{2N}\begin{pmatrix} 0 & 1 & \dots & 1 \\ 1 & 0 & \dots & 1 \\ \vdots & \vdots & \ddots & \vdots \\ 1 & 1 & \dots & 0 \end{pmatrix} \tag{5.50}$$

Under these conditions, the trace of $|\Lambda|$ is equal to $1 - 1/N$ and as a result

$$p^{\text{ERR}}_{oeq}(\beta_1, \beta_2; |+_n\rangle) \geq \frac{1}{2N} \tag{5.51}$$

In this regime, the optimal POVM can be approximated by $\{\Pi_1 = \mathbb{I}_N - \Pi_2, \Pi_2|\lambda_0\rangle\langle\lambda_0|\}$, where

$$|\lambda_0\rangle = \frac{1}{\sqrt{N}}\sum_{i=0}^{N}|\tilde{e}_i\rangle \tag{5.52}$$

We see that in general the POVM depends non trivially on time t, on the temperatures and on the structure of the bath, apart from the case $N = 2$, in which the optimal measurement is universal, i.e. is the same whatever the values of parameters and time.

Finally, comparing two out-of-equilibrium probes of dimension N_1 and N_2 in the regime just discussed, we obtain that

$$\eta_+(\beta_1,\beta_2;N_1,N_2)=1-\frac{p^{\rm ERR}_{oeq}(\beta_1,\beta_2;|+_{N_1}\rangle)}{p^{\rm ERR}_{oeq}(\beta_1,\beta_2;|+_{N_2}\rangle)}\simeq 1-\frac{N_2}{N_1} \tag{5.53}$$

In the case of qubit vs qutrit, $\eta_+(\beta_1,\beta_2;2,3)\simeq 1/3$, matching the maximum η_+ we see in the right panel of Fig. 5.3.

5.4.4 Out-of-equilibrium quantum register made of two qubits

Now, we investigate the performance of a quantum register interacting locally with the thermal bath [147, 292]. The idea is study the role of entanglement in the discrimination of pure dephasing probes.

In this case the matrix of the levels spacing is given by

$$\widehat{H}^{(2,2)}_{\mathcal{P}}=(\widehat{\sigma}_z\otimes\widehat{\mathbb{I}}_2+\widehat{\mathbb{I}}_2\otimes\widehat{\sigma}_z) \tag{5.54}$$

We thus obtain that $\delta_{00}=-2$, $\delta_{01}=0=\delta_{10}$ and $\delta_{11}=+2$ and make the identifications $|e_0\rangle\to|00\rangle$, $|e_1\rangle\to|01\rangle$, $|e_2\rangle\to|10\rangle$ and $|e_3\rangle\to|11\rangle$. The reduced dynamics is given by Eq. (5.19), with the matrix $\mathcal{V}^\beta(t)$ now given by

$$\mathcal{V}^\beta(t)=\begin{pmatrix}1 & e^{\Gamma(t|\beta)} & e^{\Gamma(t|\beta)} & e^{4\Gamma(t|\beta)}\\ e^{\Gamma(t|\beta)} & 1 & 1 & e^{\Gamma(t|\beta)}\\ e^{\Gamma(t|\beta)} & 1 & 1 & e^{\Gamma(t|\beta)}\\ e^{4\Gamma(t|\beta)} & e^{\Gamma(t|\beta)} & e^{\Gamma(t|\beta)} & 1\end{pmatrix} \tag{5.55}$$

For the register initially prepared in a maximally coherent state $|\varphi_4\rangle=\frac{1}{4}\sum_k|e_k\rangle$ we have

$$\mathrm{Tr}\{|\Lambda|\}=\frac{1}{8}\,|\mathcal{D}_3(t;\beta_1,\beta_2)|\left[1+\sqrt{1+16\left(\frac{\mathcal{D}_2(t;\beta_1,\beta_2)}{\mathcal{D}_3(t;\beta_1,\beta_2)}\right)^2}\right]. \tag{5.56}$$

The corresponding probability of error is denoted as $p^{\rm ERR}_{oeq}(\beta_1,\beta_2;|\varphi_4\rangle)$, and the POVM is given by $\{\Pi_1=\mathbb{I}_4-\Pi_2,\Pi_2=|\lambda_0\rangle\langle\lambda_0|\}$ where

$$|\lambda_0\rangle=\frac{1}{\sqrt{2+2|c^{(2,2)}_+|^2}}\left(|\tilde{e}_0\rangle+c^{(2,2)}_+|\tilde{e}_1\rangle+c^{(2,2)}_+|\tilde{e}_2\rangle+|\tilde{e}_3\rangle\right) \tag{5.57}$$

with

$$c^{(2,2)}_+=\frac{\mathcal{D}_2(3\mathcal{D}_3+\sqrt{16\mathcal{D}_2^2+\mathcal{D}_3^2})}{4\mathcal{D}_2^2+\mathcal{D}_3^2+B\sqrt{16\mathcal{D}_2^2+\mathcal{D}_3^2}} \tag{5.58}$$

Again, the optimal POVM depends both on time t and temperatures β_1,β_2.

Moreover, having at disposal two qubits, one may wonder whether entanglement may play a role in the discrimination task. We thus consider the four Bell states as possibile initial preparation of the probe register. As it may be easily seen, the states $|\Psi^\pm\rangle=1/\sqrt{2}(|01\rangle\pm|10\rangle)$ are useless since they are invariant under dynamics (5.55). Concerning the states $|\Phi^\pm\rangle=1/\sqrt{2}(|00\rangle\pm|11\rangle)$ the probability of error $p^{\rm ERR}_{oeq}(\beta_1,\beta_2;|\Phi^+\rangle)$ is equal to that of the qutrit prepared in the state $|\varphi_q\rangle$.

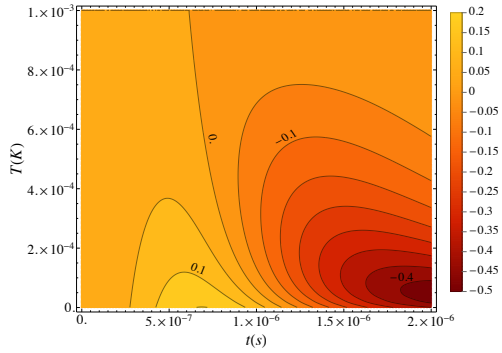

Figure 5.4: Gain factor η_e (max-coherent vs entangled probes) given in (5.59) as a function of time t and T_2. We fixed $\omega_c = 7$ kHz and $s = 1$ and $T_1 = 1$ mK

In order to evaluate whether entanglement is a resource or not in the discrimination task, we compare the error probability obtained wit a maximally coherent probe with that obtained with the Bell state $|\Phi^+\rangle$ by the factor

$$\eta_e(\beta_1, \beta_2; |\Phi^+\rangle, |\varphi_4\rangle) = 1 - \frac{p_{oeq}^{\text{ERR}}(\beta_1, \beta_2; |\Phi^+\rangle)}{p_{oeq}^{\text{ERR}}(\beta_1, \beta_2; |\varphi_4\rangle)}. \tag{5.59}$$

In Fig. 5.4, we clearly see a threshold time that splits the plot into two parts: the first, at smaller times, where entangled probes lead to a lower probability of error. In the second region, i.e. for larger times, maximally coherent probes outperform entangled ones.

5.4.5 Out-of-equilibrium entangled states in a quantum register of N qubits

In this section we explore more in detail the performance of multipartite entangled probes, providing an explanation of why entangled states are better probes at smaller times, and discussing also the optimal POVM. Our system of interest is a N-dimensional quantum register.

Firstly, let's consider N dimensional GHZ states

$$|GHZ_N\rangle = \frac{1}{\sqrt{2}}(|0\cdots 0\rangle + |1\cdots 1\rangle \tag{5.60}$$

In the basis $|\tilde{e}_j\rangle$ we have that

$$\Lambda = \frac{1}{4}\begin{pmatrix} 0 & \cdots & \mathcal{D}_N(t;\beta_1,\beta_2) \\ \vdots & \ddots & \vdots \\ \mathcal{D}_N(t;\beta_1,\beta_2) & \cdots & 0 \end{pmatrix} \tag{5.61}$$

It is straightforward to see that

$$p_{oeq}^{\text{ERR}}(\beta_1, \beta_2; N) = \frac{1}{2}\left(1 - \frac{|\mathcal{D}_N(t;\beta_1,\beta_2)|}{2}\right) \tag{5.62}$$

The probability of error has the same form of that of the qubit, with the only difference in the pre-factor of $\Gamma(t|\beta)$, which results only in a rescaling of the optimal time, as it has

been discussed for the quantum register of two qubits. The optimal POVM is given by $\{\Pi_1 = |GHZ_N\rangle\langle GHZ_N|, \Pi_2 = \mathbb{I}_{2^N} - \Pi_1\}$ and it is time and temperature independent. We notice also that this is a collective measure. In addition, we notice that in the optimal region $\Gamma(t|\beta_1) \ll 0$ and $\Gamma(t|\beta_2) \simeq 0$ we have that $p_{oeq}^{\text{ERR}} \geq 1/4$, so there is no scaling advantage in term of dimension N.

Secondly, we consider W states,

$$|W_N\rangle = \frac{1}{\sqrt{N}}(|10\cdots0\rangle + |01\cdots0\rangle + \ldots |0\cdots01\rangle). \tag{5.63}$$

All the elements in the superposition have the same energy, so the state is stationary. Thus, there is no dephasing in the state and consequently the probability of error is maximum $p_{oeq}^{\text{ERR}} = 1/2$.

We conclude that entanglement is not always necessary in temperature discrimination. Indeed, entangled state might not be sensitive at all.

5.5 Conclusion

In this chapter, we have analyzed in detail the use of quantum probes to discriminate two structured baths at different temperatures. In particular, we have addressed quantum probes interacting with their environment by a dephasing Hamiltonian and compared the discrimination performance with those at equilibrium.

At first, we have addressed the discrimination problem for an equilibrium probe and evaluated the probability of error, showing that energy measurement is optimal in this regime. We have then moved to out-of-equilibrium dephasing probes, and derived the exact reduced dynamics for a finite quantum system locally interacting with an Ohmic-like thermal bath. Upon exploiting this result, we have studied the behavior of the probability of error as a function of the interaction time and found that in the low-temperature regime out-of-equilibrium probes outperform equilibrium ones at finite times. We also found that there is a finite value of the interaction time minimizing the probability of error. In turn, it results that for qubit systems, maximally coherent states generally represent the best preparation of the probe for the discrimination task. On the other hand, when one of the two temperatures is zero, equilibrium probes may represent the optimal choice. For maximally coherent qubit probes, we have obtained the optimal POVM, which is a spin measurement along the x-axis. Remarkably, this POVM is independent of time and temperatures (except for the free evolution phase factor). Instead, for maximally coherent qudits of dimension N, we found that under some conditions, there is an optimal region where the minimum probability of error scales as $1/2N$. In general, for qudits, the optimal POVM is time and temperatures dependent, but the temperature dependency disappears in the optimal region.

We have compared qubit probes with qutrit ones, and have shown numerically that qutrits allow one to achieve lower error probability. Finally, we have also investigated the role of entanglement, showing that at variance with maximally coherent probes, there is no scaling in the minimum of the probability of error, but only a decrease in the optimal time scale. Moreover, the optimal POVM for GHZ states does not depend on the temperatures. Overall, we conclude that the optimal POVM may be easily implemented for qubit and GHZ probes, whereas it may be more challenging to realize in practice optimal discrimination with higher dimensional probes.

Our results indicate that dephasing quantum probes are useful for the task of discriminating temperatures at intermediate interaction times, and that out-of-equilibrium

coherent quantum probes represent a resource not only for quantum estimation but also for quantum discrimination.

Part III

Characterization of quantum systems

CHAPTER 6

Quantum probes for the characterization of nonlinear media

Squeezed states and entangled pairs of photons are crucial resources in current implementations of quantum technologies [62], including quantum-enhanced sensing, quantum repeaters and the realization of quantum gates in several platforms. The experimental generation of these states exploits the nonlinear response of active materials. In turn, the precise characterization of the nonlinear behaviour of active optical media represents a crucial tool for the development of novel and reliable sensors, aimed at improving protocols for non-invasive diagnosis and secure communication, among others.

The quantitative characterization of the nonlinear coupling may be in principle achieved using semiclassical probes, e.g. laser beams in optical systems [18], or thermal perturbations in optomechanical ones [58, 65]. On the other hand, quantum probes, i.e. probes with nonclassical properties, are naturally very sensitive to the environment, and can be therefore used to improve precision and make very accurate sensors. As a result of steady progress in material quality and control, cost reduction and the miniaturisation of components, these devices are now ready to be carried over into numerous applications.

From a metrological point of view, the problem of designing a characterization scheme for the nonlinearities is twofold. On the one hand, one should find the optimal measurement and evaluate the corresponding ultimate bounds to precision: this will serve as a benchmark in the design of any device using nonlinear media. On the other hand, it is necessary to determine the optimal probe signals among those achievable with current technology.

The aim of this chapter is to address the above problems for nonlinear interactions corresponding to Hamiltonians of the form $\widehat{H} = \tilde{\lambda}(\widehat{a} + \widehat{a}^{\dagger})^{\varsigma}$, where $\widehat{a}$ is the annihilation bosonic field operator satisfying $\left[\widehat{a}, \widehat{a}^{\dagger}\right] = \mathbb{I}$. In particular, we consider situations where both the *coupling parameter* $\tilde{\lambda}$ and the *order of nonlinearity* ς are to be estimated by probing the medium with suitable optical signals. These Hamiltonians are encountered rather commonly in quantum optics, and provide an effective description of the interaction between radiation and matter. In fact, they follow from the quantum interaction between a quantized single-mode field and an active medium treated parametrically [228].

As a matter of fact, the larger is the nonlinear order, the less effective is the nonlinearity. For instance, the non-linear processes naturally occurring in the optical fibers are tiny. On the other hand, they can grow and become relevant as the length of the fiber and, thus, the interaction time, increases. Effects are particularly important in single-mode fibres, in which the small field-mode dimension results in substantially high light intensities despite relatively modest input powers [321]. In turn, a long-standing goal in optical science has been the implementation of non-linear effects at progressively lower light powers or pulse energies [16].

Here, we investigate the scaling of the precision as a function of the average number of photons of the probe, and we assess the performance of different probing signals, with the goal of quantifying the improvement achievable by using nonclassical resources as squeezing. Indeed, there have been several indications in the recent years [46, 35, 60, 147, 299] that quantum probes offer advantages in terms of precision and stability compared to their classical counterparts. In particular, upon using tools from quantum estimation theory [266, 5], we are going to determine the optimal measurement to be performed at the output, and to evaluate the corresponding ultimate quantum limit to precision. Additionally, we will investigate the performance of different probe preparations in order to assess whether a nonclassical preparation of the probe may improve precision in some realistic scenarios.

Our results may find applications in different fields ranging from quantum optics to optomechanics and to more general systems involving phonons [253]. Nonetheless, in order to make the presentation more concrete, we will mostly refer to a light beam interacting with optical media. In particular, to illustrate the basic features of our proposal, we consider two kinds of probes: customary coherent signals and squeezed ones. We let the probe interact with the nonlinear medium, and then we perform a measurement in order to extract information about the parameters we want to estimate. Finally, we evaluate the corresponding quantum Fisher information (QFI) and we determine the optimal probe preparation. We will show that squeezing is indeed a resource to enhance characterization at the quantum level, especially for fragile samples where a strong constraint on the probe energy is present.

The chapter is structured as follows. In Section 6.1, we briefly review the tools of quantum estimation theory applied to unitary-encoded statistical models. We obtain the ultimate bounds to precision in Section 6.2, and illustrate our results in Sections 6.3 and 6.4, where we discuss optimal estimation for separate and joint estimation, respectively. Finally, Section 6.5 closes the chapter with some concluding remarks.

6.1 Multi-parameter metrology with unitary-encoded parameters

In this first section, we review the basic tools of local multi-parameter quantum estimation theory with unitary-encoded parameters, following the introduction given in Sec. 2.2.4 . Our case of study consists of a family of pure states

$$\varrho_{\boldsymbol{\lambda}} = |\psi_{\boldsymbol{\lambda}}\rangle\langle\psi_{\boldsymbol{\lambda}}| = \widehat{U}_{\boldsymbol{\lambda}}|\psi_0\rangle\langle\psi_0|\widehat{U}_{\boldsymbol{\lambda}}^{\dagger}, \tag{6.1}$$

for whom the SLD can be simply evaluated. Since for pure states

$$\varrho_{\boldsymbol{\lambda}}^2 = \varrho_{\boldsymbol{\lambda}} \tag{6.2}$$

it follows from a direct calculation that

$$\partial_{\lambda_n}\varrho_{\boldsymbol{\lambda}} = (\partial_{\lambda_n}\varrho_{\boldsymbol{\lambda}})\varrho_{\boldsymbol{\lambda}} + \varrho_{\boldsymbol{\lambda}}(\partial_{\lambda_n}\varrho_{\boldsymbol{\lambda}}) \tag{6.3}$$

Hence, we recognize the Lyapunov Equation that defines the SLD operators in Eq. (2.41), whose solution in this case is simply

$$\widehat{L}_{\lambda_n} = 2\partial_{\lambda_n}\varrho_{\boldsymbol{\lambda}}. \tag{6.4}$$

Since every unitary operator can be written as $\widehat{U}_{\boldsymbol{\lambda}} = \exp\{-it\widehat{H}_{\boldsymbol{\lambda}}\}$ and assuming that $[\partial_{\lambda_n}\widehat{H}_{\boldsymbol{\lambda}}, \widehat{H}_{\boldsymbol{\lambda}}] = 0$ [1], we obtain that

$$\widehat{L}_{\lambda_n} = -2it\widehat{U}_{\boldsymbol{\lambda}}[\partial_{\lambda_n}\widehat{H}_{\boldsymbol{\lambda}}, \varrho_0]\widehat{U}^{\dagger}_{\boldsymbol{\lambda}}, \tag{6.6}$$

from which we can obtain the optimal POVM for the individual estimations of the parameters. Furthermore, it is easy to extended the QFI for pure states in Eq. (2.59) to the QFIM matrix and the Uhlmann matrix, as

$$[\boldsymbol{\mathcal{Q}}(\boldsymbol{\lambda})]_{nm} = 4\Re\mathrm{e}\big[\langle\partial_{\lambda_n}\psi_{\boldsymbol{\lambda}}|\partial_{\lambda_m}\psi_{\boldsymbol{\lambda}}\rangle + \langle\partial_{\lambda_n}\psi_{\boldsymbol{\lambda}}|\psi_{\boldsymbol{\lambda}}\rangle\langle\partial_{\lambda_m}\psi_{\boldsymbol{\lambda}}|\psi_{\boldsymbol{\lambda}}\rangle\big]\,, \tag{6.7a}$$

$$\big[\boldsymbol{\mathcal{U}}(\boldsymbol{\lambda})\big]_{nm} = 4\Im\mathrm{m}\big[\langle\partial_{\lambda_n}\psi_{\boldsymbol{\lambda}}|\partial_{\lambda_m}\psi_{\boldsymbol{\lambda}}\rangle\big]\,. \tag{6.7b}$$

The inverse of the QFIM is a lower bound for the covariance matrix of any estimator, see Theorem 5. In general this bound is not tight. This is due to the lack of commutativity of the SLDs $\{\widehat{L}_{\lambda_n}\}_{n=1}^{d}$. Nonetheless, the achievability of the bound given by the QFIM is subject to a weaker condition given by Eq. (2.29), which involves the Uhlmann matrix, see Result 2 for details. In our case of unitary-encode parameters, this condition reads as

$$\big[\boldsymbol{\mathcal{U}}(\boldsymbol{\lambda})\big]_{nm} = 4t^2\langle\psi_0|[\partial_{\lambda_n}\widehat{H}_{\boldsymbol{\lambda}}, \partial_{\lambda_m}\widehat{H}_{\boldsymbol{\lambda}}]|\psi_0\rangle = 0 \tag{6.8}$$

We notice that this condition is equivalent to the one used to derive Eq. (6.6) and which is satisfied in our estimation problem. Hence, we conclude that a sufficient condition for the attainability of the matrix and scalar SLD-CRb in Eq. (2.72) is that $[\partial_{\lambda_n}\widehat{H}_{\boldsymbol{\lambda}}, \widehat{H}_{\boldsymbol{\lambda}}] = 0$. Moreover, since the SLDs do not commute only on average, but also as operator, the optimal POVM is projective and given by their common eigen-projectors. Hence, the statistical model is quasi classical, according to [5], and the bound is attainable with single-copy measurements.

6.2 QFI matrix for optical non-linearities

Let us now go into more detail and analyze multi-parameter estimation by specifying our physical system. The hamiltonian that generates the unitary depends on two parameters: the coupling parameter $\tilde{\lambda}$ and the order ζ of a non-linear interaction

$$\widehat{H} = \tilde{\lambda}\,\widehat{G}_{\zeta}\,, \tag{6.9}$$

where the generator $\widehat{G}_{\zeta}$ is given by

$$\widehat{G}_{\zeta} = (\widehat{a} + \widehat{a}^{\dagger})^{\zeta}. \tag{6.10}$$

Accordingly, the time evolution of a pure probe state $|\psi_0\rangle$ under the Hamiltonian (6.9) reads:

$$|\psi_{\boldsymbol{\lambda}}\rangle \equiv |\psi_{\boldsymbol{\lambda}}(t)\rangle = e^{-i\widehat{H}\,t}|\psi_0\rangle = e^{-i\lambda\,\widehat{G}_{\zeta}}|\psi_0\rangle. \tag{6.11}$$

[1] In general, the derivative of the exponential map is given by

$$\frac{d}{d\lambda}e^{H_\lambda} = e^{H_\lambda}\frac{1 - e^{-\mathrm{ad}_{H_\lambda}}}{\mathrm{ad}_{H_\lambda}}\frac{d}{d\lambda}H_\lambda, \tag{6.5}$$

where $\mathrm{ad}_X(Y) = [X, Y]$. This simplifies if $\mathrm{ad}_X(Y) = 0$, as discussed in the main text. In our case, this is not restrictive for us, given the form of the Hamiltonian.

where $\lambda = \tilde{\lambda} t$. For the sake of brevity, we can consider a reparametrization, and by using Eq. (2.70), we can write

$$\boldsymbol{\mathcal{Q}}(\tilde{\lambda}, \zeta) = \boldsymbol{B}\boldsymbol{\mathcal{Q}}(\lambda, \zeta)\boldsymbol{B}^T, \tag{6.12}$$

where the matrix elements of $\boldsymbol{B}$ are all null but $[\boldsymbol{B}]_{11} = t$. In this way, we can focus only on the joint estimation of λ and ζ, being this totally equivalent to the joint estimation of $\tilde{\lambda}$ and ζ.

We notice that for the individual estimation of λ, the element of the QFI matrix is given by Eq. (2.59), and, from the Hamiltonian (6.9), the QFI can be written as

$$\mathcal{Q}_{\lambda\lambda} = 4\left[\langle\psi_0|\widehat{G}_{2\zeta}|\psi_0\rangle - \langle\psi_0|\widehat{G}_{\zeta}|\psi_0\rangle^2\right].^{2} \tag{6.13}$$

Analogously, for the estimation of the order of nonlinearity ζ only, we have:

$$|\partial_\zeta \psi_{\boldsymbol{\lambda}}\rangle = -i\lambda\zeta\widehat{G}_{\zeta-1}|\psi_{\boldsymbol{\lambda}}\rangle\,, \tag{6.14}$$

and the corresponding QFI matrix element reads

$$\mathcal{Q}_{\zeta\zeta} = 4\,(\lambda\zeta)^2\left[\langle\psi_0|\widehat{G}_{2(\zeta-1)}|\psi_0\rangle - \langle\psi_0|\widehat{G}_{\zeta-1}|\psi_0\rangle^2\right]. \tag{6.15}$$

By using the expression for $|\partial_\zeta\psi_{\boldsymbol{\lambda}}\rangle$, it is straightforward to evaluate also the off-diagonal elements, obtaining

$$\mathcal{Q}_{\zeta\lambda} = 4\,\lambda\zeta\left[\langle\psi_0|\widehat{G}_{2\zeta-1}|\psi_0\rangle - \langle\psi_0|\widehat{G}_{\zeta}|\psi_0\rangle\langle\psi_0|\widehat{G}_{\zeta-1}|\psi_0\rangle\right]. \tag{6.16}$$

According to the above expressions, the bound to precision for the individual estimation of ζ may be derived from that for the estimation of λ, apart from a rescaling. Together with Eq. (6.16) this confirms that all the QFI matrix elements depend on combinations of the expectation value $\langle\psi_0|\widehat{G}_k|\psi_0\rangle$ for different values of k, therefore this quantity will be studied in great detail in the following sections.

6.3 Optimal probes for individual estimation

After having studied the estimation problem from the point of view of the measurement process, i.e. the QFI matrix corresponding to the optimal measurement, we address now the problem of finding the optimal probe, i.e. the optimal input state to achieve the ultimate bound in the precision of the estimation [6]. In this section, we separately optimize the probe for the individual estimation of λ and ζ, i.e. we find the initial states that maximize respectively $\mathcal{Q}_{\lambda\lambda}$ and $\mathcal{Q}_{\zeta\zeta}$. These optimal probes may not be the same, meaning that different preparations are necessary in order to optimally estimate λ or ζ. The joint estimation of both parameters will be discussed in the next Section.

In our analysis, we focus on the relevant class of Gaussian probes, namely, states that exhibit a Gaussian Wigner function [259, 314]. In particular, we consider the performance of the so-called *displaced coherent states*, that can be easily generated and manipulated by current quantum optics technology [97]. Coherent states are usually considered to be

[2] For the sake of brevity, we suppress the explicit dependence of the matrix elements from the parameters from here onwards.

the closest quantum states to classical ones. They are eigenstates of the annihilation operator, $\widehat{a}|\alpha\rangle = \alpha|\alpha\rangle$, where $\alpha \in \mathbb{C}$, and can be written as

$$|\alpha\rangle = \widehat{D}(\alpha)|0\rangle = e^{-|\alpha|^2/2} \sum_n \frac{\alpha^n}{\sqrt{n!}} |n\rangle \,, \tag{6.17}$$

where $\widehat{D}(\alpha) = e^{\alpha a^\dagger - \alpha^* a}$ is the displacement operator, $|0\rangle$ the vacuum state and $\{|n\rangle\}_{n\in\mathbb{N}}$ is the Fock basis. A displaced squeezed state is defined as follows [259]

$$|\alpha, \xi\rangle = \widehat{D}(\alpha)\, \widehat{S}(\xi)|0\rangle \tag{6.18}$$

where $\widehat{S}(\xi) = \exp\left\{\frac{1}{2}\left[\xi(\widehat{a}^\dagger)^2 - \xi^* \widehat{a}^2\right]\right\}$ is the single-mode squeezing operator and $\xi \in \mathbb{C}$ is the complex squeezing parameter. If $\alpha = 0$, we obtain the so-called *squeezed vacuum* state, whereas for $\xi = 0$ we have a coherent state. Given the state $|\alpha, \xi\rangle$, it is convenient to introduce the total number of photons N and the *squeezing fraction* γ, namely:

$$N = \langle \alpha, \xi | \widehat{N} | \alpha, \xi \rangle = N_{\rm ch} + N_{\rm sq} \quad \text{and} \quad \gamma = \frac{N_{\rm sq}}{N_{\rm ch} + N_{\rm sq}}, \tag{6.19}$$

where we set $\xi = r\, e^{i\theta}$, $\widehat{N} = \widehat{a}^\dagger \widehat{a}$ is the number operator and we defined the number of *squeezing* photons $N_{\rm sq} = \sinh^2 r = \gamma N$, whereas the number of *coherent* photons is $N_{\rm ch} = |\alpha|^2 = (1-\gamma)N$. If $\gamma = 0$, we have a coherent state $|\alpha\rangle$, whereas for $\gamma = 1$ we obtain the squeezed vacuum $|0, \xi\rangle$. Our ultimate goal is thus determining the optimal parameters α and ξ, which realize the maximum of the QFI at fixed N and, eventually, to determine the optimal state to probe the non-linear medium in order to estimate the two non-linearity parameters.

Following the previous section, given the probe state $|\psi_0\rangle = |\alpha, \xi\rangle$, we have to evaluate the expectation value of $\widehat{G}_\zeta$. To this aim, we start writing the following identity

$$\widehat{G}_\zeta = (\widehat{a} + \widehat{a}^\dagger)^\zeta = \zeta! \sum_{\kappa=0}^{\infty} \delta_{\zeta\kappa} \frac{1}{\kappa!} (\widehat{a} + \widehat{a}^\dagger)^\kappa \tag{6.20}$$

Moreover, we use the following expression for the Kronecker delta

$$\delta_{\kappa\zeta} = \frac{1}{2\pi} \int_{-\pi}^{\pi} dx\, e^{i(\kappa-\zeta)x}, \tag{6.21}$$

which lead us to

$$\widehat{G}_\zeta = \zeta! \int_{-\pi}^{\pi} \frac{dx}{2\pi} e^{-i\zeta x} \sum_{\kappa=0}^{+\infty} \frac{e^{i\kappa x}}{\kappa!} (\widehat{a} + \widehat{a}^\dagger)^\kappa \tag{6.22}$$

$$= \zeta! \int_{-\pi}^{\pi} \frac{dx}{2\pi} e^{-i\zeta x} e^{ix(\widehat{a}+\widehat{a}^\dagger)}. \tag{6.23}$$

Now, considering that the creation and annihilation operator satisfy $[\widehat{a}, \widehat{a}^\dagger] = \mathbb{I}$, we can

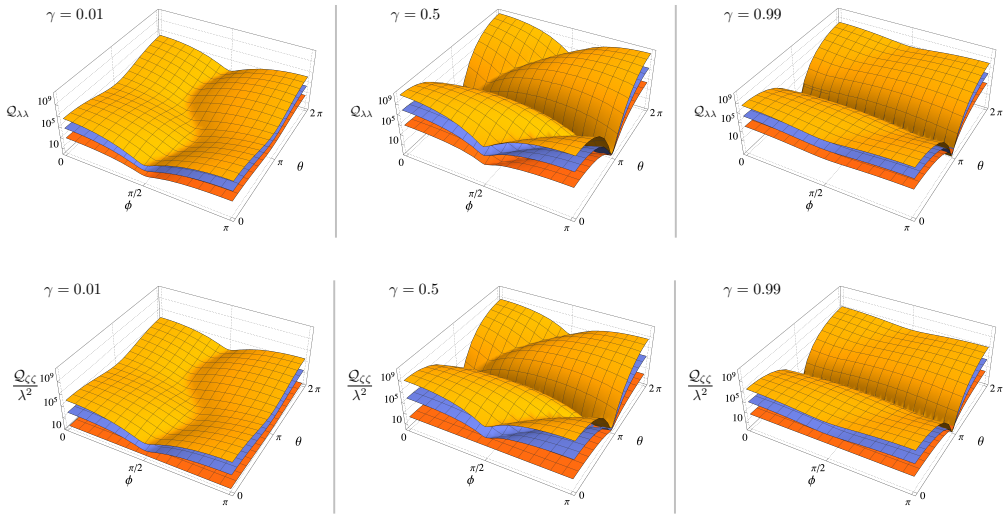

Figure 6.1: First line: The QFI $\mathcal{Q}_{\lambda\lambda}$ of Eq. (6.13) as a function of the squeezing phase θ and coherent amplitude phase ϕ for $N = 3$ and for different values of the order of nonlinearity ζ: from bottom to top $\zeta = 2, 3$ and 4. Second line: The QFI $\mathcal{Q}_{\zeta\zeta}$ of Eq. (6.15) rescaled by λ^2 as a function of the squeezing parameter phase θ and coherent amplitude phase ϕ for $N = 3$ and for different values of the order of nonlinearity ζ: from bottom to top $\zeta = 2, 3$ and 4. On both lines, the plots refer to different values of the squeezing ratio: (left panels) $\gamma = 0.01$, (middle panels) $\gamma = 0.5$ and (right panels) panel: $\gamma = 0.99$. Notice that the quantity $\mathcal{Q}_{\zeta\zeta}/\lambda^2$ is independent of λ.

write $e^{ix(\widehat{a}+\widehat{a}^\dagger)} = \exp\{e^{ix}\widehat{a}^\dagger\}\exp\{e^{ix}\widehat{a}\}\exp\{e^{2ix}/2\}$, and consequently we obtain

$$\widehat{G}_\zeta = \zeta! \int_{-\pi}^{\pi} \frac{dx}{2\pi} e^{-i\zeta x} \sum_{s=0}^{+\infty} \frac{(e^{ix}\widehat{a}^\dagger)^s}{s!} \sum_{t=0}^{+\infty} \frac{(e^{ix}\widehat{a})^t}{t!} \sum_{m=0}^{+\infty} \frac{(e^{2ix})^m}{2^m m!} = \tag{6.24}$$

$$= \zeta! \sum_{s,t,m=0}^{+\infty} \frac{(\widehat{a}^\dagger)^s(\widehat{a})^t}{s!t!m!2^m} \int_{-\pi}^{\pi} \frac{dx}{2\pi} e^{ix(s+t+2m-\zeta)} = \tag{6.25}$$

$$= \sum_{s,t,m=0}^{+\infty} \frac{\zeta!}{s!t!m!2^m} (\widehat{a}^\dagger)^s(\widehat{a})^t \delta_{\zeta,s+t+2m}. \tag{6.26}$$

In the last expression, we may perform the sum over t and, noticing that s can be at most $\zeta - 2m$, while m can be at most $\lfloor \zeta/2 \rfloor$, we finally obtain [346, 220]

$$\widehat{G}_\zeta = \sum_{m=0}^{\lfloor \zeta/2 \rfloor} \sum_{s=0}^{\zeta-2m} C(\zeta, m, s)(\widehat{a}^\dagger)^s(\widehat{a})^{\zeta-2m-s}\,, \tag{6.27}$$

where

$$C(\zeta, m, s) = \frac{\zeta!}{2^m m! s! (\zeta - 2m - s)!}\,. \tag{6.28}$$

More generally, the normal order of $(e^{i\psi}\widehat{a} + e^{-i\psi}\widehat{a}^\dagger)^\zeta$ may be obtained. In this case, we redefine the ladder operators as $\widehat{b} = e^{i\psi}\widehat{a}, \widehat{b}^\dagger = e^{-i\psi}\widehat{a}^\dagger$, which satisfy the canonical

commutation relations $\left[\widehat{b}, \widehat{b}^\dagger\right] = \mathbb{I}$. Then, it results that

$$(e^{i\psi}\widehat{a} + e^{-i\psi})^\zeta = (\widehat{b} + \widehat{b}^\dagger)^\zeta = \tag{6.29}$$

$$= \sum_{m=0}^{\lfloor \zeta/2 \rfloor} \sum_{s=0}^{\zeta-2m} \frac{\zeta!}{2^m s! m! (\zeta - s - 2m)!} (\widehat{b}^\dagger)^s (\widehat{b})^{\zeta-s-2m} = \tag{6.30}$$

$$= \sum_{m=0}^{\lfloor \zeta/2 \rfloor} \sum_{s=0}^{\zeta-2m} \frac{\zeta! e^{i\psi(\zeta-2l-2m)}}{2^m s! m! (\zeta - s - 2m)!} (\widehat{a}^\dagger)^s (\widehat{a})^{\zeta-s-2m}. \tag{6.31}$$

In turn, we have that

$$\begin{aligned}
\langle \alpha, \xi | \, \widehat{G}_\zeta \, | \alpha, \xi \rangle &= \langle 0 | \, \widehat{S}^\dagger(\xi) \, \widehat{D}^\dagger(\alpha) \, (\widehat{a} + \widehat{a}^\dagger)^\zeta \, \widehat{D}(\alpha) \, \widehat{S}(\xi) \, | 0 \rangle \\
&= \langle \beta | \left[(\mu + \nu^*)\widehat{a} + (\mu + \nu)\widehat{a}^\dagger \right]^\zeta | \beta \rangle = \eta^\zeta \langle \beta | \left(\widehat{a} e^{i\psi} + \widehat{a}^\dagger e^{-i\psi} \right)^\zeta | \beta \rangle = \\
&= \eta^\zeta \sum_{k=0}^{\lfloor \zeta/2 \rfloor} \sum_{s=0}^{\zeta-2k} C(\zeta, k, s) e^{i\psi(\zeta-2k-2s)} \, (\beta^*)^s \, \beta^{\zeta-2k-s},
\end{aligned} \tag{6.32}$$

where we have introduced $\beta = \mu\alpha + \nu\alpha^*$, $\eta = |\mu + \nu|$ and $\psi = \mathrm{Arg}(\mu + \nu^*)$, with $\mu = \cosh r$ and $\nu = e^{i\theta} \sinh r$. Starting from Eq. (6.32) we can evaluate the QFI of Eqs. (6.13) and (6.15), which are shown in Figure 6.1. As one may expect, the behaviour is qualitatively similar, except for the case $\zeta = 2$ and for $\gamma \to 0$, i.e. for a coherent probe: in this case the QFI associated with the estimation of the order of nonlinearity ζ does not depend on the parameters of the probe state and reads $\mathcal{Q}_{\zeta\zeta} = 16\lambda^2$.

In Figure 6.2 we show the QFIs for the two extreme cases, i.e a coherent probe and a squeezed vacuum one, respectively, as a function of the relevant phases. From the Figures above, it is clear that both $\mathcal{Q}_{\lambda\lambda}$ and $\mathcal{Q}_{\zeta\zeta}$ are periodic functions of the phases ϕ and θ of the probe state. Since we are interested in finding the optimal probes, i.e. states maximizing the QFIs, we set $\theta = \phi = 0$. Thereafter, we have $\alpha \in \mathbb{R}$, $\beta = \alpha \, e^r$ and $\eta = e^r$ and Eq. (6.32) can be rewritten as

$$\langle \alpha, r | \, \widehat{G}_\zeta \, | \alpha, r \rangle = (\alpha \, e^{2r})^\zeta \sum_{k=0}^{\lfloor \zeta/2 \rfloor} (\alpha \, e^r)^{-2k} \sum_{s=0}^{\zeta-2k} C(\zeta, k, s) \, , \tag{6.33}$$

and, being [2]

$$\sum_{s=0}^{\zeta-2k} C(\zeta, k, s) = \frac{2^{\zeta-3k} \zeta!}{k! (\zeta - 2k)!}, \tag{6.34}$$

we eventually obtain:

$$\langle \alpha, r | \, \widehat{G}_\zeta \, | \alpha, r \rangle = (2\alpha \, e^{2r})^\zeta \zeta! \sum_{k=0}^{\lfloor \zeta/2 \rfloor} \frac{(2\sqrt{2} \, \alpha \, e^r)^{-2k}}{k! (\zeta - 2k)!}. \tag{6.35}$$

We can now use this last result to evaluate the corresponding QFIs and look for the optimal squeezing fraction γ maximizing them.

At first, we study the low energy regime $N \ll 1$, where we may write

$$\mathcal{Q}_{\lambda\lambda} \simeq 4 \, \frac{A(\zeta)}{2^\zeta} \left(1 + 2\zeta \sqrt{\gamma N} \right) \qquad (N \ll 1) \tag{6.36}$$

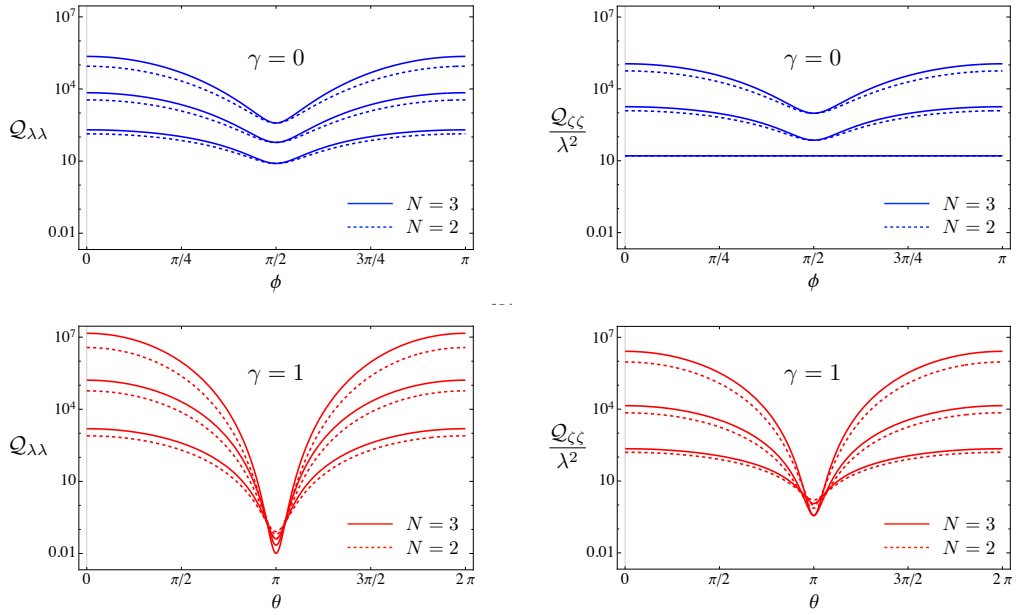

Figure 6.2: Upper plots: $\mathcal{Q}_{\lambda\lambda}$ and $\mathcal{Q}_{\zeta\zeta}/\lambda^2$ for a coherent probe, i.e. $\gamma = 0$, as a function of the coherent state phase ϕ for $N = |\alpha|^2 = 2$ (dashed lines) and $N = |\alpha|^2 = 3$ (solid lines) and different values of the order of nonlinearity: form bottom to top $\zeta = 2, 3$ and 4. Note that for $\zeta = 2$ we have $\mathcal{Q}_{\zeta\zeta}/\lambda^2 = 16$ (lower line the right panel). Lower plots: $\mathcal{Q}_{\lambda\lambda}$ and $\mathcal{Q}_{\zeta\zeta}/\lambda^2$ for a squeezed vacuum probe, i.e. $\gamma = 1$, as functions of the squeezing phase θ for $N = \sinh^2 r = 2$ (dashed lines) and $N = \sinh^2 r = 3$ (solid lines) and different values of the order of nonlinearity: from bottom to top $\zeta = 2, 3$ and 4.

and

$$\mathcal{Q}_{\zeta\zeta} \simeq 4\,\lambda^2\zeta^2\,\frac{A(\zeta-1)}{2^{\zeta-1}}\left[1+2(\zeta-1)\sqrt{\gamma N}\right] \qquad (N \ll 1) \tag{6.37}$$

where

$$A(\zeta) = \begin{cases} \dfrac{(2\zeta)!}{\zeta!} & \text{if } \zeta \text{ odd;} \\ \dfrac{(2\zeta)!}{\zeta!} - \left[\dfrac{\zeta!}{(\zeta/2)!}\right]^2 & \text{if } \zeta \text{ even.} \end{cases} \tag{6.38}$$

These expansions suggest the existence of a threshold value of N, which depends on ζ, below which the QFI reaches the maximum for $\gamma = 1$ (i.e. for a squeezed vacuum probe). Indeed, the maximization at fixed N confirms this intuition. In Figure 6.3 we show the optimal value of γ, maximizing the QFIs, as a function of N for two values of ζ.

As we can see from Figure 6.3, due to the particular mathematical relations between $\mathcal{Q}_{\lambda\lambda}$ and $\mathcal{Q}_{\zeta\zeta}$, the same optimal squeezing fraction $\gamma_{\rm opt}$ maximizing $\mathcal{Q}_{\zeta\zeta}$ for a given ζ maximizes also $\mathcal{Q}_{\lambda\lambda}$ for the order of nonlinearity $\zeta - 1$. We have an exception for $\zeta = 2$: in this peculiar case, to reach the maximum value of $\mathcal{Q}_{\zeta\zeta}$, one should always choose $\gamma = 1$ (squeezed vacuum probe), as we can see by its rather simple analytic expression:

$$\mathcal{Q}_{\zeta\zeta} = 16\lambda^2\left[1+2\gamma N+2\sqrt{\gamma N(1+\gamma N)}\right] \qquad (\zeta = 2). \tag{6.39}$$

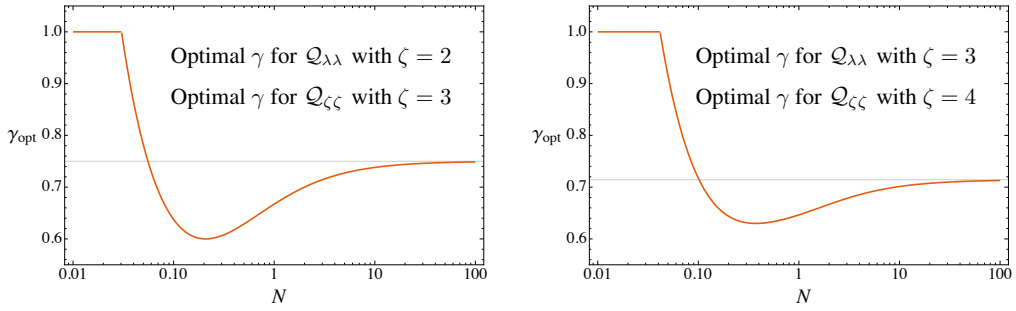

Figure 6.3: The optimal squeezing fraction $\gamma_{\rm opt}$ maximizing $\mathcal{Q}_{\lambda\lambda}$ and $\mathcal{Q}_{\zeta\zeta}$ for different values of the nonlinearity order ζ. The horizontal lines corresponds to the asymptotic value given in Eq. (6.43). See the text for details.

Apart from this case, we observe a threshold value $N_{\rm th}$ for $\gamma_{\rm opt} < 1$, i.e the squeezed vacuum is no longer the optimal probes. The values of $N_{\rm th}$ depends on the order of the non-linearity: for the estimation of λ and for even values ζ or for the estimation of ζ and for odd values of ζ (left panel of Figure 6.3) it is equal to $N_{\rm th} = (3\sqrt{2}-4)/8 \simeq 0.03$, while for the other cases (right panel of Figure 6.3) the $N_{\rm th}$ approaches $(3\sqrt{2}-4)/8$ for $\zeta \geq 5$.

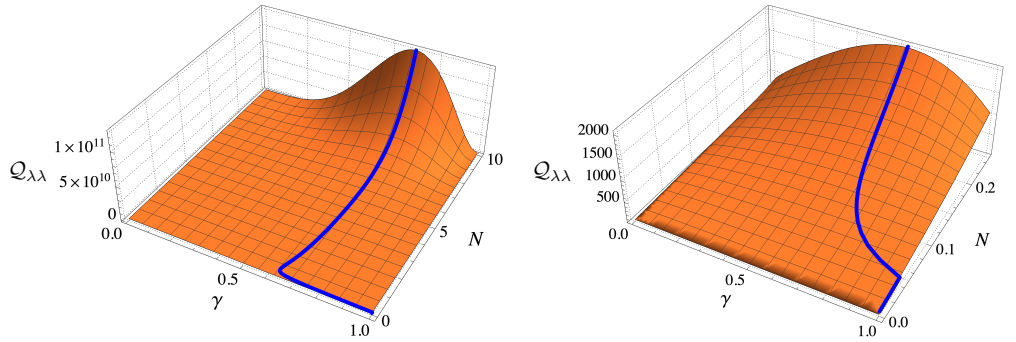

Figure 6.4: Plot of $\mathcal{Q}_{\lambda\lambda}$ as a function of γ and N for $\zeta = 3$. The right panel is a magnification of the left one to highlight the behaviour of the QFI in the regime $N \ll 1$. The blue line refers to the maximum of the QFI (see also the right panel of Figure 6.3). Analogous results can be obtained for $\mathcal{Q}_{\zeta\zeta}$ and other values of ζ. See the text for details.

In the large energy regime, the QFIs are found to grow as

$$\mathcal{Q}_{\lambda\lambda} \simeq B_\gamma(\zeta)\, N^{3\zeta-2} \qquad (N \gg 1) \tag{6.40}$$

and

$$\mathcal{Q}_{\zeta\zeta} \simeq \lambda^2\zeta^2 B_\gamma(\zeta-1)\, N^{3(\zeta-1)-2} \qquad (N \gg 1) \tag{6.41}$$

respectively, with

$$B_\gamma(\zeta) = 4^{3\zeta-1}\zeta^2(1-\gamma)^{\zeta-1}\gamma^{2\zeta-1}\,. \tag{6.42}$$

Using the results in the large energy regime $N \gg 1$ it is easy to find that the optimal squeezing fraction maximizing $\mathcal{Q}_{\lambda\lambda}$ is given by (the optimal squeezing fraction maximizing $\mathcal{Q}_{\zeta\zeta}$ can be obtained replacing ζ with $\zeta - 1$, as it is clear from the previous equations):

$$\gamma_{\rm opt}(N \gg 1) = \frac{2\zeta - 1}{3\zeta - 1}\,, \tag{6.43}$$

and, therefore, $\gamma_{\rm opt} \to 2/3$ as ζ increases, as one can also see from Figure 6.3.

Result 8: Optimal probes for individual estimation

Considering the class of pure Gaussian states $|\alpha, \xi\rangle$, we want to find the optimal preparation for the estimation of λ and ζ, i.e. the fraction of squeezing $\gamma_{\rm opt}^{(\lambda)}$ and $\gamma_{\rm opt}^{(\zeta)}$, given a fixed total energy N. We find that:

1. In the low energy regime $N \ll 1$, there are $N_{\rm th}^{(\lambda)}$ and $N_{\rm th}^{(\zeta)}$ respectively for the optimal estimation of λ and ζ such that

$$\begin{cases} \gamma_{\rm opt}^{(j)} = 1 & N < N_{\rm th}^{(j)} \\ \gamma_{\rm opt}^{(j)} < 1 & N > N_{\rm th}^{(j)} \end{cases}, \quad j = \lambda, \zeta. \tag{6.44}$$

   The threshold values depend in general from ζ, and the two optimal probes at fixed values of λ and ζ are not the same.

2. In the high energy regime $N \gg 1$ the fraction of squeezing maximizing $\mathcal{Q}_{\lambda\lambda}$ and $\mathcal{Q}_{\zeta\zeta}$ is given respectively by

$$\gamma_{\rm opt}^{(\lambda)} = \frac{2\zeta - 1}{3\zeta - 1}, \qquad \gamma_{\rm opt}^{(\zeta)} = \frac{2\zeta - 3}{3\zeta - 4} \tag{6.45}$$

   We notice that, for order $\zeta > 2$, the fraction of squeezing belongs to $\gamma_{\rm opt}^{(\lambda)} \in [3/5, 2/3]$, while $\gamma_{\rm opt}^{(\zeta)} \in [1/2, 2/3]$. The two optimal squeezing coincide only in the limit of $\zeta \to \infty$.

We summarize results in Figure 6.4, where we show the QFI as a function of γ and N for a given value of the order of nonlinearity ζ. The blue lines denote the maxima of the QFI, which are of course obtained for the value of hte optimal squeezing ratio $\gamma_{\rm opt}$ displayed in the right plot of Figure 6.3.

6.4 Optimal probes for joint estimation

In the previous Section we evaluated the optimal probes for the *individual* estimation of λ and ζ, and we have seen that they do not match, i.e. given a nonlinear media, the optimal probe for the estimation of λ may not be optimal for ζ.

In this Section we address the *joint*, or *simultaneous*, estimation of both λ and ζ and we find the optimal probe for the multiparameter scenario. In this case, the figure of merit to be maximised is neither the $\mathcal{F}_{\lambda\lambda}$ or the $\mathcal{F}_{\zeta\zeta}$, but the inverse of the scalar bound given in Eq. (2.72). For the estimation of two parameters, this can be explicitly evaluated.

If we consider the weight matrix to be $\boldsymbol{W} = \mathbb{I}_2$, i.e. we equally weight the estimation of λ and ζ, we eventually obtain

$$\mathcal{C}^{\mathrm{SLD}}[\varrho_{\boldsymbol{\lambda}}, \mathbb{I}_2] = \frac{\mathcal{Q}_{\lambda\lambda}\mathcal{Q}_{\zeta\zeta} - \mathcal{Q}_{\lambda\zeta}{}^2}{\mathcal{Q}_{\lambda\lambda} + \mathcal{Q}_{\zeta\zeta}}. \tag{6.46}$$

where $\varrho_{\boldsymbol{\lambda}} = |\psi_{\boldsymbol{\lambda}}\rangle\langle\psi_{\boldsymbol{\lambda}}|$, with $|\psi_{\boldsymbol{\lambda}}\rangle$ defined in Eq. (6.11) and with initial state $|\alpha, \xi\rangle$. Due to the periodicity of the matrix elements of the QFI matrix, we still focus on the case $\theta = \phi = 0$. In this way, we can optimize the inverse of the scalar bound $\mathcal{C}^{\mathrm{SLD}}[\varrho_{\boldsymbol{\lambda}}, \mathbb{I}_2]$ in a similar way as we did in the previous Section for the individual QFIs. However, here the expression of the scalar bound is more involved, and we have to address the problem numerically. Results are reported in Figure 6.5. From the left panel, we may see that squeezed vacuum is optimal for $N < N_{\mathrm{th}}^{\mathrm{si}}$, while in the limit of large N the optimal fraction of squeezing $\gamma_{\mathrm{opt}}^{\mathrm{si}}$ depends only on the order of non linearity. Looking at the right panel, we see that threshold value $N_{\mathrm{th}}^{\mathrm{si}}$ depends both on ζ and λ, even though there are no significant difference for the different values of λ we have considered. As for the individual estimation, the $N_{\mathrm{th}}^{\mathrm{si}}$ approaches an asymptotic value as the order of non-linearity increases. The value is slightly larger than the one found in the previous section.

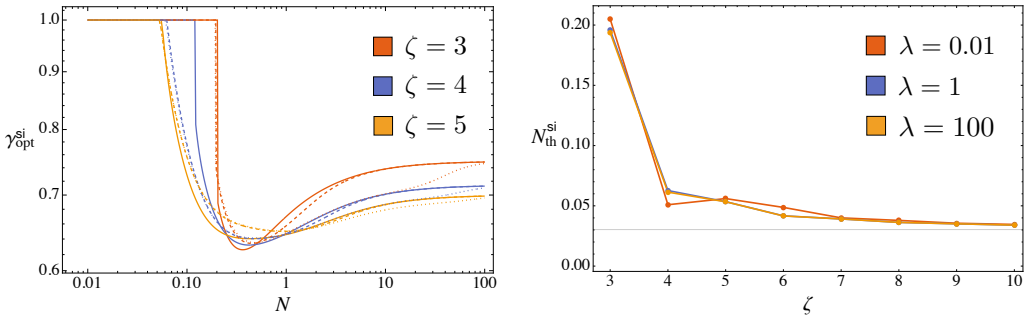

Figure 6.5: Left panel: optimal value of the fraction of squeezing γ for the scalar bound $\mathcal{C}^{\mathrm{SLD}}[\varrho_{\boldsymbol{\lambda}}, \mathbb{I}_2]$ as a function of N and for $\lambda = 0.01$ (solid lines), $\lambda = 1$ (dashed lines) and $\lambda = 100$ (dotted lines). Right panel: threshold value N_{th} we observe in the left panel. If $N < N_{\mathrm{th}}$ the squeezed vacuum is optimal, otherwise the optimal probe has $\gamma_{\mathrm{opt}} < 1$.

In Figure 6.6 we plot the quantity $\mathcal{C}^{\mathrm{SLD}}[\varrho_{\boldsymbol{\lambda}}, \mathbb{I}_2]^{-1}$ as a function of γ and N and for $\zeta = 3$. We have highlighted the optimal value of the scalar bound with a blue line. Comparing this Figure with the corresponding one for individual estimation (see Figure 6.4), we see that the qualitative behaviour is the same, while we notice that the $N_{\mathrm{th}}^{\mathrm{si}}$ is slightly larger, as we already outlined in previous considerations. This behaviour can be understood by the fact that we have to find a trade-off between the optimality for λ and ζ.

6.5 Conclusions

In this chapter of the thesis, we have addressed the use of squeezed states to improve precision in the characterization of nonlinear media. This is inherently a multiparameter estimation problem since it involves both the nonlinear coupling and the order of non-linearity. Using tools from quantum estimation theory we have firstly proved that the

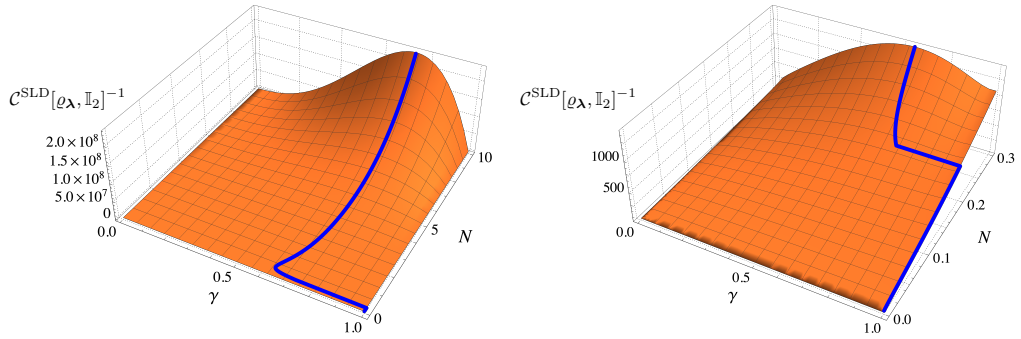

Figure 6.6: Plot of $\mathcal{C}^{\rm SLD}[\varrho_{\boldsymbol{\lambda}},\mathbb{I}_2]^{-1}$ as a function of γ and N for $\zeta = 3$. The right panel is a magnification of the left one to highlight the behaviour of the QFI in the regime $N \ll 1$. The blue line refers to the maximum of the QFI at fixed N.

two parameters are compatible, i.e. they may be jointly estimated without introducing any noise of quantum origin. In turn, this opens the possibility of exploiting squeezing as a resource to overcome the limitation of coherent probes.

We have found that using squeezed probes improves the estimation precision in any working regime, i.e. either for fragile media where one is led to use low energy probes, or when this constraint is not present, and one is free to choose probes with high energy. In the first case, squeezed vacuum represents a universally optimal probe [262, 145], where, for higher energy, squeezing should be tuned and depends itself on the value of the nonlinearity. This results hold both for the separate estimation of the two parameters, as well as for their joint estimation. In all regimes, using squeezing improves the scaling of the precision with the energy of the probe.

We conclude that quantum probes exploiting squeezing are indeed a resource for the characterization of nonlinear media. In view of the current development in quantum optics, we foresee potential applications with current technology.

CHAPTER 7

On the properties of the asymptotic incompatibility measure in multiparameter quantum estimation

The difference between the scalar SLD-CRb (2.72) and the HCRb in Eq. (2.74) bound has attracted much attention in recent times, focusing on measurement incompatibility [170, 101] and leading to the definition of measures able to capture this particular aspect [77, 31]. In particular, as we have seen in the introduction of this thesis, a quantity has been introduced in [77] to quantify the *quantumness* of a quantum multi-parameter problem. This quantity, denoted by $\mathcal{R}_{\boldsymbol{\lambda}}$, is equal to zero if and only if the Holevo bound coincides with the SLD based bound, and thus if the parameters to be estimated are *asymptotically compatible*. Similarly, it takes its largest value $\mathcal{R}_{\boldsymbol{\lambda}} = 1$ when the difference between the Holevo and the SLD bound is maximum, that is when the parameters are highly incompatible even in the asymptotic regime. Given these properties, in the following we will refer to $\mathcal{R}_{\boldsymbol{\lambda}}$ as *asymptotic incompatibility* (AI). The properties of AI has been discussed in relationship with the phase diagram of a quantum many-body system in [77], while its main properties and its behaviour for estimation problems encoded in qubit systems have been thoroughly investigated in [288].

In this chapter, we focus on the fundamental properties of the AI measure $\mathcal{R}_{\boldsymbol{\lambda}}$ in local quantum estimation theory. We study its relationship with the purity of the density operators of the quantum statistical model, and prove that for some classes of states, the two quantities are indeed in one-to-one correspondence. More in general, we find evidence that the maximum amount of incompatibility may be achieved only for purity exceeding a threshold depending on the dimension of the Hilbert space. We conjecture that this may be a general property of quantum statistical models. Moreover, we derive some bounds on the AI measure for quantum statistical *submodels*, and provide a method to directly identify the maximum number of compatible parameters in specific estimation problems.

The chapter is organized as follows: in Sec. 7.1 we review the main aspects of multiparameter quantum estimation and we introduce the AI measure $\mathcal{R}_{\boldsymbol{\lambda}}$. In Sec. 7.2, we show our main results concerning the relationship between the AI measure and the purity of the quantum states, while in Sec. 7.3 we will derive further properties regarding the AI of parameters of specific quantum statistical models. Sec. 7.4 closes the chapter with some concluding remarks.

7.1 Local quantum multiparameter estimation

In this section we briefly review the tools of local quantum multi-parameter estimation introduced in Chapter 2 in order to standardize the notation.

In the quantum realm, the parameters are encoded in a family of density operators $\varrho_{\boldsymbol{\lambda}}$ referred to as a quantum statistical model. We remark that in the following we will restrict ourselves to quantum statistical models described by quantum states $\varrho_{\boldsymbol{\lambda}}$ whose rank in the Hilbert space does not change by varying the parameters $\boldsymbol{\lambda}$ in the allowed region of the parameters' space. This will allow us to avoid discontinuities in the behaviour of the figures of merit we will consider [305, 316]. In this scenario, a lower bound to the covariance matrix of any estimator $\tilde{\boldsymbol{\lambda}}$ is given by the QFIM defined in Eq. (2.67), whose definition we report here

$$\mathcal{Q}(\boldsymbol{\theta})_{ij} = \frac{1}{2}\mathrm{tr}\left\{\varrho_{\boldsymbol{\theta}}\{\widehat{L}_{\theta_i}, \widehat{L}_{\theta_j}\}\right\} \tag{7.1}$$

and that satisfy the matrix SLD-CRb (2.71)

$$\boldsymbol{V}(\tilde{\boldsymbol{\lambda}}) \geq \boldsymbol{\mathcal{Q}}(\boldsymbol{\lambda})^{-1}. \tag{7.2}$$

It can be shown that his bound is in fact achievable for single-parameter estimation [173, 56, 266]. This means that for a single-copy of the state $\varrho_{\boldsymbol{\lambda}}$, a POVM whose Fisher Information is equal to the SLD-QFI exists, and remarkably one can prove that this optimal POVM corresponds to the projectors over the eigenstates of the SLD operator. If we now consider the multiparameter case $\mathfrak{p} > 1$, the different SLD operators may not commute, and an optimal simultaneous estimation of all the parameters can not be in general obtained. As a consequence, the QCR matrix bound may not always be achievable in the single-copy scenario and more informative bounds than the one provided by the SLD operators may exist.

When dealing with matrix inequalities, an additional problem arises already in classical estimation theory, i.e. the order of the CFIM is partial. This means that, given two experimental strategies specified by two distinct POVM $\boldsymbol{\Pi}^{(1)}$ and $\boldsymbol{\Pi}^{(2)}$ to which corresponds $\boldsymbol{\mathcal{F}}^{(1)}$ and $\boldsymbol{\mathcal{F}}^{(2)}$, it might be that both $\boldsymbol{\mathcal{F}}^{(1)} \ngeq \boldsymbol{\mathcal{F}}^{(2)}$ and $\boldsymbol{\mathcal{F}}^{(2)} \ngeq \boldsymbol{\mathcal{F}}^{(1)}$. Thus, to understand which strategies is better, scalar bounds have been introduced. Here, we study the one defined in terms of a weight matrix $\boldsymbol{W}$, a real and positive definite matrix of dimension $\mathfrak{p} \times \mathfrak{p}$. The SLD-QCR scalar bound obtainable from (7.2) can be written as follow

$$\mathrm{tr}\left\{\boldsymbol{W}\,\mathbf{Cov}_{\boldsymbol{\lambda}}[\widehat{\boldsymbol{\lambda}}]\right\} \geq C(\boldsymbol{\lambda}, \boldsymbol{W}) = \mathrm{tr}\left\{\boldsymbol{W}\boldsymbol{\mathcal{Q}}(\boldsymbol{\lambda})^{-1}\right\} = \mathcal{C}^{\mathrm{SLD}}[\varrho_{\boldsymbol{\lambda}}, \boldsymbol{W}]. \tag{7.3}$$

The role of the weight matrix $\boldsymbol{W}$ is to balance the precision of different parameters. In addition, there is a correspondence between $\boldsymbol{W}$ and a change of parametrization. Given a new set of parameter $\boldsymbol{\gamma} = \boldsymbol{\gamma}(\boldsymbol{\lambda})$ defined in terms of the previous one, the changes in the QFI-SLD matrix is determined by the reparametrization matrix $\mathcal{B}_{\alpha\beta} = \partial\lambda_\beta/\partial\gamma_\alpha$. The SLD-QFI matrix for the new parameter is [149]

$$\boldsymbol{\mathcal{Q}}(\boldsymbol{\gamma}) = \boldsymbol{B}\boldsymbol{\mathcal{Q}}(\boldsymbol{\lambda})\boldsymbol{B}^T. \tag{7.4}$$

Besides, any real symmetric positive definite matrix can be decomposed as $\boldsymbol{W} = \boldsymbol{L}\boldsymbol{L}^T$, where $\boldsymbol{L}$ is unique. We see that if $\boldsymbol{L} = \boldsymbol{B}^{-1}$, then a particular choice of $\boldsymbol{W}$ corresponds to a unique change of parametrization induced by $\boldsymbol{B}$. We stress that a weight matrix may not be symmetric. Then the decomposition is not unique and it may correspond to different reparametrization. To summarize: to a given reparametrization, the corresponding weight matrix is unique, while the existence of a unique reperamatrization given $\boldsymbol{W}$ is true if $\boldsymbol{W}$ is symmetric.

As its matrix counterpart, the SLD-QCR scalar bound (7.3) is not in general attainable due to the incompatibility of the optimal measurements corresponding to the different parameters. The problem of finding the most informative scalar bound was addressed by Holevo in [178]. The solution takes the name of Holevo Cramér-Rao bound (HCRb) and it will be denoted by $\mathcal{C}^{\rm H}[\varrho_{\boldsymbol{\lambda}}, \boldsymbol{W}]$. It represents the most informative bound for the asymptotic model in which a collective measurement is performed on an asymptotically large number of copies of the state $\varrho_{\boldsymbol{\lambda}}^{\otimes n} = \bigotimes_{j=1}^{n} \varrho_{\boldsymbol{\lambda}}$, with $n \to \infty$ [169, 163]. In this limit, the bound is indeed achievable and for this reason it is typically considered as the most fundamental scalar bound for quantum multiparameter estimation. However, the evaluation of the HCRB requires a non-trivial minimization, see Definition in 5. Nonetheless, some results have been obtained both numerically and even analytically under some assumptions on the quantum statistical model [107, 28, 330, 52, 53, 7, 325, 331, 159, 17]

7.1.1 Asymptotic incompatibility measure

As observed before, in a multiparameter scenario the optimal strategies for each single parameter estimation may not be compatible and as a result the lower bound (7.3) can not always be attained. A key object in this respect is the commutator $[\widehat{L}_\alpha, \widehat{L}_\beta]$ between the different SLD-operators: if this commutator is equal to zero for all the parameters in $\boldsymbol{\lambda}$, all the SLD-bounds for each single parameter are simultaneously achievable in the single-copy scenario by performing the same POVM, and as a result, both the matrix and scalar SLD-QCR bound given in Eq. (7.2) and (7.3). These models are known in the litterature as quasi-classical model [5, 331]. However, as we will describe in a moment, its average value over the quantum statistical model $\varrho_{\boldsymbol{\lambda}}$ plays an important role too. Typically this quantity is introduced via the so-called Uhlmann (or Berry) curvature [78, 218], defined via its matrix elements

$$\mathcal{U}_{\alpha\beta}(\boldsymbol{\lambda}) = -\frac{i}{2}\mathrm{Tr}\left\{\varrho_{\boldsymbol{\lambda}}\left[\widehat{L}_\alpha, \widehat{L}_\beta\right]\right\}. \tag{7.5}$$

One proves that a necessary and sufficient condition for the attainability of the SLD-QCR scalar bound (7.3) in the asymptotic limit is given by the compatibility condition, or weak commutativity, $\boldsymbol{\mathcal{U}} = \mathbf{0}$ [285]. If this condition is fulfilled, that is if all the SLD operators commute on average, then $\mathcal{C}^{\rm H}[\varrho_{\boldsymbol{\lambda}}, \boldsymbol{W}] = \mathcal{C}^{\rm SLD}[\varrho_{\boldsymbol{\lambda}}, \boldsymbol{W}]$, i.e. the SLD-QCR scalar bound can be attained in the asymptotic model $\varrho_{\boldsymbol{\lambda}}^{\otimes n}$ with $n \to \infty$. In the following, we will refer to models that satisfy this condition as asymptotically classical model and parameters belonging to these models as asymptotic compatible parameters [5, 331].

More recent results have shown how the HCRB can be bounded from above as

$$\mathcal{C}^{\rm SLD}[\varrho_{\boldsymbol{\lambda}}, \boldsymbol{W}] \leq \mathcal{C}^{\rm H}[\varrho_{\boldsymbol{\lambda}}, \boldsymbol{W}] \leq (1 + \mathcal{R}_{\boldsymbol{\lambda}})\mathcal{C}^{\rm SLD}[\varrho_{\boldsymbol{\lambda}}, \boldsymbol{W}] \leq 2\,\mathcal{C}^{\rm SLD}[\varrho_{\boldsymbol{\lambda}}, \boldsymbol{W}] \tag{7.6}$$

that is $\mathcal{C}^{\rm H}[\varrho_{\boldsymbol{\lambda}}, \boldsymbol{W}]$ cannot be larger than two times the SLD QCR scalar bound. In the chain of inequalities above, we have introduced the following parameter

$$\mathcal{R}_{\boldsymbol{\lambda}} = ||i\,\boldsymbol{\mathcal{Q}}(\boldsymbol{\lambda})^{-1}\boldsymbol{\mathcal{U}}(\boldsymbol{\lambda})||_\infty\,, \tag{7.7}$$

where $||\mathbf{A}||_\infty$ denotes the largest eigenvalue of the matrix $\mathbf{A}$. In the rest of the chapter we will focus on this quantity, that has been introduced, as a *quantumness* parameter, in [77] and studied in detail for qubit systems in [288]. As already suggested in Eq. (7.6), one can prove that

$$0 \leq \Delta C[\varrho_{\boldsymbol{\lambda}}, \boldsymbol{W}] \leq \mathcal{R}_{\boldsymbol{\lambda}} \leq 1\,,$$

where we have defined the renormalized difference between the Holevo and SLD-bound

$$\Delta C[\varrho_{\boldsymbol{\lambda}}, \boldsymbol{W}] = \frac{\mathcal{C}^{\mathrm{H}}[\varrho_{\boldsymbol{\lambda}}, \boldsymbol{W}] - \mathcal{C}^{\mathrm{SLD}}[\varrho_{\boldsymbol{\lambda}}, \boldsymbol{W}]}{\mathcal{C}^{\mathrm{SLD}}[\varrho_{\boldsymbol{\lambda}}, \boldsymbol{W}]} \,. \tag{7.8}$$

Moreover one also proves two relevant properties [77, 288]: (i) $\mathcal{R}_{\boldsymbol{\lambda}} = 0$ if and only if $\boldsymbol{\mathcal{U}}(\boldsymbol{\lambda}) = 0$, that is when the model is asymptotically classical; (ii) $\mathcal{R}_{\boldsymbol{\lambda}}$ is a property of the quantum statistical model $\varrho_{\boldsymbol{\lambda}}$ only, being also independent on possible reparametrization and, as a consequence, on the weight matrix $\boldsymbol{W}$. In [288] it was also studied its relationship with the quantity

$$\Delta C_{\mathsf{max}} = \max_{\mathbf{W}>0} \Delta C[\varrho_{\boldsymbol{\lambda}}, \boldsymbol{W}] \,, \tag{7.9}$$

for quantum statistical models encoded in qubit systems. The quantity ΔC_{max} stands out as a natural measure of *asymptotic incompatibility* (AI) and it is in general upper bounded by $\mathcal{R}_{\boldsymbol{\lambda}}$. It was shown that, while for several quantum statistical model the bound is indeed tight, that is one finds $\Delta C_{\mathsf{max}} = \mathcal{R}_{\boldsymbol{\lambda}}$, there exist counterexamples where ΔC_{max} is strictly smaller than $\mathcal{R}_{\boldsymbol{\lambda}}$. However, also in these examples one observes that the two quantities have the same general behaviour and in general that the order relations induced by them are equivalent.

For all these reasons, and also considering the fact that the evaluation of the quantity $\mathcal{R}_{\boldsymbol{\lambda}}$ is quite straightforward and, at difference with ΔC_{max}, does not rely on the evaluation of the Holevo bound and on its (non trivial) maximization over the weight matrices $\mathbf{W}$, in the following we will restrict to it and we will in general refer to $\mathcal{R}_{\boldsymbol{\lambda}}$ as a *AI measure* of the quantum statistical model $\varrho_{\boldsymbol{\lambda}}$.

7.2 Asymptotic incompatibility and purity of the quantum statistical model

In this section we discuss the relationship between the AI measure $\mathcal{R}_{\boldsymbol{\lambda}}$ and the purity of the quantum state $\varrho_{\boldsymbol{\lambda}}$ corresponding to the quantum statistical model under exam. We will mainly focus to scenarios where $\varrho_{\boldsymbol{\lambda}}$ describes the most general quantum state of a particular quantum system, starting from the simplest cases of a qubit and of a single-mode Gaussian continuous-variable quantum state, and then moving our attention to qudits, that is to quantum states living in a d-dimensional Hilbert space.

7.2.1 Asymptotic incompatibility of state parameters in full tomography of qubit systems

A generic mixed qubit state is typically written as

$$\varrho_{\boldsymbol{\lambda}} = \frac{1}{2}\left(\mathbb{1} + \sum_{j=1}^{3} \gamma_j \sigma_j\right) \,, \tag{7.10}$$

where the matrices σ_j denote the Pauli matrices, while $\gamma_1 = r\sin\theta\cos\phi$, $\gamma_2 = r\sin\theta\sin\phi$, $\gamma_3 = r\cos\theta$. By considering the set of $\mathfrak{p} = 3$ parameters $\boldsymbol{\lambda} = (r, \theta, \phi)$ characterizing the vector in the Bloch sphere, one can readily derive the SLD operators by solving the corresponding Lyapunov equations, and obtains the SLD-QFI and the Ulhman curvature

matrices

$$\mathcal{Q}(\boldsymbol{\lambda}) = \begin{pmatrix} 1/(1-r^2) & 0 & 0 \\ 0 & r^2 & 0 \\ 0 & 0 & r^2 \sin^2\theta \end{pmatrix}, \tag{7.11}$$

$$\mathcal{U}(\boldsymbol{\lambda}) = \begin{pmatrix} 0 & 0 & 0 \\ 0 & 0 & r^3 \sin\theta \\ 0 & -r^3 \sin\theta & 0 \end{pmatrix}. \tag{7.12}$$

The corresponding AI measure has been already derived in [288], obtaining $\mathcal{R}_{\rm qubit} = r$. The purity of the quantum state $\varrho_{\boldsymbol{\lambda}}$ can be easily evaluated, obtaining $\mu = \mathrm{Tr}\left\{\varrho_{\boldsymbol{\lambda}}^2\right\} = (1+r^2)/2$, and thus leading to the result

$$\mathcal{R}_{\rm qubit} = \sqrt{2\mu - 1}\,. \tag{7.13}$$

We thus observe that the AI for the full tomography $\mathcal{R}_{\rm qubit}$ is indeed a monotonous function of the purity of the quantum state, and that in particular it takes its limiting values $\mathcal{R}_{\rm qubit} = 0$ for the maximally mixed state, and $\mathcal{R}_{\rm qubit} = 1$ for pure states only.

7.2.2 Asymptotic incompatibility for a single-mode continuous-variable Gaussian system

As a second example we now consider a single-mode continuous-variable quantum system, described by annihilation and creation operators satisfying the canonical commutation relation $[\widehat{a}, \widehat{a}^\dagger] = \mathbb{1}$. Quantum states describing such systems belongs to an infinite-dimensional Hilbert space. A well known subclass of such states is given by Gaussian states, typically defined as those states having a Gaussian Wigner function [132, 314]. These states have been indeed studied in great detail, both for the simple mathematical formulation (they can be fully described by first and second moments of the quadrature operators $\widehat{q} = (\widehat{a} + \widehat{a}^\dagger)/\sqrt{2}$ and $\widehat{p} = i(\widehat{a}^\dagger - \widehat{a})/\sqrt{2}$) and for practical and fundamental reasons (they can be easily generated in the lab, and they can be exploited for implementing quantum technology protocols as quantum teleportation). We leave more details on Gaussian states in Appendix 7.A, along with the formulas needed to evaluate the SLD-QFI and the Uhlmann curvature matrices.

We here address the problem of complete estimating an arbitrary single mode Gaussian state, which can be parametrized by $\mathfrak{p} = 5$ parameters, resulting from the application of a complex squeezing operator $S(\xi) = \exp\left(\frac{1}{2}\xi(a^\dagger)^2 - \frac{1}{2}\xi^* a^2\right)$ and a complex displacement operator $D(\alpha) = \exp\left(\alpha a^\dagger - \alpha^* a\right)$ on a thermal state $\nu_N = e^{-\beta \widehat{a}^\dagger \widehat{a}}/Z$ with average photon number $\mathrm{Tr}\left\{\nu_N \widehat{a}^\dagger \widehat{a}\right\} = N$. The corresponding quantum statistical model is thus represented by the family of density operators [314]

$$\varrho_{\boldsymbol{\lambda}} = D(\alpha) S(\xi) \nu_N S(\xi)^\dagger D(\alpha)^\dagger\,, \tag{7.14}$$

with a parametrization in terms of the set $\boldsymbol{\lambda} = \{\mathfrak{Re}\alpha, \mathfrak{Im}\alpha, r, \varphi, N\}$, and where we have written the two complex parameters as $\xi = re^{i\varphi}$ and $\alpha = \mathfrak{Re}\alpha + i\mathfrak{Im}\alpha$. The first moments vector $\boldsymbol{d} = (\mathrm{Tr}\left\{\varrho_{\boldsymbol{\lambda}}\widehat{q}\right\}, \mathrm{Tr}\left\{\varrho_{\boldsymbol{\lambda}}\widehat{p}\right\})^T$ has elements

$$\mathrm{Tr}\left\{\varrho_{\boldsymbol{\lambda}}\widehat{q}\right\} = \sqrt{2}\mathfrak{Re}\alpha\,, \tag{7.15}$$

$$\mathrm{Tr}\left\{\varrho_{\boldsymbol{\lambda}}\widehat{p}\right\} = \sqrt{2}\mathfrak{Im}\alpha\,, \tag{7.16}$$

while the elements of the covariance matrix (CM) (see 7.A for details) can be expanded in terms of symmetric 2×2 matrices, i.e. $\boldsymbol{\sigma} = s_1\sigma_x + s_2\boldsymbol{I}_2 + s_3\sigma_z$ (with σ_x and σ_z denoting the standard Pauli matrices), obtaining

$$s_1 = -(2N+1)\sinh(2r)\sin(\varphi), \tag{7.17}$$
$$s_2 = (2N+1)\cosh(2r), \tag{7.18}$$
$$s_3 = (2N+1)\sinh(2r)\cos(\varphi). \tag{7.19}$$

The matrix elements for the SLD-QFI matrix and for the Uhlmann curvature matrix can be directly evaluated via the formulas

$$\begin{aligned}\mathcal{Q}_{\alpha\beta} = {} & \frac{1}{2}\frac{\mathrm{Tr}\left\{(\boldsymbol{\sigma}^{-1}\partial_\alpha\boldsymbol{\sigma})(\boldsymbol{\sigma}^{-1}\partial_\beta\boldsymbol{\sigma})\right\}}{1+\mu^2} + \frac{2\partial_\alpha\mu\partial_\beta\mu}{1-\mu^4} \\ & + 2\left(\partial_\alpha\boldsymbol{d}\right)^T\boldsymbol{\sigma}^{-1}(\partial_\beta\boldsymbol{d})\end{aligned} \tag{7.20}$$

$$\begin{aligned}\mathcal{U}_{\alpha\beta} = {} & \frac{\mu^2}{2(\mu^2+1)^2}\mathrm{Tr}\left\{\boldsymbol{\sigma}\Omega\left[\partial_\alpha\boldsymbol{\sigma}\boldsymbol{\sigma}^{-1}, \partial_\beta\boldsymbol{\sigma}\boldsymbol{\sigma}^{-1}\right]\right\} \\ & + 2\mu^2(\partial_\alpha\boldsymbol{d})\Omega(\partial_\beta\boldsymbol{d}),\end{aligned} \tag{7.21}$$

where the purity of single-mode Gaussian states is given by $\mu = 1/\sqrt{\det\boldsymbol{\sigma}} = 1/(2N+1)$. Notice that our result differ from that in [254] by a factor 2 in the first term of the Uhlmann matrix (for a detailed derivation, see Appendix 7.A).

In particular, for the quantum statistical model defined above, we obtain

$$\mathcal{Q}_{\mathfrak{Re}\alpha,\mathfrak{Re}\alpha} = 4\mu\left(\cosh(2r) - \cos(\varphi)\sinh(2r)\right), \tag{7.22a}$$
$$\mathcal{Q}_{\mathfrak{Im}\alpha,\mathfrak{Im}\alpha} = 4\mu\left(\cosh(2r) + \cos(\varphi)\sinh(2r)\right), \tag{7.22b}$$
$$\mathcal{Q}_{\mathfrak{Re}\alpha,\mathfrak{Im}\alpha} = 4\mu\sinh(2r)\sin(\varphi), \tag{7.22c}$$
$$\mathcal{Q}_{r,r} = \frac{4}{1+\mu^2}, \tag{7.22d}$$
$$\mathcal{Q}_{\varphi,\varphi} = \frac{\sinh(2r)^2}{1+\mu^2}, \tag{7.22e}$$
$$\mathcal{Q}_{N,N} = \frac{4\mu^2}{1-\mu^2}, \tag{7.22f}$$

and

$$\mathcal{U}_{\mathfrak{Re}\alpha,\mathfrak{Im}\alpha} = 4\mu^2, \tag{7.23a}$$
$$\mathcal{U}_{\varphi,r} = \frac{4\mu\sinh(2r)}{(1+\mu^2)^2}, \tag{7.23b}$$

while the matrix elements not reported are null. We emphasize that these values do not depend on $(\Re\alpha, \Im\alpha)$, and we also osberve that the SLD-QFI matrix is block diagonal. In particular, the second block regarding the parameters (r, φ, N) is exactly diagonal. Moreover, since most of the entries of the Uhlmann matrix are equal to 0, we conclude that most of the parameters are orthogonal globally with respect to the SLD-QFI, with the exception of the pairs $(\Re\alpha, \Im\alpha)$ and (r, φ).

The AI measure can be readily evaluated, obtaining

Result 9: AI for single-mode Gaussian states

The AI for a Gaussian state given in Eq. (7.14) is given by

$$\mathcal{R}_{\mathsf{GS}} = \frac{2\mu}{1+\mu^2}\,. \tag{7.24}$$

This depend only on the purity μ of the state.

Remarkably, we see that the contribution depending on (r, φ) cancel out in the AI $\mathcal{R}_{\mathsf{GS}}$. Also in this case we have thus obtained that AI is a monotonous function of purity μ, and that one obtains that all the parameters become asymptotically compatible only in the limit of a maximally mixed state (that is $\mathcal{R}_{\mathsf{GS}} = 0$ only for $\mu \to 0$), while the maximum value of incompatibility $\mathcal{R}_{\mathsf{GS}} = 1$ is obtained if and only if $\varrho_{\boldsymbol{\lambda}}$ is a pure state.

7.2.3 Asymptotic incompatibility for of state parameters in full tomography in qudit systems

Let us now move back to consider finite-dimensional quantum systems described via Hilbert spaces with dimension d larger than two. The most natural way to describe the most general quantum states in this scenario is by the following parametrization

$$\varrho_{\boldsymbol{\gamma}} = \frac{1}{d}\left(\mathbb{1} + \sum_{j=1}^{d^2-1} \gamma_i \Sigma_i\right) \tag{7.25}$$

where the matrices Σ_i denotes the generators of the Lie algebra $\mathfrak{su}(d)$, and thus correspond to Pauli matrices for $d = 2$ and to Gell-Mann matrices for $d = 3$. The $\mathfrak{p} = d^2 - 1$ coordinates $\boldsymbol{\gamma}$ represent the normalized Cartesian vector in the $d^2 - 1$-dimensional Bloch space and are also known as the components of the $d^2 - 1$-dimensional Bloch vector or as mixture coordinates [37]. In the following we consider the estimation of the parameters $\boldsymbol{\gamma}$, i.e. the full tomography of the state. It is known that this model is a $\mathcal{D}$-invariant model and hence the Holevo bound is equal to the right logarithmic derivative scalar bound [183].

Analytical solutions for the AI measure are very hard to derive with arbitrary dimension d. Hence, we address the problem numerically by randomly generating quantum density matrices corresponding to $d = 3$, $d = 4$ and $d = 5$. The method we used to generate random density matrix follows two steps:

1. First, we generate the eigenvalues of the density matrix $\varrho_{\boldsymbol{\gamma}}$, which belongs to the probability simplex $\boldsymbol{X}_d = \{\boldsymbol{x} = (x_1, ..., x_d) | \sum_{i=1}^{d} x_i = 1\}$.

2. Second, we randomly generate unitary matrix U. We remind that different U corresponds to different eigenvectors of $\varrho_{\boldsymbol{\gamma}}$ and thus to different quantum states and more importantly to different values of the parameters $\boldsymbol{\gamma}$.

For each random state we evaluate the AI measure from the definition (7.7) by numerically solving the Lyapunov equation for the SLD operators and then by evaluating the SLD-QFI and Uhlmann curvature matrices. The results are reported in Fig. 7.1 as function of the purity of the state. We clearly see that there is no one-to-one correspondence

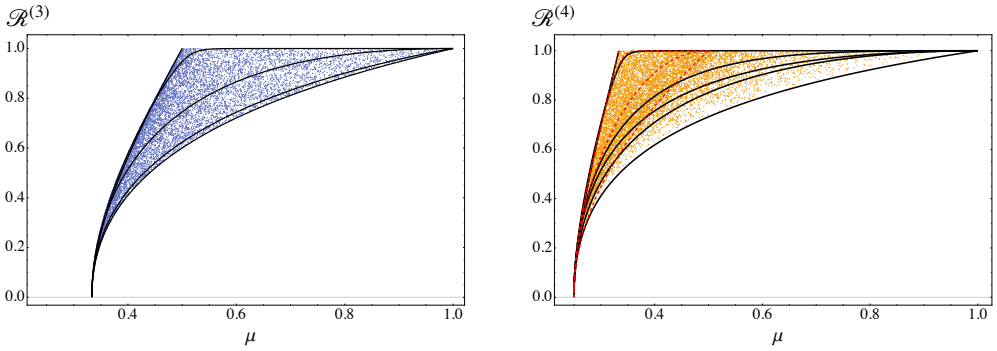

Figure 7.1: Left panel: scatter plot of the AI measure (y-axis) vs purity (x-axis) for qutrit systems. The black lines are the AI for fixed spectrum of H, see main text for details. The most left line refers to a choice of H with 2 degenerate eigenvalues. Right panel: scatter plot of the AI measure (y-axis) vs purity (x-axis) for 4-dimensional quantum systems. Again, the black lines are the AI for a fixed spectrum of H. The red-dashed lines refers to choice of H with at least 2 degenerate eigenvalues.

between the value of μ and the value of $\mathcal{R}^{(d)}$. However, we see that the AI is strictly less than one whenever the purity of the state is lower than $\mu = 1/(d-1)$. Thus, we can state the following conjecture:

Conjecture 1: Maximal amount of AI and purity

Given a quantum statistical model described by a family quantum states $\varrho_{\boldsymbol{\lambda}}$ living in a d-dimensional Hilbert space, the maximum amount of the AI measure $\mathcal{R}_{\boldsymbol{\lambda}} = 1$ may be observed only if the purity of the quantum state is larger than a minimum threshold $\mu_{\mathsf{min}} = 1/(d-1)$.

This conjecture is clearly consistent for the two cases discussed above, i.e. qubit and single-mode Gaussian states, whose AI was exactly derived, and it is surrogated by the numerical evidence in Fig. 7.1.

We now introduce a second way to parametrize a d-dimensional quantum system that will be particularly useful fo our purposes, i.e.

$$\varrho_{\boldsymbol{\lambda}} = \frac{e^{-\beta H}}{\mathrm{Tr}\left\{e^{-\beta H}\right\}}, \qquad H = \sum_{j=1}^{d^2-1} \lambda_j \Sigma_j \tag{7.26}$$

The coordinates $\boldsymbol{\lambda}$ are known as exponential coordinates [37] while the parameter β play the role of the inverse temperature of the state with respect to the Hamiltonian operator H, clearly recalling the Gibbs state form used in statistical mechanics. However, this is not a *true* coordinate since it can be included in the definition of the $\boldsymbol{\lambda}$, hence must be considered more as a rescaling parameter which allow us to constrain the exponential coordinates to be in a finite interval ($|\lambda_i| \leq 1$ in our simulations).

In general, a closed formula for the AI is hard to derive also with this parameterization. Hence, we investigate the problem by considering a simplified case, i.e. a diagonal $H = \text{diag}\{\Delta_0, \Delta_1, ..., \Delta_{d-1}\}$, with the constraint $|\Delta_i| \leq 1$. In other words, we set $\lambda_j = 0$ for the indexes j corresponding to non-diagonal operators Σ_j, and we address the estimation for all the parameters corresponding to the exponential coordinates $\boldsymbol{\lambda}$. The reason why we study this class of states is twofold: the first is that the calculations are greatly simplified, the second is that the results we find seem to be valid more generally, as we will explain later in more detail.
We have evaluated analytically the AI measure corresponding to the estimation of all the $d^2 - 1$ parameters encoded in this particular quantum statistical model, finding

$$\mathcal{R}_{\text{qudit}} = \tanh\left(\frac{\beta\Delta_M}{2}\right) \tag{7.27}$$

where $\Delta_M = \max_i \Delta_i - \min_j \Delta_j$, i.e. the maximum difference between the eigenvalues of H (we remark that the calculations are much simpler by evaluating the matrices for the parameters $\boldsymbol{\gamma}$, and exploiting the fact that $\mathcal{R}_{\boldsymbol{\lambda}}$ is invariant under reparametrization). The result in (7.27) is consistent with the AI for a qubit states, as for $d = 2$ the purity μ and the argument of the $\tanh$ are in one-to-one correspondence. Indeed, the purity can be written in terms of $\boldsymbol{\lambda}$ as $\mu = (1 + \tanh(\beta|\boldsymbol{\lambda} \cdot \boldsymbol{\lambda}|)^2)/2$. In the case of a diagonal H, we have $\lambda_1 = \lambda_2 = 0$ and $\Delta_M = 2|\lambda_3|$, and thus

$$\mu = \frac{1}{2}(1 + \tanh(\beta|\lambda_3|)^2 = \frac{1}{2}\left(1 + \tanh\left(\frac{\beta\Delta_M}{2}\right)^2\right). \tag{7.28}$$

By simply using (7.27) we indeed obtain the result in Eq. (7.13). Remarkably, also the Gaussian case might be reduced to this expression if we consider that the purity in terms of the average number of excitation N is $\mu = (2N+1)^{-1}$. By replacing the value of N by the formula for the Bose-Einstein statistics $N = 1/(\exp\beta\omega - 1)$, we obtain that the purity can be written as $\mu = \tanh(\beta\omega/2)$. Then, the AI (7.24) becomes exactly equal to (7.27) by fixing $\Delta_M = 2\omega$.

This line of reasoning of course does not prove that the AI is equal to (7.27) for arbitrary d-dimensional density matrix $\varrho_{\boldsymbol{\lambda}}$. To try to answer this question, we addressed the problem by studying these quantities for the numerically generated random quantum states of dimension $d = 3, 4, 5$. In more detaiil

1. We evaluate the quantity $\beta\Delta_M$ for each random states $\varrho_{\boldsymbol{\lambda}}$ we generate (see previous paragraph for the details of the random generation of $\varrho_{\boldsymbol{\lambda}}$) via the formulas $\beta^{(rand)}\Delta_i^{(rand)} = -\log(x_i)$, and $\beta^{(rand)}\Delta_M^{(rand)} = \max_i \beta^{(rand)}\Delta_i^{(rand)} - \min_j \beta^{(rand)}\Delta_j^{(rand)}$ (we remind that the quantities $\{x_i\}$ correspond to the eigenvalues of $\varrho_{\boldsymbol{\lambda}}$).

2. For each random state we evaluate the AI measure corresponding to its full estimation via Eq. (7.7), and we compare it with the formula (7.27) evaluated via the parameter $\beta^{(rand)}\Delta_M^{(rand)}$.

3. We find that the two quantities match for all the quantum states that we have numerical generated.

We conclude that for $d = 3, 4, 5$ the AI is fully determined only by $\beta\Delta_M$, i.e. it corresponds to a property of the spectrum of H only (to be more precise it depends only on

the maximum and minimum eigenvalues of H). For these reasons, we state a second conjecture here

Conjecture 2: AI for qudit full tomography

Given a quantum statistical model described by a family quantum states $\varrho_{\boldsymbol{\lambda}}$ living in a d-dimensional Hilbert space, the AI corresponding to the full estimation of the state is given by (7.27), where β is the fictious temperature of the state with respect to the Hamiltonian operator H in the exponential coordinates (7.26).

A further element in favour of this conjecture comes from Fig. 7.1, in which we clearly see that the AI for a fixed spectrum (black lines) span the whole area covered by the AI measure values corresponding to the random states generated. In addition, we see that the AI for a 4-dimensional system with H having two eigenvalues with degeneracy 2 reaches the maximum value of $\mathcal{R} = 1$ when the purity is $\mu = 1/2$, since in the case in which $\Delta_0 = \Delta_1$ and $\Delta_2 = \Delta_3$, we have that $\mu \to 1/2$ for $\beta \to \infty$.

We finally remark again that, as we described above, the formula in Eq. (7.27) can be readily evaluated, after diagonalizing the quantum state describing the quantum statistical model $\varrho_{\boldsymbol{\lambda}} = \sum_i x_i |\psi_i\rangle\langle\psi_i|$, and by observing that $\beta\Delta_i = -\log(x_i)$.

7.3 Further properties of asymptotic incompatibility measure

In this section we analyze in more detail some further properties of the AI measure $\mathcal{R}_{\boldsymbol{\lambda}}$, sheding more light on the relationship between a given quantum statistical model $\varrho_{\boldsymbol{\lambda}}$ and possible *sub-models* that arise when one or more parameters of the set $\boldsymbol{\lambda}$ are considered known and thus not to be estimated.

In the definition of $\mathcal{R}_{\boldsymbol{\lambda}}$ in Eq. (7.7), only the the largest eigenvalue of the matrix $\boldsymbol{\mathcal{I}} = i\,\boldsymbol{\mathcal{Q}}(\boldsymbol{\lambda})^{-1}\boldsymbol{\mathcal{U}}(\boldsymbol{\lambda})$ is considered. In the following we will study more in detail the role of the spectrum of $\boldsymbol{\mathcal{I}}$ in the characterization of the quantum statistical model. To do so, we first introduce the Cauchy interlace theorem [185]:

Theorem 6: Cauchy interlace theorem

Consider a $N\times N$ hermitian matrix $\boldsymbol{\mathcal{A}}$ and any $(N-1)\times(N-1)$ principal sub-matrix $\boldsymbol{\mathcal{B}}$ of $\boldsymbol{\mathcal{A}}$. Consider the corresponding eigenvalues in decreasing order $\boldsymbol{a} = \{a_1, \ldots, a_N\}$ and $\boldsymbol{b} = \{b_1, \ldots, b_{N-1}\}$. Then, $\boldsymbol{a}$ interlace $\boldsymbol{b}$, that is

$$a_N \leq b_{N-1} \leq a_{N-1} \leq \ldots \leq b_2 \leq a_2 \leq b_1 \leq a_1. \tag{7.29}$$

This result can now be applied for our purposes to the matrix $\boldsymbol{\mathcal{I}}$, leading to the following theorem:

Theorem 7: Bound on AI measure for quantum statistical sub-models

Given a quantum statistical model defined by a set of $\mathfrak{p}-$parameters $\boldsymbol{\lambda}$, and any other possible sub-model defined by a set of (possibly reparametrized) $(\mathfrak{p}-1)$ parameters $\tilde{\boldsymbol{\lambda}}$, then the two corresponding AI measures $\mathcal{R}_{\boldsymbol{\lambda}}^{(\mathfrak{p})}$ and $\mathcal{R}_{\tilde{\boldsymbol{\lambda}}}^{(\mathfrak{p}-1)}$ satisfy the inequality

$$r_2 \leq \mathcal{R}_{\tilde{\boldsymbol{\lambda}}}^{(\mathfrak{p}-1)} \leq \mathcal{R}_{\boldsymbol{\lambda}}^{(\mathfrak{p})}\,, \tag{7.30}$$

where r_2 denotes the second largest eigenvalue of the matrix $\boldsymbol{\mathcal{I}}$ corresponding to the quantum statistical model $\varrho_{\boldsymbol{\lambda}}$.

Proof. As observed in [77], the eigenvalues of $\boldsymbol{\mathcal{I}}$ are either 0 or given in pairs $h_i = \pm r_i$, with $0 < r_i \leq 1, i = 1, \ldots, \delta$ and $\delta \leq \lfloor(\mathfrak{p}+1)/2\rfloor$. The thesis of the theorem is thus a simple corollary of the Cauchy interlace Theorem 6 stated above.

One can further show that, if we consider smaller sub-matrices of $\boldsymbol{\mathcal{I}}$, we can recursively apply this argument to smaller statistical sub-model $\bar{\boldsymbol{\lambda}}$ with $(\mathfrak{p}-j)$ parameters. Eventually one obtains that the AI measure for the corresponding statistical sub-model is bounded as

$$r_{j+1} \leq \mathcal{R}_{\bar{\boldsymbol{\lambda}}}^{(\mathfrak{p}-j)} \leq \mathcal{R}_{\boldsymbol{\lambda}}^{(\mathfrak{p})}. \tag{7.31}$$

In particular we see that any statistical sub-model with $(\mathfrak{p}-j)$ parameters is incompatible if we restrict ourselves to $j \leq \delta - 1$, since for those j we have that $r_i > 0$. This observation leads to the following corollary:

Corollary 1: Upper bound on the number of compatible parameters

By denoting with δ the number of strictly positive eigenvalues of $\boldsymbol{\mathcal{I}}$, then the quantum statistical model $\varrho_{\boldsymbol{\lambda}}$ contains at number of compatible parameters that is upper bounded as

$$\mathfrak{p}_{\mathsf{comp}} \leq \mathfrak{p}_{\mathsf{comp}}^{(bound)} = \mathfrak{p} - \delta\,. \tag{7.32}$$

This result can be easily applied to the full estimation problem we studied in the previous section. Indeed, we can use the same evidence we have for Conjecture 2 to conjecture that the eigenvalues of the matrix $\boldsymbol{\mathcal{I}}$ are

$$\mathrm{Eig}(\boldsymbol{\mathcal{I}}) = \left\{0, ..., 0, \pm r_{(1,0)}, \pm r_{(2,0)}, \pm r_{(2,1)}, ..., \pm r_{(d-1,d-3)}, \pm r_{(d-1,d-2)}\right\} \tag{7.33}$$

where

$$r_{i,j} = \tanh\left(\frac{\beta(\Delta_i - \Delta_j)}{2}\right) \tag{7.34}$$

and $(\Delta_0, ..., \Delta_{d-1})$ are the β-normalized eigenvalues in ascending order of H, defined in Eq. (7.26). If the eigenvalues of H are non-degenerate, the number of strictly positive eigenvalues of $\boldsymbol{\mathcal{I}}$ is simply

$$\delta_{\mathsf{ndg}} = \binom{d}{2} = \frac{d(d-1)}{2}. \tag{7.35}$$

Instead, for H with degenerate spectrum, the result slightly change. Indeed, if we denote with κ the number of distinct degenerate eigenvalues and with η_i the corresponding degeneracies (with $i = 1, ..., \kappa$), then the number of strictly positive eigenvalues is

$$\delta_{\mathsf{dg}} = \binom{d}{2} - \sum_{i=1}^{\kappa} \binom{\eta_i}{2} = \frac{d(d-1)}{2} - \sum_{i=1}^{\kappa} \frac{\eta_i(\eta_i - 1)}{2}. \tag{7.36}$$

Thus, given the numerical evidence we obtained from our simulations, we conjecture the following

Conjecture 3: Upper bound on the number of compatible parameters for the full estimation of a d-dimensional quantum system

By denoting with d the dimension of the quantum system $\varrho_{\boldsymbol{\lambda}}$, the number of compatible parameters $\mathfrak{p}_{\mathsf{comp}}$ in the full estimation of the $d^2 - 1$-parameters describing $\varrho_{\boldsymbol{\lambda}}$ is upper bounded by the quantity

$$\begin{aligned} \mathfrak{p}_{\mathsf{comp}}^{(bound)} &= d^2 - 1 - \delta_{\mathsf{dg}} \\ &= \frac{(d+2)(d-1)}{2} + \sum_{i=1}^{\kappa} \frac{\eta_i(\eta_i - 1)}{2}, \end{aligned} \tag{7.37}$$

where κ is the number of distinct degenerate eigenvalues and η_i the degeneracy degree, with $i = 1, ..., \kappa$.

This conjecture shows that the value of $\mathfrak{p}_{\mathsf{comp}}^{(bound)}$ depends on the values of the parameters, and in particular on the values that makes the corresponding density matrix degenerate. Indeed, the larger is the number of degenerate eigenvalues, the larger is the maximum number of possible compatible parameters. In the limit of full degeneracy, i.e. $\kappa = 1$ and $\eta_i = d$, we see that $\mathfrak{p}_{\mathsf{comp}}^{(bound)} \to d^2 - 1$, i.e equals the number the number of parameters of the model. Instead, in the case with no degeneracy in the spectrum of H, we have the minimum value, i.e. $\mathfrak{p}_{\mathsf{comp}}^{(bound)} = (d+2)(d-1)/2$. We would also like to stress that the model is always full-rank as far as the value of β is finite, independently on the number of degenerate eigenvalues of H.

An upper bound on the number of compatible parameters has been also derived recently in [209] by following a different approach and exploiting the algebraic structure of the quantum statistical model. We have compared this bound with our bound for the full estimation of a qubit, that is by considering the estimation of the Bloch sphere parameters $\boldsymbol{\lambda} = (r, \theta, \phi)$. We found that the matrix $\boldsymbol{\mathcal{I}}$ has eigenvalues $\mathrm{Eig}(\boldsymbol{\mathcal{I}}) = \{r, -r, 0\}$, leading to the upper bound $\mathfrak{p}_{\mathsf{comp}}^{(bound)} = 2$. This results does indeed coincide with the one obtained in [209].

We also remark that, while the bound in [209] was derived for finite dimensional Hilbert space, in our case we made no assumption on the dimension of the Hilbert space. Hence we can apply our result also for infinite dimensional system. For instance, let us consider the paradigmatic case of the estimation of the parameters characterizing a single-mode Gaussian state defined as in Eq. (7.14) and already treated in Sec. 7.2. The

spectrum of the corresponding matrix $\boldsymbol{\mathcal{I}}$ is given by

$$\text{Eig}(\boldsymbol{\mathcal{I}}) = \left\{ \frac{2\mu}{1+\mu^2}, \mu, 0, -\mu, -\frac{2\mu}{1+\mu^2} \right\}. \tag{7.38}$$

This leads to the AI measure for the complete statistical model $\mathcal{R}^{(5)}_{\boldsymbol{\lambda}} = 2\mu/(1+\mu^2)$ we discussed above. By further inspecting the set of eigenvalues above we can however also conclude that for any subset of $\mathfrak{p} = 4$ parameters $\tilde{\boldsymbol{\lambda}}$, the corresponding AI parameter is bounded as

$$\mu \leq \mathcal{R}^{(4)}_{\tilde{\boldsymbol{\lambda}}} \leq \frac{2\mu}{1+\mu^2}, \tag{7.39}$$

and that there is a maximum of $\mathfrak{p}^{(bound)}_{\text{comp}} = 3$ compatible parameters. In general, by observing the form of the Uhlmann curvature matrix we also see that the only incompatible models are the one which deals with the simultaneous estimation of $\{r, \varphi\}$ or $\{\mathfrak{Re}\alpha, \mathfrak{Im}\alpha\}$.

In the examples above, if we restrict to subsets of the original parameters $\boldsymbol{\lambda} = \{\mathfrak{Re}\alpha, \mathfrak{Im}\alpha, r, \varphi, N\}$, all the results are directly availabe from the explicit solution of the SLD-QFIM (7.22a) – (7.22f) and the Uhlmann matrix (7.23a) – (7.23b). Here below we rather present an example where the results cannot be obtained straightforwardly in analytical form, while the properties discussed above can still provide a first insight without needing to solve exactly the estimation problem.

We address the estimation of two dynamical parameters, the frequency and the loss rate $\ddot{\boldsymbol{\lambda}} = \{\omega, \gamma\}$ that characterize the evolution due to the Markovian master equation

$$\dot{\varrho} = -i\frac{\omega}{2}[\widehat{q}^2 + \widehat{p}^2, \varrho] + \gamma \mathcal{D}[\widehat{a}]\varrho, \tag{7.40}$$

with $\mathcal{D}[\widehat{a}]\varrho = \widehat{a}\varrho\widehat{a}^\dagger - \frac{1}{2}\left(\widehat{a}^\dagger\widehat{a}\varrho + \varrho\widehat{a}^\dagger\widehat{a}\right)$. By consider an initial Gaussian state $\varrho(0)$ as the one in Eq. (7.14), the dynamics remains Gaussian and thus can be fully described by means of the first and second moments of its quadrature operators. In particular one can readily evaluate analytically the purity of the quantum state, obtaining

$$\mu(t) = \sqrt{(1-e^{-\gamma t})(1-e^{-\gamma t}(1-2s_2(0))) + e^{-2\gamma t}\mu(0)^2}, \tag{7.41}$$

From this result and via Eq. (7.24), we can directly evaluate $\mathcal{R}^{(5)}_{\boldsymbol{\lambda}}$, whereas the AI measure $\mathcal{R}^{(2)}_{\ddot{\boldsymbol{\lambda}}}$ for the quantum statistical model defined above is evaluated numerically by exploiting the techniques reported in Appendix 7.A. To present the results, we choose the initial state to be a pure state $N = 0$ and we parametrize it in terms of its average excitations number $\langle\widehat{a}^\dagger\widehat{a}\rangle$ and its fraction of squeezing η defined as

$$\langle\widehat{a}^\dagger\widehat{a}\rangle = |\alpha|^2 + \sinh(r)^2, \tag{7.42}$$

$$\eta = \frac{\sinh(r)^2}{\langle\widehat{a}^\dagger\widehat{a}\rangle}. \tag{7.43}$$

We plot the results in Fig. 7.2 and we see that $\mathcal{R}^{(5)}_{\boldsymbol{\lambda}}$ is, as expected, always larger than $\mathcal{R}^{(2)}_{\ddot{\boldsymbol{\lambda}}}$, confirming that $\mathcal{R}^{(5)}_{\boldsymbol{\lambda}}$ can be used as an upper bound for the quantumness for any other sub-statistical model. Besides, as we see from the left panel in Fig. 7.2, the upper bound may not be much informative, since the evolution of $\mathcal{R}^{(5)}_{\boldsymbol{\lambda}}$ and $\mathcal{R}^{(2)}_{\ddot{\boldsymbol{\lambda}}}$ in time are opposite. In addition, this example shows that the condition on the number of eigenvalue is not sufficient to have a compatible model.

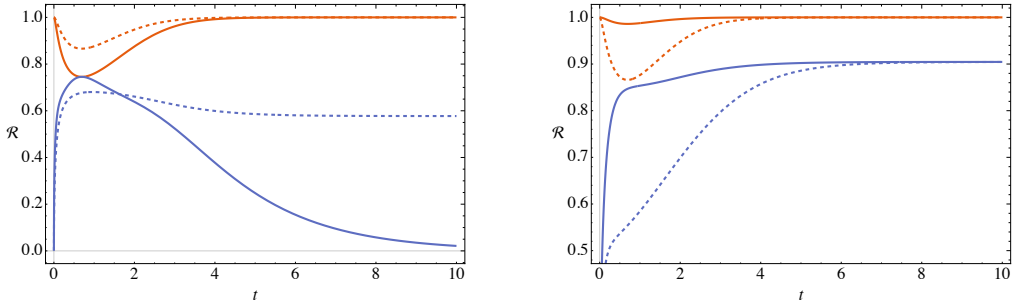

Figure 7.2: Plot of $\mathcal{R}_{\boldsymbol{\lambda}}^{(5)}$ (red line) and $\mathcal{R}_{\hat{\boldsymbol{\lambda}}}^{(2)}$ (blue line). Left panel: $\langle \hat{a}^\dagger \hat{a} \rangle = 4$; thick line: $\eta = 1$; dashed line: $\eta = 0.5$. Right panel: $\eta = 0.1$; thick line $\langle \hat{a}^\dagger \hat{a} \rangle = 4$; dashed line: $\langle \hat{a}^\dagger \hat{a} \rangle = 20$. Both panel: $\gamma = \omega = 1$.

7.4 Conclusions

In this chapter, we have studied in details the properties of the AI measure $\mathcal{R}_{\boldsymbol{\lambda}}$ of incompatibility and discussed its use in assessing the quantumness of multiparameter estimation problems. At first, we have focused on the estimation of the full set of parameters characterizing a given quantum system, showing that for qubits and single-mode Gaussian systems $\mathcal{R}_{\boldsymbol{\lambda}}$ is a simple monotonous function of the purity μ of the state. We have then considered a generic d-dimensional quantum systems and, using analytical and numerical tools, we found that in general the one-to-one correspondence between $\mathcal{R}_{\boldsymbol{\lambda}}$ and μ does not hold anymore. However, numerical results suggest that the maximum number of AI is attainable only for quantum statistical models having a purity $\mu \geq 1/(d-1)$. We conjecture that this may be a general property of d-dimensional quantum systems. Upon considering quantum statistical models described as Gibbs state of a given Hamiltonian, we have also shown that the AI measure can be written as a simple function of the *fictitious* temperature parameter and the spectrum of the Hamiltonian.

We have then studied in detail the role of the spectrum of the matrix $\boldsymbol{\mathcal{I}} = i\boldsymbol{\mathcal{Q}}(\boldsymbol{\lambda})^{-1}\boldsymbol{\mathcal{U}}(\boldsymbol{\lambda})$ and have determined bounds on $\mathcal{R}_{\boldsymbol{\lambda}}$ for quantum statistical *submodels*. In particular, we have shown that the number of strictly positive eigenvalues of $\boldsymbol{\mathcal{I}}$ determines the maximum number of compatible parameters in a given statistical model.

Very recently there has been much interest in deriving bounds that apply when one allows measurements on a finite number of copies [100, 89]; we thus expect that our approach can be extended from the asymptotic model, identifying and studying a hierarchy of incompatibility measures in this *finite copies* scenario. More in general our results pave the way to a deeper understanding of the fundamental properties of multiparameter quantum estimation, and provide potentially useful tools to approach multiparameter problems that cannot be addressed analytically.

Appendix

7.A Multiparameter estimation for continuous-variable Gaussian states

In this section we focus on estimation problems in bosonic continuous variable systems. In particular, we study n modes Gaussian state [132, 314], which are properly described in terms of quadrature operators $\widehat{\boldsymbol{r}} = \{\widehat{q}_1, \widehat{p}_1, \ldots, \widehat{q}_n, \widehat{p}_n\}$. They satisfy the canonical commutation relation

$$[\widehat{r}_j, \widehat{r}_k] = i\Omega_{jk}, \tag{7.44}$$

where $\Omega = i\sigma_y^{\oplus n}$. A Gaussian state ϱ is completely determined by its vector of first moments $\boldsymbol{d} = \mathrm{Tr}\{\varrho\widehat{\boldsymbol{r}}\}$ and its covariance matrix (CM) $\boldsymbol{\sigma} = \mathrm{Tr}\left\{\varrho\{(\widehat{\boldsymbol{r}} - \boldsymbol{d}), (\widehat{\boldsymbol{r}} - \boldsymbol{d})^T\}\right\}$, with $\{\widehat{\boldsymbol{l}}, \widehat{\boldsymbol{l}}^T\}_{jk} = \widehat{l}_j\widehat{l}_k + \widehat{l}_k\widehat{l}_j$ [132, 314].

In order to derive the SLD-QFI matrix elements, several approaches have been proposed in the literature [276, 194, 23, 314, 254, 306] . As we are interested also in the Uhlmann curvature matrix, in the following we will focus on the derivations pursued in [314, 254] that are indeed based on the writing the SLD operators in terms of the moments of the Guassian states defining the quantum statistical model. Let us then assume that a set of parameters $\boldsymbol{\lambda}$ defines a quantum statistical models in a family of Gaussian quantum states $\varrho_{\boldsymbol{\lambda}}$. One shows that the SLD for a parameter $\alpha \in \boldsymbol{\lambda}$ is at most quadratic in the moments [314] and can be written as

$$\widehat{L}_\alpha = L_\alpha^{(0)}\mathbb{I} + \boldsymbol{L}_\alpha^{(1)} \cdot \widehat{\boldsymbol{r}} + \widehat{\boldsymbol{r}}^T \cdot \boldsymbol{L}_\alpha^{(2)} \cdot \widehat{\boldsymbol{r}}, \tag{7.45}$$

where $L_\alpha^{(0)}$ is a real number, $\boldsymbol{L}_\alpha^{(1)}$ is $2n$ real vector and $\boldsymbol{L}_\alpha^{(2)}$ is a $2n \times 2n$ real symmetric matrix. After some algebra, one can find that the SLD-QFI matrix elements are given by [314, 254]

$$\mathcal{Q}_{\alpha\beta} = \frac{1}{2}\mathrm{Tr}\left\{L_\alpha^{(2)}(\partial_\beta\boldsymbol{\sigma})\right\} + 2(\partial_\alpha\boldsymbol{d}^T)\boldsymbol{\sigma}^{-1}(\partial_\beta\boldsymbol{d}) \tag{7.46}$$

Here below we derive the analogous result for the Uhlmann curvature matrix. First, we evaluate the commutator of $\widehat{L}_\alpha$ and $\widehat{L}_\beta$, that is

$$\begin{aligned}\left[\widehat{L}_\alpha, \widehat{L}_\beta\right] = &\left[\boldsymbol{L}_\alpha^{(1)^T}\widehat{\boldsymbol{r}}, \boldsymbol{L}_\beta^{(1)^T}\widehat{\boldsymbol{r}}\right] + \left[\boldsymbol{L}_\alpha^{(1)^T}\widehat{\boldsymbol{r}}, \widehat{\boldsymbol{r}}^T\boldsymbol{L}_\beta^{(2)}\widehat{\boldsymbol{r}}\right] + \\ &+ \left[\widehat{\boldsymbol{r}}^T\boldsymbol{L}_\alpha^{(2)}\widehat{\boldsymbol{r}}, \boldsymbol{L}_\beta^{(1)^T}\widehat{\boldsymbol{r}}\right] + \left[\widehat{\boldsymbol{r}}^T\boldsymbol{L}_\alpha^{(2)}\widehat{\boldsymbol{r}}, \widehat{\boldsymbol{r}}^T\boldsymbol{L}_\beta^{(2)}\widehat{\boldsymbol{r}}\right].\end{aligned} \tag{7.47}$$

By recalling that $[\widehat{r}_j, \widehat{r}_k] = i\Omega_{jk}$, the first term of the latter is (we use Einstein convention on indexes summations)

$$\left[\boldsymbol{L}_\alpha^{(1)^T}\widehat{\boldsymbol{r}}, \boldsymbol{L}_\beta^{(1)^T}\widehat{\boldsymbol{r}}\right] = L_{\alpha,i}^{(1)} L_{\beta,j}^{(1)} \left[\widehat{r}_i, \widehat{r}_j\right] = i\boldsymbol{L}_\alpha^{(1)^T}\Omega\boldsymbol{L}_\beta^{(1)}\mathbb{I}; \tag{7.48}$$

the second term is (we recall that $L_{\alpha,jk}^{(2)} = L_{\alpha,kj}^{(2)}$)

$$\begin{aligned}\left[\boldsymbol{L}_\alpha^{(1)^T}\widehat{\boldsymbol{r}}, \widehat{\boldsymbol{r}}^T\boldsymbol{L}_\beta^{(2)}\widehat{\boldsymbol{r}}\right] &= L_{\alpha,i}^{(1)} L_{\beta,jk}^{(2)} \left[\widehat{r}_i, \widehat{r}_j\widehat{r}_k\right] = \\ &= L_{\alpha,i}^{(1)} L_{\beta,jk}^{(2)} \left(\left[\widehat{r}_i, \widehat{r}_j\right]\widehat{r}_k + \widehat{r}_j\left[\widehat{r}_i, \widehat{r}_k\right]\right) = \\ &= L_{\alpha,i}^{(1)} L_{\beta,jk}^{(2)} \left(i\Omega_{ij}\widehat{r}_k + \widehat{r}_j i\Omega_{ik}\right) = \\ &= 2i\boldsymbol{L}_\alpha^{(1)^T}\Omega\boldsymbol{L}_\beta^{(2)}\widehat{\boldsymbol{r}};\end{aligned} \tag{7.49}$$

while the third term is

$$\left[\widehat{\boldsymbol{r}}^T\boldsymbol{L}_\alpha^{(2)}\widehat{\boldsymbol{r}}, \boldsymbol{L}_\beta^{(1)^T}\widehat{\boldsymbol{r}}\right] = 2i\widehat{\boldsymbol{r}}^T\boldsymbol{L}_\alpha^{(2)}\Omega\boldsymbol{L}_\beta^{(1)}; \tag{7.50}$$

and eventually the fourth term is (we used the symmetry of $L_\alpha^{(2)}$ and the skew-symmetry of Ω)

$$\begin{aligned}\left[\widehat{\boldsymbol{r}}^T\boldsymbol{L}_\alpha^{(2)}\widehat{\boldsymbol{r}}, \widehat{\boldsymbol{r}}^T\boldsymbol{L}_\beta^{(2)}\widehat{\boldsymbol{r}}\right] &= L_{\alpha,ij}^{(2)} L_{\beta,kl}^{(2)} \left[\widehat{r}_i\widehat{r}_j, \widehat{r}_k\widehat{r}_l\right] = \\ &= L_{\alpha,ij}^{(2)} L_{\beta,kl}^{(2)} \left(i\Omega_{jk}\widehat{r}_i\widehat{r}_l + i\Omega_{ik}\widehat{r}_j\widehat{r}_l + i\Omega_{jl}\widehat{r}_k\widehat{r}_i + i\Omega_{il}\widehat{r}_k\widehat{r}_j\right) = \\ &= 2i\widehat{\boldsymbol{r}}^T\left(\boldsymbol{L}_\alpha^{(2)}\Omega\boldsymbol{L}_\beta^{(2)} - \boldsymbol{L}_\beta^{(2)}\Omega\boldsymbol{L}_\alpha^{(2)}\right)\widehat{\boldsymbol{r}}.\end{aligned} \tag{7.51}$$

So eventually we obtain

$$\left[\widehat{L}_\alpha, \widehat{L}_\beta\right] = i\left(\boldsymbol{L}_\alpha^{(1)^T}\Omega\boldsymbol{L}_\beta^{(1)}\mathbb{I} + 2\boldsymbol{B}^T\widehat{\boldsymbol{r}} + 2\widehat{\boldsymbol{r}}^T\boldsymbol{A}\widehat{\boldsymbol{r}}\right) \tag{7.52}$$

where $\boldsymbol{A}$ and $\boldsymbol{B}$ are respectively a $d \times d$ symmetric matrix and a d vector

$$\boldsymbol{A} = \boldsymbol{L}_\alpha^{(2)}\Omega\boldsymbol{L}_\beta^{(2)} - \boldsymbol{L}_\beta^{(2)}\Omega\boldsymbol{L}_\alpha^{(2)} = 2\boldsymbol{L}_\alpha^{(2)}\Omega\boldsymbol{L}_\beta^{(2)}, \tag{7.53}$$

$$\boldsymbol{B} = \boldsymbol{L}_\alpha^{(2)}\Omega\boldsymbol{L}_\beta^{(1)} - \boldsymbol{L}_\beta^{(2)}\Omega\boldsymbol{L}_\alpha^{(1)} \tag{7.54}$$

Now we can evaluate

$$\mathcal{U}_{\alpha\beta} = -\frac{i}{2}\mathrm{Tr}\left\{\varrho_{\boldsymbol{\lambda}}\left[\widehat{L}_\alpha, \widehat{L}_\beta\right]\right\} = \tag{7.55}$$

$$= \frac{1}{2}\boldsymbol{L}_\alpha^{(1)^T}\Omega\boldsymbol{L}_\beta^{(1)} + \boldsymbol{L}_\alpha^{(1)^T}\Omega\boldsymbol{L}_\beta^{(2)}\boldsymbol{d} + \boldsymbol{d}^T\boldsymbol{L}_\alpha^{(2)}\Omega\boldsymbol{L}_\beta^{(1)} + \mathrm{Tr}\left\{\varrho_{\boldsymbol{\lambda}}\widehat{\boldsymbol{r}}^T\boldsymbol{A}\widehat{\boldsymbol{r}}\right\} \tag{7.56}$$

Since $A_{ij}\Omega_{ij} = 0$, we obtain that

$$\begin{aligned}\mathrm{Tr}\left\{\varrho_{\boldsymbol{\lambda}}\widehat{\boldsymbol{r}}^T\boldsymbol{A}\widehat{\boldsymbol{r}}\right\} &= A_{ij}\mathrm{Tr}\left\{\varrho_{\boldsymbol{\lambda}}\widehat{r}_i\widehat{r}_j\right\} = \\ &= A_{ij}\left(\frac{\sigma_{ij}}{2} + \frac{i\Omega_{ij}}{2} + d_i d_j\right) = \\ &= \frac{1}{2}\mathrm{Tr}\left\{\boldsymbol{A}\boldsymbol{\sigma}\right\} + \boldsymbol{d}^T\boldsymbol{A}\boldsymbol{d} = \\ &= \mathrm{Tr}\left\{\boldsymbol{L}_\alpha^{(2)}\Omega\boldsymbol{L}_\beta^{(2)}\boldsymbol{\sigma}\right\} + 2\boldsymbol{d}^T\boldsymbol{L}_\alpha^{(2)}\Omega\boldsymbol{L}_\beta^{(2)}\boldsymbol{d}\end{aligned} \tag{7.57}$$

From [314] we recall that $\boldsymbol{L}_{\alpha}^{(1)} = 2\boldsymbol{\sigma}^{-1}(\partial_{\alpha}\boldsymbol{d}) - 2\boldsymbol{L}_{\alpha}^{(2)}\boldsymbol{d}$ and so we derive the following

$$\frac{1}{2}\boldsymbol{L}_{\alpha}^{(1)^T}\Omega\boldsymbol{L}_{\beta}^{(1)} = 2\Big((\partial_{\alpha}\boldsymbol{d})^T\boldsymbol{\sigma}^{-1}\Omega\boldsymbol{\sigma}^{-1}(\partial_{\beta}\boldsymbol{d}) - \boldsymbol{d}^T\boldsymbol{L}_{\alpha}^{(2)}\Omega\boldsymbol{\sigma}^{-1}(\partial_{\beta}\boldsymbol{d}) + \tag{7.58}$$

$$- (\partial_{\alpha}\boldsymbol{d})^T\boldsymbol{\sigma}^{-1}\Omega L_{\beta}^{(2)}\boldsymbol{d} + \boldsymbol{d}^T\boldsymbol{L}_{\alpha}^{(2)}\Omega\boldsymbol{L}_{\beta}^{(2)}\boldsymbol{d}\Big) \tag{7.59}$$

$$\boldsymbol{L}_{\alpha}^{(1)^T}\Omega\boldsymbol{L}_{\beta}^{(2)}\boldsymbol{d} = 2\left((\partial_{\alpha}\boldsymbol{d})^T\boldsymbol{\sigma}^{-1}\Omega\boldsymbol{L}_{\beta}^{(2)}\boldsymbol{d} - \boldsymbol{d}^T\boldsymbol{L}_{\alpha}^{(2)}\Omega\boldsymbol{L}_{\beta}^{(2)}\boldsymbol{d}\right) \tag{7.60}$$

$$\boldsymbol{d}^T\boldsymbol{L}_{\alpha}^{(2)}\Omega\boldsymbol{L}_{\beta}^{(1)} = 2\left(\boldsymbol{d}^T\boldsymbol{L}_{\alpha}^{(2)}\Omega\boldsymbol{\sigma}^{-1}(\partial_{\beta}\boldsymbol{d}) - \boldsymbol{d}^T\boldsymbol{L}_{\alpha}^{(2)}\Omega\boldsymbol{L}_{\beta}^{(2)}\boldsymbol{d}\right) \tag{7.61}$$

By inserting these last calculations, we end up with the following Uhlmann matrix

$$\mathcal{U}_{\alpha\beta} = \mathrm{Tr}\left\{\boldsymbol{L}_{\alpha}^{(2)}\Omega\boldsymbol{L}_{\beta}^{(2)}\boldsymbol{\sigma}\right\} + 2(\partial_{\alpha}\boldsymbol{d})\boldsymbol{\sigma}^{-1}\Omega\boldsymbol{\sigma}^{-1}(\partial_{\beta}\boldsymbol{d}). \tag{7.62}$$

Please notice that our result differ from that in [254] by a factor 2 in the first term of the Uhlmann matrix.

If we now focus on single-mode Gaussian state, we can write (7.46) and (7.62) only in terms of the covariance matrix $\boldsymbol{\sigma}$, the vector $\boldsymbol{d}$ and the purity of the state $\mu = 1/\sqrt{\det\boldsymbol{\sigma}}$ as

$$\mathcal{Q}_{\alpha\beta} = \frac{1}{2}\frac{\mathrm{Tr}[(\boldsymbol{\sigma}^{-1}\partial_{\alpha}\boldsymbol{\sigma})(\boldsymbol{\sigma}^{-1}\partial_{\beta}\boldsymbol{\sigma})]}{1+\mu^2} + \frac{2\partial_{\alpha}\mu\partial_{\beta}\mu}{1-\mu^4} + 2\left(\partial_{\alpha}\boldsymbol{d}\right)^T\boldsymbol{\sigma}^{-1}(\partial_{\beta}\boldsymbol{d}) \tag{7.63}$$

$$\mathcal{U}_{\alpha\beta} = \frac{\mu^2}{2(\mu^2+1)^2}\mathrm{Tr}\left\{\boldsymbol{\sigma}\Omega\left[\partial_{\alpha}\boldsymbol{\sigma}\boldsymbol{\sigma}^{-1}, \partial_{\beta}\boldsymbol{\sigma}\boldsymbol{\sigma}^{-1}\right]\right\} + 2\mu^2(\partial_{\alpha}\boldsymbol{d})\Omega(\partial_{\beta}\boldsymbol{d}). \tag{7.64}$$

Part IV

Engineering of quantum systems

CHAPTER 8

Feedback-assisted quantum search by continuous-time quantum walks

Continuous-time quantum walk (CTQW) have been introduced in Sec. 3.2 to model the evolution of a quantum particle, or excitation, over a discrete set of positions [131, 200, 340]. Since a CTQW evolves over a graph, it is strongly related to applications over networks, including quantum spatial search [94, 189, 93, 83, 265, 36, 279]. The ability to redirect or control information over a graph in an efficient way is essential to develop protocols involving quantum networks and to deal with a large amount of structured data. To this aim, in this chapter we develop a protocol to guide the walker toward a target node on a graph by exploiting the tools of quantum control.

The theory of quantum control [350] addresses the problem of preparing a quantum system in a desired quantum state or with some desired quantum properties. In quantum feedback-control strategies the quantum system under control is measured (typically continuously in time) and the information acquired is exploited in order to optimize a feedback operation on the system itself. This kind of strategies has been studied in great detail, in particular with the aim of generating quantum states with non-classical properties such as squeezing or entanglement [349, 348, 123, 337, 315, 333, 150, 152, 177, 231, 233, 232, 64, 234, 193, 364, 300, 121] or to cool optomehcanical systems towards their ground states, with the experimental results recently demonstrated in [297, 226, 336].

In this chapter, we propose a novel approach to quantum search on graphs and establish a new and unexplored line of research combining CTQWs with quantum feedback-control protocols. In our system, the walker is interacting with an environment that is continuously monitored. As a result, the system evolution is a quantum stochastic trajectory and, based on the result of the measurement, a feedback protocol is applied. We will prove that it is possible to drive the walker towards a target state by optimizing the corresponding target fidelity at each step. Our method differs from other methods that have been developed since it allows the walker to be guided continuously to the target node. In the standard spatial search protocol the oracle is described as a projector operator onto the target state. With our approach we modify this paradigm. We consider a *dynamical* oracle encoded in the feedback operation. This means that the final projective measurement on the walker, to be performed at any time t after a certain threshold time t_{th}, has a high probability of success. In particular, we find that once the walker reaches the target node it remains stuck in it thanks to the feedback operation. This lift the burden of performing a final measurement at a very specific time, by allowing us to measure the walker position at any time $t \geq t_{th}$.

The chapter is organized as follows: in Sec. 8.1 we give a brief introduction to continuous-time quantum walks focusing on quantum spatial search on graphs. In Sec. 8.2 we introduce continuously monitored quantum systems and unitary (measurement-based) feedback strategies. In Sec. 8.3, we present our search scheme and we describe

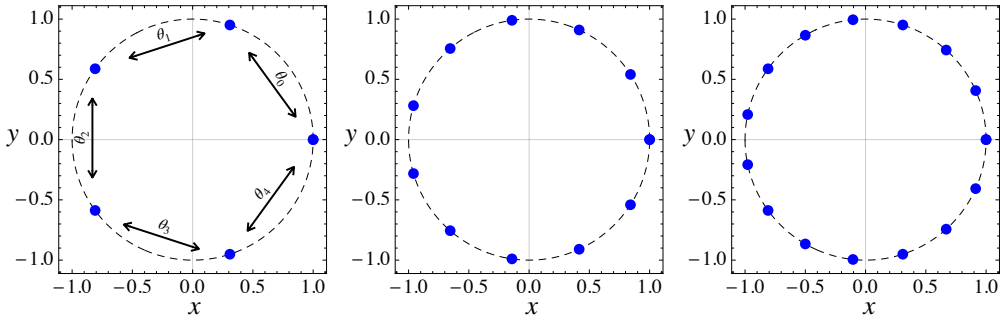

Figure 8.1.1: Cycle graph embedded in a plane on a circle of unit radius. Left panel: $N = 5$; Central panel: $N = 11$; Right panel: $N = 15$.

the idea behind our feedback protocol. In Sec. 8.4 we analyze our results for the different control strategies we have considered. In Sec. 8.5 we conclude the chapter with some remarks and outlooks. The chapter is followed by an Appendix where we analyze some side aspects of the work and results. We also mention that throughout the chapter we set $\hbar = 1$.

8.1 Quantum walks and spatial search on graphs

A continuous-time quantum walk describes the continuous motion of a quantum particle over a discrete set of positions. As we have already discussed, underlying every walk there is a graph G, which is described as a pair $G = (V, E)$ where $V = \{0, 1, \ldots, N-1\}$ is the set of vertices and E is the set of undirected edges, i.e. all the pairs of adjacent vertices in V. For a CTQW, the vertices represent the positions that the particle can occupy while the edges encode all the possible paths that a walker can move across. We denote the order of the graph as the number of nodes $N = |V|$. For a more detailed presentation of CTQWs we refer the reader to Chapter 3.2 in the introduction.

In this chapter, we are going to focus mainly on the cycle graph, see Fig. 8.1.1. Each vertex is adjacent to two other vertices, hence $d_j = 2$ for all js. This means that the cycle graph is a regular graph whose Laplacian matrix is given by

$$L = 2\mathbb{I}_N - \sum_{k=0}^{N-1}{}' \left(|k-1\rangle\langle k| + |k+1\rangle\langle k|\right) \tag{8.1}$$

The primed summation symbol denotes that periodic boundary conditions: the terms $|-1\rangle\langle 0|$ corresponds to $|N-1\rangle\langle 0|$, while $N\rangle\langle N-1|$ corresponds to $|0\rangle\langle N-1|$. The cycle is also a circulant graph, whose nice properties have been discussed in Sec. 4.5.3.

Among all the applications, CTQWs have been used to improve spatial search algorithms. In this problem, the main goal is to exploit the coherent evolution of a quantum walker to find a marked vertex on a graph faster than its classical counterpart. In the quantum spatial search of a marked node $|w\rangle$, the walker evolves under the Hamiltonian:

$$H_S = \gamma L - \beta |w\rangle\langle w| \tag{8.2}$$

where γ is a real parameter and the operator $|w\rangle\langle w|$ is the oracle Hamiltonian i.e. a projector onto the target state. The walker is usually initialized in the uniform superposition

of all nodes

$$|\psi_0\rangle = \frac{1}{\sqrt{N}} \sum_{k=0}^{N-1} |k\rangle, \tag{8.3}$$

with no bias toward the target state. The algorithm is successful if the probability of finding the target node $p_w(t_s) = |\langle w|e^{-iH_S t_s}|\psi_0\rangle|^2$ is as close as 1 as possible in a time $t_s = \mathcal{O}(\sqrt{N})$. It was shown that a $\sqrt{N}$ speedup can be obtained for specific topologies, such as the complete and hypercube graphs and $(d > 4)$-dimensional lattices [94, 131]. Later studies proved fast search for different kinds of graphs [82, 275, 352, 85, 354, 342], and a comprehensive analysis of the algorithm's performances was carried out in [84], which recovers previous graph-dependent results as special cases. It is worth mentioning here that considering different oracle operators, such as those which modify the edges connected to the target node, allows to reach a search time $t_s = \mathcal{O}(\sqrt{N \ln N})$ in two-dimensional $(d = 2)$ lattices, by building Hamiltonians that exhibit Dirac points in their dispersion relation [93, 137]. Since low dimensional lattices, such as the cycle graph, do not sustain fast search with the standard algorithm defined by Hamiltonian (8.2), novel strategies must be envisaged to boost the spatial search on these structures.

We report here the success probability of the standard search algorithm on the cycle graph to set a benchmark for our approach. The parameter β/γ in Eq. (8.2) is the oracle parameter that we need to optimize to improve the search. In this way, we can compare the different search strategies, by showing the dynamical quantities of interest in terms of the re-scaled time γt. If we apply this algorithm to one-dimensional lattices, such as the cycle graph, the success probability of finding the target does not scale well with the size of the graph. In figure 8.1.2, we show how the spatial search algorithm performs in the case of a cycle graph. We compare three different sizes: $N = 5, 11, 15$. For each graph, we numerically optimize the oracle parameter and then compute the probability of finding the target, also called reward function and defined in Eq. (8.23), as a function of time γt. We see that for already $N = 15$ the maximum probability of finding the target is less than 0.5 in the time interval considered.

8.2 Continuous monitoring and Feedback control

8.2.1 Continuously monitored quantum systems

We here provide a very basic introduction to continuously monitored quantum systems. We refer to the following references [350, 188, 63] for a more detailed introduction and for the derivation of the formulas provided in this Section.

We assume that the quantum system under exam interacts with a large Markovian environment described by a train of input bosonic operators $\widehat{a}_j(t)$ satisfying the canonical commutation relation $[\widehat{a}_j(t'), \widehat{a}_k^\dagger(t)] = \delta_{jk}\delta(t - t')$. The interaction with the system is then given in terms of the time-dependent interaction Hamiltonian

$$\widehat{H}^{int}(t) = i \sum_j \sqrt{\kappa_j} \left(\widehat{c}_j \widehat{a}_j^\dagger(t) - \widehat{c}_j^\dagger \widehat{a}_j(t) \right), \tag{8.4}$$

in which κ_j represent the coupling strengths, while $\widehat{c}_j$ are operators acting on the system Hilbert space (one should also notice that the parameter t in the operators $\widehat{a}_j(t)$ is just a label denoting the time at which each operator is interacting with the quantum system via the Hamiltonian). We also assume that the environmental modes $\widehat{a}_j(t)$

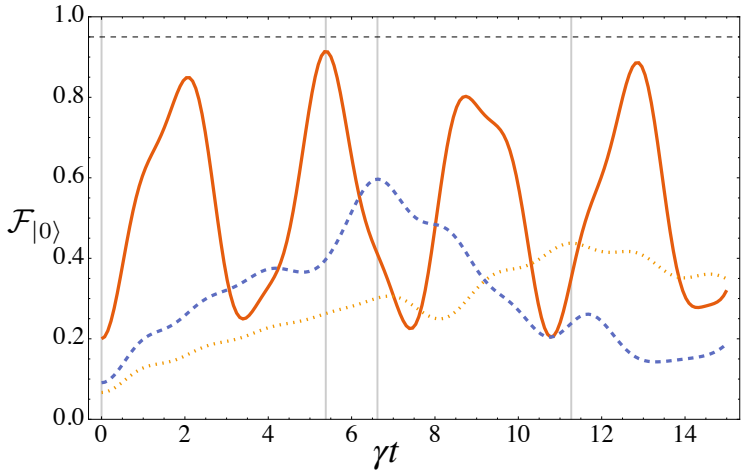

Figure 8.1.2: Reward function $\mathcal{F}_{|0\rangle}$ for the optimized standard algorithm with the projective oracle for $N = 5$ (red line), $N = 11$ (blue dashed line) and $N = 15$ (orange dotted line). For each size N, we found the optimal value for the β/γ parameter that gives the maximum value of $\mathcal{F}_{|0\rangle}$ in the considered time interval. We obtain the following: for $N = 5$, $\gamma t_{opt} = 5.38, \beta_{opt}/\gamma = 2.24$ and the maximum is $\mathcal{F}_{|0\rangle}(t_{opt}, \beta_{opt}) = 0.91$; for $N = 11$, $\gamma t_{opt} = 6.23, \beta_{opt}/\gamma = 1.19$ and the maximum is $\mathcal{F}_{|0\rangle}(t_{opt}, \beta_{opt}) = 0.60$; for $N = 15$, $\gamma t_{opt} = 11.28, \beta_{opt}/\gamma = 0.92$ and the maximum is $\mathcal{F}_{|0\rangle}(t_{opt}, \beta_{opt}) = 0.44$.

can be measured continuously in time, just after the interaction, in order to gain information on the state of the system itself. Notice that the interaction with the environment can be either considered already present, and that some degree of control on this environment is achievable in order to perform such a measurement, or that such an interaction can be effectively engineered with the purpose of weakly monitoring the system. Both these approaches are nowadays pursued efficiently in different physical platforms, in particular in circuit QED [250, 252, 165, 133, 240] and in optomechanical systems [344, 297, 296, 226, 336].

It is known that in quantum mechanics a measurement modifies the state of the quantum system that is (directly or indirectly) measured, and that the corresponding *conditional state* will depend both on the kind of measurement performed and on the outcome of the measurement. We will focus on continuous homodyne detection of the environmental modes with monitoring efficiencies η_j, corresponding to a set of continuous photocurrents

$$dy_t^{(j)} = \sqrt{\eta_j \kappa_j}\mathrm{Tr}\left\{\left(\widehat{c}_j + \widehat{c}_j^\dagger\right)\varrho^c\right\}dt + dW_t^{(j)}\,, \tag{8.5}$$

where $dW_t^{(j)}$ denotes the *innovation*, that is the difference between the result of the measurement $dy_t^{(j)}$ and the expected results, and mathematically correspond to independent Wiener increments satisfying $dW_t^{(j)}dW_t^{(k)} = \delta_{jk}dt$. The evolution of the quantum state $\varrho^c(t)$ conditioned on the photocurrents $dy_t^{(j)}$ is then given by the following stochastic

master equation (SME)

$$d\varrho^c = -i\left[\widehat{H}_s, \varrho^c(t)\right] dt + \sum_j \kappa_j \mathcal{D}\left[\widehat{c}_j\right] \varrho^c(t) dt + \sum_j \sqrt{\eta_j \kappa_j}\, \mathcal{H}\left[\widehat{c}_j\right] \varrho^c(t)\, dW_t^{(j)} \tag{8.6}$$

where $\widehat{H}_s$ is the Hamiltonian describing the evolution of the quantum system only, and where we have introduced the two following superoperators

$$\mathcal{D}\left[\widehat{c}\right] \bullet = \widehat{c} \bullet \widehat{c}^\dagger - \frac{1}{2}\left(\widehat{c}^\dagger \widehat{c} \bullet + \bullet \widehat{c}^\dagger \widehat{c}\right), \tag{8.7}$$

$$\mathcal{H}\left[\widehat{c}\right] \bullet = \widehat{c} \bullet + \bullet \widehat{c}^\dagger - \mathrm{Tr}\left\{(\widehat{c} + \widehat{c}^\dagger)\bullet\right\} \bullet . \tag{8.8}$$

The continuous outcomes of the photocurrents $\{dy_t^{(j)}\}$ thus define a particular conditional trajectory for the conditional state of the quantum system. By averaging over all the possible trajectories, i.e. over all the possible outcomes of the measurements, we obtain the evolution of the unconditional state $\varrho^u = \mathbb{E}_{\mathsf{traj}}[\varrho^c]$ that, by exploiting the property $\mathbb{E}_{\mathsf{traj}}\left[dW_t^{(j)}\right] = 0$, is desribed by a Markovian master equation in the Lindblad form

$$\frac{d\varrho^u}{dt} = -i\left[\widehat{H}_s, \varrho^u(t)\right] + \sum_j \kappa_j \mathcal{D}\left[\widehat{c}_j\right] \varrho^u(t). \tag{8.9}$$

The evolution of the conditional states described by the SME (8.6) can be equivalently described via the formula [301, 302]

$$\varrho^c(t+dt) = \frac{\widehat{M}_{\mathbf{dy}_t} \varrho^c(t) \widehat{M}^\dagger_{\mathbf{dy}_t} + \sum_j (1-\eta_j) \widehat{c}_j \varrho^c(t) \widehat{c}_j^\dagger\, dt}{\mathrm{Tr}\left\{\widehat{M}_{\mathbf{dy}_t} \varrho^c(t) \widehat{M}^\dagger_{\mathbf{dy}_t} + \sum_j (1-\eta_j) \widehat{c}_j \varrho^c(t) \widehat{c}_j^\dagger\, dt\right\}}, \tag{8.10}$$

where we have introduced the family of Kraus operators

$$\widehat{M}_{\mathbf{dy}_t} = \mathbb{I} - i\widehat{H}_s dt - \sum_j \left(\frac{\kappa_j}{2} \widehat{c}_j^\dagger \widehat{c}_j dt - \sqrt{\eta_j \kappa_j}\, \widehat{c}_j\, dy_t^{(j)}\right), \tag{8.11}$$

with $\mathbf{dy}_t = \{dy_t^{(1)}, ..., dy_t^{(K)}\}$ denoting the vector of the outcomes of the K mesaurement channels.
In our protocol we consider an initial pure state and perfect monitoring efficiency, i.e. $\eta_j = 1$ for all channels. Under these assumptions the conditional evolution is described by a stochastic Schrödinger equation, or equivalently via the Kraus operators as follows

$$|\psi^c(t+dt)\rangle = \frac{\widehat{M}_{\mathbf{dy}_t} |\psi^c(t)\rangle}{\sqrt{\langle \psi^c(t) | \widehat{M}^\dagger_{\mathbf{dy}_t} \widehat{M}_{\mathbf{dy}_t} | \psi^c(t)\rangle}}. \tag{8.12}$$

This will be extensively used in our numerical simulations to generate single trajectories at each infinitesimal time step.

8.2.2 Unitary quantum feedback

In addition to conditioning the evolution of the quantum state, the outcomes of the measurement performed can in principle be exploited to further modify the dynamics of the system. In this respect, here we briefly introduce unitary measurement-based quantum feedback. The idea is that, once the measurement outcomes $\mathbf{dy}_t$ are obtained, one performs a unitary operation $\widehat{U}_{fb}(t)$ on the quantum state, typically optimized in order to achieve a certain goal as, for example, the preparation of a certain target quantum state.

This unitary operation may depend only on the last measurement outcomes, or on the whole history of outcomes, and thus on the whole trajectory of the conditional state. In the first instance one talks about Markovian quantum feedback and one can derive a corresponding Markovian feedback master equation [348, 350]. In this work we will focus on the second kind of feedback, and thus our feedback strategy will be optimized by knowing both the last measurement outcomes and the conditional state $|\psi^c(t)\rangle$ (and as a consequence the whole measurement history). In order to obtain the corresponding evolution, we exploit the formulas involving the Kraus operators.

In particular, if the feedback operation is performed after the measurement, by assuming unit measuring efficiency, initial pure states and no-delay between measurement and feedback, the conditional state at each instant is described via the formula

$$|\psi^{fb}(t+dt)\rangle = \frac{\widehat{U}_{fb}\widehat{M}_{\mathbf{dy}_t}|\psi^{fb}(t)\rangle}{\sqrt{\langle\psi^{fb}(t)|\widehat{M}^\dagger_{\mathbf{dy}_t}\widehat{M}_{\mathbf{dy}_t}|\psi^{fb}(t)\rangle}}\,. \tag{8.13}$$

This formula is particularly useful for our numerical approach where one needs to substitute the time differential dt with a finite but small time increment Δt, while the Wiener increment $dW_t^{(j)}$ must be replaced by a Gaussian random variable $\Delta W_t^{(j)}$ with zero mean and variance Δt. The explicit formula for the finite increments to the measurement records is

$$\Delta y_t^{(j)} = \sqrt{\kappa_j}\langle\psi^c(t)|\left(\widehat{c}_j^\dagger + \widehat{c}_j\right)|\psi^c(t)\rangle\Delta t + \Delta W_t^{(j)}. \tag{8.14}$$

Due to the finite nature of Δt, the deterministic identity $\Delta W_t^{(j)2} = \Delta t$ is no longer satisfied, thus corrections must be considered. This is accomplished by adding an extra term, known as Euler-Millstein correction [302], in the Kraus operators that now read

$$\begin{aligned}\widehat{M}_{\mathbf{\Delta y}_t} &= \mathbb{I} - i\widehat{H}_s\Delta t \\ &\quad - \sum_j\left(\frac{\kappa_j}{2}\widehat{c}_j^\dagger\widehat{c}_j\Delta t - \sqrt{\kappa_j}\widehat{c}_j\Delta y_t^{(j)} - \frac{\kappa_j}{2}\widehat{c}_j^2\left(\Delta y_t^{(j)^2} - \Delta t\right)\right).\end{aligned} \tag{8.15}$$

This is the operator that will generate each stochastic trajectory according to (8.13).

8.3 Quantum search assisted by feedback

Our idea is to continuously monitor the position of a quantum walker during its evolution on a cycle graph, and then to use this information to apply feedback unitary operations as a dynamical oracle with the aim of finding a particular target node. The walker is initially prepared in the uniform superposition of all nodes of the graph as in Eq. (8.3).

The first step is to describe the continuous monitoring. In particular we assume to be able to couple our system to two different environments via the following jump operators

$$\widehat{c}_1 = \widehat{x} = \sum_{k=0}^{N-1} \cos\left(\frac{2\pi k}{N}\right) |k\rangle\langle k| \,, \tag{8.16}$$

$$\widehat{c}_2 = \widehat{y} = \sum_{k=0}^{N-1} \sin\left(\frac{2\pi k}{N}\right) |k\rangle\langle k| \,, \tag{8.17}$$

whose eigenvalues exactly correspond to the coordinates of the position of the N nodes of the graph, corresponding to equally spaced points on a unit radius ring centered on $(0,0)$ in the (x,y) plane (see Fig. 8.1.1 for cycle graphs with $N = 5, 11, 15$). By performing continuous homodyne detections one obtains two photocurrents (8.5) whose average values are indeed proportional to the the expectation values of the operators $\widehat{x}$ and $\widehat{y}$ on the conditional state ϱ^c.

We show in Appendix 8.A that the unconditional evolution, corresponding to the master equation (8.9) with the cycle graph Hamiltonian $H_S = \gamma L$ and jump operators (8.16)-(8.17), leads to a symmetric dephasing-like evolution in the position basis, thus reflecting the translation invariance of the graph's nodes and further validating our choice. In Appendix 8.B we also mention an alternative choice for the jump operator, i.e. the single non-Hermitian jump operator

$$\widehat{c}_0 = \sum_{k=0}^{N-1} e^{i2\pi k/N} |k\rangle\langle k| \,, \tag{8.18}$$

that satisfies the properties discussed above. We show that the results are comparable with the one obtained via the two Hermitian jump operators $\widehat{c}_1$ and $\widehat{c}_2$.

The second step is to define our feedback strategy. We parametrize the unitary feedback operator as

$$\widehat{U}_{fb}(\boldsymbol{\theta}) = e^{-i\widehat{H}_{fb}(\boldsymbol{\theta})dt} \,, \tag{8.19}$$

where, in general, we assume to have a finite number of control parameters $\boldsymbol{\theta} = \{\theta_k\}$ corresponding to a set of control operators $\{\widehat{h}_k\}$, such that the feedback Hamiltonian reads

$$\widehat{H}_{fb}(\boldsymbol{\theta}) = \sum_k \theta_k \widehat{h}_k \,. \tag{8.20}$$

The definition of the control operators is indeed crucial. Two natural choices can be considered: the first one is to choose the on-site projectors, i.e.

$$\widehat{h}_k^{(os)} = |k\rangle\langle k|. \tag{8.21}$$

From a physical point of view, this would mean being able to modify the on-site energies of graph. However preliminary numerical simulations show that this choice is in general not efficient. In order to understand why this is the case, one can for example observe that, being $\{|k\rangle\}$ eigenstates of the control operators above, if the walker during the evolution happens to be in a node $|\bar{k}\rangle$ different from the target, the unitary operation will not be able to change its state and thus the feedback is useless for our purposes.

The second natural choice is to consider the hopping operators

$$\widehat{h}_k^{(hop)} = |k\rangle\langle k+1| + |k+1\rangle\langle k|\,, \tag{8.22}$$

with the usual boundary condition $|N\rangle \equiv |0\rangle$. This set of feedback control operations represents the ability of individually controlling each coupling between adjacent nodes. Finally, one needs to decide how to optimize the feedback operation, that is the set of control parameters $\boldsymbol{\theta}$, in order to find the target node on the graph. This is typically done by defining a reward function $\Lambda(|\psi^{fb}\rangle)$, that in our case naturally corresponds to the fidelity between the conditional state after the feedback operation $|\psi^{fb}\rangle$ in Eq. (8.13), and the target state (that we will hereafter denote as $|0\rangle$), i.e.

$$\Lambda\left(|\psi^{fb}(t)\rangle\right) = \mathcal{F}_{|0\rangle}\left(|\psi^{fb}(t)\rangle\right) = |\langle 0|\psi^{fb}(t)\rangle|^2. \tag{8.23}$$

We will thus choose the parameters $\boldsymbol{\theta}$ as the ones maximizing the fidelity at each step of the trajectory. The same figure of merit will be then used in order to assess the performance of our protocol. We will indeed numerically evaluate

$$\overline{\mathcal{F}}_{|0\rangle} = \mathbb{E}_{\mathsf{traj}}[\mathcal{F}_{|0\rangle}(|\psi^{fb}(t)\rangle)]\,, \tag{8.24}$$

that is the fidelity averaged over all the possible trajectories conditioned by the continuous monitoring.

8.4 Results

In the following, we present our main results, dividing them in three different settings: in Sec. 8.4.1 we address the numerical optimization of the feedback operation with unbounded control parameters, that is without posing any bound on the search domain for the parameters $\{\theta_i\}$. Then, in Sec. 8.4.2 we consider numerical optimization of the feedback but with a bounded domain, that from the physical point of view may represent constraints on the physical implementation of the feedback operations. In Sec. 8.4.3 we study the case of *digital feedback* [295], in which the value of the feedback couplings are not only bounded, but can take values only from a discrete set (one should notice that unlike previous examples of digital feedback [295], we still have a continuous measurement output, and only the feedback operations are discrete). In all these examples we consider the system initially prepared in the quantum state defined in Eq. (8.3), corresponding to the uniform superposition over the N nodes of the graph.

The algorithm we used to numerically optimize the feedback couplings is provided by the `SciPi` library, and in particular the `scipy.optimize.minimize` function [312]. The method used for the different strategies are the following: for the unbounded optimization (Sec. 8.4.1) we use the `BFGS` method; for the bounded optimization (Sec. 8.4.2) we used the `L-BFGS-B` method. Differently, the method used for digital feedback (Sec. 8.4.3) is a brute force one, i.e. we consider all the possible combinations of the finite discrete values and we select the optimal one.

We remark that we have also investigated the scenario with a single feedback Hamiltonian controlling collectively all the couplings via a single parameter θ, i.e. via the Hamiltonian

$$\widehat{H}_{fb} = \theta \sum_k \widehat{h}_k^{(hop)}. \tag{8.25}$$

However, as we show in Appendix 8.C, this kind of feedback is not particularly efficient for our purposes.

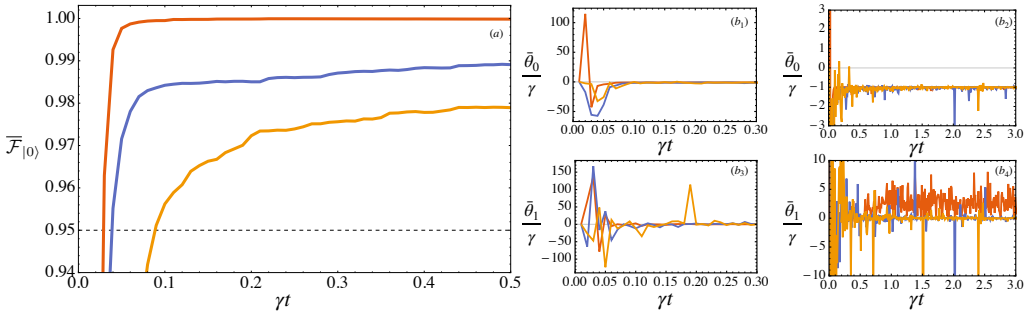

Figure 8.4.1: Results for multiple feedback control Hamiltonians $\widehat{h}_k^{(hop)}$ defined in Eq. (8.22). (a): average reward function $\overline{\mathcal{F}}_{|0\rangle}$ as a function of time (black dashed line: threshold $\mathcal{F}^{th} = 0.95$). $(b_1) - (b_4)$: averaged feedback couplings $\bar{\theta}_k$, corresponding to the kth Hamiltonian in (8.20): (b_1) and (b_3): short time behavior; (b_2) and (b_4) time-asymptotic behavior. Red line: $N = 5$; blue line: $N = 11$; orange line: $N = 15$. Other parameters: $\eta = 1$, $dt = 0.01$, number of stochastic trajectory $N_{tj} = 5000$.

8.4.1 Numerical optimization with unbounded controls

We here show the results of our protocol when considering a feedback operation via the control operators introduced in Eq. (8.22) and optimized control parameters $\{\theta_k\}$ with unbounded domain. A remark is in order here: the first attempt we have pursued was to follow the approach described by Martin et al. in [364, 234], where the feedback operation is assumed to be infinitesimal, i.e. via couplings written as

$$\boldsymbol{\theta}\, dt = A\, \mathbf{dW} + \mathbf{B}\, dt\,, \tag{8.26}$$

where $\boldsymbol{\theta} = (\theta_1, \ldots, \theta_K)^{\mathsf{T}}$ is the vector of the feedback couplings, $\mathbf{dW} = (dW_t^{(x)}, dW_t^{(y)})$ is the vector of the Wiener increments describing the measurement, while A and $\mathbf{B}$ are respectively a $(N \times 2)$-dimensional matrix and a 2-dimensional vector describing the feedback strategy. The optimization in this scenario could be done analytically if some conditions are fulfilled, as described in [234] (see Appendix 8.C for further details on this method). However for our problem we verify that these conditions are never satisfied and thus a numerical optimization with unbounded couplings has to be performed.

The results are depicted in Fig. 8.4.1 for $N = 5, 11, 15$, where we observe that the protocol is particularly efficient in reaching the target state. In order to quantify the efficiency of our protocol, we fix a threshold value for the average fidelity $\mathcal{F}^{th} = 0.95$, such that whenever the reward function is larger than this threshold value, the target search is considered successful. This efficiency decreases as the size of the graph increases, although the threshold value is reached on rather small time scales $\gamma t < 1$. This is a great improvement with respect to the performance of the standard quantum spatial search algorithm, reported in Sec. 8.1, where the success probability never reaches the threshold value (see Fig. 8.1.2 for a comparison).

In Fig. 8.4.1 we also consider the average feedback coupling $\bar{\theta}_0$ between nodes $|0\rangle$ and $|1\rangle$ and the coupling $\bar{\theta}_1$ between nodes $|1\rangle$ and $|2\rangle$ (see Fig. 8.1.1 for reference): after an initial transient, the average value of the feedback couplings reaches an asymptotic value, meaning that the feedback operation is stable after having reached the target node. We notice that the average coupling $\bar{\theta}_0$, between nodes $|0\rangle$ and $|1\rangle$, tends to the

asymptotic value $\bar{\theta}_0 \to -\gamma$. In fact, when the protocol has *almost* localized the walker in the desired node, the role of the feedback is to try to stop the dynamics by nullifying the corresponding couplings in the Hamiltonian. We have also numerical evidence that, within numerical noise, the average feedback couplings are symmetric with respect to the x-axis, i.e. $\bar{\theta}_0 = \bar{\theta}_{N-1}$, $\bar{\theta}_1 = \bar{\theta}_{N-2}$, etc., in the configuration in which the target node is placed in $(1, 0)$, see Fig. 8.1.1.

The average feedback couplings reported in Fig. 8.4.1 show however large fluctuations, especially $\bar{\theta}_1$, suggesting that in some trajectories larger values of the optimal couplings are chosen by the optimization algorithm. We propose two possible justifications for this behaviour: i) the first one is based on the stochasticity of the single random trajectory, i.e. there might be a time-step in which the measurement project the state far away from the target node, and thus a large correction is needed; ii) the second one is based on the shape of the landscape functions of the feedback couplings for a single trajectory. One can indeed observe that these landscape functions are periodic and thus have many local and equal maxima that can be reached by different values of the feedback couplings. The large fluctuations thus may arise from the fact that the algorithm does not always choose the maximum in the neighbourhood of the maximum found at the previous step (further details on the couplings' landscape functions are given in Appendix 8.D).

8.4.2 Numerical optimization with bounded controls

As we have seen in the previous Section, not only numerical optimization of the feedback strategy is necessary, but also large absolute values of the feedback couplings might be needed to perform an efficient search. Hence, to test the limits of our protocol, we consider the case where the feedback couplings $\boldsymbol{\theta}$ belong to a bounded domain. In this case each θ_k can take values from the interval $[-\xi\gamma, \xi\gamma]$, where we introduced the bounding (dimensionless) parameter ξ that quantifies the range of values admitted for the feedback couplings $\boldsymbol{\theta}$. We consider the bounding parameter $\xi \geq 1$. We have indeed numerical evidence that for $\xi < 1$, that is for feedback couplings smaller than the Laplacian parameter γ, the protocol fails. As we noticed in the example above, once the walker has been localized over the target the role of the feedback is to stop the dynamics and this effect cannot be achieved efficiently if in general $|\theta_0| < \gamma$.

The numerical results are provided in Fig. 8.4.2 for $N = 11$ (the results are qualitatively similar also for $N = 5$ and $N = 15$), and for different values of ξ ranging between $\xi = 1$ and $\xi = 100$. As expected, as ξ grows, the efficiency of the protocol improves, i.e. the minimum time t_{th} required to reach the threshold $\mathcal{F}^{th}$ decreases on average. Moreover, even for small values of ξ, this protocol is able to identify the target node with higher probability than the standard quantum algorithm in the same time interval, see again Fig. 8.1.2.

The decreasing of the optimal time γt_{th} for increasing values of ξ can also be seen from Fig. 8.4.3, where we plot the ratio of $\gamma t_{th}/\mathcal{F}^{th}$, a quantity that corresponds to the effective time necessary to reach the target on average [79]. We observe that this quantity in general quantitatively depends on the chosen threshold value $\mathcal{F}^{th}$ but it gives always the same qualitative behaviour. We see that above a certain value of ξ, the ratio reaches a minimum asymptotic value. Larger values of ξ are necessary to reduce the effective time $\gamma t_{th}/\mathcal{F}_{th}$ when the size N is increased. From Fig. 8.4.2 and 8.4.3, we notice that the order of magnitude of the t_{th} is larger if compared with the one obtained for the unbounded feedback (see Fig. 8.4.1).

In Fig. 8.4.2 we also report the average values of the feedback couplings $\bar{\theta}_0$ and

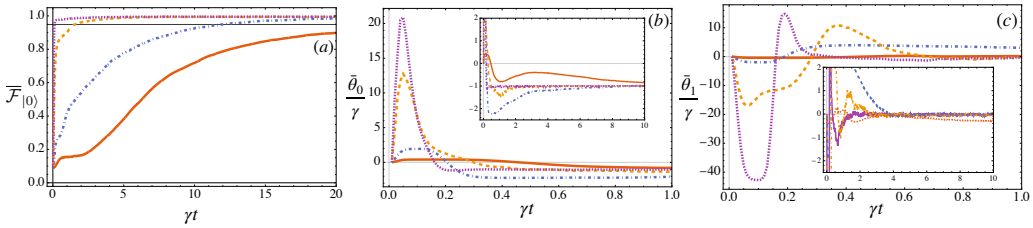

Figure 8.4.2: Results for multiple feedback Hamiltonians $\widehat{h}_k^{(hop)}$ with bounded control parameters $\boldsymbol{\theta}$ and for a graph with $N = 11$ nodes. (a): average reward function $\overline{\mathcal{F}}_{|0\rangle}$ as a function of time (black thick line: threshold $\mathcal{F}^{th} = 0.95$); (b) and (c): average feedback coupling $\bar{\theta}_0$ and $\bar{\theta}_1$ respectively, as a function of time (short time behavior). Insets: average feedback coupling $\bar{\theta}_0$ and $\bar{\theta}_1$ for a larger time t (asymptotic behavior). In all plots we used $\xi = 1$ (red thick line), $\xi = 5$ (blue dot-dashed line) $\xi = 50$ (orange dashed line), $\xi = 100$ (purple dotted line), $\eta = 1$, $dt = 0.01$, number of stochastic trajectories $N_{tj} = 5000$.

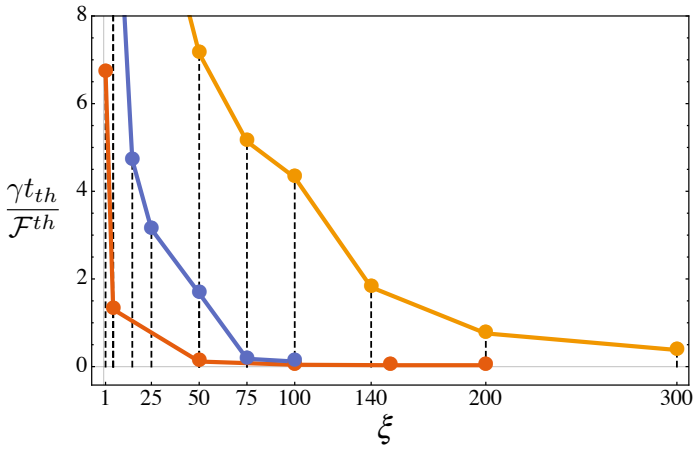

Figure 8.4.3: Plot of $\gamma t_{th}/\mathcal{F}^{th}$ as a function of the bounding parameter ξ for different graph sizes: $N = 5$ (red line) $N = 11$ (blue line) and $N = 15$ (orange line). The value t_{th} is the time at which the $\mathcal{F}^{th} = 0.95$ is reached on average. By changing the value of the threshold parameter $\mathcal{F}^{th}$ the qualitative behavior of the curves does not change and the values obtained for different ξ have the same order of magnitude. We used the same data and the same set of parameters of Fig. 8.4.2.

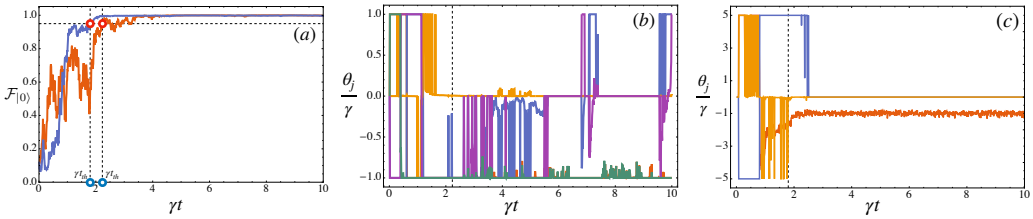

Figure 8.4.4: Single trajectory for the multiple-feedback Hamiltonian protocol with bounded domain. (a): reward function $\mathcal{F}_{|0\rangle}(\bullet)$ as a function of time for $N = 5$, $\xi = 1$ (red line) and $N = 11$, $\xi = 5$ (blue line). In this case, we have respectively $\gamma t_{th} = 1.80$ and $\gamma t_{th} = 2.23$, highlighted by the red circles. (b): feedback couplings $\boldsymbol{\theta}\, dt$ as a function of time for the $N = 5$ trajectory: Red line: θ_0; Blue line: θ_1; Orange line: θ_2; Purple line: θ_3; Green line: θ_4. (c): feedback couplings $\boldsymbol{\theta}\, dt$ as a function of time for the $N = 11$ trajectory: Red line: θ_0; Blue line: θ_1; Orange line: θ_2. All the other feedback couplings are null (apart for some numerical noise of order 10^{-8}) and we do not report them here. In (b) and (c) the vertical dashed line corresponds to the threshold time γt_{th} of the single trajectory. The parameters considered are $\eta = 1$ and $dt = 0.01$.

$\bar{\theta}_1$. Differently from the unbounded controls scenario, here the noisy fluctuations are much smaller (again, for a more detailed discussion, we refer the reader to Appendix 8.D), and we have numerical evidence that the time behaviour of $\bar{\theta}_0$ and $\bar{\theta}_1$ is equal to their symmetric counterpart $\bar{\theta}_{10}$ and $\bar{\theta}_9$. The qualitative behavior of $\bar{\theta}_0$ is the same also for the other values of N and ξ considered: after a first positive peak, it follows a minimum and then a second maximum, which is smaller than the first, and eventually it tends to the finite asymptotically value $\bar{\theta}_0 \to -\gamma$, confirming our previous intuition. The situation is slightly different for $\bar{\theta}_1$, where for $N = 11$ and $N = 15$ there is a sequence of minima and maxima which asymptotically tend to a value close to 0 while for $N = 5$ the asymptotic values remains positive. This behaviour leads to the observation that, for smaller graphs, the couplings θ_1 and θ_{N-2} are more relevant with respect to graphs with a larger size. The other feedback couplings are not particularly interesting, since their average is approximately 0 everywhere, so we decide to not report them.

So far we have discussed only averaged results on a large number of trajectories. To understand in detail the behavior of the protocol, in Fig. 8.4.4 we report the results for a single stochastic trajectory with bounded domain for $N = 5$ with $\xi = 1$ and $N = 11$ with $\xi = 5$. During the transient evolution, when the feedback is driving the walker to the target node $|0\rangle$, the value of the reward function is particularly affected by the measurement. After reaching the threshold value, the feedback operation tries to keep the walker into the target vertex. However, the stabilization procedure is not given by constant values of the feedback couplings. Similar to what we have previously discussed, this means that corrections are necessary also after having reached the target state with high fidelity. These corrections are responsible for the noise we see in the averaged feedback couplings reported in Fig. 8.4.2. By inspecting the single trajectories, we also notice that most of the values taken by $\boldsymbol{\theta}$ during the evolution are either equal to 0 or to $\pm\gamma$. So it is worth exploring a scenario where the feedback couplings $\boldsymbol{\theta}$ belong to discrete set of possible values.

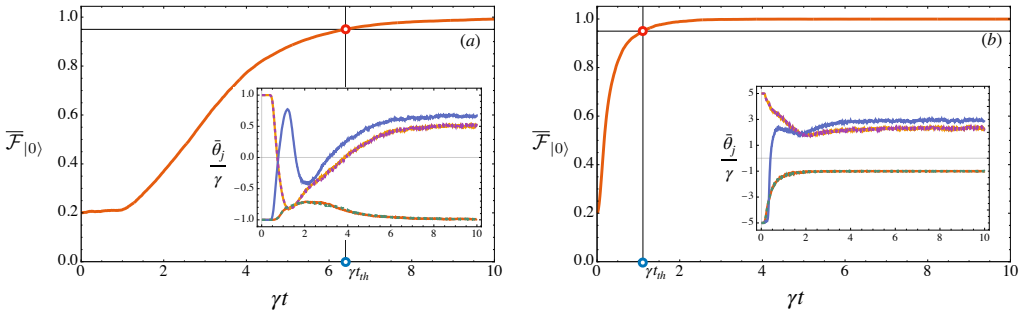

Figure 8.4.5: Digital feedback control for $N = 5$. Left panel: three possible value of the control parameters: $\{0, \pm\gamma\}$. Right panel: five possible value of the control parameters: $\{0, \pm\gamma, \pm\xi\gamma\}$ with $\xi = 5$. Main plot: averaged fidelity $\overline{\mathcal{F}}_{|0\rangle}$ as a function time. Inset: averaged feedback couplings $\overline{\boldsymbol{\theta}}$ as a function of time: Red line: θ_0; Orange line: θ_1; Blue line: θ_2; Purple dashed line: θ_3; Green dashed line: θ_4. The red and the green line are superposed, as well as the the orange and the purple. The number of trajectories is $N_{tj} = 5000$, and the parameters considered are $\eta = 1$ and $dt = 0.01$.

8.4.3 Numerical optimization with digital feedback control

We now explore a digital feedback protocol, where the feedback control parameters $\boldsymbol{\theta}$ are picked, at each time step, from a discrete number of values. We study this strategy only for a cycle graph of order $N = 5$ since the numerical algorithm we employed is particularly demanding.

First, we consider only three possible values for the couplings θ_k, belonging to the set $\{0, \pm\gamma\}$. In this case the optimization algorithm explores all the values of the reward function for all the possible combinations that the five feedback couplings $\boldsymbol{\theta}$ may realize ($5^3 = 125$ possible combinations), and select the one that realizes the maximum $\mathcal{F}_{|0\rangle}(\bullet)$. In the left panel of Fig. 8.4.5 we report the results obtained by repeating this algorithm at each step and averaging over $N_{tj} = 5000$ trajectories. We see that the threshold value of $\mathcal{F}_{th}$ is reached for a time $\gamma t_{th} = 6.40$, which is slightly larger than the value obtained via the continuous bounded protocol $\gamma t_{th} = 6.39$. Regarding the feedback couplings $\boldsymbol{\theta}$, their average values oscillate in the transient time, and after the threshold time t_{th}, they stabilize around asymptotic values. We found that approximately $\bar{\theta}_0 = \bar{\theta}_4 = -\gamma$, while $\bar{\theta}_1, \bar{\theta}_2$ and $\bar{\theta}_3$ correspond in general to positive values.

Then, we consider five possible values for the feedback couplings θ_k, belonging to the set $\{0, \pm\gamma, \pm\xi\gamma\}$, with ξ playing the same role of the bounding factor we introduced before. Here, we may consider the two extra switchers as a boosted feedback operation, i.e. a larger coupling strength than the standard γ. In this case, the number of possible combination increase and it is equal to $5^5 = 3125$. The averaged results are reported in the right panel of Fig. 8.4.5 for $\xi = 5$ and for $N_{tj} = 5000$ trajectories. The threshold value is reached, on average, by the time $\gamma t_{th} = 1.12$, which in this case is slightly smaller than the continuous-bounded protocol threshold time $\gamma t_{th} = 1.24$. This result is indeed unexpected since the digital feedback is an instance of the strategies allowed by the continuous bounded domain. This suggests that all the algorithms we employed for the optimization of the continuous bounded domain are not particularly efficient in finding the optimal values of the parameters $\boldsymbol{\theta}$, while the brute-force spanning algorithm we considered in this Section cannot fail, as all the possible combinations are tested.

The averaged values of the feedback couplings reported in the inset of Fig.s 8.4.5

show that the extra switchers are considerably used in the initial stage of the evolution. As time increases, also in this case the values of $\bar{\theta}_0$ and $\bar{\theta}_4$ reach the asymptotic value of $\bar{\theta}_0 = \bar{\theta}_4 = -\gamma$. The other couplings, instead, reach an asymptotic value larger than one and are particularly noisy. This is a sign that, in each trajectory, the walker dynamics must often be corrected by the boosted positive feedback couplings.

8.5 Conclusions

The ability to control or manipulate the dynamics of a quantum walker over a network is important for the development of quantum computation, quantum algorithms and simulations. In this work we proposed a new protocol for searching a target node over a cycle graph by means of a continuous-time quantum walk. The CTQW interacts with environmental bosonic modes that are continuously monitored and then a proper feedback operation is applied to drive the walker toward the target state. The feedback thus plays the role of a dynamic oracle, able to recognize the marked vertex and to change the values of the couplings between the nodes. In this work we analyzed and compared the performances of three different feedback strategies. In the first one, we optimized the feedback couplings without posing any bound on their values; then we considered the case of bounded control, by introducing a bounding parameter ξ; finally, we studied the case of digital feedback, where the optimal couplings were picked from a discrete set of values.

We show how all the three strategies are able to localize the walker on the target node, with higher probability with respect to the quantum spatial search algorithm with a projective oracle. In particular, as expected, the minimum time necessary to reach a threshold target fidelity is lower in the unbounded case, while the continuous bounded control and the digital feedback strategies achieve similar results. Furthermore, for all considered strategies, we show that once the target vertex is reached, the feedback operates to keep the walker in this position. This is an important difference with respect to standard spatial search protocols [94, 279], where the target is found, with higher probability, at a specific time or in a very narrow time window. The implications are relevant, especially at the experimental and operational level, as in our protocol one does not need to perform the final position measurement at a specific time, but rather at any time larger than the known threshold.

Concerning possible implementations of our scheme, we mention the cold-atom platform, where several realizations of continuous-time quantum walks have been proposed [281, 239]. Recently it has been demonstrated how one can also achieve rapid reconfigurability of the network parameters by combination with optical tweezers [359]. Moreover promising steps towards continuous monitoring of observables in this framework have been put forward [210]. Although in this work we focus on the cycle graph, our scheme can be, in principle, generalized to more general topologies with appropriate adaptations both in the feedback operations and system dynamics, i.e. respectively by changing the feedback Hamiltonian and the system-environment coupling.

Appendix

8.A Unconditional master equation and the monitoring operators $\widehat{c}_j$

In this appendix, we provide some details regarding the choice of the jump operators in Eq.s (8.16)–(8.17). We recall that the evolution of an unconditional state is described by the following master equation

$$d\varrho^u = -i\gamma[L, \varrho^u(t)]dt + \kappa \sum_j \mathcal{D}[\widehat{c}_j]\varrho^u(t)dt\,, \tag{8.27}$$

where $\{\widehat{c}_j\}$ is the set of jump operators describing the coupling of the system's degrees of freedom with the surrounding environment, and L denotes the Laplacian operator characterizing the quantum walk defined in Sec. 8.1. Since the cycle graph is symmetric under translations of the node's index and all nodes are equivalent, we expect an unconditioned dynamics to reflect this invariance. We will show how this requirement sets some constraints on the choice of $\widehat{c}_j$.

Since our goal is to monitor the position of the walker, one may consider to start with any operator diagonal in the position basis $\{|k\rangle\}$, such as for example

$$\widehat{c}_K = \widehat{K} = \sum_{k=0}^{N-1} k|k\rangle\langle k|\,. \tag{8.28}$$

Physically, each node couples with the bosonic operator of the external field and this coupling is proportional to the index of the node itself. The unconditioned dynamics in (8.27) for an initially equally superposed state given in Eq. (8.3) would eventually lead to a maximally mixed state at long times, as one expects. However, as we show in Fig. 8.A.1, during the time evolution, one observes that the symmetry of the graph is lost, as the different probabilities $p_k(t) = \langle k|\varrho^u(t)|k\rangle$ have different behaviours in time. The reason behind the broken symmetry is that one has to fix the node having eigenvalue $k = 0$.

Indeed, with a single real jump operator diagonal in the position basis, it is not possible to have an unconditioned dynamics that preserve the cycle symmetry. There are two possible ways to circumvent this problem: the first is to consider a non-Hermitian jump operator

$$\widehat{c}_0 = \sum_{k=0}^{N-1} e^{i2\pi k/N}|k\rangle\langle k|. \tag{8.29}$$

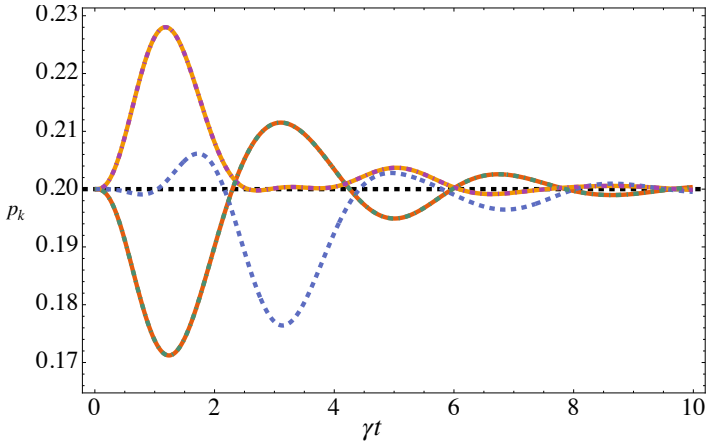

Figure 8.A.1: Time-evolution of diagonal elements of the unconditioned density matrix $p_k = \langle k|\rho^u(t)|k\rangle$ in the position basis for the unconditioned dynamics (8.27) in a cycle graph with $N = 5$ and $\kappa = \gamma$. Pair of jump operators $\widehat{c}_1$ and $\widehat{c}_2$ in Eqs. (8.16) and (8.17) or single non-Hermitian jump operator $\widehat{c}_0$ in Eq. (8.29): black dashed line $p_0 = p_1 = p_2 = p_3 = p_4 = 1/5$. Single jump operator $\widehat{c}_K$ in Eq. (8.28): green dot dashed line: $p_0(t)$; red line $p_4(t)$; purple dot dashed line: $p_1(t)$; orange line $p_3(t)$; blue dashed line: $p_2(t)$. The initial state is the uniform superposition of all nodes of the graph as in Eq. (8.3).

The second way is to use two jump operators, each diagonal in the position basis, like the one given in Eqs. (8.16)–(8.17). As remarked in the main text, the eigenvalues of these operators correspond to the coordinates of the nodes in the (x, y)-plane.

We now discuss the evolution corresponding to the unconditional dynamics for the three choices of jump operators. In Fig. 8.A.1 we report the probabilities $p_k(t) = \langle k|\varrho^u(t)|k\rangle$ of the diagonal element of the density matrix in the position basis under the master equation (8.27). We see that, both with the non-Hermitian jump operator (8.29) or with the pair of jump operators (8.16) – (8.17), the probabilities $p_k(t)$ are constant in time, and thus describe a proper pure dephasing evolution, keeping the nodes populations constant and preserving the node symmetry. This instead is lost in the evolution with the single jump operator in (8.28).

One can also show that the two unconditioned dynamics that preserve this symmetry are not equivalent. This can be seen by looking at the off diagonal elements $\varrho_{ij}(t) = \langle i|\varrho^u(t)|j\rangle$. In fact we first observe that the absolute values of these off-diagonal elements have an identical behaviour as a function of time for the same choice of the coupling constant κ, leading to the same mixed steady-state diagonal in the position basis. However a different behaviour is observed if we focus on the imaginary and real parts of these quantities. Just as an example, in Fig. 8.A.2 we report their evolution for the element $\varrho_{01}(t)$. While for the pair of jump operators $(\widehat{c}_1, \widehat{c}_2)$ the imaginary part is always equal to zero, and the real part decreases exponentially to zero, for the single jump operator $\widehat{c}_0$, one observes damped oscillations for both quantities.

In the main text we have focused on the evolution due to the pair of jump operators $\widehat{c}_1$ and $\widehat{c}_2$, as their eigenvalues directly correspond to the coordinates of the walker position. In this sense one could think to be able to couple the walker to two independent environments via quantum non demolition-like interactions, in order to perform continuous monitoring of these observables. In this sense this choice is the one that, in our

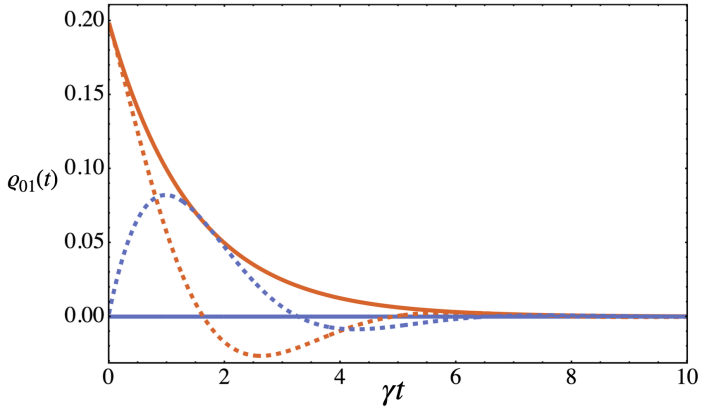

Figure 8.A.2: Real (red lines) and imaginary (blue lines) parts of the off-diagonal element $\varrho_{01}(t)$ for the unconditioned dynamics (8.27) in a cycle graph with $N = 5$ and $\kappa = \gamma$ for the single jump operator $\widehat{c}_0$ (dashed lines) and for the pair of jump operators $(\widehat{c}_1,\widehat{c}_2)$ (solid lines). The initial state is prepared in the uniform superposition of all nodes of the graph as in Eq. (8.3).

opinion, better fits the description in terms of continuous monitoring. However in the next Appendix we show that similar results are obtained by considering the dynamics with a single jump operator $\widehat{c}_0$ and with continuous heterodyne detection.

8.B Results for the single complex jump operator $\widehat{c}_0$

In this appendix, we report the results of the bounded feedback protocol with the non-Hermitian jump operator $\widehat{c}_0$ given in Eq. (8.29), analysing the reward function (8.23) for a single case of study, analogously to Fig. 8.4.2.

In this scenario, we can still obtain two distinct photocurrents yielding information on the pair of position operators $(\widehat{x},\widehat{y})$ by performing an heterodyne detection instead of two homodyne detections. In fact, in this case, one has two photocurrents given by [350, 151]

$$\begin{aligned} dy_t^{(1)} &= \sqrt{\frac{\eta\kappa}{2}}\mathrm{Tr}\left[\left(\widehat{c}_0+\widehat{c}_0^\dagger\right)\varrho^c\right]dt + dW_t^{(1)} \\ &= \sqrt{2\eta\kappa}\mathrm{Tr}\left[\widehat{x}\varrho^c\right]dt + dW_t^{(1)} \end{aligned} \tag{8.30}$$

$$\begin{aligned} dy_t^{(2)} &= \sqrt{\frac{\eta\kappa}{2}}\mathrm{Tr}\left[\left(-i\widehat{c}_0+i\widehat{c}_0^\dagger\right)\varrho^c\right]dt + dW_t^{(2)} \\ &= \sqrt{2\eta\kappa}\mathrm{Tr}[\widehat{y}\varrho^c]dt + dW_t^{(2)} \end{aligned} \tag{8.31}$$

where $dW_t^{(1)}$ and $dW_t^{(2)}$ denotes two independent Wiener increments. As explained in Sec. (8.2), the evolution of the conditional state $\varrho^c(t+dt)$, described by Eq. (8.10), is determined by a single Kraus operator, that for an heterodyne detection can be written as

$$\widehat{M}_{\mathbf{dy}_t} = \mathbb{I} - \frac{\kappa}{2}\widehat{c}_0^\dagger\widehat{c}_0 dt + \sqrt{\frac{\eta\kappa}{2}}\widehat{c}_0\left(dy_t^{(1)} - i dy_t^{(2)}\right). \tag{8.32}$$

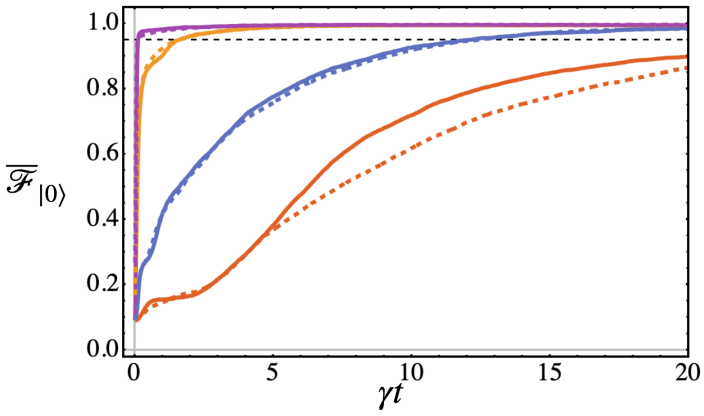

Figure 8.B.1: Comparison between the average reward function $\overline{\mathcal{F}}_{|0\rangle}$ for multiple feedback Hamiltonians $\widehat{h}_k^{(hop)}$ with the single non-Hermitian jump operator $\widehat{c}_0$ (solid) and the protocol with two jump operator (thick) already reported in Fig. 8.4.2. We consider bounded control parameters $\boldsymbol{\theta}$ and a graph with $N = 11$ nodes. Black dashed line: threshold $\mathcal{F}^{th} = 0.95$). We used $\xi = 1$ (red line), $\xi = 5$ (blue line) $\xi = 50$ (orange line), $\xi = 100$ (purple line), $\kappa = \gamma$, $\eta = 1$, $\gamma dt = 0.01$, number of stochastic trajectories $N_{tj} = 5000$.

By looking at the two photocurrents, we can use the same algorithm we used in the main text to drive the walker to the target node.

In Fig. 8.B.1 we report the behavior of the average reward function for the multiple feedback Hamiltonians protocol described in Sec. 8.3 and with bounded domains. The results reported are comparable with the one obtained in Fig. 8.4.2, meaning that the two protocols have similar performances. In particular we observe that the curves at fixed ξ are almost coincident, except for the case of $\xi = 1$. We may thus conjecture that in general the two strategies corresponding to the different jump operators lead to the similar results, but for small ξ and for the jump operator $\widehat{c}_0$ the algorithm implemented does not find the optimal feedback strategy, leading to smaller values of the average fidelity.

8.C Unitary Feedback: analytic expression of the feedback couplings

In this appendix we provide a detailed and analytical derivation for the expression of the feedback couplings in the case of a single feedback Hamiltonian, assuming that they are of the order of dt and dW_i, by following the results presented in [234].

In the interaction picture, the conditioned evolution for the density matrix due to d_M measurements is given by Eq. (8.6), and can be recasted as

$$\varrho^c(t+dt) = \varrho^c(t) + \sqrt{\kappa}\sum_{i=1}^{d_M}\mathcal{H}[\widehat{c}_i]\varrho^c(t)dW_i + \\ + \sum_{i=1}^{d_M}\kappa\mathcal{D}[\widehat{c}_i]\varrho^c(t)dt, \tag{8.33}$$

where the superoperator $\mathcal{D}[\widehat{c}_i]\bullet$ and $\mathcal{H}[\widehat{c}_i]\bullet$ are defined in Eq. (8.7) and (8.8) respectively.

As explained in the Sec. 8.3, our feedback Hamiltonian is identified with the adjacency matrix and is written as

$$\widehat{H}_{fb}(\theta) = \theta \sum_{i=0}^{N-1} \widehat{h}_i^{(hop)}, \tag{8.34}$$

with $\widehat{h}_i^{(hop)}$ defined in (8.22). The single-feedback Hamiltonian protocol proposed here is nothing but the multiple-feedback protocol in which the single couplings change synchronously and with equal strength. Here we assume that the expression for the feedback coupling θ for the step $t + dt$ can be expanded as a linear function of the Wiener increments and the time-step

$$\tilde{\theta} = \theta\, dt = \sum_{k=1}^{2} A_k dW_t^{(k)} + B dt\,, \tag{8.35}$$

with $\boldsymbol{A} = \{A_1, A_2\}$ and B are respectively a 2-dimensional real vector and a real number. Then, the unitary evolution due to the feedback can be written as

$$\widehat{U} = \exp\left\{-i\widehat{H}_{fb}(\theta)\, dt\right\} = \exp\left\{-i\,\widehat{h}_{fb} \sum_{k=1}^{2} A_k dW_t^{(k)} - i\widehat{h}_{fb}\, B dt\right\}, \tag{8.36}$$

where we have introduced the single feedback operator $\widehat{h}_{fb} = \sum_{i=0}^{N-1} \widehat{h}_i^{(hop)}$. The Taylor expansion of such operator up to first order in dt is obtained

$$\widehat{U} = \mathbb{I} - i\,\widehat{h}_{fb} \sum_{k=1}^{2} A_k dW_t^{(k)} - i\widehat{h}_{fb}\, B dt - \frac{1}{2}\widehat{h}_{fb}^2 \sum_{k=1}^{2} A_i^2 dt. \tag{8.37}$$

From the latter expression, we can derive the infinitesimal evolution after the feedback (remember that $dW_t^{(i)} dW_t^{(j)} = dt\delta_{ij}$) as

$$\varrho_{\tilde{\theta}}^f(t+dt) = \widehat{U}\varrho^c(t+dt)\widehat{U}^\dagger = \varrho_{\tilde{\theta}}^f(t) + \sqrt{\kappa}\sum_{i=1}^{2} \mathcal{H}[\widehat{c}_i]\varrho_{\tilde{\theta}}^f(t) dW_t^{(i)} + \tag{8.38}$$

$$+ \kappa \sum_{i=1}^{2} \mathcal{D}[\widehat{c}_i]\varrho_{\tilde{\theta}}^f(t)dt - i\,\left[\widehat{h}_{fb}, \varrho_{\tilde{\theta}}^f(t)\right] \sum_{i=1}^{2} A_i dW_t^{(i)} \tag{8.39}$$

$$- i\sqrt{\kappa}\left[\widehat{h}_{fb}, \mathcal{H}[\widehat{c}_i]\varrho_{\tilde{\theta}}^f(t)\right] \sum_{i=1}^{2} A_i dt - i\,\left[\widehat{h}_{fb}, \varrho_{\tilde{\theta}}^f(t)\right] B dt + \tag{8.40}$$

$$+ \sum_{i=1}^{2} A_i^2 \mathcal{D}[\widehat{h}_{fb}]\varrho_{\tilde{\theta}}^f(t)dt = \tag{8.41}$$

$$= \varrho_{\tilde{\theta}}^f(t) + \sum_{i=1}^{2} \widehat{\mathcal{W}}_i\, dW_t^{(i)} + \left(\sum_{i=1}^{2} \widehat{\mathcal{T}}_i - i\left[\widehat{h}_{fb}, \varrho_{\tilde{\theta}}^f(t)\right]\right) B dt, \tag{8.42}$$

where in the last passage we have grouped the differential factors together and defining the superoperators

$$\widehat{\mathcal{W}}_i = \sqrt{\kappa}\mathcal{H}[\widehat{c}_i]\varrho_{\tilde{\theta}}^f(t) - iA_i\left[\widehat{h}_{fb}, \varrho_{\tilde{\theta}}^f(t)\right] \tag{8.43}$$

$$\widehat{\mathcal{T}}_i = \kappa\mathcal{D}[\widehat{c}_i]\varrho_{\tilde{\theta}}^f(t) - i\sqrt{\kappa}A_i\left[\widehat{h}_{fb}, \mathcal{H}[\widehat{c}_i]\right. \varrho_{\tilde{\theta}}^f(t)] + A_i^2\mathcal{D}[\widehat{h}_{fb}]\varrho_{\tilde{\theta}}^f(t) \tag{8.44}$$

To obtain the value of $\boldsymbol{A}$ and B which determines the feedback operation at each time-step, we require that the derivative of the linear reward function $\Lambda(\varrho(t))$ with respect to $\tilde{\theta}$ at the following time step of the evolution

$$\mathcal{G}(t+dt) = \frac{\partial}{\partial\tilde{\theta}}\left(\Lambda\left(\varrho^f_{\tilde{\theta}}(t+dt)\right)\right)\Big|_{\tilde{\theta}=\tilde{\theta}_{opt}} = \Lambda\left(\frac{\partial}{\partial\tilde{\theta}}\varrho^f_{\tilde{\theta}}(t+dt)\Big|_{\tilde{\theta}=\tilde{\theta}_{opt}}\right) \tag{8.45}$$

satisfy the extremality condition

$$\mathcal{G}(t+dt) = 0. \tag{8.46}$$

In addition, since we are interested in maximizing $\Lambda(\bullet)$, we ask also that the second derivative of the reward function is negative, i.e.

$$\mathcal{V} = \Lambda\left(\frac{\partial^2\varrho^f_{\tilde{\theta}}(t+dt)}{\partial\tilde{\theta}^2}\Big|_{\tilde{\theta}=\tilde{\theta}_{opt}}\right) < 0 \tag{8.47}$$

which ensures that the feedback operation maximize the reward function. To find the solution, we first evaluate

$$\partial_{\tilde{\theta}}\varrho^f_{\tilde{\theta}}(t+dt) = i\left[\widehat{H}_{fb}(\theta), \varrho^f_{\tilde{\theta}}(t+dt)\right]. \tag{8.48}$$

Then, the condition (8.46) can be expanded as follows

$$\mathcal{G}(t+dt) = -i\Lambda\left(\left[\widehat{h}_{fb}, \varrho^f_{\tilde{\theta}}(t)\right]\right) - i\sum_{j=1}^{2}\Lambda\left(\left[\widehat{h}_{fb}, \widehat{\mathcal{W}}_j\right]\right)dW_t^{(j)} - \tag{8.49}$$

$$- i\left(\sum_{j=1}^{2}\Lambda\left(\left[\widehat{h}_{fb}, \widehat{\mathcal{T}}_j\right]\right) - iB\Lambda\left(\left[\widehat{h}_{fb}, \left[\widehat{h}_{fb}, \varrho^f_{\tilde{\theta}}(t)\right]\right]\right)\right)dt \tag{8.50}$$

Now, the first term in the latter equation is null since we assume that at the previous time step the reward function satisfy the extremality condition. Then, considering the terms proportional to dW_t^j we have that $\Lambda([\widehat{h}_{fb}, \widehat{\mathcal{W}}_j]) = 0$ for $j = 1, 2$, which is nothing but

$$A_j = -i\sqrt{\kappa}\frac{\langle 0|\left[\widehat{h}_{fb}, \mathcal{H}[\widehat{c}_j]\varrho^f_{\tilde{\theta}}(t)\right]|0\rangle}{\langle 0|\left[\widehat{h}_{fb}, \left[\widehat{h}_{fb}, \varrho^f_{\tilde{\theta}}(t)\right]\right]|0\rangle} \tag{8.51}$$

where we have considered as reward function the one defined in (8.23), i.e. $\Lambda(\bullet) = \langle 0|\bullet|0\rangle$. With the same line of reasoning, taking the term proportional to dt we can obtain the scalar function

$$B = -i\frac{\sum_{j=1}^{2}\langle 0|\left[\widehat{h}_{fb}, \widehat{\mathcal{T}}_j\right]|0\rangle}{\langle 0|\left[\widehat{h}_{fb}, \left[\widehat{h}_{fb}, \varrho^f_{\tilde{\theta}}(t)\right]\right]|0\rangle}, \tag{8.52}$$

We notice that these equations are valid if $\langle 0|[\widehat{h}_{fb}, [\widehat{h}_{fb}, \varrho^f_{\tilde{\theta}}(t)]]|0\rangle \neq 0$, a condition that must be checked at each step of the feedback operation.

In addition, the condition for maximizing the reward function at each time can be simply written as

$$\mathcal{V}_{|0\rangle}(t+dt) = -i[\widehat{h}_{fb}, [\widehat{h}_{fb}, \varrho^f_{\theta}(t+dt)]] < 0. \tag{8.53}$$

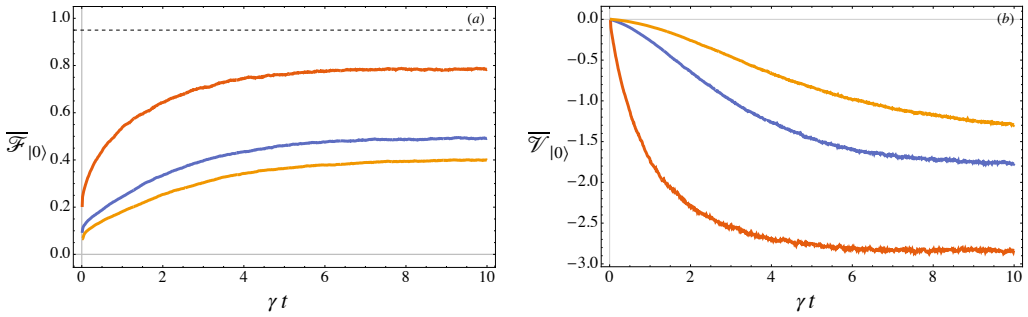

Figure 8.C.1: Single-feedback Hamiltonian protocol with $\widehat{H}_F$ defined in Eq. (8.34) for $N_{tj} = 5000$ trajectories and parameters $\eta = \kappa = 1$ and $dt = 0.01$. (a): average reward function $\overline{\mathcal{F}}_{|0\rangle}$ with respect to the target state as a function of time t. Dashed line: threshold fidelity $\mathcal{F}_{th}$. (b): average of the second derivative $\bar{\mathcal{V}}$ defined in Eq. (8.47) as a function of time t. Red line $N = 5$; Blue line $N = 11$; Orange line $N = 15$.

If this condition fails, we chose not to act with the feedback operation and skip to the next time-step, even though numerical evidence shows that this situation rarely occurs.

The numerical results of this protocol are reported in Fig. 8.C.1, left panel. The average fidelity $\overline{\mathcal{F}}_{|0\rangle}$ for $N_{tj} = 5000$ trajectories for three different values of $N = 5, 11, 15$. As the size increases, the efficiency of the protocol worsens. Moreover, it never reaches the threshold value $\overline{\mathcal{F}}^{th}_{|0\rangle}$.

In the right panel of 8.C.1 we report the average value of the second derivative, i.e. $\overline{\mathcal{V}}_{|0\rangle} = \mathbb{E}_{traj}[\mathcal{V}_{|0\rangle}(t+dt)]$. The results obtained show that the feedback operation is always optimal *on average* at each time step. However, since the threshold value $\overline{\mathcal{F}}^{th}_{|0\rangle}$ is never reached, we conclude that the single-feedback Hamiltonian is inefficient in achieving the targeting goal, even though the feedback coupling θ, found according to Eq. and (8.51) and (8.52), is the optimal one. In addition, the absolute values of $\mathcal{V}$ decrease as N increases, showing that the efficiency of the protocol worsens as the size increases, as we have already observed in the main text for the multi-coupling feedback Hamiltonian.

8.D Shape of the landscape for the reward function $\mathcal{F}_{|0\rangle}$

In this section, we discuss some details regarding the landscape of the reward function $\mathcal{F}_{|0\rangle}$ for the protocol used in the main text, i.e. with the pair of jump operators given in Eqs. (8.16)–(8.17). The aim is to provide an heuristic argument for the large fluctuations we observe in the average feedback couplings in the unbounded domain, (see Fig. 8.4.1).

The landscape is, by definition, a function of the domain of the reward function (which is $\mathbb{R}^N$, with N is the size of the cycle graph, i.e. the number of feedback couplings); for this reason it is not possible to plot the full landscape even for the smallest case we considered, i.e. $N = 5$. Nonetheless, driven by the numerical results obtained in the main text and by symmetry considerations, we can restrict the domain of our analysis. Considering the notation of Fig. 8.1.1, we can assume that $\theta_0 = \theta_4$ and $\theta_1 = \theta_3$, as confirmed by the results shown in Fig. 8.4.1, where we can clearly see this symmetry, up to some fluctuations. We further assume that $\theta_2 = 0$, which is supported by numerical results in both the unbounded and bounded case, even though we did not reported

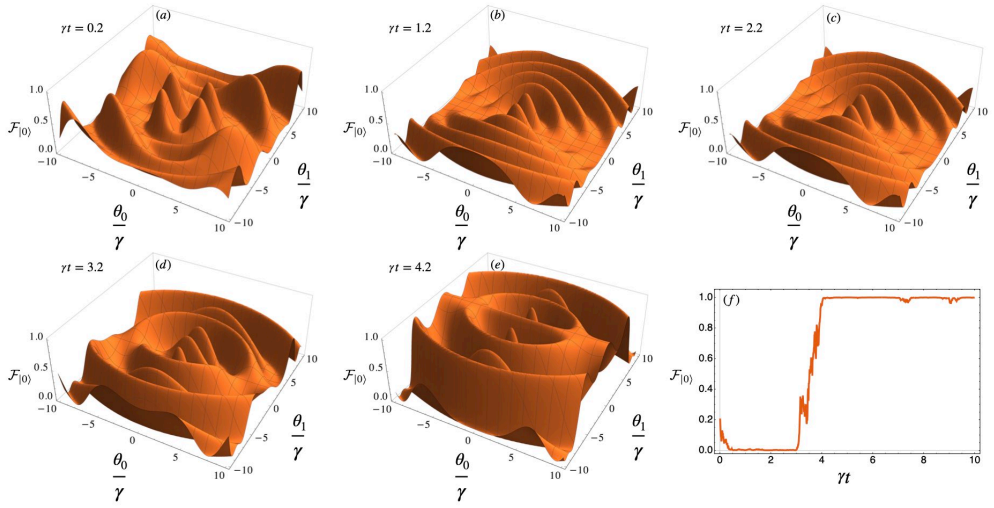

Figure 8.D.1: Landscapes for the reward function $\mathcal{F}_{|0\rangle}$ in a single trajectory at different time step. Panels $(a) - (e)$ are the landscapes, panel (f) is the evolution of the reward function as a function of γt. Comparing the two, we see the changes in the landscape as soon as the reward function increase. The parameters considered are $N = 5, \xi = 1, \kappa = \gamma, \gamma dt = 0.01, \eta = 1$. Please notice that the algorithm see only a smaller square of the values reported, as explained in Appendix 8.D.

them explicitly in the main text. In this way, we can now picture the landscape as a 3D function with two free feedback couplings, θ_0 and θ_1.

The landscapes for a single trajectory and at different times are reported in Fig. 8.D.1, with $N = 5$ and $\xi = 1$, which is the smallest domain we have studied. Please, notice that the landscape in the figure is plotted for a larger domain, i.e. $\{\theta_0/\gamma, \theta_1/\gamma\} \in \{[-10, 10], [-10, 10]\}$. This means that the bounded algorithm is going to pick values in a smaller square centered in the $3D$ plots we have reported. We show this larger domain to illustrate why smaller domains (i.e. smaller ξ) leads to a slower increase of the average fidelity: one indeed observes that the maxima of the reward function are not accessible if ξ is smaller than a certain threshold. We also stress that the algorithm that drives the walker does not assume that the angles are equal, i.e. $\theta_0 = \theta_4$ and $\theta_1 = \theta_3$ and $\theta_2 = 0$.

The landscapes reported in Fig. 8.D.1 show an oscillatory shape without a single global maximum but with many local maxima with the same height. This means that when the domain is enlarged (or even unbounded), at each step the algorithm might found a maximum outside the neighbourhood of the maximum found at the previous step. In the case of an unbounded domain, the periodicity of the landscape allows the algorithm to find maxima at very large values of the feedback coupling, which gives rise to the large fluctuations in the average feedback couplings in Fig. 8.4.1. To circumvent the problem, one could consider an algorithm in which, at each step, the feedback couplings are allowed to change in a small neighbourhood around the optimal value found at the previous step. We leave this to future investigations but we believe that this protocol should not substantially change the performance of the one used but should solve the large fluctuations problem we have observed.

Conclusions

CHAPTER 9

Concluding remarks and future perspectives

This PhD thesis has been devoted to the study of quantum information theory, more specifically quantum metrology and quantum feedback. We have focused our theoretical investigations on finding the resources, the limits and the optimal protocols to sense and control quantum systems. Besides fundamental interests, we believe that our results can pave the way to potential new applications in the field of quantum sensing and quantum control.

In Chapter 4, we characterized quantum thermometers in terms of their topological features. We identified two topological quantities that fully characterize their sensitivity, quantified by the QFI and a position-measurement FI. These are the algebraic connectivity g_1 for low temperatures, and the number of edges M for the high ones. We have also recognized coherences as a key element for achieving higher precision. Similar conclusions have been drawn in Chapter 5, but for an out-of-equilibrium probe. Again, coherences, rather than non-local correlations, proved to be the crucial resource for enhancing the probability of success in temperature discrimination. In the pure dephasing model studied, maximally coherent probes always outperformed entangled preparations. Furthermore, the possibility of measuring the probes during the transient opens up the possibility of outperforming the equilibrium discrimination.

Then, our interest turned to the theory of multi-parameter estimation. In Chapter 6, we addressed the joint estimation of parameters in a non-linear medium using Gaussian probes. In particular, we aimed to estimate the strength λ and the order ζ of the non-linearity. Remarkably, we proved that the statistical model is asymptotically classical, and as a result, no quantum noise coming from measurement incompatibility is present. The main consequence is that we can implement the optimal measurement at the single-copy level, and there is no need for collective measurements. In this way, we were able to focus our attention on another level of optimization: state preparation. This yielded the ultimate bound on the estimation precision, in which we have carried out the optimization at every possible level under experimental control, i.e. measurement and the initial state of the system. We showed that optimal probes for simultaneous estimation are not the same, providing an example of probe incompatibility. On the other side, the analysis showed that the optimal state for the joint estimation is not too much different from the two obtained for individual estimation. In particular, the squeezing ξ proved to be a resource, both in the individual and joint estimation. However, the optimal amount of squeezing must be tuned, given a fixed amount of energy.

In Chapter 7, we moved to the general framework of multi-parameter estimation and we showed why the simultaneous estimation of multiple parameters is much more intricate. Actually, the reasons behind these difficulties are already rooted in the postulates of quantum mechanics, and more precisely they are due to the presence of non-commuting observable. Indeed, in the setting of multiparameter estimation, this incompatibility

appears in the impossibility of performing the optimal measurement for each parameter. We have studied a way to quantify such incompatibility in metrology for a given statistical model, and we have provided further properties of such quantity. We have proved that it is also related to the number of compatible parameters in the statistical model, and we have also quantified such incompatibility for the full estimation of finite quantum systems, conjecturing that its value is a function of the purity of the system.

Finally, in Chapter 8, we proposed a novel protocol to perform quantum search on graphs. This is mainly based on the engineering of the interaction between a CTWQ and a collection of bosonic modes that are continuously-measured. From the observed photocurrent, a control through a feedback mechanism drive the walker to the target node. In this scenario, the oracle is not encoded in the physical Hamiltonian of the walker, rather it is the feedback mechanism that plays the role of a *dynamical oracle*. This paradigm works by synergising tools from quantum measurement, quantum control and quantum walks and provides an alternative approach to the problem of quantum search. The efficacy is supported by numerical results, and we can identify two relavant features that make this approach advantageous: first, a higher fidelity with respect to the target state if compared to the standard protocol; second, a larger optimal time interval in which we can measure the walker.

We can draw some general conclusions from the results presented here. Oour findings confirm that identifying the resources at play is fundamental for enhancing the protocol efficacy in quantum information theory. Different tasks may require completely different resources, and besides our results, theoretical studies should characterize these precisely. Furthermore, we have highlighted that the inherent weaknesses of quantum systems may instead be exploited. This idea is at the basis of quantum probing paradigms, where the harnessing of quantum systems' inherent fragilities due to their interaction with the environment can be turned into a resource. We have seen this for quantum thermometry, but these principles can be applied to other tasks as well. On the same ground, the presence of incompatible observables has always been considered one of the peculiar features of quantum mechanics. We showed that this fact is relevant not only at the fundamental level but also in the applications, given that the incompatibility of optimal observables inevitably affects the estimation precision of multiple parameters. In this sense, the careful quantification of peculiar quantum effects proved to be relevant also in the more application-oriented aspects. Following these paths may further shed light on the ultimate limits that quantum mechanics poses. As a final remark, it is important to highlight that the combination of different fields, such as quantum measurement, quantum control and quantum walks, proved fruitful and opened up new possibilities that had not yet been explored in quantum search protocols. In fact, quantum information itself was born from the union of two initially independent research fields, such as information theory and quantum theory. Therefore, continuing along this interdisciplinary path can only be beneficial to the field of quantum technologies as well.

To conclude, we would also like to provide a few outlooks coming from the outcomes of this thesis. First, future perspectives in quantum thermometry may be related to further studies in out-of-equilibrium thermometry. Actually, the understanding of out-of-equilibrium thermodynamics is relevant for many applications, in particular in the development of quantum technologies, where cooling protocols are crucial to faithfully manipulate quantum states. From another perspective, how to exploit out-of-equilibrium probes is still an emerging field, to which this thesis contributes with Chapter 5. A possible future work could study the role of topology in such a setting. Indeed, the optimization of the quantum probes may yield even more sensitive systems during the thermalization process, which can further enhance the accuracy of tempera-

ture sensing.

Several open questions regarding multi-parameter estimation are still on the table. In this thesis, we have studied the connection of the AI measure in a full tomography of finite dimensional systems. As a follow-up of this aspect, we are currently investigating more in detail the role of dimensionality of quantum systems when the parameters are unitarily encoded. The size of the Hilbert space may play a fundamental role in measurement incompatibility, and studying its relationship with the number of parameters may help reduce the quantum noise and the design of more precise probes. Furthermore, many of the results in multi-parameter estimation have been derived for asymptotic models, and several bounds have been proved to be tight only in this asymptotic limit. Furthermore, attaining these bounds often requires the implementation of collective measurements, which are usually considered to be experimentally challenging. For these reasons, it would be of crucial importance to establish bounds on a finite number of copies, which are closer to scenarios available within the current technological platforms. In this sense, it could be interesting to extend the notion of incompatibility in the finite limit. Even more important would be to address multi-parameter bounds on single-copy preparation, fully avoiding collective measurement to be performed. As a further step, a less investigated field is global multi-parameter estimation, when we have poor initial knowledge of the values of the parameters, for instance in Bayesian estimation theory. In this case, the role of measurement incompatibility is much less studied.

Finally, the possibility of continuously measuring a quantum walker unlocks the possibility of developing new methods for the manipulation and control of such systems. Furthermore, other tasks may be implemented using the information obtained by continuously monitoring the Bosonic environments. Also, other protocols relying on different engineered interactions can be proposed. For instance, we could implement the monitoring on each node rather than on the x and y axis, or we can just monitor a single node. It could be interesting to see if this can enhance quantum search, as well as other tasks implementable using quantum walks, or even simplify the processing of the data during the numerical optimization. Even more interesting would be to investigate these kinds of feedback protocols with chiral quantum walks, which are an extension of quantum walks where the Laplacian matrix allows also for complex entries.

Appendices

CHAPTER 10

Exact solution for the pure dephasing model

In this appendix we deal with the analytical evaluation of the reduced dynamics of the open quantum system interacting with a bosonic bath with total hamiltonian given by

$$H_T = \frac{\omega_0}{2} H_{\mathcal{P}}^{(\eta)} + \sum_{\boldsymbol{k}} \omega_{\boldsymbol{k}} b_{\boldsymbol{k}}^\dagger b_{\boldsymbol{k}} + H_{\mathcal{P}}^{(\eta)} \otimes \sum_{\boldsymbol{k}} \left(g_{\boldsymbol{k}} b_{\boldsymbol{k}}^\dagger + g_{\boldsymbol{k}}^* b_{\boldsymbol{k}} \right) \tag{10.1}$$

A solution for the qubit case be found in [59]. Here we deal with the more general scenario of a generic bounded energy spectrum. We split up the proof in 3 steps. First, we derive the time propagator in the interaction picture for a nilpotent interaction $\mathcal{H}_I^{int}$. Secondly, we derive the exact reduced dynamics of the open quantum system. Finally we analytically evaluate the functions which describe the dynamics.

10.1 Unitary evolution in the interaction picture for a nilpotent algebra

As it is widely known, the Schroedinger equation in the interaction picture is

$$i \frac{d}{dt} \rho^{int}(t) = \left[\mathcal{H}_I^{int}(t), \rho(t) \right], \tag{10.2}$$

and it can be rewritten in terms of the unitary operator as

$$i \frac{\partial}{\partial t} \mathcal{U}(t, t') = \mathcal{H}_I^{int}(t) \mathcal{U}(t, t') \tag{10.3}$$

A formal solution is given by the time ordered exponential

$$\mathcal{U}_I^{int}(t) = \mathcal{T} \exp \left\{ \underbrace{-i \int_0^t ds \mathcal{H}_I^{int}(t)}_{X(t,0)} \right\}, \tag{10.4}$$

where the interaction Hamiltonian in the interaction picture is $\mathcal{H}_I^{int}(t) = \mathcal{U}_0(t)^\dagger \mathcal{H}_I \mathcal{U}_0(t)$. The latter is easily evaluated as follows. Since the free unitary evolution is diagonal, it can be written as

$$\mathcal{U}_0(t) = e^{-i\mathcal{H}_0 t} = e^{-i\frac{\omega_0}{2}\mathcal{H}^{(n)} t} \otimes \prod_k e^{-i\omega_k N_k t}, \tag{10.5}$$

where N_k is the number operator of the k-th mode of the bath. It follows that the $\mathcal{H}_I^{int}$ is

$$\mathcal{H}_I^{int}(t) = \mathcal{H}^{(n)} \otimes \underbrace{\sum_j \left(e^{it\omega_j} g_j b_j^\dagger + e^{-it\omega_j} g_j^* b_j \right)}_{\mathcal{H}_I^B(t)} \tag{10.6}$$

The algebra generated by this operator evaluated at different time is nilpotent, since it holds that

$$\left[\mathcal{H}_I^{int}(t_1), \mathcal{H}_I^{int}(t_2) \right] = (\mathcal{H}^{(n)^2} \otimes \mathbb{I})(-2i\phi(t_1, t_2)) \tag{10.7}$$

where $\phi(t_1, t_2) = \sum_k |g_k|^2 \sin(\omega_k(t_1 - t_2))$. It can be easily seen thus that $[[\mathcal{H}_I^{int}(t_1), \mathcal{H}_I^{int}(t_2)], \mathcal{H}_I^{int}(t_3)] = 0$. Then, it is straightforward that

$$[X(t, t'), X(t', 0)] = -2i\varphi(t, t')\mathcal{H}^{(n)^2} \otimes \mathbb{I} \tag{10.8}$$

with

$$\varphi(t, t') = \int_{t'}^{t} \int_0^{t'} dt_1 dt_2 \phi(t_1, t_2). \tag{10.9}$$

Since the algebra generated by the argument of the exponential is nilpotent, then the (10.4) greatly simplifies. In order to see how, we use a more heuristic way. We start considering the unitary operator

$$\mathcal{U}^\star(t, t') = \exp\{X(t, t')\} \tag{10.10}$$

with

$$X(t, t') = -i \int_{t'}^{t} dt_1 \mathcal{H}_I^{int}(t_1). \tag{10.11}$$

This operator is not a solution. Indeed, we recall that the derivative of the exponential map is given by

$$\frac{d}{dt} e^{X(t,t')} = e^{X(t,t')} \frac{1 - e^{-\mathrm{ad}_X}}{\mathrm{ad}_X} \frac{d}{dt} X(t, t') \tag{10.12}$$

with

$$\frac{1 - e^{-\mathrm{ad}_X}}{\mathrm{ad}_X} = \sum_{k=0}^{+\infty} \frac{(-1)^k}{(k+1)!} (\mathrm{ad}_X)^k \tag{10.13}$$

where $\mathrm{ad}_X[Y] = [X, Y]$ is the adjoint operator. Then, in the case of a nilpotent algebra, the derivative of exponential map considerably simplifies, since in the latter series only the first two elements survive. Indeed,

$$\mathrm{ad}_X(-i\mathcal{H}_I^{int}(t)) = 2i \left(\mathcal{H}^{(n)^2} \otimes \mathbb{I} \right) \int_{t'}^{t} ds \phi(s, t), \tag{10.14}$$

and eventually

$$i\partial_t \mathcal{U}^\star(t, t') = \mathcal{U}^\star(t, t')\mathcal{H}_I^{int}(t) + \mathcal{U}^\star(t, t') \left(\mathcal{H}^{(n)^2} \otimes \mathbb{I} \right) \int_{t'}^{t} ds \phi(s, t) \tag{10.15}$$

Thus, we see that the unitary operator (10.10) does not satisfy the Schroedinger equation due to the appearance of an extra terms. Moreover, using the

Baker–Campbell–Hausdorff formula we can see that the unitary operator does not even satisfy the semigroup property, i.e. by direct computation we obtain

$$\mathcal{U}^\star(t,t')\mathcal{U}^\star(t',0) = \mathcal{U}^\star(t,0)\exp\left\{-i\varphi(t,t')\mathcal{H}^{(n)^2}\otimes\mathbb{I}\right\}. \tag{10.16}$$

Therefore, in order to have a faithful time propagator, we have to redefine $\mathcal{U}^\star(t,t')$ such that satisfy both the Schroedinger and the semigroup property. The solution is given by the following operator

$$\mathcal{U}(t,t') = \mathcal{U}^\star(t,t')\exp\left\{-i\tilde{\varphi}(t,t')\mathcal{H}^{(n)^2}\otimes\mathbb{I}\right\} \tag{10.17}$$

where $\tilde{\varphi}(t,t')$ is a slightly different version of (10.9), namely

$$\tilde{\varphi}(t,t') = \int_{t'}^{t}\int_{t'}^{t} dt_1 dt_2 \phi(t_1,t_2)\theta(t_1-t_2). \tag{10.18}$$

First, we prove that it satisfy the Schroedinger equation. Indeed, now the time derivative is

$$i\partial_t\mathcal{U}(t,t') = i\mathcal{H}_I^{int}(t)\mathcal{U}(t,t') + \mathcal{U}(t,t')\left(\mathcal{H}^{(n)^2}\otimes\mathbb{I}\right)\int_{t'}^{t} ds\phi(s,t) + \tag{10.19}$$

$$+ i\mathcal{U}^\star(t,t')\partial_t\left(\exp\{-i(\mathcal{H}^{(n)^2}\otimes\mathbb{I})\tilde{\varphi}(t,t')\}\right) \tag{10.20}$$

The derivative of the latter term is

$$i\mathcal{U}^\star(t,t')\partial_t\left(\exp\{-i(\mathcal{H}^{(n)^2}\otimes\mathbb{I})\tilde{\varphi}(t,t')\}\right) = \mathcal{U}(t,t')(\mathcal{H}^{(n)^2}\otimes\mathbb{I})\partial_t\tilde{\varphi}(t,t') = \tag{10.21}$$

$$= \mathcal{U}(t,t')(\mathcal{H}^{(n)^2}\otimes\mathbb{I})\int_{t'}^{t} ds\phi(t,s) \tag{10.22}$$

which exactly cancel out with the second term since $\phi(s,t)$ is antisymmetric. Thus $\mathcal{U}(t,t')$ satisfy the Schroedinger equation (10.3).

Second, we prove that it satisfy the semigroup property. From direct calculations, we have that

$$\mathcal{U}(t,t')\mathcal{U}(t',0) = \mathcal{U}^\star(t,t')\mathcal{U}^\star(t',0)\exp\left\{-i\left(\tilde{\varphi}(t,t')+\tilde{\varphi}(t',0)\right)\mathcal{H}^{(n)^2}\otimes\mathbb{I}\right\} =$$

$$= \mathcal{U}(t,0)\exp\left\{i\left(\tilde{\varphi}(t,0)-\varphi(t,t')-\tilde{\varphi}(t,t')-\tilde{\varphi}(t',0)\right)\mathcal{H}^{(n)^2}\otimes\mathbb{I}\right\} \tag{10.23}$$

Consequently, we have to prove that

$$\tilde{\varphi}(t,0)-\varphi(t,t')-\tilde{\varphi}(t,t')-\tilde{\varphi}(t',0) = 0 \tag{10.24}$$

Indeed since $t > t' > 0$

$$\tilde{\varphi}(t,0) = \int_{t'}^{t}\int_{t'}^{t} dt_1 dt_2\phi(t_1,t_2)\theta(t_1-t_2) + \tag{10.25}$$

$$+\int_{t'}^{t}\int_{0}^{t'} dt_1 dt_2\phi(t_1,t_2)\theta(t_1-t_2) + \tag{10.26}$$

$$+\int_{0}^{t'}\int_{t'}^{t} dt_1 dt_2\phi(t_1,t_2)\theta(t_1-t_2) \tag{10.27}$$

$$+\int_{0}^{t'}\int_{0}^{t'} dt_1 dt_2\phi(t_1,t_2)\theta(t_1-t_2) \tag{10.28}$$

We have that (10.25) and (10.28) cancel out respectively with $\tilde{\varphi}(t,t')$ and $\tilde{\varphi}(t',0)$. (10.27) is identically null since the domain of integration of t_1 is the interval $[0,t']$, while the domain of t_2 is the interval $[t',t]$. Therefore in the domain $t_1 < t_2$ and thus $\theta(t_1 - t_2) = 0$. So we are left to prove that

$$\int_{t'}^{t}\int_{0}^{t'} dt_1 dt_2 \phi(t_1,t_2)\theta(t_1-t_2) = \int_{t'}^{t}\int_{0}^{t'} dt_1 dt_2 \phi(t_1,t_2) \tag{10.29}$$

But this is true since $\theta(t_1 - t_2) = 1 - \theta(t_2 - t_1)$ and

$$\int_{t'}^{t}\int_{0}^{t'} dt_1 dt_2 \phi(t_1,t_2)\theta(t_2-t_1) = 0 \tag{10.30}$$

for the same reason on the domain stated above (namely, the domain of t_2 is $[t',0]$ and the domain of t_1 is $[t',t]$, so is always true that $t_1 > t_2$, and in this interval $\theta(t_2 - t_1) = 0$).

So we eventually recover the group property

$$\mathcal{U}(t,t')\mathcal{U}(t',0) = \mathcal{U}(t,0). \tag{10.31}$$

and for this reason we identify (10.17) with the solution of the Schroedinger equation (10.3).

10.2 The reduced dynamics of the pure dephasing model

In this section we explicitly evaluate the reduced dynamics for the open quantum system. To do so, we first need to compute the time propagator (10.17). The unitary evolution naturally decomposes in two parts, i.e.

$$\mathcal{U}_I^{int}(t) = \mathcal{U}_\varphi(t) V_I^{int}(t) \tag{10.32}$$

The first part is an unitary and temperature-independent part which, thanks to the result in 10.3, can be reduced to

$$\mathcal{U}_\varphi(t) = \exp\left\{-i\tilde{\varphi}(t,0)\mathcal{H}^{(n)^2} \otimes \mathbb{I}\right\} = \sum_{j=0}^{N-1} e^{i\xi(t)\frac{\delta_j^2}{4}} |e_j\rangle\langle e_j| \otimes \mathbb{I} \tag{10.33}$$

The function $\xi(t)$ is defined as $\xi(t) = -4\tilde{\varphi}(t,0)$ and is the temperature-independent phase function, with $\tilde{\varphi}(t,0)$ defined in (10.18). We evaluate it in 10.2.1. The second part, instead, is temperature dependent and it is given by

$$V_I^{int}(t) = \exp\left\{-i\int_0^t dt_1 \mathcal{H}_I^{int}(t_1)\right\} = \exp\left\{\mathcal{H}^{(n)} \otimes \sum_k \left(\alpha_k b_k^\dagger - \alpha_k^* b_k\right)\right\} \tag{10.34}$$

where we have defined the coefficients $\alpha_k = g_k(1 - e^{it\omega_k})/\omega_k$. Again, thanks to the the result in appendix 10.3, the $V_I^{int}(t)$ operator can be rewritten in terms of the eigenstates of $\mathcal{H}^{(n)}$ as

$$V_I^{int}(t) = \sum_{j=0}^{N-1} |e_j\rangle\langle e_j| \otimes V_j(t) \tag{10.35}$$

where we identify the operators $V_j(t)$ with

$$V_j(t) = \exp\left\{\delta_j \sum_k \left(\alpha_k b_k^\dagger - \alpha_k^* b_k\right)\right\} = \prod_k D\left(\alpha_k \delta_j\right), \tag{10.36}$$

and the $D(\alpha)$ is the displacement operator. Eventually, the unitary evolution can be written in terms of the action on each energy level of the system as

$$\mathcal{U}_I^{int}(t) = \sum_{j=0}^{N-1} e^{i\xi(t)\frac{\delta_j^2}{4}} |e_j\rangle\langle e_j| \otimes V_j(t). \tag{10.37}$$

Finally, we can evaluate the reduced dynamic of the open quantum system. We assume that the state of the total system is factorized at $t = 0$, which means that in the interaction picture $\rho^\beta(0) = \rho_S^\beta(0) \otimes \rho_B^\beta$. The most general state of system is given by

$$\rho_S^\beta(0) = \sum_{j,k=0}^{N-1} \rho_{jk}^0 |e_j\rangle\langle e_k|. \tag{10.38}$$

while we assume that the bath is in the thermal equilibrium state, i.e.

$$\rho_B^\beta = \frac{e^{-\beta \mathcal{H}_0^B}}{Z(\beta)} \tag{10.39}$$

This state commute with the free Hamiltonian $\mathcal{H}_0^B$. The evolution of the total state is given by the partial trace of the unitary evolved state, i.e

$$\rho_S^\beta(t) = \sum_{j,k=0}^{N-1} \rho_{jk}^0 e^{i\xi(t)\frac{\delta_j^2 - \delta_k^2}{4}}(\varphi) |e_j\rangle\langle e_k| \mathrm{tr}_B\left\{V_k^\dagger(t) V_j(t) \rho_B^\beta\right\}. \tag{10.40}$$

Furthermore, using the properties of the displacement operator, we have that

$$V_k^\dagger(t) V_j(t) = \prod_l D\Big(\alpha_l(\delta_j - \delta_k)\Big). \tag{10.41}$$

Defining

$$\exp\left\{\Gamma_{jk}(t|\beta)\right\} = \mathrm{Tr}\left\{\prod_l D\Big(\alpha_l(\delta_j - \delta_k)\Big)\rho_B\right\}, \tag{10.42}$$

we find out that

$$\Gamma_{jk}(t|\beta) = \frac{(\delta_j - \delta_k)^2}{4}\Gamma(t|\beta), \tag{10.43}$$

where $\Gamma(t|\beta)$ is the decoherence function, whose derivation can be found in appendix 10.2.1.

10.2.1 Decoherence and Temperature-Independent Phase Function

The explicit form of the function (10.18) is

$$\tilde{\varphi}(t, t') = \int_{t'}^t \int_{t'}^t dt_1 dt_2 \sum_k |g_k|^2 \Big(\sin\left(\omega_k(t_1 - t_2)\right)\theta(t_1 - t_2)\Big) \tag{10.44}$$

Exchanging the sum with the integrals and make the variable change $t_1 \to \tilde{t} = t_1 - t_2$, we obtain

$$\tilde{\varphi}(t,t') = \sum_k |g_k|^2 \int_{t'}^{t} dt_2 \int_{t'-t_2}^{t-t_2} d\tilde{t} \sin(\omega_k \tilde{t})\theta(\tilde{t}) = \tag{10.45}$$

$$= \sum_k |g_k|^2 \int_{t'}^{t} dt_2 \int_{0}^{t-t_2} d\tilde{t} \sin(\omega_k \tilde{t}) = \tag{10.46}$$

$$= \sum_k \frac{|g_k|^2}{\omega_k} \int_{t'}^{t} dt_2 \left(1 - \cos(\omega_k (t - t_2))\right) = \tag{10.47}$$

$$= \sum_k |g_k|^2 \left(\frac{\omega_k (t-t') - \sin(\omega_k (t-t'))}{\omega_k^2} \right) \tag{10.48}$$

As a result we obtain that the temperature-independent phase function is

$$\xi(t) = -\sum_k 4|g_k|^2 \left(\frac{\omega_k t - \sin(\omega_k t)}{\omega_k^2} \right) \tag{10.49}$$

Regarding the decoherence function, if we define $\gamma_m = \alpha_l(\delta_j - \delta_k)$ (we forget for a moment of the indices j and k, which we recover at the end), then eq. (10.42) is

$$\Gamma_{jk}(t|T) = \ln \left\{ \mathrm{Tr} \left\{ \prod_l D(\gamma_m) \rho_B \right\} \right\} = \sum_m \ln \left\{ \chi(\gamma_m) \right\}, \tag{10.50}$$

where $\chi(\gamma_m) = \mathrm{Tr}\left\{ \exp\left\{ \gamma_m b_m^\dagger - \gamma_m^* b_m \right\} \rho_B^\beta \right\}$ is the Wigner characteristic function of the bath mode l. To evaluate this function, and consequently $\Gamma_{jk}(t)$ we need to explicitly evaluate ρ_B^β. Using the resolution of the identity $\sum_{\{n^{(s)}=0\}}^{+\infty} |\vec{n}^{(i)}\rangle\langle\vec{n}^{(i)}| = \mathbb{I}$, with $|\vec{n}^{(i)}\rangle = |n^{(1)}, \dots, n^{(k)}, \dots\rangle$, we obtain

$$e^{-\beta \mathcal{H}_B} = \mathbb{I} \cdot e^{-\beta \mathcal{H}_B} \cdot \mathbb{I} = \sum_{\{n^{(s)}=0\}} \prod_l \left(e^{-\beta \omega_l n^{(l)}} \right) |\vec{n}^{(i)}\rangle\langle\vec{n}^{(i)}| \tag{10.51}$$

Then, the partition function is

$$Z_B(\beta) = \sum_{\{n^{(s)}=0\}} \prod_l e^{-\beta \omega_l n^{(l)}} = \tag{10.52}$$

$$= \prod_l \sum_{n^{(l)}=0} e^{-\beta \omega_l n^{(l)}} = \prod_l \frac{1}{1 - e^{-\beta \omega_l}}. \tag{10.53}$$

For this reason we can write the thermal state for a multimode bosonic bath as

$$\rho_B^\beta(\beta) = \sum_{\{n^{(s)}=0\}}^{+\infty} \prod_l (1 - e^{-\beta \omega_l}) e^{-\beta \omega_l n^{(l)}} |\vec{n}^{(i)}\rangle\langle\vec{n}^{(i)}| \tag{10.54}$$

Now the action of the displacement operator on the m-th mode of the thermal state is

$$D(\gamma_m)\rho_B^\beta = \sum_{\{n^{(s)}=0\}}^{+\infty} \left(\prod_l (1 - e^{-\beta \omega_l}) e^{-\beta \omega_l n^{(l)}} D(\gamma_m) |\vec{n}^{(i)}\rangle\langle\vec{n}^{(i)}| \right) \tag{10.55}$$

Computing the trace we obtain

$$\mathrm{Tr}\left\{(D(\gamma_m)\rho_B^\beta)\right\} = \sum_{\{n'^{(s)}=0\}}^{+\infty} \langle \vec{n'}^{(s)}|D(\gamma_m)\rho_B^\beta|\vec{n'}^{(s)}\rangle = \tag{10.56}$$

$$= \sum_{\{n^{(s)}=0\}}^{+\infty} \prod_l (1-e^{-\beta\omega_l})e^{-\beta\omega_l n^{(l)}}\langle \vec{n}^{(i)}|D(\gamma_m)|\vec{n}^{(i)}\rangle = \tag{10.57}$$

$$= \sum_{n^{(m)}=0}^{+\infty} (1-e^{-\beta\omega_m})e^{-\beta\omega_m n^{(m)}}\langle n^{(m)}|D(\gamma_m)|n^{(m)}\rangle = \tag{10.58}$$

$$= (1-e^{-\beta\omega_m})e^{-\frac{|\gamma_m|^2}{2}} \sum_{n^{(m)}=0}^{+\infty} e^{-\beta\omega_m n^{(m)}} L_{n^{(m)}}\left(|\gamma_m|^2\right) \tag{10.59}$$

Considering that for the Laguerre polynomials $L_n(x)$ it holds

$$\sum_n t^n L_n(x) = \frac{1}{1-t}e^{-t\frac{x}{1-t}} \tag{10.60}$$

we obtain

$$\chi(\gamma_m) = (1-e^{-\beta\omega_m})\frac{e^{-\frac{1}{2}|\gamma_m|^2}}{1-e^{-\beta\omega_m}}e^{-e^{-\beta\omega_m}\frac{|\gamma_m|^2}{1-e^{-\beta\omega_m}}} =$$
$$= e^{-\frac{|\gamma_m|^2}{2}-\frac{|\gamma_m|^2}{e^{\beta\omega_m}-1}} = e^{-\frac{1}{2}|\gamma_m|^2\coth\left(\frac{\beta\omega_m}{2}\right)}. \tag{10.61}$$

This result lead us to

$$\Gamma_{jk}(t|T) = \sum_m \ln\chi(\gamma_m) = -\frac{1}{2}\sum_m |\gamma_m|^2\coth\left(\frac{\beta\omega_m}{2}\right) = \frac{(\delta_j-\delta_k)^2}{4}\Gamma(t|T) \tag{10.62}$$

where

$$\Gamma(t|T) = -\sum_l 4\frac{|g_l|^2}{\omega_l^2}(1-\cos(\omega_l t))\coth\left(\frac{\omega_l}{2T}\right) \tag{10.63}$$

is the decoherence function. For an explicit form in terms of analytical functions, see [308].

10.3 Exponential of tensor products

Let's consider the tensor product $\mathbb{H}_n \otimes \tilde{\mathbb{H}}$ of an n-dimensional Hilbert space $\mathbb{H}_n$ and a generic Hilbert space $\tilde{\mathbb{H}}$. Consider now a diagonal matrix in $\mathbb{H}_n$, namely $\mathcal{D} = \sum_{i=0}^{N-1} d_i|i\rangle\langle i|$, and a liner operator $A \in \tilde{\mathbb{H}}$. We want to evaluate the operator $\exp\{\mathcal{D}\otimes A\}$.

Considering the Taylor expansion we have

$$\begin{aligned}
\exp\{\mathcal{D}\otimes A\} &= \sum_{m=0}^{+\infty}\frac{1}{m!}\left(\mathcal{D}\otimes A\right)^m = \\
&= \sum_{m=0}^{+\infty}\frac{1}{m!}\mathcal{D}^m\otimes A^m = \\
&= \sum_{m=0}^{+\infty}\frac{1}{m!}\left(\sum_{i=0}^{N-1} d_i^m |i\rangle\langle i|\otimes A^m\right) = \\
&= \sum_{i=0}^{N-1}\left(|i\rangle\langle i|\otimes\sum_{m=0}^{+\infty}\frac{d_i^m A^m}{m!}\right) = \\
&= \sum_{i=0}^{N-1}|i\rangle\langle i|\otimes e^{d_i A}. \qquad (10.64)
\end{aligned}$$

No assumption is made on the Hilbert space and on the liner operator A.

Bibliography

[1] AASI, J., ABADIE, J., ABBOTT, B., ABBOTT, R., ABBOTT, T., ABERNATHY, M., ADAMS, C., ADAMS, T., ADDESSO, P., ADHIKARI, R., ET AL. Enhanced sensitivity of the ligo gravitational wave detector by using squeezed states of light. *Nature Photonics 7*, 8 (2013), 613–619. (Cited on page 17)

[2] ABRAMOWITZ, M., AND STEGUN, I. A. *Handbook of mathematical functions with formulas, graphs, and mathematical tables*, vol. 55. US Government printing office, 1964. (Cited on page 95)

[3] AHARONOV, D., AMBAINIS, A., KEMPE, J., AND VAZIRANI, U. Quantum walks on graphs. In *Proceedings of the thirty-third annual ACM symposium on Theory of computing* (2001), pp. 50–59. (Cited on page 39)

[4] AHARONOV, Y., DAVIDOVICH, L., AND ZAGURY, N. Quantum random walks. *Physical Review A 48*, 2 (1993), 1687. (Cited on page 39)

[5] ALBARELLI, F., BARBIERI, M., GENONI, M. G., AND GIANANI, I. A perspective on multiparameter quantum metrology: from theoretical tools to applications in quantum imaging. *Physics Letters A 384*, 12 (2020), 126311. (Cited on pages 30, 34, 90, 91, and 103)

[6] ALBARELLI, F., AND DEMKOWICZ-DOBRZAŃSKI, R. Probe incompatibility in multiparameter noisy quantum metrology. *Physical Review X 12*, 1 (2022), 011039. (Cited on pages 17, 37, and 92)

[7] ALBARELLI, F., FRIEL, J. F., AND DATTA, A. Evaluating the holevo cramér-rao bound for multiparameter quantum metrology. *Physical review letters 123*, 20 (2019), 200503. (Cited on pages 17, 31, and 103)

[8] ALBARELLI, F., ROSSI, M. A., TAMASCELLI, D., AND GENONI, M. G. Restoring heisenberg scaling in noisy quantum metrology by monitoring the environment. *Quantum 2* (2018), 110. (Cited on page 18)

[9] ALDOUS, J. M., AND WILSON, R. J. *Graphs and applications: an introductory approach*. Springer Science & Business Media, 2003. (Cited on page 55)

[10] ALIPOUR, S., AND REZAKHANI, A. T. Extended convexity of quantum fisher information in quantum metrology. *Physical Review A 91*, 4 (2015), 042104. (Cited on page 27)

[11] AMARI, S.-I. A foundation of information geometry. *Electronics and Communications in Japan (Part I: Communications) 66*, 6 (1983), 1–10. (Cited on page 16)

[12] AMARI, S.-I. *Differential-geometrical methods in statistics*, vol. 28. Springer Science & Business Media, 2012. (Cited on page 16)

[13] AMARI, S.-I. *Information geometry and its applications*, vol. 194. Springer, 2016. (Cited on page 16)

[14] AMARI, S.-I., AND NAGAOKA, H. *Methods of information geometry*, vol. 191. American Mathematical Soc., 2000. (Cited on pages 16, 23, and 24)

[15] AMBAINIS, A. Quantum walks and their algorithmic applications. *International Journal of Quantum Information 1*, 04 (2003), 507–518. (Cited on page 39)

[16] ANDERSEN, U. L., GEHRING, T., MARQUARDT, C., AND LEUCHS, G. 30 years of squeezed light generation. *Physica Scripta 91*, 5 (2016), 053001. (Cited on page 89)

[17] ASSAD, S. M., LI, J., LIU, Y., ZHAO, N., ZHAO, W., LAM, P. K., OU, Z. Y., AND LI, X. Accessible precisions for estimating two conjugate parameters using gaussian probes. *Phys. Rev. Research 2* (May 2020), 023182. (Cited on page 103)

[18] ASSELBERGHS, I., PÉREZ-MORENO, J., AND CLAYS, K. Characterization techniques of nonlinear optical materials. In *Non-Linear Optical Properties of Matter*. Springer, 2006, pp. 419–459. (Cited on page 89)

[19] AUDENAERT, K. M. R., CALSAMIGLIA, J., MUÑOZ TAPIA, R., BAGAN, E., MASANES, L., ACIN, A., AND VERSTRAETE, F. Discriminating states: The quantum chernoff bound. *Phys. Rev. Lett. 98* (Apr 2007), 160501. (Cited on page 16)

[20] BAE, J., HWANG, W.-Y., AND HAN, Y.-D. No-signaling principle can determine optimal quantum state discrimination. *Phys. Rev. Lett. 107* (Oct 2011), 170403. (Cited on page 12)

[21] BAE, J., AND KWEK, L.-C. Quantum state discrimination and its applications. *Journal of Physics A: Mathematical and Theoretical 48*, 8 (2015), 083001. (Cited on pages 12 and 16)

[22] BAIMURATOV, A. S., RUKHLENKO, I. D., TURKOV, V. K., BARANOV, A. V., AND FEDOROV, A. V. Quantum-dot supercrystals for future nanophotonics. *Scientific reports 3*, 1 (2013), 1–9. (Cited on page 51)

[23] BANCHI, L., BRAUNSTEIN, S. L., AND PIRANDOLA, S. Quantum fidelity for arbitrary gaussian states. *Phys. Rev. Lett. 115* (Dec 2015), 260501. (Cited on page 115)

[24] BARIK, S., BAPAT, R. B., AND PATI, S. On the laplacian spectra of product graphs. *Applicable Analysis and Discrete Mathematics* (2015), 39–58. (Cited on page 64)

[25] BARNDORFF-NIELSEN, O. E., AND GILL, R. D. Fisher information in quantum statistics. *Journal of Physics A: Mathematical and General 33*, 24 (2000), 4481. (Cited on page 26)

[26] BARNETT, S. M., AND CROKE, S. Quantum state discrimination. *Advances in Optics and Photonics 1*, 2 (2009), 238–278. (Cited on page 12)

[27] BARZANJEH, S., GUHA, S., WEEDBROOK, C., VITALI, D., SHAPIRO, J. H., AND PIRANDOLA, S. Microwave quantum illumination. *Physical review letters 114*, 8 (2015), 080503. (Cited on page 17)

[28] BAUMGRATZ, T., AND DATTA, A. Quantum Enhanced Estimation of a Multidimensional Field. *Phys. Rev. Lett. 116*, 3 (jan 2016), 030801. (Cited on page 103)

[29] BECERRA, F., FAN, J., BAUMGARTNER, G., GOLDHAR, J., KOSLOSKI, J., AND MIGDALL, A. Experimental demonstration of a receiver beating the standard quantum limit for multiple nonorthogonal state discrimination. *Nature Photonics 7*, 2 (2013), 147–152. (Cited on page 12)

[30] BECERRA, F., FAN, J., AND MIGDALL, A. Implementation of generalized quantum measurements for unambiguous discrimination of multiple non-orthogonal coherent states. *Nature communications 4*, 1 (2013), 1–6. (Cited on page 12)

[31] BELLIARDO, F., AND GIOVANNETTI, V. Incompatibility in quantum parameter estimation. *New Journal of Physics 23*, 6 (jun 2021), 063055. (Cited on page 101)

[32] BELTRÁN, J., AND LUIS, A. Breaking the heisenberg limit with inefficient detectors. *Physical review A 72*, 4 (2005), 045801. (Cited on page 18)

[33] BENATTI, F., FLOREANINI, R., AND MARZOLINO, U. Sub-shot-noise quantum metrology with entangled identical particles. *Annals of Physics 325*, 4 (2010), 924–935. (Cited on page 18)

[34] BENATTI, F., FLOREANINI, R., AND MARZOLINO, U. Entanglement and squeezing with identical particles: ultracold atom quantum metrology. *Journal of Physics B: Atomic, Molecular and Optical Physics 44*, 9 (2011), 091001. (Cited on page 18)

[35] BENEDETTI, C., BUSCEMI, F., BORDONE, P., AND PARIS, M. G. Quantum probes for the spectral properties of a classical environment. *Physical Review A 89*, 3 (2014), 032114. (Cited on page 90)

[36] BENEDETTI, C., TAMASCELLI, D., PARIS, M. G., AND CRESPI, A. Quantum spatial search in two-dimensional waveguide arrays. *Physical Review Applied 16*, 5 (2021), 054036. (Cited on pages 39, 40, and 121)

[37] BENGTSSON, I., AND ŻYCZKOWSKI, K. *Geometry of quantum states: an introduction to quantum entanglement*. Cambridge university press, 2017. (Cited on pages 107 and 108)

[38] BENNETT, C. H. Quantum cryptography using any two nonorthogonal states. *Phys. Rev. Lett. 68* (May 1992), 3121–3124. (Cited on page 12)

[39] BERGOU, J. A. Quantum state discrimination and selected applications. In *Journal of Physics: Conference Series* (2007), vol. 84, IOP Publishing, p. 012001. (Cited on page 12)

[40] BERGOU, J. A. Discrimination of quantum states. *Journal of Modern Optics 57*, 3 (2010), 160–180. (Cited on pages 12 and 13)

[41] BERGOU, J. A., HERZOG, U., AND HILLERY, M. *11 Discrimination of Quantum States*. Springer Berlin Heidelberg, Berlin, Heidelberg, 2004, pp. 417–465. Edited by Paris, Matteo and Řeháček, Jaroslav. (Cited on pages 12 and 13)

[42] BERRY, D. W., AND WISEMAN, H. M. Optimal states and almost optimal adaptive measurements for quantum interferometry. *Phys. Rev. Lett. 85* (Dec 2000), 5098–5101. (Cited on page 18)

[43] BERRY, D. W., AND WISEMAN, H. M. Adaptive quantum measurements of a continuously varying phase. *Phys. Rev. A 65* (Mar 2002), 043803. (Cited on page 18)

[44] BERRY, D. W., AND WISEMAN, H. M. Adaptive phase measurements for narrowband squeezed beams. *Phys. Rev. A 73* (Jun 2006), 063824. (Cited on page 18)

[45] BHATIA, R. *Matrix analysis*, vol. 169. Springer Science & Business Media, 2013. (Cited on page 35)

[46] BINA, M., GRASSELLI, F., AND PARIS, M. G. Continuous-variable quantum probes for structured environments. *Physical Review A 97*, 1 (2018), 012125. (Cited on page 90)

[47] BOEYENS, J., SEAH, S., AND NIMMRICHTER, S. Uninformed bayesian quantum thermometry. *Phys. Rev. A 104* (Nov 2021), 052214. (Cited on page 47)

[48] BOIXO, S., DATTA, A., DAVIS, M. J., FLAMMIA, S. T., SHAJI, A., AND CAVES, C. M. Quantum metrology: dynamics versus entanglement. *Physical review letters 101*, 4 (2008), 040403. (Cited on page 18)

[49] BOIXO, S., FLAMMIA, S. T., CAVES, C. M., AND GEREMIA, J. M. Generalized limits for single-parameter quantum estimation. *Physical review letters 98*, 9 (2007), 090401. (Cited on page 18)

[50] BOLLINGER, J. J. ., ITANO, W. M., WINELAND, D. J., AND HEINZEN, D. J. Optimal frequency measurements with maximally correlated states. *Phys. Rev. A 54* (Dec 1996), R4649–R4652. (Cited on page 17)

[51] BOUTON, Q., NETTERSHEIM, J., ADAM, D., SCHMIDT, F., MAYER, D., LAUSCH, T., TIEMANN, E., AND WIDERA, A. Single-atom quantum probes for ultracold gases boosted by nonequilibrium spin dynamics. *Phys. Rev. X 10* (Jan 2020), 011018. (Cited on page 73)

[52] BRADSHAW, M., ASSAD, S. M., AND LAM, P. K. A tight cramér–rao bound for joint parameter estimation with a pure two-mode squeezed probe. *Physics Letters A 381*, 32 (2017), 2598–2607. (Cited on page 103)

[53] BRADSHAW, M., LAM, P. K., AND ASSAD, S. M. Ultimate precision of joint quadrature parameter estimation with a gaussian probe. *Physical Review A 97*, 1 (2018), 012106. (Cited on page 103)

[54] BRAUN, D. Parameter estimation with mixed quantum states. *The European Physical Journal D 59*, 3 (2010), 521–523. (Cited on page 27)

[55] BRAUN, D., ADESSO, G., BENATTI, F., FLOREANINI, R., MARZOLINO, U., MITCHELL, M. W., AND PIRANDOLA, S. Quantum-enhanced measurements without entanglement. *Reviews of Modern Physics 90*, 3 (2018), 035006. (Cited on page 18)

[56] BRAUNSTEIN, S. L., AND CAVES, C. M. Statistical distance and the geometry of quantum states. *Physical Review Letters 72*, 22 (1994), 3439. (Cited on pages 17, 24, and 102)

[57] BRAUNSTEIN, S. L., CAVES, C. M., AND MILBURN, G. J. Generalized uncertainty relations: theory, examples, and lorentz invariance. *annals of physics 247*, 1 (1996), 135–173. (Cited on page 17)

[58] BRAWLEY, G., VANNER, M., LARSEN, P. E., SCHMID, S., BOISEN, A., AND BOWEN, W. Nonlinear optomechanical measurement of mechanical motion. *Nature communications 7*, 1 (2016), 1–7. (Cited on page 89)

[59] BREUER, H.-P., PETRUCCIONE, F., ET AL. *The theory of open quantum systems*. Oxford University Press on Demand, 2002. (Cited on pages 74 and 151)

[60] BRIDA, G., DEGIOVANNI, I. P., FLORIO, A., GENOVESE, M., GIORDA, P., MEDA, A., PARIS, M. G., AND SHURUPOV, A. Experimental estimation of entanglement at the quantum limit. *Physical review letters 104*, 10 (2010), 100501. (Cited on page 90)

[61] BRITES, C. D., LIMA, P. P., SILVA, N. J., MILLÁN, A., AMARAL, V. S., PALACIO, F., AND CARLOS, L. D. Thermometry at the nanoscale. *Nanoscale 4*, 16 (2012), 4799–4829. (Cited on page 46)

[62] BROWNE, D., BOSE, S., MINTERT, F., AND KIM, M. From quantum optics to quantum technologies. *Progress in Quantum Electronics 54* (2017), 2–18. (Cited on page 89)

[63] BRUN, T. A. A simple model of quantum trajectories. *Am. J. Phys. 70*, 7 (2002), 719–737. (Cited on page 123)

[64] BRUNELLI, M., MALZ, D., AND NUNNENKAMP, A. Conditional dynamics of optomechanical two-tone backaction-evading measurements. *Phys. Rev. Lett. 123* (Aug 2019), 093602. (Cited on page 121)

[65] BRUNELLI, M., OLIVARES, S., AND PARIS, M. G. Qubit thermometry for micromechanical resonators. *Physical Review A 84*, 3 (2011), 032105. (Cited on pages 48 and 89)

[66] BRUNELLI, M., OLIVARES, S., PATERNOSTRO, M., AND PARIS, M. G. A. Qubit-assisted thermometry of a quantum harmonic oscillator. *Phys. Rev. A 86* (Jul 2012), 012125. (Cited on page 48)

[67] BUFFONI, L., AND CAMPISI, M. Thermodynamics of a quantum annealer. *Quantum Science and Technology 5*, 3 (2020), 035013. (Cited on page 51)

[68] CALLISON, A., CHANCELLOR, N., MINTERT, F., AND KENDON, V. Finding spin glass ground states using quantum walks. *New Journal of Physics 21*, 12 (2019), 123022. (Cited on page 39)

[69] CAMPBELL, S., GENONI, M. G., AND DEFFNER, S. Precision thermometry and the quantum speed limit. *Quantum Science and Technology 3*, 2 (2018), 025002. (Cited on page 47)

[70] CANDELORO, A., BENEDETTI, C., GENONI, M. G., AND PARIS, M. G. Feedback-assisted quantum search by continuous-time quantum walks. *arXiv preprint arXiv:2201.04566* (2022). (Cited on page xvi)

[71] CANDELORO, A., AND PARIS, M. G. Discrimination of ohmic thermal baths by quantum dephasing probes. *Physical Review A 103*, 1 (2021), 012217. (Cited on page xvi)

[72] CANDELORO, A., PARIS, M. G., AND GENONI, M. G. On the properties of the asymptotic incompatibility measure in multiparameter quantum estimation. *Journal of Physics A: Mathematical and Theoretical 54*, 48 (2021), 485301. (Cited on page xvi)

[73] CANDELORO, A., RAZAVIAN, S., PICCOLINI, M., TEKLU, B., OLIVARES, S., AND PARIS, M. G. Quantum probes for the characterization of nonlinear media. *Entropy 23*, 10 (2021), 1353. (Cited on page xvi)

[74] CANDELORO, A., RAZZOLI, L., BORDONE, P., AND PARIS, M. G. Role of topology in determining the precision of a finite thermometer. *Physical Review E 104*, 1 (2021), 014136. (Cited on page xv)

[75] CARCASSI, G., MACCONE, L., AND AIDALA, C. A. Four postulates of quantum mechanics are three. *Physical Review Letters 126*, 11 (2021), 110402. (Cited on page 3)

[76] CARLOS, L. D., AND PALACIO, F. *Thermometry at the nanoscale: techniques and selected applications*. Royal Society of Chemistry, 2015. (Cited on page 46)

[77] CAROLLO, A., SPAGNOLO, B., DUBKOV, A. A., AND VALENTI, D. On quantumness in multi-parameter quantum estimation. *Journal of Statistical Mechanics: Theory and Experiment 2019*, 9 (2019), 094010. (Cited on pages 36, 101, 103, 104, and 111)

[78] CAROLLO, A., SPAGNOLO, B., AND VALENTI, D. Uhlmann curvature in dissipative phase transitions. *Scientific reports 8*, 1 (2018), 1–16. (Cited on pages 33 and 103)

[79] CATTANEO, M., ROSSI, M. A. C., PARIS, M. G. A., AND MANISCALCO, S. Quantum spatial search on graphs subject to dynamical noise. *Phys. Rev. A 98* (Nov 2018), 052347. (Cited on page 130)

[80] CAVES, C. M. Quantum-mechanical noise in an interferometer. *Physical Review D 23*, 8 (1981), 1693. (Cited on page 17)

[81] CAVES, C. M., THORNE, K. S., DREVER, R. W., SANDBERG, V. D., AND ZIMMERMANN, M. On the measurement of a weak classical force coupled to a quantum-mechanical oscillator. i. issues of principle. *Reviews of Modern Physics 52*, 2 (1980), 341. (Cited on page 17)

[82] CHAKRABORTY, S., NOVO, L., AMBAINIS, A., AND OMAR, Y. Spatial search by quantum walk is optimal for almost all graphs. *Physical review letters 116*, 10 (2016), 100501. (Cited on pages 39 and 123)

[83] CHAKRABORTY, S., NOVO, L., AND ROLAND, J. Finding a marked node on any graph via continuous-time quantum walks. *Physical Review A 102*, 2 (2020), 022227. (Cited on pages 39 and 121)

[84] CHAKRABORTY, S., NOVO, L., AND ROLAND, J. Optimality of spatial search via continuous-time quantum walks. *Physical Review A 102*, 3 (2020), 032214. (Cited on pages 39 and 123)

[85] CHAKRABORTY, S. AND NOVO, L. AND DI GIORGIO, S. AND OMAR, Y. Optimal quantum spatial search on random temporal networks. *Phys. Rev. Lett. 119* (Nov 2017), 220503. (Cited on page 123)

[86] CHANG, H. *Inventing temperature: Measurement and scientific progress*. Oxford University Press, 2004. (Cited on page 45)

[87] CHAPEAU-BLONDEAU, F. Indefinite causal order for quantum metrology with quantum thermal noise. *Physics Letters A 447* (2022), 128300. (Cited on page 18)

[88] CHEFLES, A. Quantum state discrimination. *Contemporary Physics 41*, 6 (2000), 401–424. (Cited on page 12)

[89] CHEN, H., CHEN, Y., AND YUAN, H. Hierarchical incompatibility measures in multi-parameter quantum estimation. *arXiv:2109.05807 [quant-ph]* (Sept. 2021). arXiv: 2109.05807. (Cited on page 114)

[90] CHILDS, A. M. Universal computation by quantum walk. *Physical review letters 102*, 18 (2009), 180501. (Cited on page 39)

[91] CHILDS, A. M., CLEVE, R., DEOTTO, E., FARHI, E., GUTMANN, S., AND SPIELMAN, D. A. Exponential algorithmic speedup by a quantum walk. In *Proceedings of the thirty-fifth annual ACM symposium on Theory of computing* (2003), pp. 59–68. (Cited on page 39)

[92] CHILDS, A. M., FARHI, E., AND GUTMANN, S. An example of the difference between quantum and classical random walks. *Quantum Information Processing 1*, 1 (2002), 35–43. (Cited on page 39)

[93] CHILDS, A. M., AND GE, Y. Spatial search by continuous-time quantum walks on crystal lattices. *Physical Review A 89*, 5 (2014), 052337. (Cited on pages 39, 121, and 123)

[94] CHILDS, A. M., AND GOLDSTONE, J. Spatial search by quantum walk. *Physical Review A 70*, 2 (2004), 022314. (Cited on pages 39, 121, 123, and 134)

[95] CIAGLIA, F. M., DI COSMO, F., DI NOCERA, F., AND VITALE, P. Monotone metric tensors in quantum information geometry. *arXiv preprint arXiv:2203.10857* (2022). (Cited on page 17)

[96] CIAGLIA, F. M., JOST, J., AND SCHWACHHÖFER, L. Differential geometric aspects of parametric estimation theory for states on finite-dimensional c^*-algebras. *Entropy 22*, 11 (2020), 1332. (Cited on page 17)

[97] CIALDI, S., SUERRA, E., OLIVARES, S., CAPRA, S., AND PARIS, M. G. Squeezing phase diffusion. *Physical Review Letters 124*, 16 (2020), 163601. (Cited on page 92)

[98] COENEN, C., GRINBAUM, A., GRUNWALD, A., MILBURN, C., AND VERMAAS, P. Quantum technologies and society: Towards a different spin. *NanoEthics 16*, 1 (2022), 1–6. (Cited on page xiv)

[99] COHEN-TANNOUDJI, C., DIU, B., AND LALOE, F. Quantum mechanics, volume 2. *Quantum Mechanics 2* (1986), 626. (Cited on page 3)

[100] CONLON, L. O., SUZUKI, J., LAM, P. K., AND ASSAD, S. M. Efficient computation of the nagaoka–hayashi bound for multiparameter estimation with separable measurements. *npj Quantum Information 7*, 1 (2021), 110. (Cited on page 114)

[101] CONLON, L. O., SUZUKI, J., LAM, P. K., AND ASSAD, S. M. The gap persistence theorem for quantum multiparameter estimation. *arXiv preprint arXiv:2208.07386* (2022). (Cited on pages 34 and 101)

[102] CORREA, L. A., MEHBOUDI, M., ADESSO, G., AND SANPERA, A. Individual quantum probes for optimal thermometry. *Phys. Rev. Lett. 114* (Jun 2015), 220405. (Cited on page 47)

[103] CORREA, L. A., PERARNAU-LLOBET, M., HOVHANNISYAN, K. V., HERNÁNDEZ-SANTANA, S., MEHBOUDI, M., AND SANPERA, A. Enhancement of low-temperature thermometry by strong coupling. *Phys. Rev. A 96* (Dec 2017), 062103. (Cited on page 48)

[104] CÔTÉ, R., RUSSELL, A., EYLER, E. E., AND GOULD, P. L. Quantum random walk with rydberg atoms in an optical lattice. *New Journal of Physics 8*, 8 (2006), 156. (Cited on page 39)

[105] CRAMÉR, H. *Mathematical methods of statistics*, vol. 43. Princeton university press, 1999. (Cited on page 23)

[106] CROKE, S., ANDERSSON, E., BARNETT, S. M., GILSON, C. R., AND JEFFERS, J. Maximum confidence quantum measurements. *Physical review letters 96*, 7 (2006), 070401. (Cited on page 13)

[107] CROWLEY, P. J. D., DATTA, A., BARBIERI, M., AND WALMSLEY, I. A. Tradeoff in simultaneous quantum-limited phase and loss estimation in interferometry. *Phys. Rev. A 89*, 2 (feb 2014), 023845. (Cited on page 103)

[108] DATTA, A., AND SHAJI, A. Quantum metrology without quantum entanglement. *Modern Physics Letters B 26*, 18 (2012), 1230010. (Cited on page 18)

[109] DE CAEN, D. An upper bound on the sum of squares of degrees in a graph. *Discrete Mathematics 185*, 1-3 (1998), 245–248. (Cited on page 56)

[110] DE DANILOFF, C., THARRAULT, M., ENESA, C., SALOMON, C., CHEVY, F., REIMANN, T., AND STRUCK, J. In situ thermometry of fermionic cold-atom quantum wires. *Phys. Rev. Lett. 127* (Sep 2021), 113602. (Cited on page 48)

[111] DE JONG, E. Own the unknown: An anticipatory approach to prepare society for the quantum age. *Digital Society 1*, 2 (2022), 1–23. (Cited on page xiii)

[112] DE PASQUALE, A., ROSSINI, D., FAZIO, R., AND GIOVANNETTI, V. Local quantum thermal susceptibility. *Nature communications 7*, 1 (2016), 1–8. (Cited on page 47)

[113] DE PASQUALE, A., YUASA, K., AND GIOVANNETTI, V. Estimating temperature via sequential measurements. *Phys. Rev. A 96* (Jul 2017), 012316. (Cited on page 48)

[114] DEGEN, C. L., REINHARD, F., AND CAPPELLARO, P. Quantum sensing. *Reviews of modern physics 89*, 3 (2017), 035002. (Cited on pages xiii and 17)

[115] DELVECCHIO, M., GROISEAU, C., PETIZIOL, F., SUMMY, G. S., AND WIMBERGER, S. Quantum search with a continuous-time quantum walk in momentum space. *Journal of Physics B: Atomic, Molecular and Optical Physics 53*, 6 (2020), 065301. (Cited on page 39)

[116] DEMKOWICZ-DOBRZAŃSKI, R., BANASZEK, K., AND SCHNABEL, R. Fundamental quantum interferometry bound for the squeezed-light-enhanced gravitational wave detector geo 600. *Physical Review A 88*, 4 (2013), 041802. (Cited on page 17)

[117] DEMKOWICZ-DOBRZAŃSKI, R., GORECKI, W., AND GUŢĂ, M. Multi-parameter estimation beyond quantum fisher information. *Journal of Physics A: Mathematical and Theoretical 53*, 36 (2020), 363001. (Cited on pages 17, 31, and 32)

[118] DEMKOWICZ-DOBRZAŃSKI, R., JARZYNA, M., AND KOŁODYŃSKI, J. Quantum limits in optical interferometry. *Progress in Optics 60* (2015), 345–435. (Cited on page 17)

[119] DEMKOWICZ-DOBRZAŃSKI, R., KOŁODYŃSKI, J., AND GUŢĂ, M. The elusive heisenberg limit in quantum-enhanced metrology. *Nature communications 3*, 1 (2012), 1–8. (Cited on page 17)

[120] DEMKOWICZ-DOBRZAŃSKI, R., AND MACCONE, L. Using entanglement against noise in quantum metrology. *Physical review letters 113*, 25 (2014), 250801. (Cited on page 18)

[121] DI GIOVANNI, A., BRUNELLI, M., AND GENONI, M. G. Unconditional mechanical squeezing via backaction-evading measurements and nonoptimal feedback control. *Phys. Rev. A 103* (Feb 2021), 022614. (Cited on page 121)

[122] DIEKS, D. Overlap and distinguishability of quantum states. *Physics Letters A 126*, 5-6 (1988), 303–306. (Cited on page 13)

[123] DOHERTY, A. C., AND JACOBS, K. Feedback control of quantum systems using continuous state estimation. *Phys. Rev. A 60* (Oct 1999), 2700–2711. (Cited on page 121)

[124] DOWLING, J. P., AND MILBURN, G. J. Quantum technology: the second quantum revolution. *Philosophical Transactions of the Royal Society of London. Series A: Mathematical, Physical and Engineering Sciences 361*, 1809 (2003), 1655–1674. (Cited on page xiii)

[125] EFRON, B. Defining the curvature of a statistical problem (with applications to second order efficiency). *The Annals of Statistics* (1975), 1189–1242. (Cited on page 16)

[126] ELSPAS, B., AND TURNER, J. Graphs with circulant adjacency matrices. *Journal of Combinatorial Theory 9*, 3 (1970), 297–307. (Cited on page 58)

[127] ERCOLESSI, E. A short course on quantum mechanics and methods of quantization. *International Journal of Geometric Methods in Modern Physics 12*, 08 (2015), 1560008. (Cited on pages 3 and 4)

[128] ESCHER, B., DE MATOS FILHO, R., AND DAVIDOVICH, L. General framework for estimating the ultimate precision limit in noisy quantum-enhanced metrology. *Nature Physics 7*, 5 (2011), 406–411. (Cited on page 17)

[129] EULER, L. Solutio problematis ad geometriam situs pertinentis. *Commentarii academiae scientiarum Petropolitanae* (1741), 128–140. (Cited on page 55)

[130] EZRATTY, O. Mitigating the quantum hype. *arXiv preprint arXiv:2202.01925* (2022). (Cited on page xiv)

[131] FARHI, E., AND GUTMANN, S. Quantum computation and decision trees. *Physical Review A 58*, 2 (1998), 915. (Cited on pages 39, 42, 121, and 123)

[132] FERRARO, A., OLIVARES, S., AND PARIS, M. G. A. Gaussian states in continuous variable quantum information. *arXiv preprint quant-ph/0503237* (2005). (Cited on pages 105 and 115)

[133] FICHEUX, Q., JEZOUIN, S., LEGHTAS, Z., AND HUARD, B. Dynamics of a qubit while simultaneously monitoring its relaxation and dephasing. *Nat. Commun. 9*, 1 (2018), 1926. (Cited on page 124)

[134] FISCHER, J., AND FELLMUTH, B. Temperature metrology. *Reports on progress in physics 68*, 5 (2005), 1043. (Cited on page 45)

[135] FISHER, R. A. On the mathematical foundations of theoretical statistics. *Philosophical transactions of the Royal Society of London. Series A, containing papers of a mathematical or physical character 222*, 594-604 (1922), 309–368. (Cited on pages 16 and 23)

[136] FLATT, K., LEE, H., CARCELLER, C. R. I., BRASK, J. B., AND BAE, J. Contextual advantages and certification for maximum-confidence discrimination. *PRX Quantum 3*, 3 (2022), 030337. (Cited on page 12)

[137] FOULGER, I., GNUTZMANN, S., AND TANNER, G. Quantum search on graphene lattices. *Phys. Rev. Lett. 112* (2014), 070504. (Cited on page 123)

[138] FRÉROT, I., AND ROSCILDE, T. Quantum critical metrology. *Phys. Rev. Lett. 121* (Jul 2018), 020402. (Cited on page 18)

[139] FRIGERIO, M., BENEDETTI, C., OLIVARES, S., AND PARIS, M. G. A. Generalized quantum-classical correspondence for random walks on graphs. *Phys. Rev. A 104* (Sep 2021), L030201. (Cited on page 42)

[140] FRIGERIO, M., BENEDETTI, C., OLIVARES, S., AND PARIS, M. G. A. Quantum-classical distance as a tool to design optimal chiral quantum walks. *Phys. Rev. A 105* (Mar 2022), 032425. (Cited on page 42)

[141] FRISTEDT, B. E., AND GRAY, L. F. *A modern approach to probability theory*. Springer Science & Business Media, 2013. (Cited on pages 19 and 20)

[142] FUJIWARA, A. Strong consistency and asymptotic efficiency for adaptive quantum estimation problems. *Journal of Physics A: Mathematical and General 39*, 40 (sep 2006), 12489–12504. (Cited on page 26)

[143] FUJIWARA, A., AND HASHIZUMÉ, T. Additivity of the capacity of depolarizing channels. *Physics Letters A 299*, 5-6 (2002), 469–475. (Cited on page 27)

[144] FUJIWARA, A., AND IMAI, H. A fibre bundle over manifolds of quantum channels and its application to quantum statistics. *Journal of Physics A: Mathematical and Theoretical 41*, 25 (2008), 255304. (Cited on pages 17 and 28)

[145] GAIBA, R., AND PARIS, M. G. Squeezed vacuum as a universal quantum probe. *Physics Letters A 373*, 10 (2009), 934–939. (Cited on page 100)

[146] GARBE, L., BINA, M., KELLER, A., PARIS, M. G. A., AND FELICETTI, S. Critical quantum metrology with a finite-component quantum phase transition. *Phys. Rev. Lett. 124* (Mar 2020), 120504. (Cited on page 18)

[147] GEBBIA, F., BENEDETTI, C., BENATTI, F., FLOREANINI, R., BINA, M., AND PARIS, M. G. Two-qubit quantum probes for the temperature of an ohmic environment. *Physical Review A 101*, 3 (2020), 032112. (Cited on pages 83 and 90)

[148] GELMAN, A., CARLIN, J. B., STERN, H. S., AND RUBIN, D. B. *Bayesian data analysis*. Chapman and Hall/CRC, 1995. (Cited on page 16)

[149] GENONI, M. G., GIORDA, P., AND PARIS, M. G. A. Optimal estimation of entanglement. *Phys. Rev. A 78* (Sep 2008), 032303. (Cited on page 102)

[150] GENONI, M. G., MANCINI, S., AND SERAFINI, A. Optimal feedback control of linear quantum systems in the presence of thermal noise. *Phys. Rev. A 87* (Apr 2013), 042333. (Cited on page 121)

[151] GENONI, M. G., MANCINI, S., AND SERAFINI, A. General-dyne unravelling of a thermal master equation. *Russian Journal of Mathematical Physics 21*, 3 (2014), 329–336. (Cited on page 137)

[152] GENONI, M. G., ZHANG, J., MILLEN, J., BARKER, P. F., AND SERAFINI, A. Quantum cooling and squeezing of a levitating nanosphere via time-continuous measurements. *New Journal of Physics 17*, 7 (jul 2015), 073019. (Cited on page 121)

[153] GHOREISHI, S. A., AND ZIMAN, M. Minimum-error discrimination of thermal states. *Phys. Rev. A 104* (Dec 2021), 062402. (Cited on page 71)

[154] GIAZOTTO, F., HEIKKILÄ, T. T., LUUKANEN, A., SAVIN, A. M., AND PEKOLA, J. P. Opportunities for mesoscopics in thermometry and refrigeration: Physics and applications. *Rev. Mod. Phys. 78* (Mar 2006), 217–274. (Cited on page 46)

[155] GIOVANNETTI, V., LLOYD, S., AND MACCONE, L. Quantum-enhanced measurements: beating the standard quantum limit. *Science 306*, 5700 (2004), 1330–1336. (Cited on page 17)

[156] GIOVANNETTI, V., LLOYD, S., AND MACCONE, L. Advances in quantum metrology. *Nature photonics 5*, 4 (2011), 222–229. (Cited on page 17)

[157] GOLIN, M. J., AND LEUNG, Y. C. Unhooking circulant graphs: A combinatorial method for counting spanning trees and other parameters. In *International Workshop on Graph-Theoretic Concepts in Computer Science* (2004), Springer, pp. 296–307. (Cited on page 58)

[158] GONG, M., WANG, S., ZHA, C., CHEN, M.-C., HUANG, H.-L., WU, Y., ZHU, Q., ZHAO, Y., LI, S., GUO, S., ET AL. Quantum walks on a programmable two-dimensional 62-qubit superconducting processor. *Science 372*, 6545 (2021), 948–952. (Cited on page 40)

[159] GORECKI, W., ZHOU, S., JIANG, L., AND DEMKOWICZ-DOBRZAŃSKI, R. Quantum error correction in multi-parameter quantum metrology. *arXiv:1901.00896* (2019). (Cited on page 103)

[160] GRAY, R. M., ET AL. Toeplitz and circulant matrices: A review. *Foundations and Trends® in Communications and Information Theory 2*, 3 (2006), 155–239. (Cited on page 58)

[161] GUALTIERI, V., BENEDETTI, C., AND PARIS, M. G. Quantum-classical dynamical distance and quantumness of quantum walks. *Physical Review A 102*, 1 (2020), 012201. (Cited on page 39)

[162] GUŢĂ, M., JANSSENS, B., AND KAHN, J. Optimal estimation of qubit states with continuous time measurements. *Communications in Mathematical Physics 277*, 1 (2008), 127–160. (Cited on page 17)

[163] GUŢĂ, M., AND KAHN, J. Local asymptotic normality for qubit states. *Phys. Rev. A 73*, 5 (may 2006), 052108. (Cited on page 103)

[164] GUTA, M., AND KIUKAS, J. Equivalence classes and local asymptotic normality in system identification for quantum markov chains. *Communications in Mathematical Physics 335*, 3 (2015), 1397–1428. (Cited on page 17)

[165] HACOHEN-GOURGY, S., MARTIN, L. S., FLURIN, E., RAMASESH, V. V., WHALEY, K. B., AND SIDDIQI, I. Quantum dynamics of simultaneously measured noncommuting observables. *Nature 538*, 7626 (2016), 491–494. (Cited on page 124)

[166] HAYASHI, M. *Asymptotic theory of quantum statistical inference: selected papers*. World Scientific, 2005. (Cited on pages 24, 25, and 31)

[167] HAYASHI, M. *Quantum information*. Springer, 2006. (Cited on pages 24 and 27)

[168] HAYASHI, M. *Quantum Information Theory: Mathematical Foundation*. Springer, 2016. (Cited on page 23)

[169] HAYASHI, M., AND MATSUMOTO, K. Asymptotic performance of optimal state estimation in qubit system. *Journal of Mathematical Physics 49*, 10 (2008), 102101. (Cited on pages 31 and 103)

[170] HAYASHI, M., AND OUYANG, Y. Tight cram\'{e} r-rao type bounds for multiparameter quantum metrology through conic programming. *arXiv preprint arXiv:2209.05218* (2022). (Cited on page 101)

[171] HELSTROM, C., AND KENNEDY, R. Noncommuting observables in quantum detection and estimation theory. *IEEE Transactions on Information Theory 20*, 1 (1974), 16–24. (Cited on page 17)

[172] HELSTROM, C. W. Quantum detection and estimation theory. *Journal of Statistical Physics 1*, 2 (1969), 231–252. (Cited on pages 13, 15, and 24)

[173] HELSTROM, C. W., AND HELSTROM, C. W. *Quantum detection and estimation theory*, vol. 84. Academic press New York, 1976. (Cited on pages 17 and 102)

[174] HIGGINS, B. L., BERRY, D. W., BARTLETT, S. D., WISEMAN, H. M., AND PRYDE, G. J. Entanglement-free heisenberg-limited phase estimation. *Nature 450*, 7168 (2007), 393–396. (Cited on page 18)

[175] HINES, A. P., AND STAMP, P. Quantum walks, quantum gates, and quantum computers. *Physical Review A 75*, 6 (2007), 062321. (Cited on page 39)

[176] HOFER, P. P., BRASK, J. B., PERARNAU-LLOBET, M., AND BRUNNER, N. Quantum thermal machine as a thermometer. *Phys. Rev. Lett. 119* (Sep 2017), 090603. (Cited on page 48)

[177] HOFER, S. G., AND HAMMERER, K. Entanglement-enhanced time-continuous quantum control in optomechanics. *Phys. Rev. A 91*, 3 (Mar. 2015), 033822. (Cited on page 121)

[178] HOLEVO, A. S. *Probabilistic and statistical aspects of quantum theory*, vol. 1. Springer Science & Business Media, 2011. (Cited on pages 13, 17, 24, 30, 31, and 103)

[179] HOLLAND, M., AND BURNETT, K. Interferometric detection of optical phase shifts at the heisenberg limit. *Physical review letters 71*, 9 (1993), 1355. (Cited on page 17)

[180] HOOFNAGLE, C. J., AND GARFINKEL, S. L. *Law and Policy for the Quantum Age*. Cambridge University Press, 2022. (Cited on page xiv)

[181] HORODECKI, P., RUDNICKI, Ł., AND ŻYCZKOWSKI, K. Five open problems in quantum information theory. *PRX Quantum 3*, 1 (2022), 010101. (Cited on page 17)

[182] HOVHANNISYAN, K. V., JØRGENSEN, M. R., LANDI, G. T., ALHAMBRA, A. M., BRASK, J. B., AND PERARNAU-LLOBET, M. Optimal quantum thermometry with coarse-grained measurements. *PRX Quantum 2* (May 2021), 020322. (Cited on page 47)

[183] HUANGJUN, Z. *Quantum state estimation and symmetric informationally complete POMs*. PhD thesis, PhD thesis, National University of Singapore, 2012. 1, 5, 2012. (Cited on page 107)

[184] HUNTER, K. Measurement does not always aid state discrimination. *Physical Review A 68*, 1 (2003), 012306. (Cited on page 16)

[185] HWANG, S.-G. Cauchy's interlace theorem for eigenvalues of hermitian matrices. *The American Mathematical Monthly 111*, 2 (2004), 157–159. (Cited on page 110)

[186] ISHAM, C. J. *Lectures on quantum theory Mathematical and structural foundations*. Allied Publishers, 2001. (Cited on page 3)

[187] IVANOVIC, I. D. How to differentiate between non-orthogonal states. *Physics Letters A 123*, 6 (1987), 257–259. (Cited on page 13)

[188] JACOBS, K., AND STECK, D. A. A straightforward introduction to continuous quantum measurement. *Contemp. Phys. 47*, 5 (Sept. 2006), 279. (Cited on page 123)

[189] JANMARK, J., MEYER, D. A., AND WONG, T. G. Global symmetry is unnecessary for fast quantum search. *Physical Review Letters 112*, 21 (2014), 210502. (Cited on pages 39 and 121)

[190] JAQUE, D., AND VETRONE, F. Luminescence nanothermometry. *Nanoscale 4*, 15 (2012), 4301–4326. (Cited on page 46)

[191] JARZYNA, M., AND ZWIERZ, M. Quantum interferometric measurements of temperature. *Phys. Rev. A 92* (Sep 2015), 032112. (Cited on page 48)

[192] JEVTIC, S., NEWMAN, D., RUDOLPH, T., AND STACE, T. M. Single-qubit thermometry. *Phys. Rev. A 91* (Jan 2015), 012331. (Cited on page 49)

[193] JIANG, Y., WANG, X., MARTIN, L., AND WHALEY, K. B. Optimality of feedback control for qubit purification under inefficient measurement. *Phys. Rev. A 102* (Aug 2020), 022612. (Cited on page 121)

[194] JIANG, Z. Quantum fisher information for states in exponential form. *Phys. Rev. A 89* (Mar 2014), 032128. (Cited on page 115)

[195] JØRGENSEN, M. R., KOŁODYŃSKI, J., MEHBOUDI, M., PERARNAU-LLOBET, M., AND BRASK, J. B. Bayesian quantum thermometry based on thermodynamic length. *Phys. Rev. A 105* (Apr 2022), 042601. (Cited on page 47)

[196] JØRGENSEN, M. R., POTTS, P. P., PARIS, M. G., AND BRASK, J. B. Tight bound on finite-resolution quantum thermometry at low temperatures. *Physical Review Research 2*, 3 (2020), 033394. (Cited on page 47)

[197] KAHN, J., AND GUŢĂ, M. Local asymptotic normality for finite dimensional quantum systems. *Communications in Mathematical Physics 289*, 2 (2009), 597–652. (Cited on page 17)

[198] KATARIYA, V., AND WILDE, M. M. Geometric distinguishability measures limit quantum channel estimation and discrimination. *Quantum Information Processing 20*, 2 (2021), 1–170. (Cited on page 17)

[199] KAY, A. Perfect, efficient, state transfer and its application as a constructive tool. *International Journal of Quantum Information 8*, 04 (2010), 641–676. (Cited on page 39)

[200] KEMPE, J. Quantum random walks: an introductory overview. *Contemporary Physics 44*, 4 (2003), 307–327. (Cited on pages 39 and 121)

[201] KENDON, V. Quantum walks on general graphs. *International Journal of Quantum Information 4*, 05 (2006), 791–805. (Cited on pages 39 and 42)

[202] KLINE, R. R. *The cybernetics moment: Or why we call our age the information age*. JHU Press, 2015. (Cited on page xiii)

[203] KOLMOGOROV, ANDREĬ, N., AND BHARUCHA-REID, A. T. *Foundations of the theory of probability: Second English Edition*. Courier Dover Publications, 2018. (Cited on page 18)

[204] KOŁODYŃSKI, J., AND DEMKOWICZ-DOBRZAŃSKI, R. Phase estimation without a priori phase knowledge in the presence of loss. *Physical Review A 82*, 5 (2010), 053804. (Cited on page 17)

[205] KOŁODYŃSKI, J., AND DEMKOWICZ-DOBRZAŃSKI, R. Efficient tools for quantum metrology with uncorrelated noise. *New Journal of Physics 15*, 7 (2013), 073043. (Cited on page 17)

[206] KOSOROK, M. R. *Introduction to empirical processes and semiparametric inference.* Springer, 2008. (Cited on page 21)

[207] KRAUS, K., BÖHM, A., DOLLARD, J. D., AND WOOTTERS, W. *States, Effects, and Operations Fundamental Notions of Quantum Theory: Lectures in Mathematical Physics at the University of Texas at Austin*. Springer, 1983. (Cited on page 6)

[208] KUCSKO, G., MAURER, P. C., YAO, N. Y., KUBO, M., NOH, H. J., LO, P. K., PARK, H., AND LUKIN, M. D. Nanometre-scale thermometry in a living cell. *Nature 500*, 7460 (2013), 54–58. (Cited on page 46)

[209] KUKITA, S. An upper bound on the number of compatible parameters in simultaneous quantum estimation. *Journal of Physics A: Mathematical and Theoretical 53*, 9 (Feb. 2020), 095303. Publisher: IOP Publishing. (Cited on page 112)

[210] LAFLAMME, C., YANG, D., AND ZOLLER, P. Continuous measurement of an atomic current. *Physical Review A 95*, 4 (2017), 043843. (Cited on pages 40 and 134)

[211] LATUNE, C. L., SINAYSKIY, I., AND PETRUCCIONE, F. Collective heat capacity for quantum thermometry and quantum engine enhancements. *New Journal of Physics 22*, 8 (2020), 083049. (Cited on page 48)

[212] LECHNER, W., HAUKE, P., AND ZOLLER, P. A quantum annealing architecture with all-to-all connectivity from local interactions. *Science advances 1*, 9 (2015), e1500838. (Cited on page 51)

[213] LEE, H., KOK, P., AND DOWLING, J. P. A quantum rosetta stone for interferometry. *Journal of Modern Optics 49*, 14-15 (2002), 2325–2338. (Cited on page 17)

[214] LEHMANN, E. L., AND CASELLA, G. *Theory of point estimation*. Springer Science & Business Media, 2006. (Cited on pages 16, 20, and 24)

[215] LEIBFRIED, D., BARRETT, M. D., SCHAETZ, T., BRITTON, J., CHIAVERINI, J., ITANO, W. M., JOST, J. D., LANGER, C., AND WINELAND, D. J. Toward heisenberg-limited spectroscopy with multiparticle entangled states. *Science 304*, 5676 (2004), 1476–1478. (Cited on page 17)

[216] LEIFER, M. S., AND MARONEY, O. J. E. Maximally epistemic interpretations of the quantum state and contextuality. *Phys. Rev. Lett. 110* (Mar 2013), 120401. (Cited on page 12)

[217] LEVERRIER, A., AND GRANGIER, P. Unconditional security proof of long-distance continuous-variable quantum key distribution with discrete modulation. *Phys. Rev. Lett. 102* (May 2009), 180504. (Cited on page 12)

[218] LIU, J., YUAN, H., LU, X.-M., AND WANG, X. Quantum fisher information matrix and multiparameter estimation. *Journal of Physics A: Mathematical and Theoretical 53*, 2 (2019), 023001. (Cited on pages 17 and 103)

[219] LLOYD, S. Enhanced sensitivity of photodetection via quantum illumination. *Science 321*, 5895 (2008), 1463–1465. (Cited on page 17)

[220] LOUISELL, W. H. *Quantum statistical properties of radiation*. John Wiley and Sons, Inc., New York, 1973. (Cited on page 94)

[221] LU, D. AND BIAMONTE, J. D. AND LI, J. AND LI, H. AND JOHNSON, T. H. AND BERGHOLM, V. AND FACCIN, M. AND ZIMBORÁS, Z. AND LAFLAMME, R. AND BAUGH, J. AND LLOYD, S. Chiral quantum walks. *Phys. Rev. A 93* (Apr 2016), 042302. (Cited on page 42)

[222] LUIS, A. Nonlinear transformations and the heisenberg limit. *Physics Letters A 329*, 1-2 (2004), 8–13. (Cited on page 18)

[223] MA, J., WANG, X., SUN, C., AND NORI, F. Quantum spin squeezing. *Physics Reports 509*, 2 (2011), 89–165. (Cited on page 17)

[224] MACIEL, T. Recipe for a quantum thermometer. *Physics 8* (2015), 52. (Cited on page 46)

[225] MACIESZCZAK, K., GUŢĂ, M. U. U. U. U., LESANOVSKY, I., AND GARRAHAN, J. P. Dynamical phase transitions as a resource for quantum enhanced metrology. *Phys. Rev. A 93* (Feb 2016), 022103. (Cited on page 18)

[226] MAGRINI, L., ROSENZWEIG, P., BACH, C., DEUTSCHMANN-OLEK, A., HOFER, S. G., HONG, S., KIESEL, N., KUGI, A., AND ASPELMEYER, M. Real-time optimal quantum control of mechanical motion at room temperature. *Nature 595*, 7867 (2021), 373–377. (Cited on pages 121 and 124)

[227] MANCINO, L., GENONI, M. G., BARBIERI, M., AND PATERNOSTRO, M. Nonequilibrium readiness and precision of gaussian quantum thermometers. *Phys. Rev. Research 2* (Sep 2020), 033498. (Cited on page 48)

[228] MANDEL, L., AND WOLF, E. *Optical coherence and quantum optics*. Cambridge university press, 1995. (Cited on page 89)

[229] MARSH, S., AND WANG, J. B. Combinatorial optimization via highly efficient quantum walks. *Physical Review Research 2*, 2 (2020), 023302. (Cited on page 39)

[230] MARSHALL, J., VENTURELLI, D., HEN, I., AND RIEFFEL, E. G. Power of pausing: Advancing understanding of thermalization in experimental quantum annealers. *Physical Review Applied 11*, 4 (2019), 044083. (Cited on page 51)

[231] MARTIN, L., MOTZOI, F., LI, H., SAROVAR, M., AND WHALEY, K. B. Deterministic generation of remote entanglement with active quantum feedback. *Phys. Rev. A 92* (Dec 2015), 062321. (Cited on page 121)

[232] MARTIN, L., SAYRAFI, M., AND WHALEY, B. Optimal protocols for remote entanglement generation. In *Quantum Information and Measurement (QIM) 2017* (2017), Optical Society of America, p. QF6C.3. (Cited on page 121)

[233] MARTIN, L., SAYRAFI, M., AND WHALEY, K. B. What is the optimal way to prepare a bell state using measurement and feedback? *Quantum Sci. Technol. 2*, 4 (2017), 044006. (Cited on page 121)

[234] MARTIN, L. S. Quantum feedback for measurement and control, 2020. (Cited on pages 121, 129, and 138)

[235] MASANES, L., GALLEY, T. D., AND MÜLLER, M. P. The measurement postulates of quantum mechanics are operationally redundant. *Nature communications 10*, 1 (2019), 1–6. (Cited on page 3)

[236] MATSUMOTO, K. A new approach to the cramér-rao-type bound of the pure-state model. *Journal of Physics A: Mathematical and General 35*, 13 (2002), 3111. (Cited on page 31)

[237] MEHBOUDI, M., JØRGENSEN, M. R., SEAH, S., BRASK, J. B., KOŁODYŃSKI, J., AND PERARNAU-LLOBET, M. Fundamental limits in bayesian thermometry and attainability via adaptive strategies. *Phys. Rev. Lett. 128* (Apr 2022), 130502. (Cited on page 47)

[238] MEHBOUDI, M., SANPERA, A., AND CORREA, L. A. Thermometry in the quantum regime: recent theoretical progress. *Journal of Physics A: Mathematical and Theoretical 52*, 30 (2019), 303001. (Cited on pages 46 and 48)

[239] MEIER, E. J., AN, F. A., AND GADWAY, B. Atom-optics simulator of lattice transport phenomena. *Phys. Rev. A 93* (May 2016), 051602. (Cited on pages 39 and 134)

[240] MINEV, Z. K., MUNDHADA, S. O., SHANKAR, S., REINHOLD, P., GUTIÉRREZ-JÁUREGUI, R., SCHOELKOPF, R. J., MIRRAHIMI, M., CARMICHAEL, H. J., AND DEVORET, M. H. To catch and reverse a quantum jump mid-flight. *Nature 570*, 7760 (2019), 200–204. (Cited on page 124)

[241] MITCHELL, M. W., LUNDEEN, J. S., AND STEINBERG, A. M. Super-resolving phase measurements with a multiphoton entangled state. *Nature 429*, 6988 (2004), 161–164. (Cited on page 17)

[242] MITCHISON, M. T., FOGARTY, T., GUARNIERI, G., CAMPBELL, S., BUSCH, T., AND GOOLD, J. In situ thermometry of a cold fermi gas via dephasing impurities. *Phys. Rev. Lett. 125* (Aug 2020), 080402. (Cited on page 48)

[243] MODI, K., CABLE, H., WILLIAMSON, M., AND VEDRAL, V. Quantum correlations in mixed-state metrology. *Physical Review X 1*, 2 (2011), 021022. (Cited on page 18)

[244] MOHSENI, M., REBENTROST, P., LLOYD, S., AND ASPURU-GUZIK, A. Environment-assisted quantum walks in photosynthetic energy transfer. *The Journal of chemical physics 129*, 17 (2008), 11B603. (Cited on page 39)

[245] MOK, W.-K., BHARTI, K., KWEK, L.-C., AND BAYAT, A. Optimal probes for global quantum thermometry. *Communications physics 4*, 1 (2021), 1–8. (Cited on page 47)

[246] MØLMER, K. Hypothesis testing with open quantum systems. *Physical Review Letters 114*, 4 (2015), 040401. (Cited on page 12)

[247] MONTENEGRO, V., GENONI, M. G., BAYAT, A., AND PARIS, M. G. A. Mechanical oscillator thermometry in the nonlinear optomechanical regime. *Phys. Rev. Research 2* (Dec 2020), 043338. (Cited on page 48)

[248] MUKHERJEE, V., ZWICK, A., GHOSH, A., CHEN, X., AND KURIZKI, G. Enhanced precision bound of low-temperature quantum thermometry via dynamical control. *Communications Physics 2*, 1 (2019), 1–8. (Cited on page 46)

[249] MÜLKEN, O., AND BLUMEN, A. Continuous-time quantum walks: Models for coherent transport on complex networks. *Physics Reports 502*, 2-3 (2011), 37–87. (Cited on page 39)

[250] MURCH, K. W., WEBER, S. J., MACKLIN, C., AND SIDDIQI, I. Observing single quantum trajectories of a superconducting quantum bit. *Nature 502*, 7470 (2013), 211–214. (Cited on page 124)

[251] NAGATA, T., OKAMOTO, R., O'BRIEN, J. L., SASAKI, K., AND TAKEUCHI, S. Beating the standard quantum limit with four-entangled photons. *Science 316*, 5825 (2007), 726–729. (Cited on page 17)

[252] NAGHILOO, M., FOROOZANI, N., TAN, D., JADBABAIE, A., AND MURCH, K. W. Mapping quantum state dynamics in spontaneous emission. *Nat. Commun. 7*, 1 (2016), 11527. (Cited on page 124)

[253] NAKAMURA, K. *Quantum Phononics*. Springer, 2019. (Cited on page 90)

[254] NICHOLS, R., LIUZZO-SCORPO, P., KNOTT, P. A., AND ADESSO, G. Multiparameter gaussian quantum metrology. *Physical Review A 98*, 1 (2018), 012114. (Cited on pages 106, 115, and 117)

[255] NIELSEN, F. The many faces of information geometry. *Not. Am. Math. Soc 69* (2022), 36–45. (Cited on page 17)

[256] NIELSEN, F., AND BHATIA, R. *Matrix information geometry*. Springer, 2013. (Cited on page 17)

[257] NIELSEN, M. A., AND CHUANG, I. L. *Quantum Computation and Quantum Information: 10th Anniversary Edition*. Cambridge University Press, 2010. (Cited on pages 3 and 73)

[258] NIGG, S. E., LÖRCH, N., AND TIWARI, R. P. Robust quantum optimizer with full connectivity. *Science advances 3*, 4 (2017), e1602273. (Cited on page 51)

[259] OLIVARES, S. Quantum optics in the phase space. *The European Physical Journal Special Topics 203*, 1 (2012), 3–24. (Cited on pages 92 and 93)

[260] O'CONNOR, E., VACCHINI, B., AND CAMPBELL, S. Stochastic collisional quantum thermometry. *Entropy 23*, 12 (2021). (Cited on page 48)

[261] PALMA, G. M., SUOMINEN, K.-A., AND EKERT, A. Quantum computers and dissipation. *Proceedings of the Royal Society of London. Series A: Mathematical, Physical and Engineering Sciences 452*, 1946 (1996), 567–584. (Cited on pages 74 and 76)

[262] PARIS, M. G. Small amount of squeezing in high-sensitive realistic interferometry. *Physics Letters A 201*, 2-3 (1995), 132–138. (Cited on page 100)

[263] PARIS, M. G. The modern tools of quantum mechanics. *The European Physical Journal Special Topics 203*, 1 (2012), 61–86. (Cited on pages 3 and 10)

[264] PARIS, M. G. Achieving the landau bound to precision of quantum thermometry in systems with vanishing gap. *Journal of Physics A: Mathematical and Theoretical 49*, 3 (2015), 03LT02. (Cited on page 47)

[265] PARIS, M. G., BENEDETTI, C., AND OLIVARES, S. Improving quantum search on simple graphs by pretty good structured oracles. *Symmetry 13*, 1 (2021), 96. (Cited on pages 39 and 121)

[266] PARIS, M. G. A. Quantum estimation for quantum technology. *International Journal of Quantum Information 7*, supp01 (2009), 125–137. (Cited on pages 16, 24, 25, 90, and 102)

[267] PASQUALE, A. D., AND STACE, T. M. Quantum thermometry. In *Thermodynamics in the quantum regime*. Springer, 2018, pp. 503–527. (Cited on page 46)

[268] PERES, A. How to differentiate between non-orthogonal states. *Physics Letters A 128*, 1-2 (1988), 19. (Cited on page 13)

[269] PERETS, H. B., LAHINI, Y., POZZI, F., SOREL, M., MORANDOTTI, R., AND SILBERBERG, Y. Realization of quantum walks with negligible decoherence in waveguide lattices. *Physical review letters 100*, 17 (2008), 170506. (Cited on page 39)

[270] PERUZZO, A., LOBINO, M., MATTHEWS, J. C., MATSUDA, N., POLITI, A., POULIOS, K., ZHOU, X.-Q., LAHINI, Y., ISMAIL, N., WÖRHOFF, K., ET AL. Quantum walks of correlated photons. *Science 329*, 5998 (2010), 1500–1503. (Cited on page 39)

[271] PESTMAN, W. R. *Mathematical statistics: an introduction*. Walter de Gruyter GmbH & Co KG, 2021. (Cited on page 16)

[272] PETZ, D. *Quantum information theory and quantum statistics*. Springer Science & Business Media, 2007. (Cited on pages 16 and 17)

[273] PETZ, D., AND GHINEA, C. Introduction to quantum fisher information. In *Quantum probability and related topics*. World Scientific, 2011, pp. 261–281. (Cited on page 28)

[274] PEZZE, L., SMERZI, A., OBERTHALER, M. K., SCHMIED, R., AND TREUTLEIN, P. Quantum metrology with nonclassical states of atomic ensembles. *Reviews of Modern Physics 90*, 3 (2018), 035005. (Cited on page 17)

[275] PHILIPP, P., TARRATACA, L., AND BOETTCHER, S. Continuous-time quantum search on balanced trees. *Physical Review A 93*, 3 (2016), 032305. (Cited on pages 39 and 123)

[276] PINEL, O., JIAN, P., TREPS, N., FABRE, C., AND BRAUN, D. Quantum parameter estimation using general single-mode gaussian states. *Phys. Rev. A 88* (Oct 2013), 040102. (Cited on page 115)

[277] PIRANDOLA, S., BARDHAN, B. R., GEHRING, T., WEEDBROOK, C., AND LLOYD, S. Advances in photonic quantum sensing. *Nature Photonics 12*, 12 (2018), 724–733. (Cited on page 17)

[278] PLENIO, M. B., AND HUELGA, S. F. Dephasing-assisted transport: quantum networks and biomolecules. *New Journal of Physics 10*, 11 (2008), 113019. (Cited on page 39)

[279] PORTUGAL, R. *Quantum walks and search algorithms*, vol. 19. Springer, 2013. (Cited on pages 39, 121, and 134)

[280] POTTS, P. P., BRASK, J. B., AND BRUNNER, N. Fundamental limits on low-temperature quantum thermometry with finite resolution. *Quantum 3* (2019), 161. (Cited on page 47)

[281] PREISS, P. M., MA, R., TAI, M. E., LUKIN, A., RISPOLI, M., ZUPANCIC, P., LAHINI, Y., ISLAM, R., AND GREINER, M. Strongly correlated quantum walks in optical lattices. *Science 347*, 6227 (2015), 1229–1233. (Cited on pages 39 and 134)

[282] PUGLISI, A., SARRACINO, A., AND VULPIANI, A. Temperature in and out of equilibrium: A review of concepts, tools and attempts. *Physics Reports 709-710* (2017), 1–60. Temperature in and out of equilibrium: a review of concepts, tools and attempts. (Cited on page 46)

[283] PUSEY, M. F., BARRETT, J., AND RUDOLPH, T. On the reality of the quantum state. *Nature Physics 8*, 6 (2012), 475–478. (Cited on page 12)

[284] QUINN, T., AND KOVALEVSKY, J. The development of modern metrology and its role today. *Philosophical Transactions of the Royal Society A: Mathematical, Physical and Engineering Sciences 363*, 1834 (2005), 2307–2327. (Cited on page 11)

[285] RAGY, S., JARZYNA, M., AND DEMKOWICZ-DOBRZAŃSKI, R. Compatibility in multiparameter quantum metrology. *Physical Review A 94*, 5 (2016), 052108. (Cited on pages 34 and 103)

[286] RAO, C. R. Information and the accuracy attainable in the estimation of statistical parameters. In *Breakthroughs in statistics*. Springer, 1992, pp. 235–247. (Cited on pages 16 and 23)

[287] RAZAVIAN, S., BENEDETTI, C., BINA, M., AKBARI-KOURBOLAGH, Y., AND PARIS, M. G. Quantum thermometry by single-qubit dephasing. *The European Physical Journal Plus 134*, 6 (2019), 284. (Cited on pages 49 and 78)

[288] RAZAVIAN, S., PARIS, M. G. A., AND GENONI, M. G. On the quantumness of multiparameter estimation problems for qubit systems. *Entropy 22*, 11 (2020), 1197. (Cited on pages 101, 103, 104, and 105)

[289] RAZZOLI, L., GHIRARDI, L., SILOI, I., BORDONE, P., AND PARIS, M. G. A. Lattice quantum magnetometry. *Phys. Rev. A 99* (Jun 2019), 062330. (Cited on page 39)

[290] RAZZOLI, L., PARIS, M. G. A., AND BORDONE, P. Continuous-time quantum walks on planar lattices and the role of the magnetic field. *Phys. Rev. A 101* (Mar 2020), 032336. (Cited on page 63)

[291] REBENTROST, P., MOHSENI, M., KASSAL, I., LLOYD, S., AND ASPURU-GUZIK, A. Environment-assisted quantum transport. *New Journal of Physics 11*, 3 (2009), 033003. (Cited on page 39)

[292] REINA, J. H., QUIROGA, L., AND JOHNSON, N. F. Decoherence of quantum registers. *Physical Review A 65*, 3 (2002), 032326. (Cited on page 83)

[293] RELEASE: THE NOBEL PRIZE IN PHYSICS 2022, P. The nobel prize in physics 2022. (Cited on page xiv)

[294] RIEDEL, M. F., BINOSI, D., THEW, R., AND CALARCO, T. The european quantum technologies flagship programme. *Quantum Science and Technology 2*, 3 (2017), 030501. (Cited on page xiv)

[295] RISTÈ, D., AND DICARLO, L. Digital feedback in superconducting quantum circuits. *arXiv:1508.01385 [cond-mat, physics:quant-ph]* (Aug. 2015). arXiv: 1508.01385. (Cited on page 128)

[296] ROSSI, M., MASON, D., CHEN, J., AND SCHLIESSER, A. Observing and verifying the quantum trajectory of a mechanical resonator. *Phys. Rev. Lett. 123* (Oct 2019), 163601. (Cited on page 124)

[297] ROSSI, M., MASON, D., CHEN, J., TSATURYAN, Y., AND SCHLIESSER, A. Measurement-based quantum control of mechanical motion. *Nature 563*, 7729 (2018), 53–58. (Cited on pages 121 and 124)

[298] ROSSI, M. A., CATTANEO, M., PARIS, M. G., AND MANISCALCO, S. Non-markovianity is not a resource for quantum spatial search on a star graph subject to generalized percolation. *Quantum Measurements and Quantum Metrology 5*, 1 (2018), 40–49. (Cited on page 39)

[299] ROSSI, M. A., AND PARIS, M. G. Entangled quantum probes for dynamical environmental noise. *Physical Review A 92*, 1 (2015), 010302. (Cited on page 90)

[300] ROSSI, M. A. C., ALBARELLI, F., TAMASCELLI, D., AND GENONI, M. G. Noisy quantum metrology enhanced by continuous nondemolition measurement. *Phys. Rev. Lett. 125* (Nov 2020), 200505. (Cited on page 121)

[301] ROUCHON, P. Models and feedback stabilization of open quantum systems, 2015. (Cited on page 125)

[302] ROUCHON, P., AND RALPH, J. F. Efficient quantum filtering for quantum feedback control. *Phys. Rev. A 91* (Jan 2015), 012118. (Cited on pages 125 and 126)

[303] ROY, S., AND BRAUNSTEIN, S. L. Exponentially enhanced quantum metrology. *Physical review letters 100*, 22 (2008), 220501. (Cited on page 18)

[304] RUBIO, J., ANDERS, J., AND CORREA, L. A. Global quantum thermometry. *Phys. Rev. Lett. 127* (Nov 2021), 190402. (Cited on page 47)

[305] ŠAFRÁNEK, D. Discontinuities of the quantum fisher information and the bures metric. *Phys. Rev. A 95* (May 2017), 052320. (Cited on page 102)

[306] ŠAFRÁNEK, D. Estimation of gaussian quantum states. *Journal of Physics A: Mathematical and Theoretical 52*, 3 (dec 2018), 035304. (Cited on page 115)

[307] ŠAFRÁNEK, D. Simple expression for the quantum fisher information matrix. *Physical Review A 97*, 4 (2018), 042322. (Cited on page 27)

[308] SALARI SEHDARAN, F., BINA, M., BENEDETTI, C., AND PARIS, M. G. Quantum probes for ohmic environments at thermal equilibrium. *Entropy 21*, 5 (2019), 486. (Cited on page 157)

[309] SCHIRBER, M. Nobel prize: Quantum entanglement unveiled. *Physics 15* (2022), 153. (Cited on page xiv)

[310] SCHLOSSHAUER, M., AND FINE, A. Implications of the pusey-barrett-rudolph quantum no-go theorem. *Phys. Rev. Lett. 108* (Jun 2012), 260404. (Cited on page 12)

[311] SCHMID, D., AND SPEKKENS, R. W. Contextual advantage for state discrimination. *Physical Review X 8*, 1 (2018), 011015. (Cited on page 12)

[312] SCIPY. https://docs.scipy.org/doc/scipy/reference/generated/scipy.optimize.minimize.html. (Cited on page 128)

[313] SEAH, S., NIMMRICHTER, S., GRIMMER, D., SANTOS, J. P., SCARANI, V., AND LANDI, G. T. Collisional quantum thermometry. *Phys. Rev. Lett. 123* (Oct 2019), 180602. (Cited on page 48)

[314] SERAFINI, A. *Quantum continuous variables: a primer of theoretical methods*. CRC press, 2017. (Cited on pages 92, 105, 115, and 117)

[315] SERAFINI, A., AND MANCINI, S. Determination of Maximal Gaussian Entanglement Achievable by Feedback-Controlled Dynamics. *Phys. Rev. Lett. 104*, 22 (June 2010), 220501. (Cited on page 121)

[316] SEVESO, L., ALBARELLI, F., GENONI, M. G., AND PARIS, M. G. A. On the discontinuity of the quantum fisher information for quantum statistical models with parameter dependent rank. *Journal of Physics A: Mathematical and Theoretical 53*, 2 (dec 2019), 02LT01. (Cited on page 102)

[317] SEVESO, L., BENEDETTI, C., AND PARIS, M. G. The walker speaks its graph: global and nearly-local probing of the tunnelling amplitude in continuous-time quantum walks. *Journal of Physics A: Mathematical and Theoretical 52*, 10 (2019), 105304. (Cited on page 39)

[318] SEVESO, L., AND PARIS, M. G. Quantum enhanced metrology of hamiltonian parameters beyond the cramèr–rao bound. *International Journal of Quantum Information 18*, 03 (2020), 2030001. (Cited on page 20)

[319] SEVESO, L., ROSSI, M. A., AND PARIS, M. G. Quantum metrology beyond the quantum cramér-rao theorem. *Physical Review A 95*, 1 (2017), 012111. (Cited on page 25)

[320] SHAJI, A., AND SUDARSHAN, E. C. G. Who's afraid of not completely positive maps? *Physics Letters A 341*, 1-4 (2005), 48–54. (Cited on page 7)

[321] SHELBY, R. M., LEVENSON, M. D., PERLMUTTER, S. H., DEVOE, R. G., AND WALLS, D. F. Broad-band parametric deamplification of quantum noise in an optical fiber. *Physical review letters 57*, 6 (1986), 691. (Cited on page 89)

[322] SHENVI, N., KEMPE, J., AND WHALEY, K. B. Quantum random-walk search algorithm. *Physical Review A 67*, 5 (2003), 052307. (Cited on page 39)

[323] SHERRY, D. Thermoscopes, thermometers, and the foundations of measurement. *Studies in History and Philosophy of Science Part A 42*, 4 (2011), 509–524. (Cited on page 45)

[324] SIDHU, J. S., AND KOK, P. Geometric perspective on quantum parameter estimation. *AVS Quantum Science 2*, 1 (2020), 014701. (Cited on pages 17 and 25)

[325] SIDHU, J. S., OUYANG, Y., CAMPBELL, E. T., AND KOK, P. Tight bounds on the simultaneous estimation of incompatible parameters. *Physical Review X 11*, 1 (2021), 011028. (Cited on page 103)

[326] SMIRNE, A., KOŁODYŃSKI, J., HUELGA, S. F., AND DEMKOWICZ-DOBRZAŃSKI, R. Ultimate precision limits for noisy frequency estimation. *Physical review letters 116*, 12 (2016), 120801. (Cited on page 17)

[327] STACE, T. M. Quantum limits of thermometry. *Physical Review A 82*, 1 (2010), 011611. (Cited on page 48)

[328] STINESPRING, W. F. Positive functions on c*-algebras. *Proceedings of the American Mathematical Society 6*, 2 (1955), 211–216. (Cited on page 7)

[329] STRELTSOV, A., ADESSO, G., AND PLENIO, M. B. Colloquium: Quantum coherence as a resource. *Reviews of Modern Physics 89*, 4 (2017), 041003. (Cited on pages 67 and 77)

[330] SUZUKI, J. Explicit formula for the holevo bound for two-parameter qubit-state estimation problem. *Journal of Mathematical Physics 57*, 4 (2016), 042201. (Cited on pages 31 and 103)

[331] SUZUKI, J. Information geometrical characterization of quantum statistical models in quantum estimation theory. *Entropy 21*, 7 (2019), 703. (Cited on page 103)

[332] SZCZYKULSKA, M., BAUMGRATZ, T., AND DATTA, A. Multi-parameter quantum metrology. *Advances in Physics: X 1*, 4 (2016), 621–639. (Cited on page 17)

[333] SZORKOVSZKY, A., DOHERTY, A. C., HARRIS, G. I., AND BOWEN, W. P. Mechanical squeezing via parametric amplification and weak measurement. *Phys. Rev. Lett. 107* (Nov 2011), 213603. (Cited on page 121)

[334] TAMASCELLI, D., OLIVARES, S., ROSSOTTI, S., OSELLAME, R., AND PARIS, M. G. Quantum state transfer via bloch oscillations. *Scientific Reports 6*, 1 (2016), 1–7. (Cited on page 39)

[335] TANG, H., LIN, X.-F., FENG, Z., CHEN, J.-Y., GAO, J., SUN, K., WANG, C.-Y., LAI, P.-C., XU, X.-Y., WANG, Y., ET AL. Experimental two-dimensional quantum walk on a photonic chip. *Science advances 4*, 5 (2018), eaat3174. (Cited on page 40)

[336] TEBBENJOHANNS, F., MATTANA, M. L., ROSSI, M., FRIMMER, M., AND NOVOTNY, L. Quantum control of a nanoparticle optically levitated in cryogenic free space. *Nature 595*, 7867 (2021), 378–382. (Cited on pages 121 and 124)

[337] THOMSEN, L. K., MANCINI, S., AND WISEMAN, H. M. Spin squeezing via quantum feedback. *Phys. Rev. A 65*, 6 (June 2002), 061801. (Cited on page 121)

[338] TÓTH, G., AND APELLANIZ, I. Quantum metrology from a quantum information science perspective. *Journal of Physics A: Mathematical and Theoretical 47*, 42 (2014), 424006. (Cited on page 16)

[339] TURNER, J., AND BIAMONTE, J. Topological classification of time-asymmetry in unitary quantum processes. *Journal of Physics A: Mathematical and Theoretical 54*, 23 (2021), 235301. (Cited on page 42)

[340] VENEGAS-ANDRACA, S. E. Quantum walks: a comprehensive review. *Quantum Information Processing 11*, 5 (2012), 1015–1106. (Cited on pages 39 and 121)

[341] WANG, J., AND MANOUCHEHRI, K. *Physical implementation of quantum walks*. Springer, 2013. (Cited on page 40)

[342] WANG, Y. AND WU, S. AND WANG, W. Optimal quantum search on truncated simplex lattices. *Phys. Rev. A 101* (Jun 2020), 062333. (Cited on page 123)

[343] WEINSTEIN, E., AND WEISS, A. J. A general class of lower bounds in parameter estimation. *IEEE Transactions on Information Theory 34*, 2 (1988), 338–342. (Cited on page 16)

[344] WIECZOREK, W., HOFER, S. G., HOELSCHER-OBERMAIER, J., RIEDINGER, R., HAMMERER, K., AND ASPELMEYER, M. Optimal state estimation for cavity optomechanical systems. *Phys. Rev. Lett. 114* (Jun 2015), 223601. (Cited on page 124)

[345] WIENER, N. *Cybernetics or Control and Communication in the Animal and the Machine*. MIT press, 2019. (Cited on page xiii)

[346] WILCOX, R. M. Exponential operators and parameter differentiation in quantum physics. *Journal of Mathematical Physics 8*, 4 (1967), 962–982. (Cited on page 94)

[347] WINELAND, D. J., BOLLINGER, J. J., ITANO, W. M., MOORE, F. L., AND HEINZEN, D. J. Spin squeezing and reduced quantum noise in spectroscopy. *Phys. Rev. A 46* (Dec 1992), R6797–R6800. (Cited on page 17)

[348] WISEMAN, H. M. Quantum theory of continuous feedback. *Phys. Rev. A 49* (Mar 1994), 2133–2150. (Cited on pages 121 and 126)

[349] WISEMAN, H. M., AND MILBURN, G. J. Quantum theory of optical feedback via homodyne detection. *Phys. Rev. Lett. 70* (Feb 1993), 548–551. (Cited on page 121)

[350] WISEMAN, H. M., AND MILBURN, G. J. *Quantum Measurement and Control*. Cambridge University Press, New York, 2010. (Cited on pages 121, 123, 126, and 137)

[351] WONG, T. G., AND AMBAINIS, A. Quantum search with multiple walk steps per oracle query. *Physical Review A 92*, 2 (2015), 022338. (Cited on page 39)

[352] WONG, T. G., AND MEYER, D. A. Irreconcilable difference between quantum walks and adiabatic quantum computing. *Physical Review A 93*, 6 (2016), 062313. (Cited on pages 39 and 123)

[353] WONG, T. G., TARRATACA, L., AND NAHIMOV, N. Laplacian versus adjacency matrix in quantum walk search. *Quantum Information Processing 15*, 10 (2016), 4029–4048. (Cited on page 42)

[354] WONG, T. G., WÜNSCHER, K., LOCKHART, J., AND SEVERINI, S. Quantum walk search on kronecker graphs. *Phys. Rev. A 98* (Jul 2018), 012338. (Cited on page 123)

[355] WOOTTERS, W. K., AND ZUREK, W. H. A single quantum cannot be cloned. *Nature 299*, 5886 (1982), 802–803. (Cited on page 12)

[356] XIE, D., XU, C., AND WANG, A. M. Optimal quantum thermometry by dephasing. *Quantum information processing 16*, 6 (2017), 1–15. (Cited on page 49)

[357] YAN, Z., ZHANG, Y.-R., GONG, M., WU, Y., ZHENG, Y., LI, S., WANG, C., LIANG, F., LIN, J., XU, Y., ET AL. Strongly correlated quantum walks with a 12-qubit superconducting processor. *Science 364*, 6442 (2019), 753–756. (Cited on page 40)

[358] YANG, Y., CHIRIBELLA, G., AND HAYASHI, M. Attaining the ultimate precision limit in quantum state estimation. *Communications in Mathematical Physics 368*, 1 (2019), 223–293. (Cited on pages 17 and 31)

[359] YOUNG, A. W., ECKNER, W. J., SCHINE, N., CHILDS, A. M., AND KAUFMAN, A. M. Tweezer-programmable 2d quantum walks in a hubbard-regime lattice. *Science 377*, 6608 (2022), 885–889. (Cited on pages 40 and 134)

[360] YUEN, H., AND LAX, M. Multiple-parameter quantum estimation and measurement of nonselfadjoint observables. *IEEE Transactions on Information Theory 19*, 6 (1973), 740–750. (Cited on page 17)

[361] ZANARDI, P., PARIS, M. G. A., AND CAMPOS VENUTI, L. Quantum criticality as a resource for quantum estimation. *Phys. Rev. A 78* (Oct 2008), 042105. (Cited on page 18)

[362] ZATELLI, F., BENEDETTI, C., AND PARIS, M. G. Scattering as a quantum metrology problem: A quantum walk approach. *Entropy 22*, 11 (2020), 1321. (Cited on page 39)

[363] ZHANG, N., CHEN, C., BAI, S.-Y., WU, W., AND AN, J.-H. Non-markovian quantum thermometry. *Phys. Rev. Applied 17* (Mar 2022), 034073. (Cited on page 48)

[364] ZHANG, S., MARTIN, L. S., AND WHALEY, K. B. Locally optimal measurement-based quantum feedback with application to multiqubit entanglement generation. *Phys. Rev. A 102* (Dec 2020), 062418. (Cited on pages 121 and 129)

[365] ZHANG, Z.-Z., AND WU, W. Non-markovian temperature sensing. *Physical Review Research 3*, 4 (2021), 043039. (Cited on page 48)

[366] ZHAO, X., YANG, Y., AND CHIRIBELLA, G. Quantum metrology with indefinite causal order. *Physical Review Letters 124*, 19 (2020), 190503. (Cited on page 18)

[367] ZHUANG, Q., ZHANG, Z., AND SHAPIRO, J. H. Entanglement-enhanced neyman–pearson target detection using quantum illumination. *JOSA B 34*, 8 (2017), 1567–1572. (Cited on page 17)

[368] ZIV, J., AND ZAKAI, M. Some lower bounds on signal parameter estimation. *IEEE transactions on Information Theory 15*, 3 (1969), 386–391. (Cited on page 16)